



The
University
Of
Sheffield.

**Optimising the peptide mediated synthesis of Pt alloy
magnetic nanoparticles in patterned arrays for future data
storage**

By:

Rosie Jarrald

A thesis submitted in partial fulfilment of the requirements for the degree of
Doctor of Philosophy

The University of Sheffield
Faculty of Science
Department of Chemistry

August 2019

ABSTRACT

Traditional magnetic data storage is starting to reach its physical limits, meaning there is little scope for fabrication of much smaller devices whilst still storing large amounts of data. Due to the ever-increasing demand to store more data an alternative approach needs to be realised to overcome this. One solution to this is bit patterned media. Bit patterned media is where each bit of information is stored on an individual magnetic island, therefore increasing the areal density of hard-drives and allowing a theoretical areal density of 50 Tbit/in² to be achieved. However, a cost-effective method for producing this type of media has yet to be realised. In this thesis the development and optimisation of magnetic nanoparticles and the nanoscale patterning of these on a surface is investigated with the aim of developing greener biological routes to nanotechnological devices.

One type of materials that has received a great deal of interest for this application is platinum alloy nanoparticles of CoPt and FePt. Pt alloy nanoparticles are one of the few magnetic materials that have a high enough magnetocrystalline anisotropy to remain magnetically stable at dimensions of a few nanometres. However, only nanoparticles in a certain crystal phase possess these magnetic properties. This phase is known as the L1₀ phase and current synthesis methods require a high temperature annealing step to achieve the formation of this phase. This high temperature annealing step leads to problems with sintering and agglomeration of the nanoparticles as well as this harsh reaction conditions and solvents are required.

An alternative approach for the synthesis of these nanoparticles is through the use of biology. Previously, peptides that show specificity for L1₀ phase CoPt and FePt nanoparticles were identified from biopanning techniques. These peptides were incorporated into nanoparticle mineralisation reactions with the aim of directing the synthesis towards L1₀ in a more sustainable synthetic method (without annealing), however resultant NPs did not possess the expected magnetic properties for the L1₀ phase. In this thesis, these known peptides are investigated using SPOT peptide array technology to understand how the peptides interact with the materials, which regions of the peptide are important and if any improvements to these sequences can be made. Screening was carried out against nanoparticles, metal ion precursors and during synthesis reactions. Peptides identified from screening were then selected for use in nanoparticle synthesis reactions. Using these peptides in synthesis reactions it has been possible to generate NPs with increased coercivities compared to control NPs. Peptides KLSRMDHIHHH and KLSRHMHIHHH were

used in a CoPt synthesis reaction and resulted in coercivity values of 107 and 104 Oe respectively. Using peptide KLSMKPSRP in an FePt synthesis reaction resulted in the highest coercivity of 141 Oe being obtained.

Literature has also shown that small quantities of soft metal dopants have improved L_{10} properties. In this thesis several candidates (Ag and Bi) were investigated and optimised, 2% bismuth doping was identified as optimum for the synthesis of CoPt and FePt NPs. The research then combines both approaches of using bismuth doping and synthesis in the presence of peptides to achieve even higher coercivities. Synthesis of CoPt NPs in the presence of bismuth and peptide KLSRMDHIHHH resulted in an increased coercivity value of 125 Oe, this is higher than bismuth doping alone (55 Oe) and synthesis in the presence of the peptide only (107 Oe).

Finally, nanoscale patterned surfaces were generated using interferometric lithography. Using this method, it was possible to generate periodic dot patterns with a period of 204 nm, making this a step towards the fabrication of bit patterned media.

TABLE OF CONTENTS

Abstract.....	I
Table of Contents.....	I
List of Figures.....	I
List of Tables.....	XI
List of Abbreviations.....	XIII
List of Amino Acids.....	XV
Author Declarations and Contributions.....	XVII
Acknowledgements.....	XVIII
1 Introduction.....	2
1.1 Magnetism.....	2
1.1.1 Atomic Magnetism.....	2
1.1.2 Magnetic Ordering.....	2
1.1.3 Magnetic Domains.....	3
1.1.4 Magnetic Anisotropy.....	4
1.1.5 Magnetic Hysteresis.....	4
1.1.6 Magnetism on the nanoscale.....	6
1.2 Magnetic Data Storage.....	7
1.2.1 History.....	7
1.2.2 Basic principles of data storage.....	7
1.2.3 Increasing areal density.....	9
1.2.4 Patterned media.....	9
1.2.5 Requirements for bit patterned media.....	11
1.3 Magnetic Nanoparticles.....	11
1.3.1 Pt alloy nanoparticles.....	11
1.4 Synthesis of magnetic nanoparticles.....	12
1.4.1 High temperature chemical reduction.....	13
1.4.2 Reverse micelle method.....	14
1.4.3 Sol-gel method.....	14
1.4.4 Polymer or colloid synthesis.....	15
1.4.5 Use of biological templates.....	16
1.4.6 Summary of synthesis methods.....	22
1.5 SPOT Peptide Technology.....	28
1.6 Nanoscale Patterning.....	30
1.6.1 Self-assembled monolayers (SAMs).....	30
1.6.2 Alkane thiol SAMs.....	31
1.6.3 Micro-contact printing (μ CP).....	32
1.6.4 Photo and electron beam lithography (EBL).....	33
1.6.5 Interferometric Lithography (IL).....	34
1.7 Conclusions and Project Outline.....	36
1.8 Summary of Chapters.....	37
2 Materials and Methods.....	40
2.1 Expression and Purification of MjHSP.....	40
2.1.1 Starter Cultures.....	40
2.1.2 IPTG Induction.....	40
2.1.3 Purification of MjHsp.....	40
2.1.4 SDS-PAGE.....	41
2.2 SPOT peptide synthesis.....	41

2.2.1	Synthesis of SPOT peptide arrays	41
2.2.2	Deprotection of SPOT peptide arrays	44
2.2.3	Binding assays	44
2.2.4	Peptide Synthesis	45
2.3	Synthesis of magnetic nanoparticles	45
2.3.1	CoPt nanoparticles	45
2.3.2	FePt nanoparticles	47
2.3.3	Annealing of nanoparticles	47
2.3.4	Synthesis of NPs in the presence of free peptide	47
2.4	Formation of self-assembled monolayers	47
2.4.1	Preparation of titania surfaces.....	47
2.4.2	Preparation of gold surfaces.....	48
2.5	Characterisation of self-assembled monolayers.....	48
2.5.1	Water contact angles	48
2.5.2	X-ray Photoelectron Spectroscopy (XPS)	49
2.6	Patterning of surfaces	50
2.6.1	Interferometric Lithography (IL)	50
2.7	Attachment of peptides to titania surfaces	51
2.7.1	Glutaraldehyde crosslinking.....	51
2.7.2	GMBS crosslinking.....	51
2.8	Mineralisation of NPs on surfaces	52
2.9	Characterisation of Nanoparticles and Surfaces.....	52
2.9.1	Transmission electron microscopy (TEM)	52
2.9.2	Scanning Electron Microscopy (SEM).....	54
2.9.3	Powder X-ray diffraction (XRD)	55
2.9.4	Vibrating sample magnetometry (VSM)	56
2.9.5	Inductively Coupled Plasma Optical Emission Spectrometry (ICP-OES)	57
2.9.6	Atomic Force Microscopy (AFM).....	57
3	Patterning on the nanoscale	61
3.1	Nanoscale patterning of titania surfaces	62
3.1.1	APTES formation on titania.....	62
3.1.2	Attachment of peptides and proteins to surfaces	64
3.1.3	Interferometric lithography (IL)	71
3.2	Nanoscale patterning of gold surfaces	72
3.2.1	Formation of amine terminated SAMs on gold	72
3.2.2	Interferometric lithography (IL)	73
3.3	Summary	79
4	Synthesis and doping of Pt alloy magnetic nanoparticles	82
4.1	L1 ₀ , L1 ₂ and A1 phase Pt alloy nanoparticles	83
4.2	CoPt Nanoparticle Synthesis and Characterisation	84
4.3	FePt Nanoparticle Synthesis and Characterisation	87
4.3.1	Synthesis of Annealed FePt.....	90
4.4	Doping the nanoparticle reactions	92
4.4.1	Silver doping.....	92
4.4.2	Bismuth Doping.....	96
4.5	CoPt synthesised in the presence of MjHSP	100
4.5.1	Silver doped CoPt synthesised in the presence of MjHSP	104
4.5.2	Bismuth doped CoPt synthesised in the presence of MjHSP.....	108
4.6	Summary	110
5	SPOT Peptide Array Design and Optimisation	113
5.1	Lead Sequences.....	113

5.2	Peptide Array Design.....	116
5.2.1	Alanine Scanning.....	116
5.2.2	Truncation.....	116
5.2.3	Positional Scanning.....	116
5.2.4	High frequency.....	117
5.2.5	Reversal and scrambling of sequences.....	117
5.2.6	Cyclisation.....	117
5.2.7	Overall Array Design.....	117
5.3	Optimisation of binding conditions for nanoparticle binding.....	119
5.3.1	Concentration of NPs and binding time.....	119
5.3.2	Use of blocking buffers.....	120
5.3.3	Washing conditions.....	121
5.4	Binding conditions for metal ion binding.....	122
5.5	Binding conditions for synthesis reactions.....	122
5.6	Comparison of detection and imaging software.....	123
5.7	Signal to noise ratio.....	124
5.7.1	Sources of Error and Random Variation.....	124
6	CoPt Peptide Array Screening.....	127
6.1	Nanoparticle Binding.....	127
6.1.1	Lead sequences.....	127
6.1.2	Alanine Scanning.....	127
6.1.3	Truncation.....	128
6.1.4	Positional Scanning.....	133
6.1.5	High frequency.....	137
6.1.6	Reversal and Scrambling.....	138
6.1.7	Cyclic.....	140
6.2	Metal Ion Binding.....	141
6.2.1	Lead sequences.....	142
6.2.2	Alanine Scanning.....	143
6.2.3	Truncation.....	145
6.2.4	Positional Scanning.....	150
6.2.5	High Frequency.....	153
6.3	Screening against a synthesis reaction.....	154
6.3.1	Lead sequences.....	155
6.3.2	Truncation.....	156
6.3.3	Positional Scanning.....	157
6.3.4	High Frequency.....	158
6.4	Summary and Discussion.....	158
7	FePt Peptide Array Screening.....	164
7.1	Nanoparticle binding.....	164
7.1.1	Lead sequences.....	164
7.1.2	Alanine scanning.....	164
7.1.3	Truncation.....	165
7.1.4	Positional scanning.....	169
7.1.5	High frequency.....	172
7.1.6	Reversal and scrambling.....	173
7.1.7	Cyclic.....	173
7.2	Metal ion binding.....	174
7.2.1	Lead sequences.....	176
7.2.2	Alanine scanning.....	176
7.2.3	Truncation.....	178

7.2.4	Positional scanning	179
7.2.5	High frequency	179
7.3	Screening against a synthesis reaction	181
7.3.1	Lead sequences	182
7.3.2	Alanine scanning	182
7.3.3	Truncation	183
7.3.4	Positional scanning	185
7.3.5	High frequency	187
7.4	Summary and Discussion	187
8	Design and selection of peptides for use in nanoparticle synthesis reactions	191
8.1	Comparison of FePt and CoPt peptide arrays	191
8.1.1	Lead sequences	195
8.1.2	High affinity sequences	197
8.2	Peptide selection and design	198
8.3	Synthesis of CoPt using designed and selected peptides	200
8.4	Synthesis of FePt using designed and selected peptides	205
8.5	Synthesis of CoPt with peptides and bismuth doping	210
8.6	Synthesis of FePt with peptides and bismuth doping	215
8.7	Summary and Discussion	218
9	Conclusions and Future Work	224
9.1	Synthesis of magnetic nanoparticles	224
9.1.1	Silver and Bismuth Doping	224
9.1.2	Synthesis of CoPt in the presence of MjHSP	224
9.1.3	Peptide array screening	225
9.1.4	Synthesis of MNPs using designed and selected peptides	226
9.2	Nanoscale Patterning	228
9.3	Outlook and Future Directions	230
10	References	232
11	Appendix	240
11.1	SPOT Peptide Array Data	240
11.2	XPS Data	247

LIST OF FIGURES

Figure 1.1.1 – Illustration of magnetic ordering in bulk materials, arrow direction – direction of magnetisation and arrow size – the magnitude of magnetisation on the atoms.	3
Figure 1.1.2 – Unit cell of bcc iron highlighting the easy, medium and hard axes.	4
Figure 1.1.3 – Magnetisation curve of a ferro or ferrimagnetic material. H – applied magnetic field, M – magnetisation, M_s – saturation magnetisation, M_r – residual magnetisation and H_c – coercivity.	5
Figure 1.2.1 - Image showing the components of a hard disk drive.	8
Figure 1.2.2 - Schematic showing the recording principle for longitudinal magnetic recording (left) and perpendicular magnetic recording (right).	9
Figure 1.2.3 – Schematic showing bits patterned in conventional granular media and lithographically patterned discrete track media and bit patterned media.	10
Figure 1.3.1 – A) A1 disordered face centered cubic structure and B) $L1_0$ ordered face centered tetragonal structure.	12
Figure 1.4.1 – Schematic showing an overview of the phage display process. Schematic showing an overview of the phage display process. Peptide library is exposed to nanoparticles, unbound phage is washed away, and eluted phage are amplified. Amplified phage is then exposed to nanoparticles again, unbound phage is washed away, and tight binders are eluted. This process is repeated three times so that three panning rounds are performed.	16
Figure 1.5.1 – A) Example of an autopeptide spotter (Intavis MultiPepRSi) and B) photograph of a peptide array during synthesis once bromophenol blue has been added to check synthesis is progressing correctly.	28
Figure 1.6.1 – Schematic of a SAM. Blue circle represents chemisorbing headgroup and red circle represents the end group. Adapted from figure 2 in reference 109.	31
Figure 1.6.2 – Schematic showing the micro-contact printing process. 1) Stamp is inked with SAM 2) Stamp is placed in conformal contact with surface and 3) Stamp is removed to produce SAM on surface.	32
Figure 1.6.3 – Schematic of photo beam lithography. Alkanethiol SAM (pink) on gold surface is exposed to UV light through a photomask. Areas not covered by the photomask are photo oxidised and can be removed.	33
Figure 1.6.4 – Lloyds mirror arrangement set up for interferometric lithography.	34
Figure 1.7.1 - Schematic showing a biotemplated dot array of MNPs, built up on a gold surface with a self-assembled monolayer that peptide/protein is able to bind to (either directly or indirectly through the use of crosslinkers) and MNPs attached via this peptide/protein. ...	37
Figure 1.8.1 – Schematic showing the overall project aims and how they link together, as well as highlighting the content of each chapter.	38
Figure 2.2.1 – Preparation of the membrane and amino acid coupling. 1) Untreated cellulose with available hydroxyl groups are reacted with Fmoc-beta-alanine followed by deprotection with piperidine 2) Reaction with Fmoc-11-aminoundecanoic acid followed by deprotection with piperidine to give membrane with free amino group ready for amino acid coupling 3) Reaction of membrane with activated amino acid 4) Deprotection with piperidine to give free amino group ready for further amino acid coupling reactions. Steps 3 and 4 will be repeated until desired peptide has been synthesised on the membrane.	43
Figure 2.4.1 - Chemical structure of 3-aminopropyltriethoxysilane.	48
Figure 2.4.2 - Chemical structure of 6-amino-1-hexanethiol hydrochloride.	48
Figure 2.5.1 - Schematic of the XPS process highlighting photoionisation of an atom that occurs by ejection of a 1s electron. (Figure adapted from Figure 1.2 in reference ¹²⁷).	49
Figure 2.6.1 - Schematic showing Lloyd's mirror setup for interferometric lithography.	50

Figure 2.7.1 - Mechanism for crosslinking peptide to an amine terminated SAM using glutaraldehyde.....	51
Figure 2.7.2 - Mechanism for crosslinking peptides to an amine terminated SAM using GMBS.	52
Figure 2.9.1 - Schematic of TEM (Figure adapted from figure 2.8 in reference ⁸).....	53
Figure 2.9.2 - Schematic showing typical set up of an SEM. (Figure adapted from figure 2.6 in reference ⁸).	55
Figure 2.9.3 - Schematic of a VSM (Figure adapted from figure 1 in reference ¹³³).	56
Figure 2.9.4 - Schematic showing set up of an AFM. The sample is mounted onto a scanner, and the cantilever and tip are positioned near the surface. Cantilever deflections are recorded by a photodiode that detects the position of the laser beam that is deflected off the back of the cantilever. (Figure adapted from figure 2.14 in reference ¹²⁹).....	58
Figure 3.1.1 – Chemical structure of 3-aminopropyltriethoxysilane (APTES).....	62
Figure 3.1.2 – Contact angle measurements for APTES formation on titania surfaces. A) Different volumes of APTES used per 20 ml and all incubated in solution for 1 hour. B) 0.1 ml APTES per 20 ml used and kept in solution for different lengths of time. C) 1.0 ml APTES used per 20 ml and kept in solution for different lengths of time. Dotted line represents literature value for contact angle. ^{138,139}	63
Figure 3.1.3 – Schematic showing the process of GMBS and GA crosslinking cysteine tagged peptide or MjHSP cage protein to amine terminated SAMs on titania. Followed by surfaces being put into NP mineralisation reactions. For mechanism of crosslinking process refer to Figure 2.7.1 and Figure 2.7.2.	65
Figure 3.1.4 – SEM micrographs for glutaraldehyde crosslinking MjHSP using different incubation times of 1.5 hours (left) and 3 hours (right). Scale bars represent 300 μm and images at 400 x magnification.	66
Figure 3.1.5 – SEM micrographs for GA crosslinking carried out in 1 or 2 steps. 3-hour incubation time used for both methods and a concentration of 1% v/v. Scale bars represent 300 μm on 400 x magnification image and 50 μm on 1600 x magnification image.	67
Figure 3.1.6 – SEM micrographs of GA crosslinking carried out for 3 hours followed by mineralisation of NPs and mineralisation carried out on a surface containing only the amine terminated SAM (no crosslinker). Images were recorded before and after sonication of the samples to ensure that NPs were chemisorbed and not just physisorbed. All images are at 220 x magnification and scale bars represent 500 μm	69
Figure 3.1.7 - SEM micrographs for GMBS crosslinking carried out using 0.25 mg/ml (left) and 0.5 mg/ml (right) peptide concentration. Scale bars represent 300 μm and images are at 400 x magnification.....	70
Figure 3.1.8 - SEM micrographs of GMBS crosslinking followed by mineralisation of NPs and mineralisation carried out on a surface containing only the amine terminated SAM (no crosslinker). Images were recorded before and after sonication of the samples to ensure that NPs were chemisorbed and not just physisorbed. All images are at 220 x magnification and scale bars represent 500 μm . Black spots on bottom right image are from where ‘burning’ of the sample has occurred during imaging.....	71
Figure 3.1.9 – AFM images of APTES SAMs on titania that were patterned using IL. A) sample exposed to dose of 2.81 Jcm^{-2} and B) sample exposed to dose of 1.08 Jcm^{-2} . Angle of exposure is 20°.....	72
Figure 3.2.1 – Schematic showing the process used to generate line patterns on gold. 1) Gold surface with amine terminated thiol SAM was exposed to laser light in a Lloyd’s mirror configuration 2) Degraded SAM was washed away to leave line array of the SAM and 3) Sample is placed in gold etch solution so that remaining gold between the regions of SAM is removed.....	73

Figure 3.2.2 - AFM Images of A) Exposure dose of 36 Jcm^{-2} and B) and C) exposure dose of 48 Jcm^{-2} . All samples were placed in etch solution for 12 minutes and an exposure angle of 20° was used. 74

Figure 3.2.3 – AFM images collected from sample produced using an exposure dose of 48 Jcm^{-2} followed by etching for 12 minutes and at an exposure angle of 20° . Dotted lines represent regions used to calculate average period of pattern and this has been presented graphically. Average line width of 158 nm and height of 8.3 nm was calculated. 75

Figure 3.2.4 – Sample generated from using an exposure dose of 40 Jcm^{-2} followed by etching time for 12 mins and an exposure angle of 20° . Line width calculated as 151 nm and height of SAM as 10.7 nm. Dotted lines represent where data was collected to calculate period of pattern and height of SAM. 76

Figure 3.2.5 – Schematic showing the process used to generate dot patterns on gold surfaces. 1) Gold surface with amine terminated thiol SAM was exposed to laser light in a Lloyd's mirror configuration 2) After one exposure this would result in a line array generated 3) Sample was rotated by 90° and exposed to laser light once again and 4) Degraded SAM was washed away to leave a dot array pattern on gold. 77

Figure 3.2.6 – **Top:** First exposure was at a dose of 48 Jcm^{-2} , sample was then rotated 90° and exposed to a dose of 38 Jcm^{-2} . A line width of 204 nm and height of 7.3 nm was calculated. **Bottom:** First exposure was at a dose of 40 Jcm^{-2} , sample was then rotated 90° and exposed to a dose of 33 Jcm^{-2} . A line width of 194 nm and height of 5.3 nm was calculated. Samples were placed into etch solution for 12 minutes and angle of exposure was set to 20° 78

Figure 4.1.1 – Theoretical powder XRD for the A1 and $L1_0$ phases of Co/Fe Pt alloys with lattice planes labelled. Crystallographic data downloaded from the crystallography open database and modelled using Mercury software. 83

Figure 4.2.1 - ICP-OES analysis of CoPt NPs synthesised from different ratios of cobalt and platinum. Y axis – the percentage cobalt in the final product. X axis – the equivalents of cobalt and platinum used. 84

Figure 4.2.2 - XRD data for synthesised CoPt with lattice planes labelled. Particle size calculated from the Scherrer equation is 7.8 nm. 85

Figure 4.2.3 – Magnetic hysteresis of CoPt nanoparticles at 300 K. Y axis is magnetic moment in emu/g and X axis is magnetic field strength in kOe. Coercivity of 15 Oe. 86

Figure 4.2.4 - pH profile for a CoPt synthesis reaction. Addition of Co^{2+} and Pt^{2+} salts after 10 minutes and addition of NaBH_4 at 15 minutes followed by incubation of the reaction for 45 minutes. 86

Figure 4.3.1 – ICP-OES analysis of FePt NPs synthesised from different ratios of cobalt and platinum. Y axis is the percentage iron in the final product. X axis is the equivalents of iron and platinum used. 87

Figure 4.3.2 - XRD data collected for FePt nanoparticles with lattice planes labelled. Diameter calculated from the Scherrer equation is 8.5 nm. Broad peak at $\approx 20^\circ$ is from glass capillary. 88

Figure 4.3.3 – Magnetic hysteresis of FePt NPs carried out at 300 K. X axis is magnetic field strength in kOe and Y axis is normalised magnetic moment. Coercivity of 11 Oe. 88

Figure 4.3.4 - TEM micrographs of FePt nanoparticles and histogram showing particle size distribution. Scale bars represent 50 nm. 89

Figure 4.3.5 - pH profile of a FePt synthesis reaction, addition of Fe^{2+} and Pt^{2+} occurs after 1 minute and addition of NaBH_4 at 11 minutes. 90

Figure 4.3.6 – XRD spectrum of FePt pre (grey) and post annealing (black). Lattice planes for A1 and $L1_0$ phase FePt have been labelled. Broad peak at $\approx 20^\circ$ is from glass capillary. 91

Figure 4.3.7 – Room temperature (300 K) VSM of annealed FePt. Y axis is magnetic moment in emu/g. X axis is magnetic field strength in kOe. Coercivity of 10.8 kOe. 91

Figure 4.4.1 - XRD spectrum of CoPt (black line), 2% Ag doped CoPt (dark grey) and 10% Ag doped CoPt (light grey).	92
Figure 4.4.2 - VSM data collected at 300 K for 0, 2, 5, 7 and 10% Ag doped CoPt. Inset figure shows coercivity values for each sample.	94
Figure 4.4.3 – ICP-OES data for Ag doped CoPt samples. Left: Purple – molar percentage of Co present, yellow – molar percentage of Pt present and grey – molar percentage of Ag present. Right: Molar percentage of Ag present in samples plotted against theoretical percentage Ag doping.	95
Figure 4.4.4 - XRD for FePt (black) and 5% Ag doped FePt (grey). Lattice planes that are typical of FePt have been labelled. Room temperature VSM data for FePt (black) and 5% Ag doped FePt (blue) with coercivity values of 11 Oe and 240 Oe respectively. X axis is magnetic field strength in kOe and Y axis is normalised magnetic moment. Broad peak at $\approx 20^\circ$ is from glass capillary.	96
Figure 4.4.5 - XRD spectrum of CoPt and 5% Bi doped CoPt with lattice planes labelled that are typical of CoPt.	97
Figure 4.4.6 - Room temperature (300 K) VSM data for 0, 1, 2, 3 and 5% Bi doped CoPt. Inset figure shows coercivity values for each sample.	98
Figure 4.4.7 – ICP-OES data for bismuth doped CoPt samples. Left: purple – molar percentage Co, yellow – molar percentage Pt and grey – molar percentage Bi. Right: Difference between actual and theoretical doping in final NP.	99
Figure 4.4.8 - XRD for FePt (black) and 2% Bi FePt (grey) with lattice planes labelled that are typical of FePt. * represents peaks caused by the presence of Bi or BiPt in the sample. ¹⁵⁷ Room temperature VSM of FePt (black) and 2% Bi doped FePt blue with coercivity values of 11 Oe and 278 Oe respectively. X axis represents magnetic field strength in kOe and Y axis is normalised magnetic moment. Broad peak at $\approx 20^\circ$ is from glass capillary.	100
Figure 4.5.1 - Gel filtration curves for the purification of MjHSP and SDS-PAGE gel for the corresponding gel filtration runs.	101
Figure 4.5.2 - TEM micrograph of MjHSP stained with 0.75 % uranyl acetate, scale bar represents 100 nm. Histogram showing size distribution of the protein cages.	102
Figure 4.5.3 – XRD spectrum of CoPt (black) and CoPt synthesised in the presence of MjHSP (grey) with lattice planes typical of CoPt labelled. Room temperature (300 K) VSM data for CoPt synthesised in the presence of MjHSP. Coercivity value of 41 Oe.	102
Figure 4.5.4 - XRD of CoPt synthesised in the presence of MjHSP before (grey) and after (black) annealing at 825 °C under an argon atmosphere for 1 hour. Lattice planes for A1 and L1 ₀ phase CoPt have been labelled. Broad peak at $\approx 20^\circ$ is from glass capillary.	103
Figure 4.5.5 - Room temperature (300 K) VSM data for annealed CoPt particles. Coercivity of 225 Oe.	104
Figure 4.5.6 - TEM micrographs of a) 0% Ag doped b) 2 % Ag doped c) 5 % Ag doped d) 7 % Ag doped and e) 10 % Ag doped all synthesised in the presence of MjHSP. Scale bars represent 50 nm (a, c, d and e) and 10 nm (b). Histogram showing particle size distribution for Ag doped samples.	105
Figure 4.5.7 - SDS-PAGE of CoPt nanoparticles synthesised in the presence of MjHSP and containing different amounts of Ag doping. Units of molecular weight are kDa.	106
Figure 4.5.8 - XRD of CoPt synthesised in the presence of MjHSP (black), with 5% (grey) and 2% (light grey) Ag doping. Peaks characteristic of CoPt have been labelled. * represent peaks that relate to Ag. Broad peak at $\approx 20^\circ$ is from glass capillary.	107
Figure 4.5.9 - Room temperature (300 K) VSM of Ag doped CoPt synthesised in the presence of MjHSP. Inset figure shows coercivity values for each sample.	108
Figure 4.5.10 - XRD data for CoPt and 2% Bi doped CoPt both synthesised in the presence of MjHSP.	109

Figure 4.5.11 - Room temperature (300 K) VSM data for Bi doped CoPt synthesised in the presence of MjHSP. Inset figure showing coercivity values for each sample.....	109
Figure 5.1.1 – Schematic showing the binding assays carried out for CoPt and FePt nanoparticles i) metal ion binding ii) nanoparticle binding and iii) synthesis reaction.	115
Figure 5.2.1 – Overview of the process used for peptide array design and synthesis.	118
Figure 5.2.1 - Schematic to show the layout of test peptide arrays	119
Figure 5.2.2 - Test arrays after binding CoPt NPs for 1 and 3 hours at concentrations of 0.036, 0.18, 0.4 and 4 mg/ml.....	120
Figure 5.2.3 - Test arrays used to investigate the effects of different blocking buffers on NP binding. All binding was carried out at 0.18 mg/ml.....	121
Figure 5.2.4 - Test arrays used to investigate different washing conditions after particles have been bound. All particle binding was carried out at 0.18 mg/ml.	122
Figure 5.5.1 – SNR data for all five lead sequences that have been screened against CoPt NPs. Dark green – ImageQuantTL software used for detection and grey – ImageLab software used for detection. Dotted grey line represents background noise. Signal to Noise Ratio (SNR)	123
Figure 6.1.1 - Peptide arrays after NP binding has been carried out A) 1 st generation array and B) 2 nd generation array.....	127
Figure 6.1.2 – SNR data for all five lead sequences screened against CoPt nanoparticles. Dotted grey line represents background noise.	127
Figure 6.1.3 – A) Truncation data for LS1. Dark green – LS1, teal – sequence with similar intensity to lead, dark blue – increased binding and light blue – decreased binding B) Truncation data highlighting the importance of lysine. Dark green - lead peptide, teal - sequence containing lysine and light blue - sequence with lysine removed. Dotted grey line represents background noise.	129
Figure 6.1.4 - A) Truncation data for LS2. Dark green – LS2, teal – sequence with similar intensity to lead, dark blue – increased binding and light blue – decreased binding B) Truncation data highlighting the importance of lysine. Dark green - lead peptide, teal - sequence containing lysine and light blue - sequence with lysine removed. Dotted grey line represents background noise.	130
Figure 6.1.5 – Truncation data for LS3. Dark green – LS3, teal – sequence with similar intensity, dark blue – increased binding and light blue – decreased binding. Dotted grey line represents background noise.	131
Figure 6.1.6 - Truncation data for LS4 highlighting the importance of basic residues, lysine and arginine. Dark green – LS4, Teal - sequences containing either lysine or arginine and light blue - sequences with lysine or arginine removed. Dotted grey line represents background noise.....	132
Figure 6.1.7 - A) Truncation data for LS5. Dark green – LS5, teal – sequence with similar intensity to lead, dark blue – increased binding intensity and light blue – decreased binding B) Truncation data showing glutamic acid is unfavourable. Dark green - lead peptide, light blue - sequence containing glutamic acid and dark blue - sequence with glutamic acid removed. Dotted grey line represents background noise.	133
Figure 6.1.8 - Positional scanning data for LS2. Dark green – LS2, teal – similar intensity to LS2, light blue – decreased binding. Red boxes highlighted the amino acid residues that have been substituted. Dotted grey line represents background noise.	134
Figure 6.1.9 – Positional scanning data for LS3. Dark green – LS3, dark blue – increased intensity to LS3, light blue – decreased binding and teal – similar intensity to LS3. Red boxes highlighted the amino acid residues that have been substituted. Dotted grey line represents background noise.....	135
Figure 6.1.10 - Positional scanning data for LS4. Dark green – LS4, teal - similar intensity to LS4, light blue – decreased binding. Red boxes highlighted the amino acid residues that have been substituted. Dotted grey line represents background noise.	136

Figure 6.1.11 - Positional scanning data for LS5. Dark green – LS5, teal - similar intensity to LS5, light blue – decreased binding. Red boxes highlighted the amino acid residues that have been substituted. Dotted grey line represents background noise.	137
Figure 6.1.12 – High frequency binding intensity data compared to the original high frequency sequence (HHSSPKLR), highlighting sequences that have a reduction binding intensity (light blue) and those with an increased binding intensity (dark blue). Dotted grey line represents background noise.....	138
Figure 6.1.13 - Sequences with the highest binding intensity from the high frequency array compared to the original lead peptide sequences. Light blue - reduced binding intensity and dark blue - increased binding intensity. Dotted grey line represents background noise.	138
Figure 6.1.14 - Scrambling and reversal of lead peptide sequences. Teal - lead peptide sequences, grey - reversed sequence and diagonal striped - scrambled sequence. Dotted grey line represents background noise.....	139
Figure 6.1.15 - Comparison of cyclic and linear lead peptide sequences. Teal - lead peptide sequence, diagonal striped - constrained in a loop and grey – corresponding sequence with cysteines replaced with serine. Dotted grey line represents background noise.	140
Figure 6.2.1 - Peptide arrays that have been incubated in Co ²⁺ solution overnight to assess binding. A) Cobalt (II) sulphate used and B) Cobalt (II) chloride used.	142
Figure 6.2.2 – Peptide array that was incubated in Pt ²⁺ solution overnight to assess binding.	142
Figure 6.2.3 – SNR data for all five lead sequences screened against Pt ²⁺	143
Figure 6.2.4 - Alanine scanning data for LS1. Dark green - lead peptide sequence and light blue - sequences that have decreased SNR.	143
Figure 6.2.5 - Alanine scanning data for LS2. Dark green – LS2, dark blue - increased SNR and light blue - decreased SNR.	144
Figure 6.2.6 - Alanine scanning data for LS4. Dark green – LS4, dark blue - increased SNR and light blue - decreased SNR.	144
Figure 6.2.7 - Alanine scanning data for LS5. Dark green - lead peptide sequence, dark blue - increased SNR and light blue - decreased SNR.	145
Figure 6.2.8 – Truncation data for LS1. Dark green – LS1, teal - similar SNR to lead sequence and light blue - decreased SNR.	146
Figure 6.2.9 - Truncation data for LS2. Dark green – LS2 and light blue - decreased SNR. .	147
Figure 6.2.10 - Truncation data for LS3. Dark green – LS3, dark blue - increased SNR and light blue - decreased SNR.	148
Figure 6.2.11 - A) Truncation data for LS4 and B) Truncation data highlighting the importance of methionine. Dark green – LS4, teal - similar SNR to lead, dark blue - increased SNR and light blue - decreased SNR.	149
Figure 6.2.12 - Truncation data for LS5. Dark green – LS5, teal - similar SNR to lead and light blue - decreased SNR.	150
Figure 6.2.13 - Positional scanning data highlighting the importance of methionine for binding to Pt ²⁺ . Teal - lead peptide sequences, grey - sequences where methionine has been incorporated. Red boxes highlighted the amino acid residues that have been substituted.	151
Figure 6.2.14 - Positional scanning data highlighting the importance of lysine and histidine. Teal - lead peptide sequences, grey - sequences where lysine and histidine has been incorporated. Red boxes highlighted the amino acid residues that have been substituted.	152
Figure 6.2.15 - Positional scanning data for the incorporation of glutamic acid. Teal - lead peptide sequences, grey - sequences where glutamic acid has been incorporated. Red boxes highlighted the amino acid residues that have been substituted.	153

Figure 6.2.16 - Signal to noise ratio for high frequency screening. Dark green - lead peptide sequences, dark blue - increased SNR and light blue - decreased SNR. Inset figure highlights charge plotted against SNR values, purple line highlights increasing SNR relates to higher overall charge.....	154
Figure 6.3.1 - Synthesis arrays for screening against a CoPt synthesis reaction. A) 1st generation peptide array and B) 2nd generation peptide array	155
Figure 6.3.2 – SNR data for all five lead sequences screened against an CoPt synthesis reaction. Dotted grey line represents background noise.	156
Figure 6.3.3 - Truncation data for LS3. Dark green - lead peptide sequence, teal - similar SNR to the lead and light blue - reduced SNR. Grey dotted line represents background noise.	157
Figure 6.3.4 - Positional scanning data for LS3, LS4 and LS5. Dark green - lead peptide sequence, dark blue - increased SNR and light blue - decreased SNR.....	158
Figure 7.1.1 – Peptide arrays after NP binding has been carried out for 16 hours A) 1 st generation array and B) 2 nd generation array.....	164
Figure 7.1.2 – SNR data for all five lead sequences screened against FePt nanoparticles. Dotted grey line represents background noise.	164
Figure 7.1.3 – Alanine scanning data for LS1. Dark green – LS1 and light blue – sequences with decreased SNR. Dotted grey line represents background noise.	165
Figure 7.1.4 – Alanine scanning data for LS4. Dark green – LS4 and light blue – sequences with decreased SNR. Dotted grey line represents background noise.	165
Figure 7.1.5 – Truncation data for LS1. Dark green – LS1, teal – similar SNR to LS1 and light blue – decreased SNR. Dotted grey line represents background noise.....	166
Figure 7.1.6 – A) Truncation data for LS2 and B) Data highlighting the importance of peptide length. Dark green – LS2, dark blue – increased SNR, teal – similar SNR and light blue – decreased SNR all compared to LS2. Dotted grey line represents background noise.....	167
Figure 7.1.7 – Truncation data for LS4. Dark green – LS4, teal – similar SNR and light blue – decreased SNR all compared to LS4. Dotted grey line represents background noise. Red boxes highlight where arginine/lysine has been removed from sequence.	168
Figure 7.1.8 - Truncation data for LS5. Dark green – LS5, teal – similar SNR and light blue – decreased SNR all compared to LS5. Dotted grey line represents background noise.....	169
Figure 7.1.9 – Positional scanning data for LS4. Dark green – LS4 and light blue – decreased SNR compared to LS4. Dotted grey line represents background noise. Red boxes highlight positions at which substitutions have been made.	170
Figure 7.1.10 – Positional scanning data for LS5. Dark green – LS5 and light blue – decreased SNR compared to LS5. Dotted grey line represents background noise. Red boxes highlight positions at which substitutions have been made.	170
Figure 7.1.11 – Positional scanning data for LS4 and LS5 highlighting the effect of glutamic acid. Dark green – lead sequences and light blue – decreased SNR compared to LS. Dotted grey line represents background noise. Red boxes highlight positions at which substitutions have been made.....	171
Figure 7.1.12 – Positional scanning data for LS4 and LS5 highlighting the effect of different basic residues. Dark green – lead sequences and light blue – decreased SNR compared to LS. Dotted grey line represents background noise. Red boxes highlight positions at which substitutions have been made.....	171
Figure 7.1.13 – High frequency binding intensity data compared to the five original sequences and the two high frequency peptides that show an increase in SNR. Dark green – lead sequences and dark blue – high frequency peptides. Dotted grey line represents background noise.....	172
Figure 7.1.14 – Scrambling and reversal of lead peptide sequences. Teal – lead peptide, grey – reversed sequence and diagonal striped – scrambled sequence. Dotted grey line represents background noise.....	173

Figure 7.1.15 – Comparison of cyclic and linear lead peptide sequences. Teal – lead sequence, grey – constrained in a loop and diagonal striped – corresponding sequence with cysteines replaced with serine. Dotted grey line represents background noise.....	174
Figure 7.2.1 – Peptide arrays that have been incubated in Fe ²⁺ solution overnight to assess binding. A) 1 st generation array and B) second generation array.....	176
Figure 7.2.2 – SNR data for all five lead sequences screened against Fe ²⁺ (green) and Pt ²⁺ (orange).....	176
Figure 7.2.3 – Alanine scanning data for LS1. Dark green – LS1 and light blue – decreased SNR compared to LS1.	177
Figure 7.2.4 – Alanine scanning for LS2. Dark green – LS2, dark blue – increased SNR and light blue – decreased SNR both compared to LS2.....	177
Figure 7.2.5 – Alanine scanning for LS4. Dark green – LS4 and dark blue – increased SNR compared to LS4.	178
Figure 7.2.6 – Alanine scanning for LS5. Dark green – LS5 and dark blue – increased SNR compared to LS5.	178
Figure 7.2.7 – Positional scanning data for LS2. Dark green – LS2 and dark blue – increased SNR compared to LS2. Red boxes highlight positions at which substitutions have taken place.	179
Figure 7.2.8 – High frequency binding intensity data compared to original lead sequences. Dark green – lead sequences, light blue – decreased SNR and dark blue – increased SNR. Inset figure highlights overall charge on peptide plotted against SNR values.	181
Figure 7.3.1 – Outcome of arrays used for screening against an FePt synthesis reaction. A) 1 st generation array and B) 2 nd generation array.....	182
Figure 7.3.2 – SNR data for all five lead sequences screened against an FePt synthesis reaction. Dotted grey line represents background noise.	182
Figure 7.3.3 – Alanine scanning data for LS1. Dark green – lead sequence and light blue – decreased SNR. Dotted grey line represents background noise.	183
Figure 7.3.4 – Truncation data for LS3. Dark green – LS3, dark blue – increased SNR and light blue – decreased SNR compared to LS3. Dotted grey line represents background noise. .	184
Figure 7.3.5 – A) Truncation data for LS4 B) highlighting the importance of methionine. Dark green – LS4, dark blue – increased SNR and light blue – decreased SNR both compared to LS4. Dotted grey line represents background noise. Red boxes highlight positions at which methionine has been removed.....	185
Figure 7.3.6 – Positional scanning data for LS2. Dark green – LS2, dark blue – increased SNR and light blue – decreased SNR both compared to LS2. Dotted grey line represents background noise. Red boxes highlight positions at which substitutions have taken place.	185
Figure 7.3.7 – Positional scanning data for LS3. Dark green – LS3, dark blue – increased SNR and light blue – decreased SNR both compared to LS3. Dotted grey line represents background noise. Red boxes highlight positions at which substitutions have taken place.	186
Figure 7.3.8 – Positional scanning data for LS5. Dark green – LS5, dark blue – increased SNR and light blue – decreased SNR both compared to LS5. Dotted grey line represents background noise. Red boxes highlight positions at which substitutions have taken place.	187
Figure 8.1.1 – Normalised nanoparticle truncation data for A) LS1, B) LS2 and C) LS3. Star represents lead sequence.....	193
Figure 8.1.2 – Normalised nanoparticle truncation data for A) LS4 and B) LS5. Star represents lead sequence	194
Figure 8.1.3 – Normalised SNR values for lead sequences screened against CoPt and FePt nanoparticles, Pt ²⁺ , Fe ²⁺ and CoPt and FePt synthesis reactions.....	195

Figure 8.3.1 – ICP-OES data (circle) for CoPt NPs synthesised in the presence of different peptides plotted against signal to noise ratio data (diamond) for peptides binding ability to Pt ²⁺ . Purple dotted line represents ideal 50:50 ratio.....	202
Figure 8.3.2 – X-ray diffraction data for CoPt nanoparticles synthesised in the presence of peptides. Characteristic planes of CoPt are labelled.	203
Figure 8.3.3 – Room temperature (290 K) vibrating sample magnetometry data for CoPt NPs synthesised in the presence of peptides. X axis – normalised magnetic moment and Y axis – magnetic field strength in kOe. Inset figure shows coercivity values for each sample.....	205
Figure 8.4.1 – ICP-OES data for FePt NPs synthesised in the presence of different peptides. Dotted line represents ratio expected for FePt and FePt ₃	206
Figure 8.4.2 – X-ray diffraction data for FePt NPs synthesised in the presence of different peptides. Characteristic planes of FePt are labelled.....	207
Figure 8.4.3 – Top: Room temperature (290 K) VSM data for FePt NPs synthesised in the presence of designed and selected peptides. X axis is magnetic field strength (Oe) and Y-axis is normalised emu. Bottom: coercivity values for each sample in oersteds.	210
Figure 8.5.1 – ICP-OES data for CoPt NPs synthesised in the presence of peptides and the presence of peptides and 2% bismuth doping. Purple – molar percentage of cobalt, yellow – molar percentage of platinum and grey – molar percentage of bismuth.	212
Figure 8.5.2 – XRD data for CoPt NPs synthesised in the presence of peptides KLSLRHD (red) and KLSLRMDHIHHH (blue) and 2% bismuth doping. Planes characteristic of CoPt are labelled. Broad peak at ≈ 20° is from glass capillary.....	213
Figure 8.5.3 – Room temperature (290 K) VSM data. CoPt NPs (red), 2% Bi or 5% doped CoPt (green), NPs synthesised in presence of peptide (blue) and NPs synthesised in presence of peptide and 2% bismuth (purple).	215
Figure 8.6.1 - ICP-OES data for FePt NPs synthesised in the presence of peptides and the presence of peptides and 2% bismuth doping. Green – molar percentage of iron, yellow – molar percentage of platinum and grey – molar percentage of bismuth.	216
Figure 8.6.2 – XRD data for FePt NPs synthesised in the presence of peptides KLSLRHD (blue) and KLSMKPSRP (red). Characteristic planes of FePt are labelled. * peaks caused by presence of Bi or BiPt in sample. ¹⁵⁷ Broad peak at ≈ 20° is from glass capillary.	217
Figure 8.6.3 – Room temperature (290 K) VSM data. FePt NPs (red), 2% Bi doped FePt (green), NPs synthesised in presence of peptide (blue) and NPs synthesised in presence of peptide and 2% bismuth (purple).	218
Figure 9.3.1 – Schematic showing the process of incorporating dot arrays into a nanoparticle mineralisation reaction for the production of biotemplated nanoscale dot arrays of MNPs.	230
Figure 9.3.2 – TEM of a freeze etched and metal shadowed bacterial cell (<i>Desulfotomaculum nigrificans</i> strain NCIB 8706) revealing an s-layer with square lattice symmetry. Scale bar represents 200 nm. Reprinted from Figure 1 in Pum, D. and U.B Sleytr, Reassembly of s-layer proteins. Nanotechnology, 2014 with permission from Nanotechnology, Institute of Physics.	231
Figure 11.1.1 – Truncation data for LS4 from screening against CoPt NPs. White – reduced SNR, grey – similar SNR and teal – increased SNR.	240
Figure 11.1.2 – Alanine scanning data for LS1 from screening against Pt ²⁺	240
Figure 11.1.3 – Alanine scanning data for LS4 from screening against Pt ²⁺	241
Figure 11.1.4 – Alanine scanning data for LS5 from screening against Pt ²⁺	241
Figure 11.1.5 – Truncation data for LS3 from screening against a CoPt synthesis reaction.	242
Figure 11.1.6 – Alanine scanning data for LS1 screened against FePt NPs.....	242
Figure 11.1.7 – Alanine scanning data for LS4 from screening against FePt NPs.	243
Figure 11.1.8 – Truncation data for LS4 from screening against FePt NPs.....	243

Figure 11.1.9 – Alanine scanning data for LS1 screened against Fe ²⁺	244
Figure 11.1.10 – Alanine scanning data for LS2 screened against Fe ²⁺	244
Figure 11.1.11 – Alanine scanning data for LS4 screened against Fe ²⁺	245
Figure 11.1.12 – Alanine scanning data for LS5 screened against Fe ²⁺	245
Figure 11.1.13 – Alanine scanning for LS1 screened against an Fe ²⁺	246
Figure 11.1.14 – Truncation data for LS3 from screening against an FePt synthesis reaction.	246
Figure 11.1.15 – Truncation data for LS4 from screening against an FePt synthesis reaction.	247
Figure 11.2.1 – Survey scan for APTES on Ti at 0 degrees.	247
Figure 11.2.2 – Survey Scan for APTES on titania at 53 degrees.	248
Figure 11.2.3 – Survey scan for APTES on titania at 78 degrees.....	248
Figure 11.2.4 – Nitrogen 1s scan for APTES on titania at 0 degrees.....	249
Figure 11.2.5 – Nitrogen 1s scan for APTES on titania at 53 degrees.....	249

LIST OF TABLES

Table 1.4.1 - Binding loop sequences of selected Adhirons. ⁵⁷	17
Table 1.4.2 – Summary of different synthesis methods used for the production of CoPt nanoparticles. Data obtained from XRD and magnetic measurements has been summarised.	23
Table 1.4.3 – Summary of different synthesis methods used for the production of FePt nanoparticles. Data obtained from XRD and magnetic measurements has been summarised.	26
Table 2.1.1 - Components required for LB media and LB agar, this is then made up to 1 litre using ultrapure water and then autoclaved at 125 °C.....	40
Table 2.1.2 - Components required for making SDS-PAGE gels.....	41
Table 2.3.1 - Silver doping levels for each mineralisation reaction	46
Table 2.3.2 - Bismuth doping levels for each mineralisation reaction.....	46
Table 3.1.1 – Surface composition determined by quantifying XPS survey scans (600 to 0 eV) of an APTES SAM on a titania surface.	64
Table 3.1.2 – Results from curve fitting of the N 1s high resolution spectra of an APTES SAM on a titania surface.	64
Table 3.2.1 – Contact angle measurements for 6-amino-1-hexanethiol SAM on gold surface. Contact angle measurements repeated a minimum of five times on different areas of the surface.....	73
Table 4.1.1 – Table highlighting the difference in characteristic features as determined by XRD and VSM for the L1 ₂ , L1 ₀ and A1 crystal phases of Pt alloy NPs. XRD peaks in black – common to all phases, red – unique to L1 ₀ , blue – unique to L1 ₂ and orange – common to both L1 ₂ and L1 ₀ . ^{36,154}	84
Table 4.4.1 - Particle size for CoPt, 2 and 5 % Ag doped CoPt calculated from XRD using the Scherrer equation.	93
Table 4.4.2 – ICP-OES data for 0 and 5 % Ag doped FePt NPs.	96
Table 4.4.3 - Particle size for CoPt and 5 % Bi doped CoPt calculated from XRD using the Scherrer equation.	97
Table 4.4.4 – ICP-OES data for 0 and 2% bismuth doped samples.	100
Table 4.5.1 - Particle sizes calculated for CoPt and CoPt synthesised in the presence of MjHSP from XRD using the Scherrer equation.	102
Table 4.5.2 - Particle size for CoPt and annealed CoPt determined from XRD using the Scherrer equation.	103
Table 4.5.3 – Elemental composition of Ag doped samples synthesised in the presence of MjHSP.....	106
Table 4.5.4 - Particle size for cage CoPt, 2% Ag doped cage CoPt and 5% Ag doped cage CoPt as determined by the Scherrer equation from XRD.	107
Table 4.5.5 – Elemental composition of Bi doped samples synthesised in the presence of MjHSP.....	110
Table 4.6.1 – Summary of different synthesis methods used for CoPt and FePt and properties of resultant NPs formed.....	111
Table 5.1.1 – The isoelectric point (pI) and amino acid composition were analysed for the five lead peptide sequences using the ProtParam tool in ExPASy.	115
Table 6.1.1 – Change in signal to noise ratio compared to the original high frequency peptide HHSSPKLR. Green - increase in SNR greater than 0.1, red - decrease in SNR greater than 0.1 and grey - no significant change in SNR.....	137
Table 6.2.1 – Calculated charge densities for truncated peptides related to their SNR values.	146

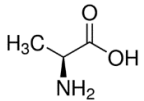
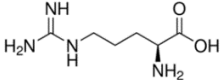
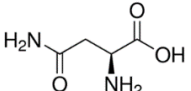
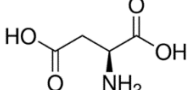
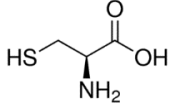
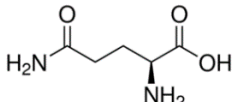
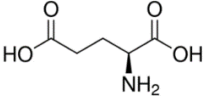
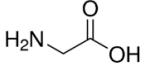
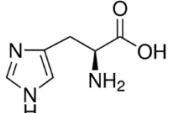
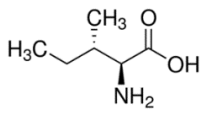
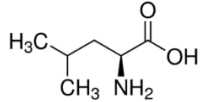
Table 6.2.2 - Signal to noise ratio compared to the lead high frequency peptide (HHSSPKLR). Green represents SNR increased by more than 10, red represents SNR decreased by more than 10 and grey represents sequences that have similar intensity to the lead.....	154
Table 7.1.1 – Change in signal to noise ratio compared to the original high frequency peptide HHSSPKLR. Green – increase in SNR greater than 0.1, red – decrease in SNR greater than 0.1 and grey – no significant change in SNR.	172
Table 7.2.1 – Summary of screening carried out against Pt ²⁺ . Green highlights represent important residues and red highlights represent unfavourable residues. Full data and graphs can be found in chapter 6.2.	175
Table 7.2.2 – Change in signal to noise ratio compared to the original high frequency peptide HHSSPKLR. Green – increase in SNR greater than 0.5, red – decrease in SNR greater than 0.5 and grey – no significant change in SNR.	180
Table 8.1.1 – Sequences with the highest SNR values for screening carried out against CoPt NPs, FePt NPs, Pt ²⁺ , Fe ²⁺ , a CoPt synthesis reaction and an FePt synthesis reaction. Yellow – presence of lysine at end of sequence for binding to NPs and green – highlights amino acid residues that were changed from the original lead sequence.	197
Table 8.2.1 – Designed and selected peptide sequences and which synthesis reactions they will be used in.	200
Table 8.3.1 – Table highlighting the difference in characteristic features as determined by XRD and VSM for the L1 ₂ , L1 ₀ and A1 crystal phases of Pt alloy NPs. XRD peaks in black – common to all phases, red – unique to L1 ₀ , blue – unique to L1 ₂ and orange – common to both L1 ₂ and L1 ₀ . ^{36,154}	200
Table 8.3.2 – Particle sizes calculated using the Scherrer equation for FePt NPs synthesised in the presence of different peptides.	203
Table 8.4.1 – Particle sizes calculated using the Scherrer equation for FePt NPs synthesised in the presence of different peptides, their suggested composition based on particle size and composition determined by ICP-OES.....	208
Table 8.5.1 – Particle sizes calculated using the Scherrer equation for CoPt NPs synthesised in the presence of different peptides and 2% bismuth doping.	213
Table 8.6.1 – Particle sizes calculated using the Scherrer equation for FePt NPs synthesised in the presence of different peptides and 2% bismuth doping.	217

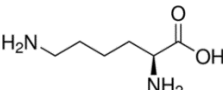
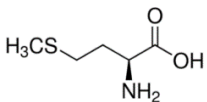
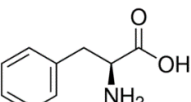
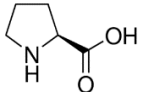
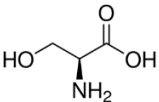
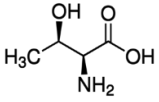
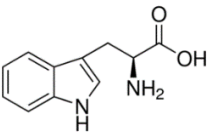
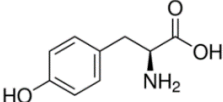
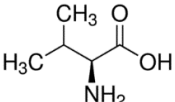
LIST OF ABBREVIATIONS

μCP	Micro contact printing
AFM	Atomic force microscopy
APS	Ammonium persulfate
APTES	3-aminopropyltriethoxysilane
BPB	Bromophenol Blue
BPM	Bit patterned media
BSA	Bovine serum albumin
CPMV	Cowpea mosaic virus
DAP	Dual affinity peptide
DCM	Dichloromethane
DMF	Dimethylformamide
DMSO	Dimethylsulphoxide
DTM	Discrete track media
EBL	Electron beam lithography
EDTA	Ethylenediaminetetraacetic acid
EDX	Energy dispersive x-ray
fcc	Face centered cubic
fct	Face centered tetragonal
Fmoc	Fluorenylmethyloxycarbonyl
FWHM	Full width half maximum
GA	Glutaraldehyde
GMBS	N-γ-maleimidobutyryl-oxysuccinimide ester
H_c	Coercivity
HDD	Hard disk drive
HEPES	4-(2-hydroxyethyl)-1-piperazineethanesulfonic acid
ICP-OES	Inductively coupled plasma optical emission spectrometry
IL	Interferometric lithography
IPTG	Isopropyl β-D-1-thiogalactopyranoside
LB	Luria-Bertani broth
LMR	Longitudinal magnetic recording
LS1	Lead sequence 1 – HNKHLPSTQPLA
LS2	Lead sequence 2 – KTHEIHSPLLHK
LS3	Lead sequence 3 – KSLSRHDHIHHH
LS4	Lead sequence 4 – SVSVGMPKSPRP
LS5	Lead sequence 5 – VISNHRESSRPL
MjHSP	<i>Methanococcus jannaschii</i> heat shock protein
MNP	Magnetic nanoparticle

M_r	Remnant magnetisation
M_s	Magnetic saturation
NP	Nanoparticle
PBS	Phosphate buffered saline
PDMS	Polydimethylsiloxane
PEG	Polyethylene glycol
PMR	Perpendicular magnetic recording
PSD	Photosensitive diode
QCM-D	Quartz crystal microbalance with dissipation
RAMAC	Random access method of accounting and computing
SAED	Small area electron diffraction
SAM	Self-assembled monolayer
SDS	Sodium dodecyl sulphate
SDS-PAGE	Sodium dodecyl sulphate polyacrylamide gel electrophoresis
SEM	Scanning electron microscopy
SQUID	Superconducting quantum interference device
tBu	Tertiary butyl
TEM	Transmission electron microscopy
TEMED	Tetramethylethylenediamine
UV	Ultraviolet
VSM	Vibrating sample magnetometry
XPS	X-ray photoelectron spectroscopy
XRD	X-ray diffraction

LIST OF AMINO ACIDS

Name and Structure	3 letter code	1 letter code
<p>Alanine</p> 	Ala	A
<p>Arginine</p> 	Arg	R
<p>Asparagine</p> 	Asn	N
<p>Aspartic Acid</p> 	Asp	D
<p>Cysteine</p> 	Cys	C
<p>Glutamine</p> 	Gln	Q
<p>Glutamic Acid</p> 	Glu	E
<p>Glycine</p> 	Gly	G
<p>Histidine</p> 	His	H
<p>Isoleucine</p> 	Ile	I
<p>Leucine</p> 	Leu	L

Lysine	Lys	K
		
Methionine	Met	M
		
Phenylalanine	Phe	F
		
Proline	Pro	P
		
Serine	Ser	S
		
Threonine	Thr	T
		
Tryptophan	Trp	W
		
Tyrosine	Tyr	Y
		
Valine	Val	V
		

AUTHOR DECLARATIONS AND CONTRIBUTIONS

Except where specific references have been made to other sources the work. This thesis is the original work of the author and has not been submitted wholly or in part for another degree.

Chapter 3: Data in this chapter was collected with the help of Katie Lewthwaite (MChem) at The University of Sheffield who assisted with the optimisation of attachment of NPs onto surfaces. Katie carried out work under my supervision and direction as part of a Sheffield Undergraduate Research Experiment summer placement. IL and AFM was performed in collaboration with Anna Lishchuk and Charlie Smith in The Leggett Group at The University of Sheffield. SEM analysis was performed in collaboration with Cheryl Shaw at the Sorby Centre based at The University of Sheffield. All XPS data was collected by Deborah Hammond at The University of Sheffield.

Chapter 4: Data in this chapter was collected with the help of Tom Blundell (MChem) at The University of Sheffield who assisted with bismuth doping work carried out. Tom carried out work under my supervision and direction as part of his final year project. All ICP-OES data was collected by Neil Bramall at The University of Sheffield. VSM data was collected in collaboration with Mannan Ali at The University of Leeds. Annealing of nanoparticles was carried out by Neil Hind in the Department of Materials Science and Engineering at The University of Sheffield. XRD data was collected in collaboration with Craig Robertson at The University of Sheffield.

Chapters 5, 6 and 7: SPOT Peptide arrays were produced in collaboration with the Okochi group at Tokyo Institute of Technology. Optimisation of binding conditions for screening peptide arrays was carried out in collaboration with Masayoshi Tanaka and Aw Wei Liang Alvin (Tokyo Institute of Technology).

Chapter 8: ICP-OES data was collected by Neil Bramall at the University of Sheffield. VSM data was collected in collaboration with Mannan Ali at The University of Leeds. XRD data was collected in collaboration with Craig Robertson at The University of Sheffield.

ACKNOWLEDGEMENTS

Firstly, I would like to thank my supervisor Sarah for all her help, support and guidance over the past four years. Her positive attitude and way of coming up with new ideas has helped to keep me motivated and not get too disheartened when lab work didn't always go to plan! Sarah has always supported my development throughout my PhD and encouraged me to take on different opportunities, from carrying out research placements in Japan, to presenting posters and talks at conferences and supporting applications for funding. Thank you, Sarah!

Secondly, thank you to the rest of the Staniland Group (past and present), Andrea, Jenny, Scott, Lori, Zainab, Pawel, Lukas, Chris, Laura and Sam. You've all made working in the lab an enjoyable experience, even with all our differing music tastes! A special thanks goes to Andrea for all the times she has helped me troubleshoot experiments and for putting up with my never-ending questions about peptides! I'd also like to thank undergraduate students, Tom and Katie, for all their hard work.

To our collaborators at Tokyo Institute of Technology, Masayoshi, Okochi-sensei, Ilfa and Alvin. Thank you, for all your help and expertise relating to peptide arrays. As well as showing me what a fantastic country Japan is and how fun karaoke can be!

I would also like to thank everyone who has helped to train me on equipment and for sharing their expertise. Thanks goes to Mannan Ali for training and helping me with all VSM related issues and Craig Robertson for all his help with XRD. Special thanks go to Anna Lishchuk and Charlie Smith for all their help with interferometric lithography and AFM, without them generating patterned surfaces would have been even more of a challenge.

I also owe big thanks to my other chemistry family: Joe, Alec and Oli who have been there with me since day one of undergrad. I'm not sure I would've made it this far without you guys! Thanks for all the distractions and the fun two years spent living together. A big shout out goes to all the friends I've made across the chemistry department especially Jenna, Matt, Charlie, Sally and Hiwa. Jayne, Chrissie, Alice and Laura thanks for always asking how the lab work was going and most importantly providing a world away from science!

One of the biggest thanks goes to Chris for the endless encouragement and support you've given me over the past few years, and I look forward to our next adventures together whatever they might be.

Finally, I'd like to thank my parents for all the support and reassurance they've given me, since I decided to move to Sheffield and study chemistry, almost eight years ago. As well as trying and pretending to understand what it is that I do. Most of all thank you for putting up with me moving back home to write my thesis!

CHAPTER ONE: INTRODUCTION

1 INTRODUCTION

As traditional magnetic data storage is starting to reach its physical limits and due to the ever-increasing demand to store more data, an alternative solution needs to be realised to overcome this. Therefore, in this introduction chapter background that is relevant to the use of Pt alloy nanoparticles for future data storage applications will be discussed. Due to the multi-disciplinary nature of this project the background spans a number of distinct areas. As a result, the introduction has been split into three topics, magnetism and magnetic data storage (1.1 and 1.2), magnetic nanoparticles and their synthesis (1.3 and 1.4) and nanoscale patterning (1.6). Finally, the introduction includes an overview of the project aims as well as a summary of each chapter in this thesis.

1.1 MAGNETISM

Magnetism is a phenomenon that occurs when a charged particle is moved, for example a moving electron is able to generate a magnetic field. It can also be described as the response of a material to an external applied magnetic field.¹ The location of the electron and the structure of a material determine its magnetic properties.

1.1.1 ATOMIC MAGNETISM

All materials have some magnetic characteristics due to atoms containing electrons. In the absence of an external magnetic field some materials will have no remnant magnetism. It is possible that magnetism, at an atomic level, can still exist in these materials in the form of diamagnetism or paramagnetism.¹

A diamagnetic atom has no net magnetic moment in the absence of an applied field, and this is due to all the electrons being paired up. When a magnetic field is applied to the atom, the orbits of the electron around the nucleus are altered. This leads to an increase in the antiparallel alignment of the magnetic moments, which causes a slight magnetic repulsion.²

In a paramagnetic atom, at least one electron is unpaired, so the atom has a net spin. When no magnetic field is applied the spins are randomly orientated, leading to no magnetic moment. On application of an external magnetic field, realignment of the electrons dipoles occurs to align with the magnetic field. The result is a net magnetic moment in the direction of the applied field. However, if the external field is removed, the magnetic properties are lost and thermal fluctuations cause the spins to randomly orientate.¹

1.1.2 MAGNETIC ORDERING

Atomic structures that are ordered give rise to paramagnetic materials, here long-range ordering and remnant magnetism are observed in the absence of an external field. If ordering

is antiparallel across the entire lattice, then atomic spins will cancel out. This results in a bulk magnetic moment that is zero and these types of materials are called antiferromagnetic.²

When all atomic magnetic moments are aligned parallel to one another then long-range ordering causes remnant magnetism when the external field is removed. In this case the material is known as ferromagnetic.² This is the rarest form of magnetism and is typically only exhibited by certain transition metals (Fe, Co and Ni) and f-block elements as well as alloys and oxides of these elements.³

When there is a difference in the magnitude of the atomic magnetic moments and they are aligned antiparallel to each other, the moments do not cancel, and an overall net magnetisation is observed. In this case the material is known as ferrimagnetic.² These three types of magnetic ordering are represented schematically in Figure 1.1.1.

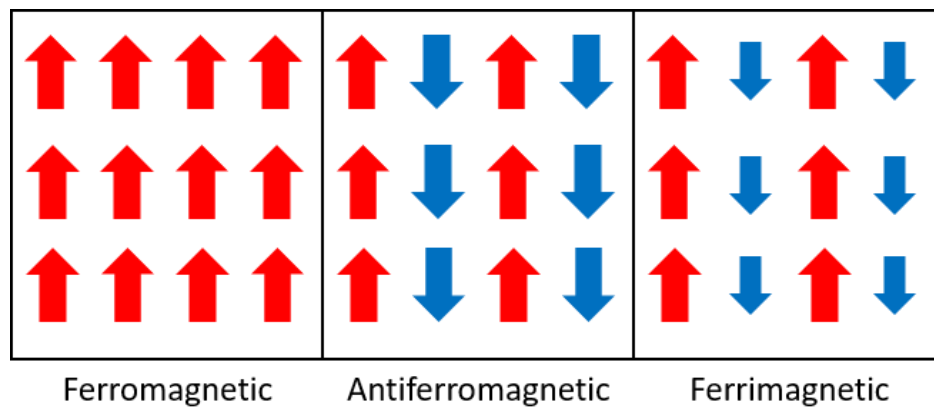


Figure 1.1.1 – Illustration of magnetic ordering in bulk materials, arrow direction – direction of magnetisation and arrow size – the magnitude of magnetisation on the atoms.

1.1.3 MAGNETIC DOMAINS

In 1907 it was proposed by Weiss *et al* that individual crystals of magnetic materials could be divided into magnetic zones, known as domains.⁴ It was not until 24 years later that these domains were observed.⁵ Bitter *et al* covered a crystal of nickel with an aqueous solution of magnetite particles and observed the sample under a microscope, noticing that the magnetite particles collected along the boundaries of the domain walls.⁵

Magnetic domains are believed to form to minimise the internal energy of the structure in magnetic materials.¹ During formation of domains magnetic poles do not form at the surface, this minimises the magnetostatic energy that is required for the material to generate a magnetic field.¹ To maintain the walls between domains, energy is required. This results in domains growing at a certain width that will reduce the energy balance between magnetocrystalline and exchange energy.¹

Application of an external field to a material results in the net magnetisation being changed. This occurs by either causing the domain walls to move or alignment of magnetisation within

domains in the direction of the applied field.² Domains that are favourably orientated with the external magnetic field will grow at the expense of unfavourably orientated areas, this results in domain walls migrating within the material until all domains are aligned.²

1.1.4 MAGNETIC ANISOTROPY

Magnetic anisotropy is the directional dependence of the magnetic properties of a material.⁶ There are several different types of anisotropy: magnetocrystalline, shape, stress, exchange and anisotropy induced by annealing, deformation and irradiation.⁶ However, of all these types only magnetic anisotropy is a property of the material and all others are induced.⁶ Materials that have magnetocrystalline anisotropy have different values of magnetisation in different directions and magnetisation tends to align along specific crystal planes. When a low field is required to saturate a particular axis this is known as the easy axis and when high field is required this is known as the hard axis.⁷ Different crystal structures have different easy and hard axes. For example, iron has a body centered cubic (bcc) structure and its easy axis lies along the (100) plane. Whereas the hard axis runs along the (111) plane and an intermediate plane is along the (110) plane.⁶ Therefore, it is easier to magnetise iron when a field is applied along the (100) plane as saturation magnetisation is achieved using much smaller fields. Materials with high magnetocrystalline anisotropy tend to be harder to demagnetise and as a result have higher coercivity values, making these materials ideal for applications in data storage.

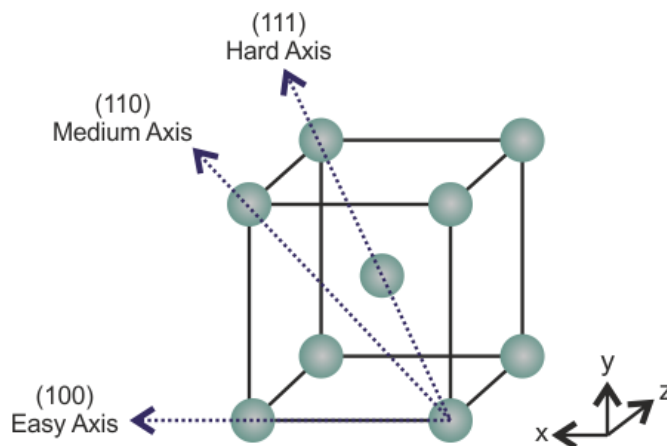


Figure 1.1.2 – Unit cell of bcc iron highlighting the easy, medium and hard axes.

1.1.5 MAGNETIC HYSTERESIS

Creating a hysteresis loop for a magnetic material allows identification of some key magnetic properties such as magnetic saturation (M_s), remnant magnetisation (M_r) and coercivity (H_c). All of these properties can be used to determine whether a material is magnetically hard or soft. A hysteresis loop can also be referred to as an MH curve this is because it shows the magnetisation (M) of a sample in an applied magnetic field of strength H .⁷ From an MH curve

it is possible to determine the susceptibility (χ) of a material by how magnetised (M) per unit volume it becomes in the presence of a magnetic field of strength (H):

$$M = \chi H \quad (1.1.1)$$

A hysteresis loop is generated by placing the material into an increasing magnetic field and the material is magnetised in this direction, until M_s is reached. M_s is the maximum value that the magnetic dipole moment per unit volume can take in the direction of an applied magnetic field.⁷ At M_s all the contributing atomic moments are aligned in the direction of the applied field. Once M_s is reached the field is then returned to zero. This allows any remnant magnetisation to be observed as this is the magnetisation remaining in the sample when the applied field is reduced to zero. Once the field has returned to zero an opposing magnetic field is used to magnetise the material in the opposite direction. This cycle is repeated several times and the switching between positive and negative fields is what generates the hysteresis loop. Finally, once the hysteresis loop has been generated it is possible to determine the coercivity of the sample. Coercivity relates to the width of the hysteresis loop and is the field required to reduce the magnetisation to zero from saturation.⁷ This process can be seen schematically in Figure 1.1.3.

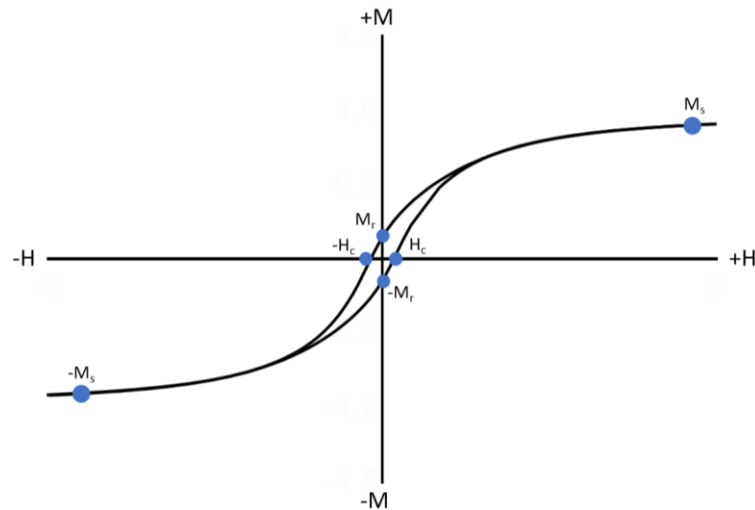


Figure 1.1.3 – Magnetisation curve of a ferro or ferrimagnetic material. H – applied magnetic field, M – magnetisation, M_s – saturation magnetisation, M_r – residual magnetisation and H_c – coercivity.

From a hysteresis loop it is possible to determine whether a material is magnetically hard or soft. This depends on the strength of the magnetic field required to reorder the magnetic domains. If a material is magnetically hard then application of a large magnetic field is required to reorder magnetic domains. Whereas for magnetically soft materials a much smaller magnetic field can be applied.⁶ This results in magnetically hard materials having a

large coercivity (≥ 100 Oe) and magnetically soft materials having a low coercivity (0 – 100 Oe). Materials that have coercivity values greater than 100 Oe are said to be magnetically hard, however materials with coercivities between 100 – 1000 Oe are termed as semi-hard and those that are greater than or equal to 1000 Oe are defined as hard magnets.¹ When a material must have stable magnetic properties magnetically hard materials are used. For example they are used in electric motors and generators as well as being suitable for the application of data storage.⁶ Magnetically soft materials are used when a change in magnetisation is required and are typically used in the core of transformers.⁶

1.1.6 MAGNETISM ON THE NANOSCALE

The magnetic properties of small particles are determined by their size. As a material is reduced in size down to the nanoscale the material can exhibit unique or sometimes even enhanced properties. Nanoparticles have a high surface area to volume ratio and therefore properties are dominated by surface atom contributions.⁸ As the size of a magnetic material is reduced, a critical volume is reached; at this point the energy required to create a domain wall is greater than the demagnetisation energy. Therefore, particles become single domain below the critical volume. Another factor for forming single domain particles is that a domain wall is typically 100 nm^2 and so cannot fit inside a nanoparticle.

Particles may become too small to maintain their magnetisation against thermal fluctuations and at this point the particle exhibits superparamagnetic behaviour. They are unable to retain bulk magnetic properties and are said to be magnetically unstable at room temperature. The thermal energy competes with the anisotropy energy of the grains and this is described by:

$$k_B T = k_u V_g \quad (1.1.2)$$

where k_B is the Boltzmann constant, T is the temperature, k_u is the magnetic anisotropy and V_g is the grain volume.⁹ Therefore, as the temperature increases the particle itself behaves like a paramagnetic atom.

Magnetic nanoparticles that are above the critical size limit can form multi domain particles.¹⁰ In multi domain particles some domains can be aligned in different directions or the direction of magnetisation can be rotated between domains. This allows a balance between the domain wall and demagnetisation energy to be achieved. In the absence of an applied field the magnetisation of the material is not saturated in one single direction and therefore multi domain particles tend to have lower remnant magnetisation than single domain particles.¹⁰

1.2 MAGNETIC DATA STORAGE

1.2.1 HISTORY

Magnetic recording was invented by Valdemar Poulsen more than a century ago.¹¹ However, it took more than 30 years for magnetic recording to become successfully commercialised in the form of magnetic tapes. Magnetic tapes were originally used in sound recording and data was stored by writing an electrical signal into a ferromagnetic tape using an electromagnetic head.^{12,13} By passing the tape over the electromagnetic head so that the magnetic pattern will induce the same electrical signal that produced the original signal allows data to be read. A disadvantage of using magnetic tapes is that they do not possess random access capability and as such data is only able to be read in a serial manner, meaning that it takes a long time to access data at different points in the recording.

In 1956 IBM introduced the 305 RAMAC (random access method of accounting and computing) that was capable of storing up to 5 MB of data.¹⁴⁻¹⁶ This was the first hard disk drive that combined the advantages of magnetic recording with random access capability. The 305 RAMAC stored data on approximately 50 spinning horizontal disks covered in a magnetic material and was comparable in size to two refrigerators.¹⁴

1.2.2 BASIC PRINCIPLES OF DATA STORAGE

The key requirements for a potential data storage system are that it should be possible to write, read and interpret the data on a suitable storage medium. Traditional magnetic recording involves information being written by flying read or write heads onto a rotating magnetic disk.¹⁴ Figure 1.2.1 highlights the key components that make up a typical hard disk drive (HDD). These key components are disk media, read and write heads, a spindle motor and an actuator. The disk is a magnetic recording medium that stores information and typically consists of a thin granular layer of a Co based alloy that is sputter coated onto a supporting layer of glass or aluminium.¹⁷ A head has two functions – to read and write information to the disk. The spindle motor spins the disk so that the actuator can carry the head to any part of the disk to read or write information.¹⁴

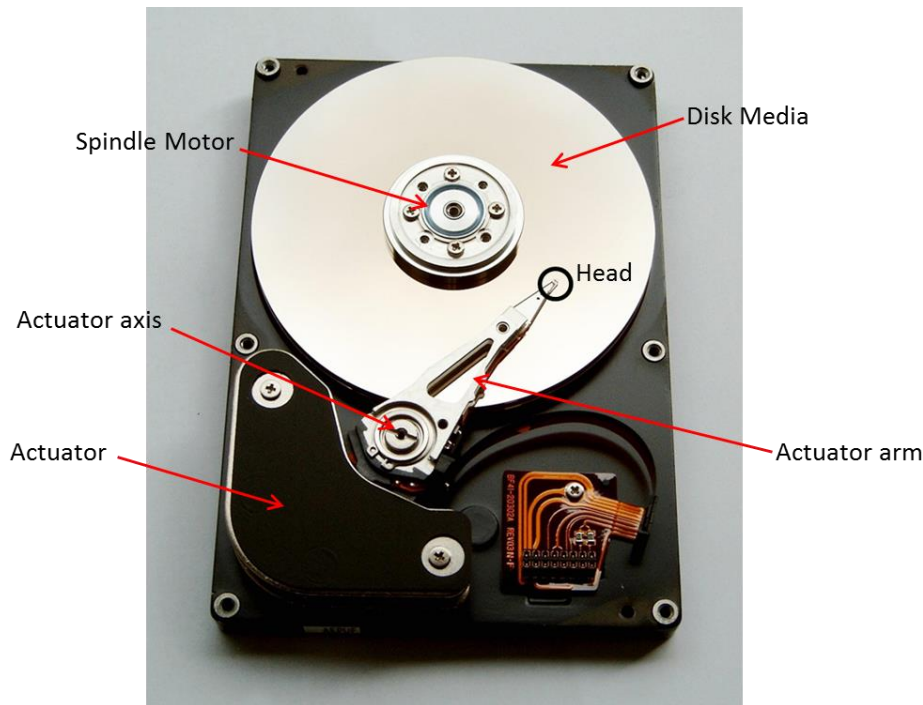


Figure 1.2.1 - Image showing the components of a hard disk drive.

In longitudinal magnetic recording (LMR) the polarities of magnetic grains lie along circular tracks that are parallel to the surface.¹⁸ This method of magnetic recording relies on two basic principles. The first is that magnets have south and north poles that emanate a magnetic field. This magnetic field can then be sensed by a magnetic field sensor and this is the basis of reading information. The second principle is that the polarity of magnets can be changed by applying an external magnetic field and this is used to write information to the disk.¹⁴ When two identical magnetic poles are placed next to each other (S-S or N-N) a strong magnetic field is emitted, whereas no field emerges when opposite poles (S-N) are next to each other. Therefore, when a magnetic field sensor moves across the surface, a voltage is only produced when it scans regions where like poles meet and this is represented as a '1'. When a magnetic field sensor scans regions where opposite poles meet then no voltage is produced and this is represented as '0'.¹⁴ Data can be stored as 1s and 0s known as binary code and this is how data is stored digitally. LMR has now been surpassed by perpendicular magnetic recording (PMR).¹⁸ PMR works in the same way as LMR but now the polarities of the magnetic domains lie perpendicular to the circular recording track instead of parallel. This results in the magnetic grains taking up less space than in LMR and as a result allows higher storage densities to be achieved.¹⁸

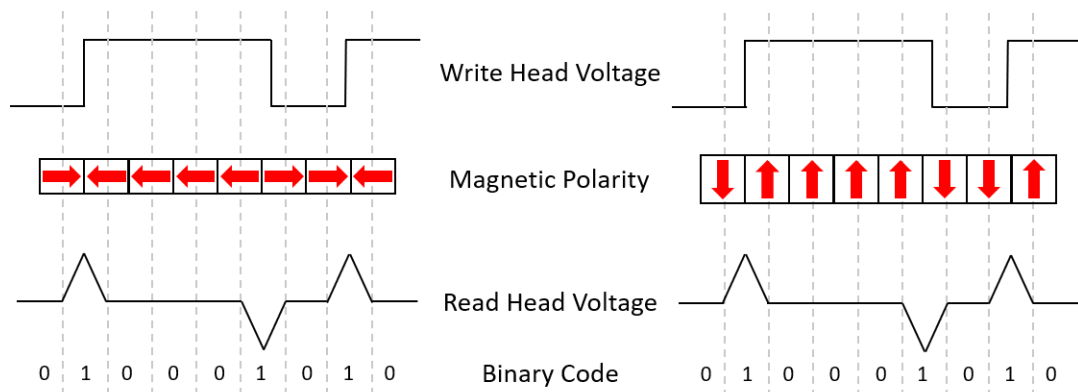


Figure 1.2.2 - Schematic showing the recording principle for longitudinal magnetic recording (left) and perpendicular magnetic recording (right).

1.2.3 INCREASING AREAL DENSITY

A bit is the basic unit of data storage and can only have two values, 1 or 0.¹⁷ Areal density is the number of bits stored in a given area and is used to measure progress in data storage technology.¹⁷ The RAMAC had an areal density of 2 Kbits/in² and in 2012 an areal density of 1 Tbit/in² was achieved.¹⁹ Very little improvement of PMR has been achieved since 2012 and instead research has focused on alternative data storage technologies. At the same time areal density has been increasing, the cost of storing data has decreased exponentially. In 1980 a 26 MB HDD cost \$5000 relating to a price of \$193,000 per GB, now in 2019 a 14TB HDD can be bought for \$668 relating to a price of \$0.04 per GB.²⁰

However, scaling cannot continue forever as physical limitations start to be reached. This is due to enhanced thermal effects that occur at smaller dimensions and results in the onset of superparamagnetism.²¹ The energy in one grain is denoted by $k_u V_g$ (Equation 1.1.2).¹⁸ $k_u V_g$ competes against the thermal energy ($k_B T$) and so $k_u V_g$ needs to be large enough to prevent reversal of the magnetic orientation. If reversal of the magnetic orientations occurs, then this will lead to stored information being lost. It is possible to decrease V_g but only if k_u is increased so that $k_u V_g > k_B T$ is satisfied.¹⁸ However increasing k_u requires application of a larger magnetic field to orient the grain. The saturation magnetisation of the write head material limits the amount that k_u can be increased by. Current designs are approaching the limit imposed by $k_u V_g < k_B T$, therefore new technologies are required if the current demand for increasing data storage density is to be met.

1.2.4 PATTERNED MEDIA

Conventional granular media has now reached the areal density limit of 1 Tb/in² and to achieve areal densities beyond this a new method needs to be developed. Lithographically patterned media is an alternative that could replace current granular recording media. There

are two different types of lithographically patterned media and these are discrete track media (DTM) and bit patterned media (BPM).

DTM involves lithographically patterning a magnetic film to produce tracks that are separated by a non-magnetic material.²² In conventional granular recording the bit size is defined by the write head and this can lead to errors if the head does not follow the track perfectly. Defining the tracks on the recording medium removes this source of error and allows smaller read/write heads to be used and increases track density.

Another method to improve areal density even further is bit patterned media. In BPM each bit of information is stored on an individual magnetic island. Bit size is now defined by the size of the magnetic island and not by the write head. BPM would be able to use current head designs and it would allow for the production of magnetic islands as small as 8 nm with 12 nm spacing between the islands.¹² As a result it has been predicted that through use of BPM storage densities of 50 Tbit/in² could be achieved.¹² However before these storage densities can be achieved a cost effective and high throughput reliable method of fabrication of patterned magnetic arrays needs to be realised. This forms the basis of one of the aims of my PhD.

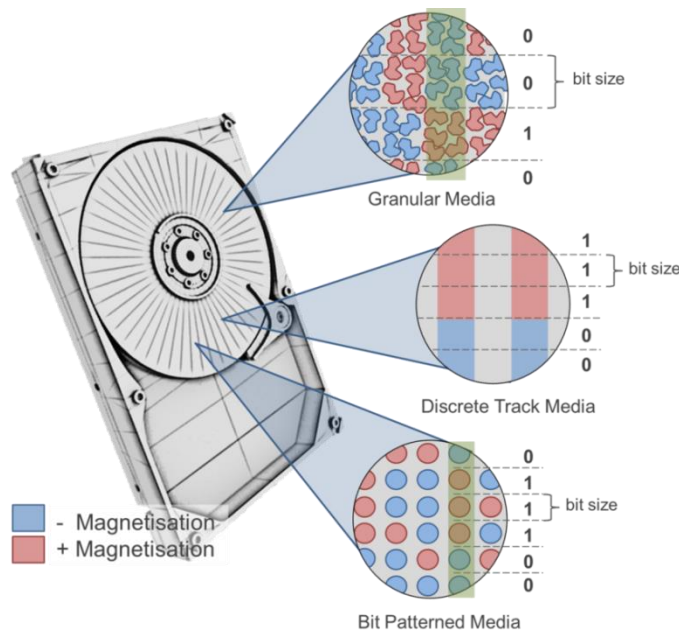


Figure 1.2.3* – Schematic showing bits patterned in conventional granular media and lithographically patterned discrete track media and bit patterned media.

* Image produced by Scott Bird using CorelDraw Software.

1.2.5 REQUIREMENTS FOR BIT PATTERNED MEDIA

For BPM to become a reality there are certain requirements that need to be met:

- Reliable, consistent and cost effective method that produces nanoscale patterns over large areas
- Individual magnetic islands must have a high magnetocrystalline anisotropy at small sizes (8 – 12 nm) and exhibit single domain behaviour
- Magnetic islands (magnetic nanoparticles) must be consistent, easily reproduced and uniform in size throughout
- Individual magnetic islands need to be spaced apart by approximately 20 nm

1.3 MAGNETIC NANOPARTICLES

Magnetic nanoparticles (MNPs) are small particles, usually 1 – 100 nm in diameter, that can be manipulated by an external magnetic field.²³ MNPs have a high surface-area-to-volume ratio and this makes them particularly versatile and reactive compared to the bulk state. Due to their unique properties MNPs have a wide range of potential applications.^{24,25} For example in biomedical diagnostics and therapies, such as MRI contrast reagents, hyperthermia treatments for tumours and magnetically targeted drug delivery.^{26,27} They also have applications in magnetic data storage and biotechnology.²⁸ As well as environmental applications such as for pollutant removal, water treatment and purification.²⁹

The magnetic properties of MNPs determines which applications they may be useful for. For example, magnetically hard NPs can be used for spintronics and high-density data storage. An example of this is the use of FePt MNPs that are able to self-assemble into superlattices or be patterned for data storage.^{30,31} Whereas magnetically softer MNPs, such as FeCo and iron oxides, can be used in high frequency electronic circuits.^{32,33} MNPs that possess superparamagnetic behaviour can be used in biomedical applications.^{34,35} For all these applications MNPs must have a uniform magnetic response to an applied magnetic field. Therefore, it is important that the size, shape and purity of MNPs are consistent to achieve this. As the focus of this project is the use of MNPs for their potential application in data storage it is important that MNPs used must be magnetically hard and have a large coercivity. As a result, only MNPs that are suitable for this application are discussed in further detail in this section.

1.3.1 Pt ALLOY NANOPARTICLES

There are three possible ordered phases of Pt alloy NPs which are XPt_3 ($L1_2$), XPt ($L1_0$) and X_3Pt ($L1_2$), where X can represent either Fe or Co.³⁶ However, it is the $L1_0$ phase that has received a lot of interest for BPM due to being one of the few magnetic materials that has a

high enough magnetocrystalline anisotropy to remain magnetically stable at volumes of a few nanometres.³⁷ This phase has an ordered face centered tetragonal (fct) structure where two faces are occupied by one type of atom and the other face is occupied by a different atom resulting in a layered structure.³⁸ However, when CoPt and FePt NPs are formed from a solid solution they usually have a disordered face centered cubic (fcc) structure and this is known as the A1 phase.³⁹ In the A1 phase the probability that each site is occupied by either a Co/Fe or Pt atom is the same.³⁸ Both the A1 and L1₀ phase are represented schematically in Figure 1.3.1. These two phases have very different magnetic properties, with the A1 phase having very low coercivity values (0 – 50 Oe) and the L1₀ phase having very high coercivity values (1 – 10 kOe). This highlights the dramatic effect the crystal phase has on the magnetic properties of the NPs. The large increase in coercivity is usually only observed after high temperature annealing (> 600 °C).^{39,40} During this high temperature annealing step the fcc disordered structure transforms into an fct ordered structure.

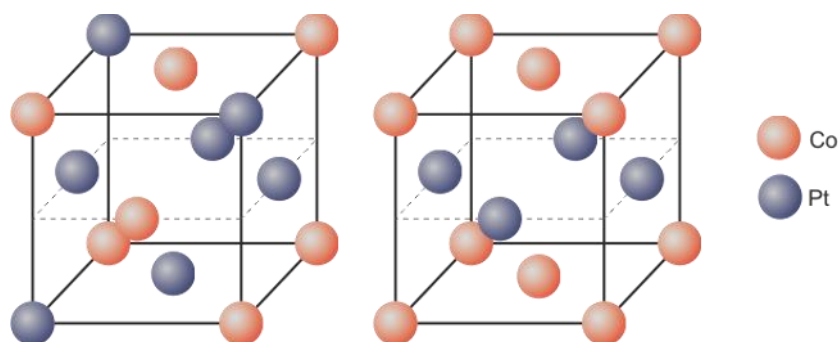


Figure 1.3.1 – A) A1 disordered face centered cubic structure and B) L1₀ ordered face centered tetragonal structure.

The two other ordered phases of Pt alloy NPs have a fcc crystal structure and do not possess the same magnetic properties as the L1₀ phase. L1₂XPt₃ is paramagnetic and L1₂X₃Pt is ferromagnetic, and they typically exhibit much lower coercivities (0 – 200 Oe).³⁶

Therefore, due to the high magnetocrystalline anisotropy energy of the L1₀ phase the magnetic properties remain stable at dimensions of a few nanometres and this makes L1₀ CoPt or FePt a suitable material for magnetic data storage.³⁷ However there are problems with current methods to generate the L1₀ phase due to the use of a high temperature annealing step, which leads to agglomeration and sintering of the particles.⁴¹

1.4 SYNTHESIS OF MAGNETIC NANOPARTICLES

There are a wide range of different synthesis methods for the formation of Pt alloy MNPs (Table 1.4.2 and Table 1.4.3). This section will focus on the synthesis of CoPt and FePt alloys. Some examples of the different synthesis routes include high temperature reduction, reverse

micelle method, sol-gel method, polymer or colloid synthesis and the use of biological templates.

1.4.1 HIGH TEMPERATURE CHEMICAL REDUCTION

High temperature chemical reduction is the most common method for the synthesis of Pt alloy NPs. This method involves cobalt/iron and platinum metal salts being reduced to form CoPt or FePt NPs, the reaction generally requires temperatures greater than 200 °C and a variety of harsh solvents are also used.

One variation of this method is the super-hydride reduction of CoCl_2 and $\text{Pt}(\text{acac})_2$ at 200 °C in the presence of oleic acid, oleylamine and 1,2-hexadecanediol followed by refluxing at 260 °C to synthesise CoPt NPs.⁴² Work by Shen *et al* modified this super-hydride reduction method by using readily available PtCl_2 and CoCl_2 as metal precursors and super-hydride as the reducing agent. This synthesis allows simultaneous reduction of both metal precursors to facilitate formation of CoPt NPs.⁴³ NPs synthesised using this method are typically in the A1 phase and only after annealing at 700 °C do they possess any $L1_0$ character, confirmed by the presence of (001) and (110) planes in x-ray diffraction (XRD) and a large coercivity (1.25 kOe).⁴³ The super-hydride reduction method has also been used for the synthesis of FePt NPs.⁴⁴ The resulting FePt NPs were in the A1 phase and had no coercivity when measured at room temperature. After annealing at 700 °C the NPs were transformed to the $L1_0$ phase, confirmed by the presence of the (001) and (110) planes in the XRD spectrum and a large coercivity value of 7.6 kOe.⁴⁴

An alternative high temperature chemical reduction method that avoids the use of organometallic precursors is the polyol method. This is a simple one step, non-aqueous method that can produce metal alloy NPs in powder form. The reduction of the metal precursors is usually carried out by refluxing in ethylene glycol (190 °C) where ethylene glycol acts as a solvent and reducing agent simultaneously.⁴⁵ Synthesised CoPt NPs did not possess any $L1_0$ character and only after annealing at 700 °C was $L1_0$ character obtained, this was confirmed by presence of the (001) and (110) planes from XRD and a large coercivity of 6 kOe.⁴⁵ Other examples of CoPt NPs synthesised using the polyol method can be seen in Table 1.4.2. FePt NPs have also been synthesised using the polyol method, and resultant NPs had some $L1_0$ character due to the presence of the (001) and (110) planes.^{46,47} However, these NPs had a lower than expected coercivity (370 Oe) for $L1_0$ phase NPs.⁴⁶ More examples of FePt NPs synthesised using the polyol method can be seen in Table 1.4.3.

1.4.2 REVERSE MICELLE METHOD

The reverse micelle method was previously known to be used for reducing single element metal ions into metal particles.⁴⁸ Single element nanoparticles of Co and Pt were obtained via this method by reducing the corresponding metal ions with sodium borohydride (NaBH_4).^{49,50} Inversed micelles were formed by dissolving surfactants in organic solvents either in the presence or absence of water. The micelles that were formed were then able to solubilise inorganic reagents, such as Co or Pt, and mixing of solutions created very small particles. Work by Yu *et al* identified that modifications of this method would make it possible to synthesise CoPt NPs.⁵¹ To produce CoPt NPs, a reverse micellar solution containing Co^{2+} and Pt^{4+} ions was reduced simultaneously using NaBH_4 . The initial solution was yellow and after mixing with NaBH_4 a black solution was observed indicating that CoPt NPs had been synthesised. The colloidal NPs were extracted and then characterised using XRD, vibrating sample magnetometry (VSM) and superconducting quantum interference device (SQUID). In the XRD data the (110) plane is present which is indicative of $L1_0$ character. The as-synthesised NPs do not have any coercivity at room temperature but have a coercivity of 40 Oe at 5 K.⁵¹ This is a much lower coercivity value than would be expected if the NPs are in the $L1_0$ phase as indicated by XRD. Only after annealing at 550 °C do the NPs have coercivity at room temperature, a value of 5.5 kOe was obtained, confirming that $L1_0$ NPs had been synthesised but only after high temperature annealing.⁵¹

1.4.3 SOL-GEL METHOD

Using a modified version of the sol-gel method has made it possible to synthesise CoPt NPs.^{52,53} In the sol-gel method a mixture of cobalt, platinum and citric acid are mixed. Citric acid acts as a chelating agent and reacts with both precursor metals to block their reactive functions and so a homogenous mixture is achieved. This mixture is then homogenised by further stirring to form a sol, heating at 80 °C is then required to polymerise the sol into a gel. Further heating of the gel is required (120 °C) and after this heat treatment the resulting NPs can then be ground into a powder.^{52,53} Using this method combined with post-synthesis annealing it was possible to obtain CoPt NPs with $L1_0$ character. Zhang *et al* used this method to obtain NPs with a room temperature coercivity value of 4.4 kOe after annealing at 700 °C, planes (001) and (110) indicative of $L1_0$ character were present in XRD data.⁵² Work carried out by Liu *et al* also synthesised CoPt NPs using this method, here a coercivity of 3.2 kOe was obtained after annealing at 800 °C and $L1_0$ planes (001) and (110) were also present in the XRD spectrum.⁵³

1.4.4 POLYMER OR COLLOID SYNTHESIS

Polymer or colloid synthesis is an alternative route that has been used to synthesise Pt alloy NPs. In this method a polymer with alternating sites that can bind Co and Pt is first synthesised, the polymer is then mixed with Co and Pt salts followed by addition of a reducing agent to form the NPs. An additional step of high temperature annealing is usually carried out so that the particles are transformed into the L1₀ phase.

One example of this method is work carried out by Du *et al* that used a two-stage procedure for the preparation of CoPt NPs using only NaBH₄ as the reducing agent.⁵⁴ Pure cobalt particles were formed first in the presence of polyvinylpyrrolidone (PVP), followed by reduction of platinum in the presence of the cobalt seeds. Colloid dispersions of CoPt were then filtered and wash before being dried in a vacuum oven at 40 °C.⁵⁴ This reaction uses ambient synthesis conditions and some stages of the reaction are even carried out at 0 °C, these are the lowest reaction temperatures observed so far for the synthesis of CoPt NPs. However, NPs produced in this way do not have L1₀ character and a coercivity is only observed when measured at 5 K (980 Oe).⁵⁴ Although this coercivity value is relatively high it was measured at 5 K rather than room temperature and so it would be expected that at room temperature a much lower coercivity would be obtained. A low coercivity value at room temperature would be consistent with the absence of any L1₀ character.

Another example is work carried out by Dong *et al* that uses a novel organometallic polymer which contains both Co and Pt atoms as a precursor to generate L1₀ CoPt NPs.⁵⁵ The novel organometallic polymer takes advantage of porphyrins templating ability to introduce cobalt into the polymer. This cobalt-porphyrin complex can then couple to a coordinated platinum(II) dichloride complex resulting in the CoPt containing porphyrin based polymer.⁵⁵ After synthesis, the metallopolymer was then annealed at 800 °C so that L1₀ CoPt NPs were obtained. This was confirmed by the presence of characteristic L1₀ planes in the XRD spectrum and the large coercivity (5.8 kOe) obtained. A similar process has been used for the synthesis of FePt NPs, in this case a series of block co-polymers were synthesised and a FePt bimetallic complex was incorporated into a nitrogen donor segment of the polymer.⁵⁶ This synthesis route required multi steps to achieve the final bimetallic block co-polymer as well as heating at high temperatures and the use of harsh solvents. The resulting polymer was then annealed at 800 °C and NPs produced had L1₀ character confirmed by XRD and VSM data.⁵⁶

1.4.5 USE OF BIOLOGICAL TEMPLATES

The use of biological templates is one approach that has been investigated to overcome the issues associated with conventional Pt alloy MNP synthesis. Reactions carried out in the presence of biological templates generally use lower reaction temperatures, are carried out in an aqueous medium and are completed in two steps. The first step being the mixing of metal precursors with the biological template and the second is the addition of reducing agent, typically NaBH_4 , for formation of Pt alloy NPs. This offers an environmentally friendly method to produce the desired magnetic materials for use in bit patterned media. Here the use of biological templates for the synthesis of CoPt and FePt MNPs is discussed.

1.4.5.1 Biopanning

Biopanning is a process that can be used to discover new peptides that are able to interact with specific targets. A very large peptide library, typically in the order of 10^{12} , is used and gene sequences are inserted into bacterial cells (cell display) or the bacteriophage (phage display) so that the virus or bacteria display the peptide on their surface.⁵⁷ The peptide library is screened against the substrate material in successive rounds of peptide binding, washing of the substrate, peptide elution and sequence amplification.⁵⁷ A schematic of this process can be seen in Figure 1.4.1. Biopanning allows peptides that have a high affinity for the target substrate to be selectively enriched and this method has been used to identify peptides that bind to a wide range of substrates.⁵⁸

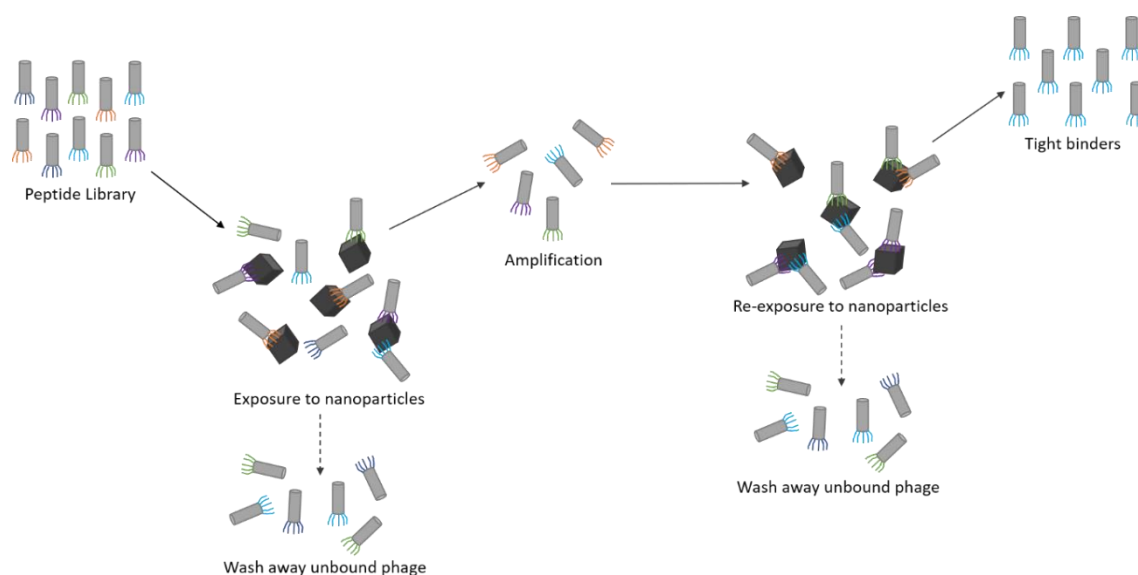


Figure 1.4.1 – Schematic showing an overview of the phage display process. Peptide library is exposed to nanoparticles, unbound phage is washed away, and eluted phage are amplified. Amplified phage is then exposed to nanoparticles again, unbound phage is washed away, and tight binders are eluted. This process is repeated three times so that three panning rounds are performed.

Biopanning can also be used to screen against a library of proteins. To screen against a library of proteins, the peptide sequence is inserted into a scaffold protein. This constrains the binding peptide and is thought to alter the binding mode of the peptide to the material it is selected for.⁵⁷ As the peptide is now constrained different binding affinities and effects can be observed compared to the free peptide. Using a scaffold protein allows the protein to be tailored for different applications more readily through genetic manipulation.⁵⁷ A recent study compared free peptide binders and antibody recognition to specific crystal planes, and found that a protein constrained in a binding loop has a greater potential for discriminating between rigid material surfaces than a flexible peptide.⁵⁹ This is thought to be because the peptide is rigid and fixed in a certain conformation.

One protein scaffold that has been investigated for this method is the Adhiron. The Adhiron has two variable loop regions, each of 9 amino acids in length.⁶⁰ It is extremely robust and can be produced in high quantities therefore making it suitable to use as a scaffold protein.⁶⁰ A recent study has used the Adhiron as a protein scaffold to identify binding sequences specific to (100) faces of magnetite nanoparticles.⁵⁷ Two magnetite interacting Adhirons were identified and the sequences can be seen in Table 1.4.1. When these proteins are used in room temperature magnetite precipitation reactions, particles with cubic morphology are observed. Harsh reaction conditions have previously been required for the formation of cubic magnetite nanoparticles.⁵⁷ Therefore, the Adhiron proteins are able to control and regulate the morphology of magnetite nanoparticles.

Table 1.4.1 - Binding loop sequences of selected Adhirons.⁵⁷

Adhiron	Loop 1	Loop 2
MIA-1	QKFVPKSTN	PKKSKIELK
MIA-2	IKKKKKYKY	ETLTHKVIR

1.4.5.2 FePt Peptides

Biopanning carried out by Reiss *et al* identified four peptide sequences that show specificity for L1₀ FePt. These peptide sequences are: HNKHLPSTQPLA, SVSVGMKPSRP, VISNHRESSRPL, and KLSLRHDHIIHH.⁶¹ HNKHLPSTQPLA was identified through biopanning against FePt NPs and a thin film of L1₀ phase FePt, whereas sequences SVSVGMKPSRP, VISNHRESSRPL, and KLSLRHDHIIHH were only identified from biopanning against L1₀ thin films. Therefore, HNKHLPSTQPLA was the only peptide used in subsequent mineralisation experiments. In this study FePt NPs were produced by mixing FeCl₂, H₂PtCl₆ and NaBH₄ in a 1:1:1 molar ratio under ambient conditions, with 1 ml of engineered phage present. NPs with a diameter of 4 nm were produced and selected area diffraction patterns showed rings corresponding to (001),

(110), (111) and (200). The presence of the (001) and (110) planes indicate that a proportion of the NPs are in the L1₀ phase.⁶¹ Magnetic measurements performed at 300 K showed coercivities of 200 Oe.⁶¹ The coercivity measured at room temperature is higher than expected for A1 phase (typically 0 – 50 Oe) but is lower than that expected for a sample containing L1₀ NPs (1 – 10 kOe). This could be because the particles produced in the reaction are close to the superparamagnetic limit of L1₀ FePt or the NPs have less L1₀ character than predicted. As a control experiment, FePt particles were synthesised in the presence of a peptide that is not specific to FePt (SPPRNYSSMSS).⁶¹ From the SAED of these particles only one band can be seen and this relates to the (111) plane of FePt, this plane is not indicative of L1₀ phase and therefore suggests that very little chemical ordering occurs when a non-specific peptide is used.⁶¹

1.4.5.3 CoPt Peptide and MjHSP

A well-studied example of a protein cage is the small heat shock protein cage from *Methanococcus jannaschii* (MjHSP). MjHSP assembles into an empty 24 subunit cage with exterior and interior diameters of 12 nm and 6 nm respectively. Large 3 nm pores at the 3 fold axes allow exchange between the interior of the cage and the bulk solution.⁶² The protein cage is stable up to 70 °C and in a pH range of 5 - 11.

By combining sequences obtained from phage display with protein cage architectures allows magnetic nanoparticles to be synthesised inside the protein cage. Phage display was carried out against thin films of L1₀ CoPt to identify a peptide that shows specificity for this phase. The peptide KTHEIHSPLLHK was identified through this process. MjHSP has external and internal surfaces that can be chemically or genetically modified and so this sequence was incorporated at the N-terminus displaying the peptide on the interior of the cage.⁶³ Reaction of Co²⁺ and Pt²⁺ salts under reducing conditions led to the formation of CoPt NPs inside the protein cage. Nanoparticles synthesised in this reaction were analysed by TEM and had a mean diameter of 6.5 nm, which corresponds to the interior diameter of the protein cage.⁶³ Magnetic measurements of MNPs produced in the presence of the modified protein cage showed a coercivity of 150 Oe at room temperature. No hysteresis was observed at room temperature for NPs mineralised in the presence of the wild type protein cage and this is consistent with the absence of L1₀ structure.⁶³ High temperature annealing (650 °C) lead to a coercivity of 650 Oe for NPs mineralised with the modified protein cage. This high temperature annealing step leads to the alignment of the c-axis and therefore increased magnetism.⁶³ Although an increase in coercivity was obtained this value is not as high as NPs synthesised using methods described in sections 1.4.1 to 1.4.4. High temperature annealing

can also cause agglomeration of particles, which increases particle size and size distributions, therefore removing the advantages of the biotemplating process.

1.4.5.4 Dual affinity peptide

Biopanning carried out by Klem *et al* identified one key CoPt L1₀ peptide sequence (KTHEIHSPLLHK).⁶³ This peptide has been used to create a dual affinity peptide (DAP) that is able to bind to a silica surface.⁶⁴ The DAP contains a peptide sequence known to bind to silica (HPPMNASHPHMH) connected to the CoPt binding peptide by a flexible linker (GSG) so the DAP has the sequence HPPMNASHPHMH-GSG-KTHEIHSPLLHK.^{63,65} In this study surfaces were prepared via micro contact printing (μ CP), a PDMS stamp was inked with 1 mg/ml CoPt-DAP solution and after 1 minute excess solution was removed and the stamp dried. The inking and drying procedure was repeated at least 10 times before the stamp was placed into conformal contact with a silicon surface. The surface was then placed into a reaction of Co²⁺ and Pt²⁺ salts under reducing conditions, at room temperature. This led to the formation of CoPt NPs attached to a silica surface via the DAP.⁶⁴ XRD data suggests that the DAP is able to biotemplate the L1₀ phase of CoPt. This is due to the presence of (001) and (100) planes that are expected for CoPt L1₀.⁶⁴ It is thought that the DAP is able to lower the activation energy for the formation of the L1₀ phase in the aqueous phase. This is because the DAP is more closely packed when on a silica surface and therefore may enhance crystallographic alignment and improve the templating abilities of the peptide. Another possibility is that the peptide may organise particles into the tetragonal phase and aid in the reduction to metallic CoPt when bound to the surface.⁶⁴ However, magnetisation data shows that the coercivity is very low and this could be because the biotemplated MNPs are not aligned in the same way as sputtered L1₀ films. When hysteresis measurements have been carried out for sputtered films that have misaligned grains, loops with reduced or no coercivity are visible.⁶⁴ Therefore, it is possible that the magnetic orientations of the MNPs are not aligned correctly to achieve maximum coercivity. It is also possible that a mixture of disordered and ordered character is present within the NPs and so a much lower coercivity value is observed.

1.4.5.6 CPMV

The cowpea mosaic virus (CPMV) is an example of a virus that has been used for the formation of NPs. CPMV is 28 nm in diameter and the surface of the particle has exposed amino acids that provide functional groups that allow for the attachment of proteins.⁶⁶ For example there are exposed amines (lysine), carboxylates (aspartic acid and glutamic acid) and hydroxyl (tyrosine) groups. Peptides specific for the mineralisation of FePt (HNKHLPTQPLA) and CoPt (CNAGDHANC) were bound to CPMV through chemical coupling

of exposed surface amine groups.^{67,68} The peptide that has been used in this study for the mineralisation of CoPt is different to in previous studies (KTHEIHSPLLHK), this because it is not specific for the L1₀ phase of CoPt but only to CoPt.⁶³ By attaching these peptides to the surface of CPMV allowed for the formation of CoPt and FePt coated nanospheres with a diameter of 32 nm at room temperature.⁶⁸

1.4.5.7 PepA

PepA is protein shell from *Streptococcus pneumoniae* that has a hollow tetrahedral structure with a 6 nm interior cavity and a 12 nm exterior diameter. The cavity at the centre has four wide channels, at the faces of the tetrahedron, and four narrow channels at the edges.⁶⁹ The wide and narrow channels have a diameter of 4 nm and 1 nm respectively. PepA has been used to mediate the growth of CoPt NPs inside the protein cavity under ambient reaction conditions.⁶⁹ The mechanism of how the protein shell facilitates NP growth is unclear.⁷⁰ However, it has been suggested that it occurs via a complementary electrostatic mechanism. In this proposed method it is thought that Co²⁺ and Pt²⁺ diffuse in and accumulate in PepA through the channels. The positively charged precursor metals interact with the negatively charged interior of the cage resulting in the formation of nucleating intermediates. CoPt NPs then grow by further deposition at the NP seeds.⁷⁰

CoPt NPs synthesised using this method have a size range of 1.1 – 2.8 nm. The 1.1 nm particles exhibit superparamagnetic behaviour whilst NPs greater than 2.1 nm exhibit ferromagnetic behaviour, but only at 5 K. XRD data shows diffraction peaks at (111), (200), (220) and (311) all of which are typical for CoPt. Coercivities of 775 and 800 Oe were observed for particles of 2.1 nm and 2.8 nm respectively and a general trend of decreased magnetisation was observed as particle size decreased.⁷⁰

1.4.5.8 Apoferritin

Ferritin has 24 nearly identical subunits that self-assemble to form a spherical 12 nm diameter cage with a 7.5 – 8.0 nm cavity.⁷¹ This cavity is usually used for the biological storage of iron as ferrihydrite.⁷² Apoferritin is the protein without its native iron oxide core and has been used in the synthesis of CoPt NPs.⁷¹

Native ferritin was first demineralised to produce the empty protein apoferritin, the protein was heated to 45 °C followed by addition of cobalt and platinum salt solutions.⁷³ Reduction took place by addition of NaBH₄ to the mixture, resulting NPs were washed and freeze dried. Followed by annealing of the NPs at 650 °C. NPs synthesised using this method possessed L1₀ character due to the (001) and (110) planes observed from electron diffraction. A coercivity of 315 Oe was obtained, this is much lower than what would be expected for L1₀

phase NPs.⁷³ Work by Mayes *et al* also used this method for the synthesis of CoPt NPs.⁷¹ Here the resultant synthesised NPs were spin coated onto a glass substrate followed by annealing at 650 °C. The films of CoPt NPs produced were L1₀ confirmed by XRD and the presence of a large coercivity (9.5 kOe).⁷¹

1.4.6 SUMMARY OF SYNTHESIS METHODS

There are many different methods that can be used for the synthesis of Pt alloy NPs and alternative approaches are always being investigated due to the unique magnetic properties of these NPs. However, current inorganic methods to synthesise L1₀ NPs all require a high temperature annealing step which can lead to sintering and agglomeration of the NPs, losing their morphological properties. As well as high temperatures being used harsh solvents are also used. The majority of the synthesis methods are carried out in multi-step reactions making it a lengthy and time-consuming process. Overall, current synthesis methods are costly and environmentally unfriendly. Therefore, a greener more sustainable process that uses ambient conditions and can be completed in fewer stages is required. The use of biological templates is one method that has been investigated to try and overcome the problems associated with traditional synthesis of MNPs. Reactions carried out in the presence of biological templates generally use lower reaction temperatures, are carried out in aqueous medium and completed in two steps. Therefore, using biological templates as part of the synthesis offers an environmentally friendly method to produce the desired magnetic materials that are suitable for use in bit patterned media and this approach for synthesis will be used in this study.

Table 1.4.2 – Summary of different synthesis methods used for the production of CoPt nanoparticles. Data obtained from XRD and magnetic measurements has been summarised.

Synthesis Method	Example	Particle Size /nm	X-ray diffraction planes	Coercivity values
High temperature reduction – polyol process	Synthesis of CoPt nanoparticles by a modified polyol method: characterization and magnetic properties. ⁴⁵	3	As synthesised (111), (200), (220), (311) After annealing at 700 °C (001), (110), (111), (200), (002), (201), (112), (220), (202), (221), (131), (113)	After annealing at 700 °C for 4 hours 6 kOe (Measured at 300 K)
	Polyol-process-derived CoPt nanoparticles: Structural and magnetic properties. ⁷⁴	5	After annealing at 600 °C (001), (110), (111), (200), (002), (201), (112), (220), (311), (222), (040) After annealing at 500 °C (111), (220), (311) XRD is questionable	As synthesised 380 Oe After annealing at 500 °C 1.34 kOe After annealing at 600 °C 3.67 kOe
	Synthesis of “Solid Solution” and “Core-Shell” Type Cobalt–Platinum Magnetic Nanoparticles via Transmetalation Reactions. ⁷⁵	6.27	(111) and (002) planes	As synthesised 330 Oe (At 5 K)
	Synthesis of spherical FePd and CoPt Nanoparticles. ⁷⁶	7	Not given	As synthesised - No coercivity Annealing at 600 °C – 145 Oe Annealing at 700 °C – 466 Oe
High temperature reduction – super-hydride method	Synthesis and magnetic properties of CoPt nanoparticles. ⁴²	8	As synthesised (111) and (200) After annealing at 650 °C (001), (110), (111), (200), (002), (201)	As synthesised 36 Oe After annealing at 650 °C 12 kOe (Both measured at 300 K)

	Monodisperse CoPt Nanoparticles Synthesized Using Chemical Reduction Method. ⁴³	2.2	As synthesised (111), (200), (220), (311) After annealing at 700 °C for 2 hours (001), (110), (111), (200), (002), (201), (220), (202), (311)	After annealing at 700 °C for 2 hours 1.25 kOe (Measured at 300 K)
Reverse micelle method	Colloidal Synthesis and Self-Assembly of CoPt ₃ Nanocrystals. ⁷⁷	20	After annealing at 400 °C for 4 hours (111), (220), (311)	As prepared – 25 Oe After annealing at 400 °C for 4 hours – 500 Oe (Both measured at 300 K)
	Structural characteristics and magnetic properties of chemically synthesized CoPt nanoparticles. ⁵¹	2 – 5	(110) planes present in XRD and HRTEM electron diffraction	No coercivity at room temperature for as synthesised particles After annealing at 550 °C for 4 hours – 5500 Oe (Co ₅₀ Pt ₅₀) After annealing at 550 °C for 4 hours – 163 Oe (Co ₃₄ Pt ₆₆)
Sol-gel method	A novel approach to the synthesis of CoPt magnetic nanoparticles. ⁵²	13.3	After annealing at 700 °C (001), (110), (111), (200), (002), (201), (112), (220), (202), (221)	After annealing at 700 °C 4.4 kOe (Measured at 300 K)
	A facile route to synthesis of CoPt magnetic nanoparticles. ⁵³	16	After annealing at 800 °C (001), (110), (111), (200), (002), (201), (112), (220), (202), (221)	After annealing at 800 °C 3.2 kOe
Polymer or colloid synthesis	Preparation and characterization of Co–Pt bimetallic MNPs. ⁵⁴	2.6	As synthesised (111), (200), (220)	As synthesised 980 Oe (Measured at 5 K)
	Metallopolymer precursors to L1 ₀ -CoPt nanoparticles: synthesis, characterization, nanopatterning and potential application. ⁷⁸	3.4	As synthesised (001), (110), (111), (200), (002), (201), (112), (220), (202), (311), (113)	As synthesised 5.8 kOe (Measured at 300 K)

	Synthesis of L1 ₀ ferromagnetic CoPt nanopowders using a single-source molecular precursor and water-soluble support. ⁷⁹	11	(001), (110), (111), (200), (002), (201), (112), (220), (202), (331), (113)	4 kOe (Measured at 300 K)
Biological templates	MjHSP with CoPt binding peptide incorporated (KTHEIHSPLLHK). ⁶³ 65 °C synthesis 1:1 Co:Pt ratio	6.5	(110), (111), (021), (112), (022) and (130)	150 Oe – before annealing 610 Oe – after annealing at 650 °C (Both measured at 300 K)
	Synthesis using dual affinity peptide . ⁶⁴	17	As synthesised (001), (100), (111), (101), (002)	Not provided
	CPMV virus . ⁶⁸ CNAGDHANC CoPt specific peptide used.	32	Not given	Not given
	Synthesis in PepA . ⁶⁹ Co-precipitation method	1.1 – 3.6	Before and after annealing (111), (200), (220), (311)	720 – 800 Oe (Measured at 5 K)
	Synthesis in apoferritin . ⁷¹ 45 °C synthesis 1.8:1 Co:Pt ratio	Not provided	Before annealing (220), (202), (111), (200), (002) After annealing at 630 °C (110), (222), (311), (113)	After annealing into a nanoparticulate thin film 9500 Oe (Measured at 300 K)
	Synthesis in apoferritin . ⁷³ Co-precipitation method	4.1	After annealing at 650 °C for 1 hour (111), (200), (220), (001), (110), (311)	After annealing 300 Oe (Measured at 300 K)

Table 1.4.3 – Summary of different synthesis methods used for the production of FePt nanoparticles. Data obtained from XRD and magnetic measurements has been summarised.

Synthesis Method	Example	Particle Size /nm	X-ray diffraction planes	Coercivity values
High temperature chemical reduction – polyol process	Polyol Process Synthesis of Monodispersed FePt Nanoparticles. ⁴⁷	3	After annealing at 650 °C for 30 mins (001), (110), (111), (200), (002), (201)	After annealing at 650 °C for 30 mins 9 kOe
	Ultrafine FePt Nanoparticles Prepared by the Chemical Reduction Method. ⁸⁰	2	As synthesised - (111) After annealing at 600 °C (001), (110), (111), (200), (201), (112), (220), (311)	After annealing at 600 °C 18 kOe
	Monodisperse FePt Nanoparticles and Ferromagnetic FePt Nanocrystal Superlattices. ⁸¹	3 – 10	As synthesised (111), (200) and (220) After annealing at 600 °C (001), (110), (111), (200), (002), (210), (112), (220), (202)	As synthesised 0 Oe (room temp) After annealing at 600 °C 6.5 kOe
	Compositionally Controlled FePt Nanoparticle Materials. ⁸²	4	After annealing at 580 °C (001), (110), (111), (200), (002), (210), (112), (220), (202)	As synthesised Very low After annealing at 580 °C 9 kOe
High temperature chemical reduction – super-hydride method	Controlled Synthesis and Assembly of FePt Nanoparticles. ⁴⁴	4	As synthesised (111), (200) and (220) After annealing at 725 °C for 2 mins in helium atmosphere (001), (110), (111), (200), (210), (112), (202)	As synthesised 0 Oe After annealing at 725 °C for 2 mins in helium atmosphere 2400 Oe After annealing at 725 °C for 20 mins in helium atmosphere 7600 Oe

	Direct Synthesis of fct-FePt Nanoparticles by Chemical Route. ⁴⁶	5 – 10	Synthesised at 260 °C (111), (200), (220), (311) Synthesised at 300 °C (001), (110), (111), (200), (201), (112), (220), (311), (222)	370 Oe Low for L1 ₀ phase believed to be due to the strong magnetostatic interaction between particles
Polymer or colloid synthesis	Nanostructured Bimetallic Block Copolymers as Precursors to Magnetic FePt Nanoparticles. ⁵⁶	3.7 – 19.2	After annealing at 800 °C (001), (110), (111), (200), (002), (201), (102), (310), (311)	After annealing at 800 °C 8.7 kOe
Biological templates	Co-reduction of Fe and Pt salts HNKHLPTQPLA L1 ₀ specific peptide used. ⁶¹	4	As synthesised with peptide (111), (001), (110), (200), (002)	As synthesised (without peptide) 200 Oe As synthesised with peptide 670 Oe
	CPMV virus. ⁶⁸ HNKHLPTQPLA FePt specific peptide used.	32	Not given	Not given

1.5 SPOT PEPTIDE TECHNOLOGY

SPOT peptide arrays were first introduced in 1992 by Frank *et al* and have allowed for the synthesis and screening of large amounts of synthetic peptides.⁸³ Peptide spots are arranged onto nitrocellulose membranes into an array and each spot can be treated as an individual reaction vessel. Peptides are synthesised onto membranes using solid phase peptide synthesis, the side-chain protection strategy for the amino acids typically follows Fmoc and tBu chemistry.⁸⁴ Coupling is monitored throughout by using bromophenol blue solution, and after coupling a colour change from yellow to blue is observed.⁸⁵ The exact coupling procedure used is outlined in section 2.2.

The first arrays using the SPOT method were synthesised manually, although this process does not require special equipment it is very time consuming and as such manual SPOT synthesis was only used for generating very small peptide arrays.⁸³ Therefore, to screen larger numbers of peptides the synthesis process needed to become automated. As a result semi-automated and automated synthesisers were developed by Intavis in Germany.⁸⁶ Automation of the technique has made it one of the most frequently used array methods for screening large numbers of peptides.⁸⁴

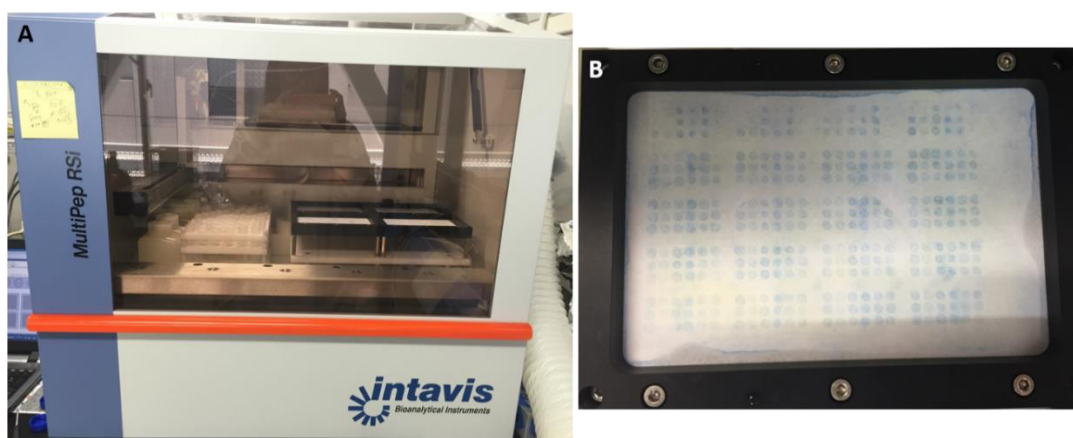


Figure 1.5.1 – A) Example of an autopeptide spotter (Intavis MultiPepRSi) and B) photograph of a peptide array during synthesis once bromophenol blue has been added to check synthesis is progressing correctly.

The most widely used solid support for SPOT synthesis is cellulose, this is due to being readily available in most laboratories as well as being relatively inexpensive. It is able to withstand organic solvents and acids that are used during peptide synthesis.⁸⁷ Nitrocellulose is also stable in aqueous solutions and non-toxic, making it suitable for studying biological samples. To ensure that the cellulose is suitable for the synthesis of peptides it is necessary to modify the surface, the surface hydroxyl groups are converted to amino groups.⁸⁴ Modification typically involves inserting a spacer molecule that allows better access to the amino groups

on the membrane. Another benefit of using a spacer is that this increases the distance between the peptides and the membrane making them more available and accessible when the arrays are screened.⁸⁴ Typically β -alanine is used as the spacer.

Using the SPOT method it is possible to synthesise peptides up to 50 amino acids in length, however the optimal range is between 6 and 18 amino acids in length.⁸⁸ The quality of the peptides synthesised using this method have been investigated and it was found that peptides up to 15 amino acids in length have a similar purity to those synthesised by traditional solid phase methods.⁸⁹ Peptide purities as high as 92 % have been reported, but typically purities in the range 74 – 91 % are observed.⁹⁰⁻⁹² Using the SPOT method it is possible to synthesis up to 8000 peptides per 20 x 29 cm sheet of nitrocellulose membrane.⁹¹

There are several different array strategies that can be used when designing arrays for SPOT peptide synthesis. The most commonly used are: peptide scans, substitution analyses, length analyses, random libraries and combinatorial libraries.⁸⁴ All of these strategies were well known before SPOT peptide array technology was developed however they have been adapted for this method and become the standard types of screening used. A peptide scan is used to detect a region of interest within a selected protein with a known sequence.⁸⁴ This is carried out by fragmenting the protein sequence into different peptide sequences, it is possible that the fragmented peptides may overlap. This allows the whole protein sequence to be narrowed down to one or a few peptide sequences. A substitution analyses is where each amino acid in the original sequence is substituted with all other 19 amino acids.⁸⁴ This technique allows for easy identification of the importance of each amino acid, from this it is then possible to identify key amino acids or patterns for the desired interaction. As a result, it is possible to optimise peptides for the desired activity. A simplified substitution analysis would be replacement of the amino acids with only one amino acid, usually alanine or glycine. This is known as alanine or glycine scanning.^{93,94} A length analysis is typically used to identify the shortest possible peptide sequence for the interaction of interest. By identifying a minimal peptide length it is possible that this can have economic and time saving benefits for further screening and method developments.⁸⁴ Using SPOT peptide arrays it is also possible to screen against random peptide libraries. Peptide libraries can be generated by a random algorithm or it is possible that they can be semi-random.^{95,96} By using a semi-random library this means selected amino acids or properties can be fixed within the library. Using this method combined with automated SPOT peptide synthesis has made it possible to screen against tens of thousands of random peptides. Finally, screening against a combinatorial peptide library is also possible. This library would contain all possible

combinations of peptide sequences for a peptide of a certain length. Using this approach allows for systematic and fast screening of large numbers of peptides.

Due to the advantages of SPOT peptide technology this type of screening has been used for a wide range of applications. These applications can be for mapping of epitopes for antibody binding,^{97,98} protein-peptide recognition,⁹⁹ enzyme specificity,¹⁰⁰ identifying peptides for cell adhesion^{101–103} and the interactions between peptides and inorganic materials.^{104–107}

1.6 NANOSCALE PATTERNING

There are many different techniques that can be used to generate nanoscale patterns, common to all techniques is the use of a self-assembled monolayer (SAM). Depending on the technique used the SAM can be stamped onto a surface, exposed to a laser beam or photooxidised using UV light to generate a pattern in the SAM. In this section the basics of SAM formation and a commonly used SAM system are discussed. Following this different patterning techniques are discussed as there are many different techniques that can be used, to pattern SAMs, it would be impossible to review all of the different techniques here.¹⁰⁸ Therefore, only the most commonly used approaches (micro-contact printing and electron beam lithography) and those that have been used in this work (interferometric lithography) are discussed.

1.6.1 SELF-ASSEMBLED MONOLAYERS (SAMs)

There are three parts that make up a SAM, a head group, a molecular backbone and an end group, this can be seen schematically in Figure 1.6.1. The driving factor for the formation of a SAM is that the head group will have specificity for the substrate.¹⁰⁹ Interactions among the molecular backbone result in efficient packing of the monolayer and also help to stabilise structures with longer chain lengths, typically this is from van der Waals and hydrophobic forces.¹¹⁰ A wide range of functional groups can be incorporated into the alkyl chain and at the end group. Changing the end group can result in the formation of hydrophobic or hydrophilic SAMs, for example a SAM with -CH₃ or -CF₃ end groups will result in a hydrophobic SAM whereas end groups such as -OH, -NH₂ and -COOH results in a hydrophilic SAM.¹¹⁰ The head group can also be used to anchor different molecules through weak interactions or covalent bonds.

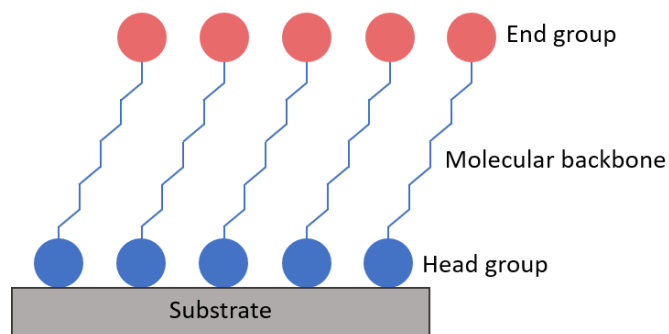


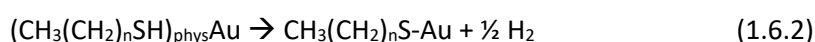
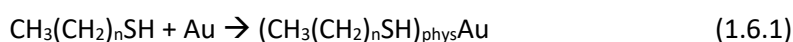
Figure 1.6.1 – Schematic of a SAM. Blue circle represents chemisorbing headgroup and red circle represents the end group. Adapted from figure 2 in reference 109.

SAMs have gained a great deal of interest for their application in nanotechnology due to their ease of preparation and the possibility to tune the surface properties through modification of the molecular backbone and end group.¹⁰⁹ For example, SAMs are used in device fabrication, as resists and inks in lithography processes and for the immobilisation of biomolecules to surfaces for the generation of sensors and biosensors. Some of the most well-studied SAMs are thiols, dithiols and other sulfur containing head group molecules on metal surfaces (Au, Ag, Fe and Mg) and some semiconductors (Ga/As).¹⁰⁸

1.6.2 ALKANE THIOL SAMs

Alkane thiol SAMs on gold substrates are one of the most studied examples, this is due to their easy preparation and high stability due to the strength of the Au-S bond formed ($\approx 184 \text{ kJmol}^{-1}$).¹¹¹ A thiol molecule consists of three parts: the sulfur head group that forms a strong covalent bond with Au surfaces, the hydrocarbon chain that stabilises the SAM through van der Waals interactions and the end group which can have different functionalities.¹¹⁰ Low concentrations (1 – 10 mM) of the thiol are required to form a SAM, chemisorption begins within seconds and is completed within minutes and typically a $\approx 90 \%$ monolayer thickness is achieved.¹¹²

Even though the interaction of thiol SAMs on Au (111) surfaces is well studied it is still a complex process. It is thought that after physisorption of the thiol molecules, chemisorption occurs through the sulfur headgroup forming a strong covalent bond. During this process the thiol molecule loses its mercaptan H atom and transforms into a thiolate.



Equation $\text{CH}_3(\text{CH}_2)_n\text{SH} + \text{Au} \rightarrow (\text{CH}_3(\text{CH}_2)_n\text{SH})_{\text{phys}}\text{Au}$ (1.6.1) corresponds to the thiol physisorption and equation 1.6.2 to the chemisorption. The nature and mechanism

of equation 1.6.2 is not completely understood. It is suggested that this reaction proceeds via an oxidative adsorption of the alkanethiol RS-H bond to the Au surface.¹¹³ However, it is unknown exactly how the mechanism proceeds and whether it includes an ion, a radical or another species.

1.6.3 MICRO-CONTACT PRINTING (μ CP)

Micro-contact printing is a method that allows patterning of SAMs on the micron length scale.¹¹⁴ It is similar to printing ink onto paper using a rubber stamp. For example, the SAM would act as the ink and a polymeric material would be used as the stamp. The SAM would coat the surface of the polymeric material that is then placed onto a bare surface such as glass, metal or a metal oxide substrate. For transfer of the SAM onto the bare surface the stamp and surface would need to be left in contact for a few minutes before being removed. This process can be seen in Figure 1.6.2. It is also possible for another SAM to backfill the bare regions by immersing the surface into another SAM solution. Micro-contact printing of alkanethiol SAMs has been used to produce nanoparticle arrays of magnetite on a gold surface with patterns of $\approx 20 \mu\text{m}$ being formed.¹¹⁵

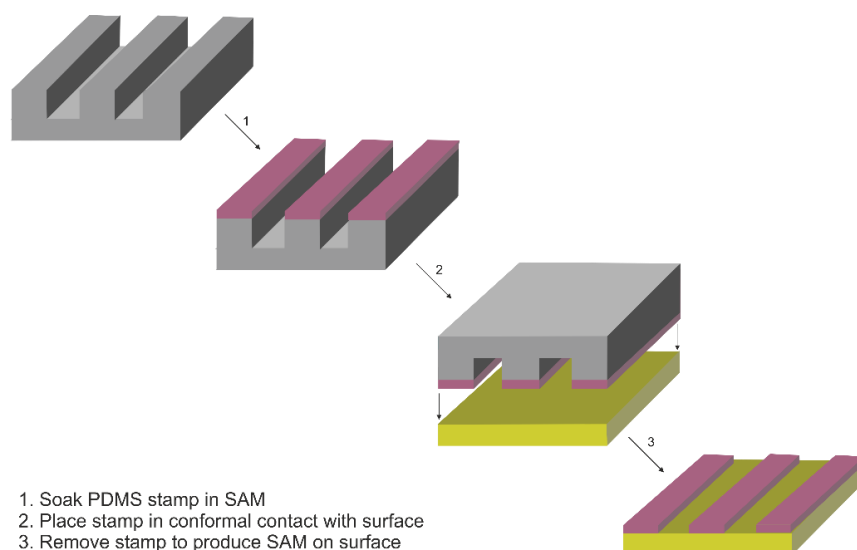


Figure 1.6.2 – Schematic showing the micro-contact printing process. 1) Stamp is inked with SAM 2) Stamp is placed in conformal contact with surface and 3) Stamp is removed to produce SAM on surface.

Poly(dimethyl siloxane) (PDMS) is the most common material used for the fabrication of stamps for μ CP as it is non-toxic and readily available. Patterning with soft PDMS stamps allows patterns with feature sizes greater than 500 nm to be produced.¹¹⁴ To achieve feature sizes smaller than 500 nm an alternative formulation of PDMS is required, known as hard PDMS. By using hard PDMS it is possible to generate feature sizes as small as $\approx 20 \text{ nm}$. Although formation of nanoscale features is possible using μ CP it is operationally more

difficult. There are two factors that determine the limit of resolution: 1) lateral diffusion of the molecules and 2) distortions of the stamp.¹⁰⁸ When there are small features on the stamp spaced apart by distances comparable to their size ($\approx 50 - 300$ nm), this can cause distortions as features may collapse into one another on manipulation of the stamp.¹¹⁴ Distortions also arise from non-uniform pressure being applied to the stamp during the printing process and this can result in broadening of features.¹¹⁶

1.6.4 PHOTO AND ELECTRON BEAM LITHOGRAPHY (EBL)

Photolithography involves the irradiation of a SAM with UV light through a photomask, this leads to the photooxidation of the SAM in regions not protected by the mask. It is then possible to remove the oxidised species by rinsing with a polar solvent.¹¹⁷ However, optical lithography is limited in resolution by the wavelength (λ) of light used and the systems numerical aperture (NA), and so a minimum feature size can be determined by the following equation:

$$\text{Minimum feature size} \approx \frac{\lambda}{2NA} \quad (1.6.3)$$

Electron beam lithography is one of the most widely used methods for fabricating sub 100 nm structures. This method uses a beam of electrons (10 – 100 eV) that is fired at a sample, this induces a number of chemical changes in the SAM and results in pattern formation.¹¹⁸ For example, if a thiolate SAM was used this could result in bonds breaking (C-S and C-H) and bonds forming (C=C).¹¹⁹ Unlike photolithography resolution is not limited by the wavelength used but instead is limited by the diameter of the electron beam and the exposure and development characteristics of the resist.¹⁷ EBL is a serial writing process and as a result is expensive and slow. Therefore, it is unlikely to have the desired low cost and throughput required for direct writing that is needed to produce patterned media.¹⁷

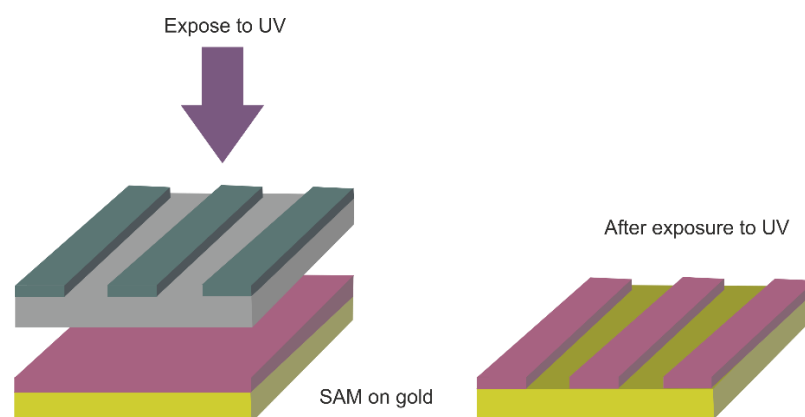


Figure 1.6.3 – Schematic of photo beam lithography. Alkanethiol SAM (pink) on gold surface is exposed to UV light through a photomask. Areas not covered by the photomask are photo oxidised and can be removed.

1.6.5 INTERFEROMETRIC LITHOGRAPHY (IL)

Interferometric lithography (IL) is a lithographic technique that uses a SAM surface as a resist to produce patterned and chemically functionalised surfaces by exposure with an ultra violet (UV) laser interference pattern.¹²⁰ There are three main stages to fabrication using IL: first SAM coated substrates are prepared, these are then exposed to UV light to pattern and finally samples are chemically processed.¹²⁰ IL uses a set-up of a bench top laser in a Lloyds mirror arrangement; in this setup the laser beam is directed onto a sample placed at an angle 2θ from a mirror. This results in half of the laser beam being focused directly onto the sample whilst the other half reflects off the mirror and onto the sample (Figure 1.6.4). This generates an interference pattern, a series of bright and dark fringes, across the entire sample. The SAM degrades more quickly where bright fringes are formed and results in a SAM pattern, of lines, being generated. The period (d) of these bands can be expressed by the equation below:

$$d = \frac{\lambda}{2n \cdot \sin\theta} \quad (1.6.4)$$

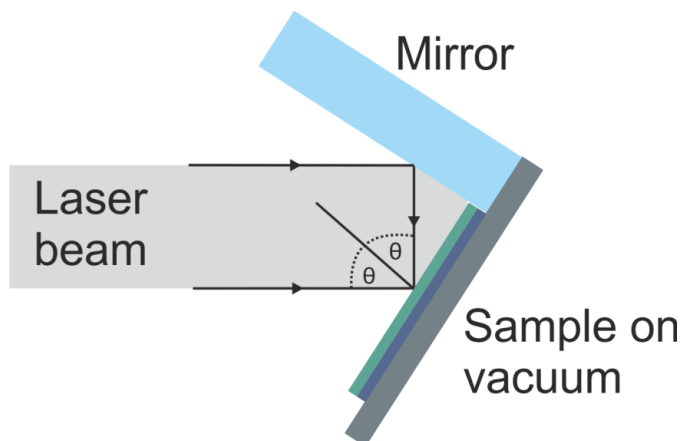


Figure 1.6.4 – Lloyds mirror arrangement set up for interferometric lithography.

Unlike serial techniques such as electron beam lithography (EBL), IL forms patterns over wide areas, approximately 1 cm^2 and has been shown to form patterns with feature sizes $< 50 \text{ nm}$.¹²¹ Therefore, this makes IL an attractive technique for nanofabrication. IL has been used to produce 46 nm lines using SAMs of alkylphosphonates on titanium dioxide.¹²¹ The width of the lines can be changed by varying the angle of exposure, this resulted in widths from 46 nm up to 126 nm being formed.¹²¹ It is possible to create patterns other than lines by carrying out more than one exposure and rotation of the sample. This results in the period of the interference pattern being modified. For example rotating the sample by 60° produces periodic hexagonal arrays, whilst a rotation of 90° produces a square dot pattern.¹²² The main

drawback of IL is that the technique is limited to fabricating periodic patterns; however this is ideal for the types of patterns required for BPM.

1.6.5.1 Generation of Biotemplated surfaces using IL

Previous work in the Staniland group has used both μ CP and IL to produce micro and nanoscale lines on gold surfaces. The peptide (KT₁HEIHSPLLHK), previously identified from biopanning as being specific to the L1₀ phase of CoPt, was modified for attachment onto surfaces. This modification involved incorporation of a cysteine amino acid residue connected to the original peptide via a flexible linker (GSG), creating the sequence C-GSG-KT₁HEIHSPLLHK.¹²³

A SAM of polyethylene glycol (PEG) was first formed on gold surfaces, for μ CP this was done by 'stamping' the PEG onto the surface in a line pattern. Whereas for IL the entire surface was covered with a PEG SAM followed by exposure to a laser beam that resulted in generation of a nanoscale line pattern being formed. Bare regions on both IL and μ CP surfaces were then backfilled with the cys_CoPt peptide before mineralisation of CoPt was carried out. SEM images of the biotemplated surfaces show that regions functionalised with cys_CoPt were covered in a densely packed thin film of MNPs whereas PEG SAM regions remained free of any NPs.¹²³ Grain size analysis was performed on these SEM images and MNPs mineralised using cys_CoPt had an average diameter of 12 nm.¹²³ A previous study that uses a dual affinity peptide to mineralise NPs had an average diameter of 17 nm.⁶⁴ Therefore, this suggests that immobilisation of the cys_CoPt peptide onto a substrate enhances its ability to control the formation of uniform MNPs. As the cys_CoPt is smaller than the DAP, 18 amino acids residues compared to 27 amino acid residues in length, this could result in closer packing of the peptide onto the surface and enhance templating of smaller more uniform particles. EDX data for the biotemplated surfaces shows that CoPt has been formed in a 1:1 stoichiometric ratio by using the cys_CoPt peptide; this is typical for L1₀ CoPt. From XRD and SAED data, peaks that correspond to the (001), (101) and (110) planes of L1₀ CoPt were observed for the biotemplated surfaces. Therefore, due to the EDX data the peaks on the XRD were tentatively assigned as L1₀ CoPt. No L1₀ structure was observed for bulk particles therefore suggesting that immobilisation of the cys_CoPt peptide to a surface shows control over the particles formed.¹²³ Magnetic data showed that the nanoparticles formed on the surface were ferromagnetic at room temperature with coercivities of 20 – 30 Oe. This is much lower than expected for L1₀ CoPt, this suggests that they lack c-axis

alignment. Mineralisation was also carried out in the presence of a 0.2 T magnetic field; these surfaces did not show any increase in coercivity and showed a lack of long-range ordering.

1.7 CONCLUSIONS AND PROJECT OUTLINE

In this chapter many different synthesis methods for the formation of Pt alloy NPs were discussed, this included traditional inorganic methods (high temperature chemical reduction, reverse micelle method, sol-gel method and polymer/colloid synthesis) and the use of biological templates. Traditional inorganic synthesis methods typically resulted in the formation of L1₀ NPs with very high coercivity values (≥ 1 kOe). However, these values were only obtained after NPs had undergone high temperature annealing. Using a high temperature annealing step results in sintering and agglomeration of NPs. Also, these methods generally use high temperatures throughout the synthesis as well as harsh solvents and involve lengthy reaction procedures. Therefore, greener and more environmentally friendly alternatives have been investigated. One method that has gained a lot of interest is the inclusion of biological molecules in the synthesis to try and template formation of the L1₀ phase. Examples of this approach include: incorporation of a peptide specific to L1₀ CoPt NPs into MjHSP which resulted in the formation of NPs with a coercivity of 610 Oe and synthesis of FePt NPs in the presence of a peptide that had specificity for the L1₀ FePt NPs resulted in a coercivity of 670 Oe.^{61,63} Prior to annealing traditional inorganic methods generate NPs with very low or no coercivity and so through the use of peptides it has been possible to greatly increase coercivity using a room temperature synthesis method. However, for BPM larger coercivities, typically around 1 kOe are required. Therefore, this is one area that needs to be optimised and improved before BPM can become a reality. Another challenge that needs to be overcome is that a reliable, consistent and cost-effective method to produce nanoscale patterns over large areas is required. As well as this, magnetic islands need to be 8-12 nm in size and spaced apart by ≈ 20 nm so that the theoretical limit for BPM (50 Tbit/in²) can be achieved.

Previous work in the Staniland Group started to work towards these aims for the production of BPM. However, the main focus of previous work was the development of a method that allowed for biomineralisation of MNPs to take place on a surface.^{64,115,123,124} Previous work focused mainly on using magnetite NPs and patterned surfaces were produced using micro-contact printing. This formed the initial proof of concept that this top down bottom up approach could be suitable for BPM. Once this process had been established work was then carried out using CoPt NPs as they are magnetically harder than magnetite NPs and

interferometric lithography was used to generate smaller nanoscale line patterns (1.6.5.1).¹²³ However, coercivity values obtained for CoPt were much lower than expected and only line patterns were generated, dot patterns would be required for BPM.

Therefore, the work completed in this study focuses on the synthesis of Pt alloy NPs in the L1₀ phase as this would allow much higher coercivity values to be obtained. Different methods to achieve this were investigated such as through the use of biological molecules and addition of dopants to the synthesis. Further optimisation of the interferometric lithography technique is carried out so that nanoscale dot patterned arrays can be generated. A schematic of an ideal biotemplated array of MNPs can be seen in Figure 1.7.1. Ideally magnetic islands would be 8-12 nm in size and spaced 20 nm apart from each other by regions of non-magnetic material, this would allow the theoretical areal density of 50 Tbit/in² to be achieved. MNPs on this nanoscale dot array would also need to have high coercivity values (≥ 1 kOe) and be synthesised using a low temperature synthesis method where a peptide or protein may help to template the formation of the MNPs. This would allow for the formation of a biotemplated nanoscale dot array of MNPs.

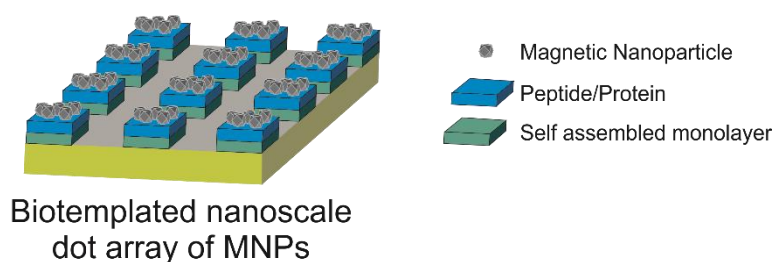


Figure 1.7.1 - Schematic showing a biotemplated dot array of MNPs, built up on a gold surface with a self-assembled monolayer that peptide/protein is able to bind to (either directly or indirectly through the use of crosslinkers) and MNPs attached via this peptide/protein.

1.8 SUMMARY OF CHAPTERS

In the following chapters the theory and ideas introduced in this chapter are built upon with the aim of developing biotemplated arrays of Pt alloy NPs into patterned arrays. Firstly, all methods used throughout this study are outlined in chapter 2. Chapter 3 investigates the use of interferometric lithography to generate nanoscale line and dot patterns on a gold surface. Chapter 4 covers the synthesis of CoPt and FePt NPs and looks into ways of optimising the synthesis by including dopants (silver and bismuth). As well as the use of a peptide that shows specificity for L1₀ CoPt from literature that was constrained into a protein cage. Chapter 5 introduces the technique of SPOT peptide array technology and how I have used this technique to screen peptides identified from literature against CoPt and FePt NPs, array design is outlined as well as optimisation of conditions for binding assays performed.

Chapters 6 and 7 discuss the results obtained from screening peptide arrays against CoPt and FePt NPs, metal precursors and a synthesis reaction for both materials. Chapter 8 draws comparisons between the trends identified from screening peptide arrays against both materials. This information is then used for the selection and design of peptides that can be used in synthesis reactions. The final part of this chapter characterises NPs synthesised in the presence of the free peptide.

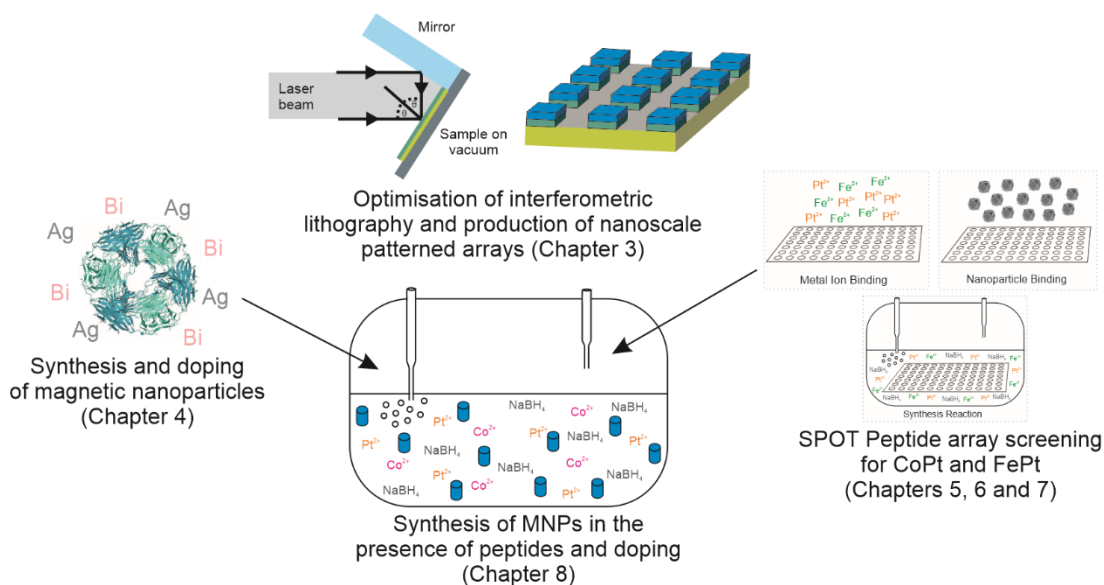


Figure 1.8.1 – Schematic showing the overall project aims and how they link together, as well as highlighting the content of each chapter.

CHAPTER TWO: MATERIALS AND METHODS

2 MATERIALS AND METHODS

2.1 EXPRESSION AND PURIFICATION OF MJHSP

2.1.1 STARTER CULTURES

Glycerol stocks of the heatshock protein (MjHSP) were plated out onto Luria-Bertani (LB) agar plates that contained kanamycin antibiotic. Agar plates were incubated overnight at 37 °C and colonies were picked the following day. To make a starter culture 5 ml of LB was inoculated with a colony picked from the agar plates. 10 µl of kanamycin was added and cells were incubated overnight at 37 °C.

Table 2.1.1 - Components required for LB media and LB agar, this is then made up to 1 litre using ultrapure water and then autoclaved at 125 °C.

Component	Amount per litre /g
Tryptone	10
Yeast Extract	5
Sodium Chloride	10
Agar	15

2.1.2 IPTG INDUCTION

400 ml sterile LB was inoculated with 5 ml of overnight starter culture and 800 µl of kanamycin was added. Flasks were incubated at 37 °C and optical density measurements were taken using a UV-vis spectrometer, until readings of 0.8 were achieved. At this point 400 µl of isopropyl β-D-1-thiogalactopyranoside (IPTG) was added and the flask was incubated overnight at 30 °C.

2.1.3 PURIFICATION OF MJHSP

Cultures were harvested by centrifugation at 3700 rpm for 15 minutes at 4 °C in a Megafuge 40R (Thermo Scientific) using a swinging bucket rotor (75003607). Cells were then resuspended in HEPES buffer (100 mM, pH 8) and lysozyme and DNase added (1 mg/ml and 1 mg/L). The resuspended cells were incubated at room temperature for 30 minutes. Sonication (Vibracell Sonicator, Sonics) was carried out for 15 minutes at 50 % amplitude with pulse times of 5 minutes on and 3 minutes off. The lysate was further cleared of insoluble material by further centrifugation at 12000 rpm for 20 minutes. The supernatant was then heated to 60 °C for 15 minutes to denature any heat labile *E. coli* proteins, followed by further centrifugation at 12000 rpm for 20 minutes. Protein was then dialysed against ultrapure water (2 L) overnight at 4 °C. Dialysed protein was purified further using gel filtration chromatography (HiPrep 16/60 Sephacryl S-300 HR, GE Healthcare). The concentration of protein was calculated by measuring the absorbance at 280 nm.

2.1.4 SDS-PAGE

Sodium dodecyl sulphate polyacrylamide gel electrophoresis (SDS-PAGE) is used to separate proteins based on their electrophoretic mobility. Sodium dodecyl sulphate (SDS) is an ionic detergent that dissociates proteins into their individual polypeptide subunits and gives a uniform net charge along each denatured polypeptide. As a result, the polypeptides have the same charge and are able to migrate according to their molecular size.¹²⁵

5 µl of sample was added to 5 µl of loading dye and heated to 95 °C for 5 minutes. 5 µl of PAGERuler (molecular marker for proteins) was loaded into the first well of the acrylamide gel and 10 µl of each sample was loaded into subsequent wells. A voltage of 200 V was applied to the gel and electrophoresed for 40 minutes. The gel was stained using Instant Blue (Expedeon), which selectively stains proteins for visualisation.

Table 2.1.2 - Components required for making SDS-PAGE gels

Gel Solution	Component	Volume
Resolving gel	Sterile water	3.43 ml
	4 x resolving buffer	2.50 ml
	30% acrylamide	4 ml
	10% ammonium persulfate (APS)	60 µl
	Tetramethylethylenediamine (TEMED)	13 µl
Stacking gel	Sterile water	3 ml
	4 x stacking buffer	1.25 ml
	30% acrylamide	700 µl
	10% APS	25 µl
	TEMED	20 µl
Running buffer	Tris base	30 g
	SDS	10 g
	Glycine	144 g
	Sterile water	Make up to 1 litre

2.2 SPOT PEPTIDE SYNTHESIS

2.2.1 SYNTHESIS OF SPOT PEPTIDE ARRAYS

SPOT peptide arrays were first introduced by Frank *et al* in 1992.⁸³ The concept was developed using observations from combinatorial oligonucleotide and peptide synthesis on separate membrane disks. Only when the volume of the reagents is the same as the volume taken up by the support material can the reaction go to completion. Therefore, it was suggested that individual amino acid coupling reactions could be carried out simultaneously on defined areas of a membrane. These distinct areas of the membrane are known as spots.

These spots can form when a small amount of liquid is dispensed onto the surface of a porous membrane, the droplet is adsorbed, and a circular spot formed. Each spot can be treated as an individual reaction vessel and used for conventional solid phase peptide synthesis. Arranging many of these spots onto a larger area allows a peptide array to be generated. Spot size is determined by the volume of liquid dispensed and the absorptive capacity of the membrane. Spot size also controls the minimum distance between spots and the maximum density of the array. Synthetic steps that are common to all spots on the membrane are carried out by washing the entire membrane with the required reagents and solvents.^{83,126}

A cellulose membrane (Grade 542, Whatman) was first activated by using β -alanine as a basal spacer. An additional spacer was also used, and this was Fmoc-11-aminoundecanoic. Activated Fmoc-derivatised amino acids were spotted at a concentration of 0.5 M, with a diameter of 2 mm and at intervals of 2 mm, using a peptide auto-spotter (ASP222; Intavis AG, Cologne, Germany). Once amino acids had been spotted onto the membrane washing with N,N'-dimethylformamide (DMF) was carried out. Following this, the Fmoc groups were removed by treatment with 20 % piperidine in DMF. Further washing steps using DMF and methanol were carried out. These steps were repeated in the same order for each elongation step until all peptides were synthesised. Bromophenol blue (BPB) was added during the synthesis to ensure that peptides were being synthesised correctly.

Cyclisation of peptides on SPOT arrays

To form the disulphide bridge by oxidation of the cysteine residues, the membrane was treated with 10% (v/v) dimethyl sulfoxide (DMSO) in 10 mM phosphate buffered saline (PBS) (pH 7.2 – 7.4) with shaking and incubated in solution overnight. This solution was discarded, and the membrane washed with PBS (30 ml, 10 mM) for 2 minutes, this wash step was repeated twice. Finally, the wash step was repeated with ultrapure water. Cyclisation was performed after synthesis of peptides had been completed but before the final deprotection step (2.2.2) was carried out.

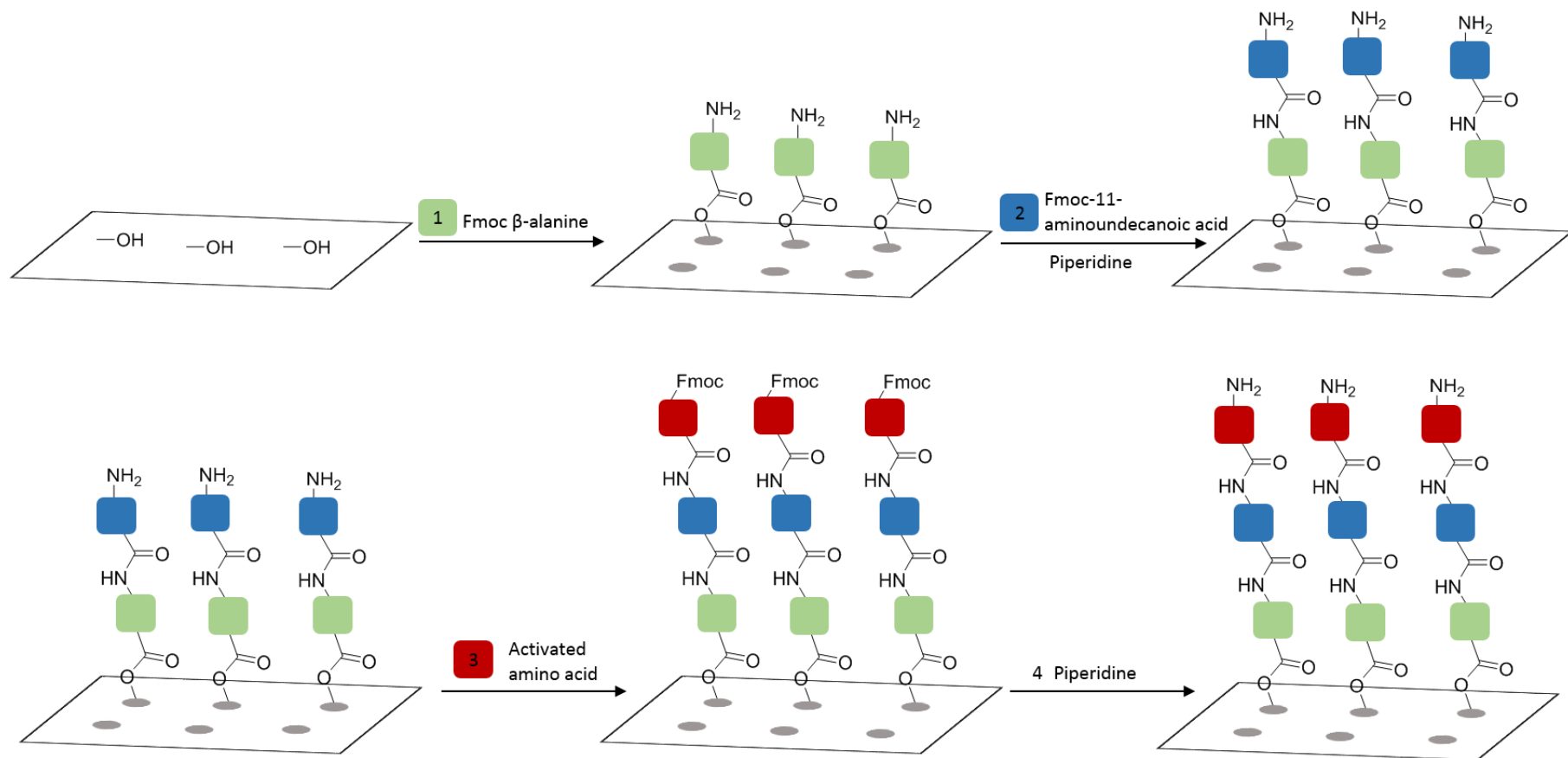


Figure 2.2.1 – Preparation of the membrane and amino acid coupling. 1) Untreated cellulose with available hydroxyl groups are reacted with Fmoc-beta-alanine followed by deprotection with piperidine 2) Reaction with Fmoc-11-aminoundecanoic acid followed by deprotection with piperidine to give membrane with free amino group ready for amino acid coupling 3) Reaction of membrane with activated amino acid 4) Deprotection with piperidine to give free amino group ready for further amino acid coupling reactions. Steps 3 and 4 will be repeated until desired peptide has been synthesised on the membrane.

2.2.2 DEPROTECTION OF SPOT PEPTIDE ARRAYS

The cellulose membranes need to be deprotected before they can be used in binding experiments. Side chain protecting groups were removed by treatment with a reagent containing trifluoroacetic acid, triisopropylsilane and water in a 95:3:2 ratio by volume for 1 hour. After removal of the protecting groups the membrane was washed several times with dichloromethane, DMF and methanol then allowed to dry. The membrane was then equilibrated with ultrapure water as this is what binding experiments would be carried out in.

2.2.3 BINDING ASSAYS

Synthesis and nucleation of NPs can depend on many factors therefore screening has been carried out against all aspects involved during the synthesis of FePt and CoPt NPs. Screening has been carried out against precursor metal ions (Co^{2+} , Fe^{2+} and Pt^{2+}), already synthesised NPs (CoPt and FePt) as well as against a synthesis reaction. The methods used for all three types of screening have been outlined in this section.

Particle Binding

CoPt and FePt NPs were synthesised as described in section 2.3. The peptide array was then screened for CoPt or FePt nanoparticle binding peptides as follows. The cellulose membrane containing the synthesised peptides was immersed in a solution of bovine serum albumin (3 % in ultrapure water) for 60 minutes, with gentle shaking. The membrane was immersed in a solution of either CoPt or FePt NPs in ultrapure water (0.18 mg/ml, 50 ml) for 16 hours, with gentle shaking. The membranes were washed with either ultrapure water or a 0.5% tween solution and then finally dried. Spots that had adsorbed CoPt or FePt NPs became grey/black in colour and an image of the peptide spot was taken using an image scanner. Each spot was identified as a circle figure and the darkness of the pixels in the circle was digitised using DNA microarray analysis software (ImageQuant TL and ImageLab).

Metal Binding Assay

Deprotected membranes were immersed in a solution of skim-milk (3 % in ultrapure water) for 60 minutes, with gentle shaking. The membrane was then immersed in ethylenediaminetetraacetic acid (EDTA) solution (0.1 M) for 60 minutes followed by washing with ultrapure water. Finally, the membranes were placed into an aqueous solution of either iron, cobalt or platinum (75 mM FeCl_2 , 30 mM $\text{CoSO}_4 \cdot 7\text{H}_2\text{O}$ and 25 mM H_2PtCl_6 respectively) for 16 hours under an inert atmosphere. The membranes were washed with ultrapure water and imaged using Bio-Rad clarity western blot reagents and an image of the array taken. The

darkness of the pixel in the circle was digitised using DNA microarray analysis software (ImageQuant TL and ImageLab).

Particle Synthesis Assay

Deprotected membranes were immersed in a solution of skim-milk (3 % in ultrapure water) for 60 minutes, with gentle shaking. The membrane was then immersed in EDTA solution (0.1 M) for 60 minutes followed by washing with ultrapure water. Membranes were then placed into a solution of either iron and platinum salts (75 mM FeCl₂ and 25 mM H₂PtCl₆) or cobalt and platinum salts (30 mM CoSO₄·7H₂O and 10 mM Na₂PtCl₄) for 1 hour under an inert atmosphere. NaBH₄ (10 mM) was then added to reduce the metal salts and the reaction was incubated for 40 minutes. Membranes were washed with ultrapure water and then finally dried. An image of the peptide array was taken using an image scanner and each spot was identified using DNA microarray analysis software (ImageQuant TL and ImageLab).

2.2.4 PEPTIDE SYNTHESIS

Peptides that were designed and selected for use in NP synthesis reactions were synthesised by GenScript Biotech (Netherlands). All peptides were synthesised at purities greater than 75%, followed by TFA removal to form a hydrochloride salt. Peptide powders were resuspended in ultrapure water to a known concentration. Peptide solutions were aliquoted and stored at -20 °C.

2.3 SYNTHESIS OF MAGNETIC NANOPARTICLES

2.3.1 CoPt NANOPARTICLES

Reactants were dissolved in anaerobic ultrapure water that had been vacuum degassed for 1 hour and nitrogen sparged for 1 hour to form stock solutions of 30 mM CoSO₄·7H₂O (126.5 mg in 15 ml), 10 mM Na₂PtCl₄ (57.4 mg in 15 ml) and 25 mM NaBH₄ (28.4 mg in 30 ml). 15 ml of each of the CoSO₄·7H₂O and Na₂PtCl₄ stock solutions were added to the reaction vessel under an inert atmosphere. After five minutes 30 ml of NaBH₄ was injected into the reaction vessel to reduce the metal salts, the nitrogen atmosphere was maintained, and the reaction incubated for 45 minutes. The particles were then magnetically separated and washed with ultrapure water 5 times. Samples were dried in a vacuum oven for 1 hour (40 °C).

Synthesis can also be run with or without the addition of a pH probe (SevenMulti, Mettler Toledo) that records pH at five second intervals.

2.3.1.1 Silver doped CoPt nanoparticles

Stock solutions of CoSO₄·7H₂O, Na₂PtCl₄ and NaBH₄ were prepared in the same way as previously described in section 2.3.1. A stock solution of 10 mM AgNO₃ (4.7 mg in 10 ml) was

prepared using anaerobic ultrapure water. The metal salt solutions were added to the reaction vessel under an inert atmosphere, volumes added can be seen in Table 2.3.1 below.

Table 2.3.1 - Silver doping levels for each mineralisation reaction

Sample Number	% Ag doped	Volume of Co ²⁺ /ml	Volume of Pt ²⁺ /ml	Volume of AgNO ₃ /ml	Volume of NaBH ₄ /ml
1	0	15.00	15.00	0.0	30
2	2	14.70	14.70	0.6	30
3	5	14.25	14.25	1.5	30
4	7	13.95	13.95	2.1	30
5	10	13.50	13.50	3.0	30

2.3.1.2 Bismuth doped CoPt nanoparticles

Stock solutions of CoSO₄·7H₂O, Na₂PtCl₄ and NaBH₄ were made up as described in section 2.3.1. A stock solution of 10 mM BiCl₃ (0.0315 g in 10 ml methanol) was prepared. Bismuth doping was carried out between 0 and 5 % of all metal salt solutions used in the reaction can be seen in Table 2.3.2.

Table 2.3.2 - Bismuth doping levels for each mineralisation reaction

Sample Number	% Bi doped	Volume of Co ²⁺ /ml	Volume of Pt ²⁺ /ml	Volume of BiCl ₃ /ml	Volume of NaBH ₄ /ml
1	0	15.00	15.00	0.0	30
2	1	14.85	14.85	0.3	30
3	2	14.70	14.70	0.6	30
4	3	14.55	14.55	0.9	30
5	5	14.25	14.25	1.5	30

2.3.1.3 Synthesis of CoPt nanoparticles with MjHsp cage protein

Stock solutions of CoSO₄·7H₂O, Na₂PtCl₄ and NaBH₄ were made up as described in section 2.3.1. 200 µl of cage protein was dissolved in 800 µl of HEPES buffer (50 mM HEPES, 100 mM NaCl, pH 7.5) to give a total concentration of 0.5 mg/ml. The cage protein and HEPES buffer were added to the reaction vessel and heated to 60 °C under an inert atmosphere. 2 mls of each metal salt solution were added dropwise to the reaction vessel and after 5 minutes 2 mls of NaBH₄ was added to reduce the metal salts. The reaction was then incubated at 60 °C with the nitrogen turned off for 40 minutes. The reaction was then allowed to cool before magnetically separating and washing the particles with anaerobic ultrapure water 5 times.

2.3.4.1 Silver doping MjHSP

Stock solutions of CoSO₄·7H₂O, Na₂PtCl₄, NaBH₄ and AgNO₃ were made up as previously described in section 2.3.1.1 and the same levels of doping were carried out. However, the reaction method followed was the same as that described in section 2.3.1.3.

2.3.4.2 Bismuth doping MjHSP

Stock solutions of $\text{CoSO}_4 \cdot 7\text{H}_2\text{O}$, Na_2PtCl_4 , NaBH_4 and BiCl_3 were made up as previously described in section 2.3.1.2 and the same levels of doping were carried out. However, the reaction method followed was the same as that described in section 2.3.1.3.

2.3.2 FePt NANOPARTICLES

Reactants were dissolved in anaerobic ultrapure water to form stock solutions of 75 mM FeCl_2 (0.01491 g in 1 ml), 25 mM H_2PtCl_6 (0.01024 g in 1 ml) and 10 mM NaBH_4 (0.003783 g in 1 ml). Ultrapure water was vacuum degassed for 1 hour and nitrogen sparged for 1 hour before use. 1 ml of the iron and platinum salts was added to the reaction vessel and sonicated for 10 minutes. 1 ml of NaBH_4 was then added to reduce the metal salts. The particles were magnetically collected and washed with ultrapure water 5 times. Samples were dried in a vacuum oven for 1 hour (40 °C).

Synthesis can also be run with or without the addition of a pH probe (SevenMulti, Mettler Toledo) that records pH at five second intervals.

2.3.2.1 Bismuth and silver doped FePt NPs

Stock solutions of FeCl_2 , H_2PtCl_6 , NaBH_4 , AgNO_3 and BiCl_3 were made up as previously described in sections 2.3.2, 2.3.1.1 and 2.3.1.2 and the same methods followed. However, silver doping was carried out only at 5% and bismuth doping only at 2%.

2.3.3 ANNEALING OF NANOPARTICLES

Annealing of NPs was carried out so that NPs would undergo a phase transformation from $A1$ (disordered) to $L1_0$ (ordered). Annealing was carried out at 825 °C for 1 hour under an argon atmosphere. A single zone horizontal tube furnace (TSH18/75/300, Elite Thermal Systems) was used to carry out annealing.

2.3.4 SYNTHESIS OF NPs IN THE PRESENCE OF FREE PEPTIDE

CoPt and FePt NPs synthesised in the presence of free peptide was carried out as described above (2.3.1 and 2.3.2). Peptide was added to the reaction at a concentration of 0.1 mg/ml alongside metal pre-cursors. All following stages of the reaction and washing procedures were carried out as previously described.

2.4 FORMATION OF SELF-ASSEMBLED MONOLAYERS

2.4.1 PREPARATION OF TITANIA SURFACES

Glass slides were immersed in piranha solution (H_2SO_4 70%: H_2O_2 30% v/v) for 1 hour, the slides were then immersed in RCA cleaning solution (ultra-pure water, hydrogen peroxide and ammonia in a 5:1:1 ratio) and heated to 273 °C for 30 minutes. After RCA cleaning the

slides were thoroughly rinsed with ultrapure water and dried in an oven (120 °C) overnight. An Edwards Auto 306 thermal evaporator was used to evaporate a layer of titania on the clean slides. After slides were placed inside the chamber was sealed and pumped to $<2 \times 10^{-6}$ mbar before ≈ 20 nm of titania was evaporated onto the slides at a rate of 0.1 nm s^{-1} . Once the desired thickness was reached the slides were removed and stored until required. Self-assembled monolayers were formed on the titania substrate by immersing them in 3-aminopropyltriethoxysilane (1 mM in toluene) for 12 – 48 hours. Following the formation of the SAM, the samples were rinsed with toluene and dried in a vacuum oven (1 hour at 120 °C).

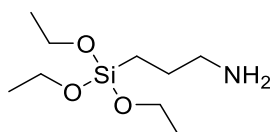


Figure 2.4.1 - Chemical structure of 3-aminopropyltriethoxysilane

2.4.2 PREPARATION OF GOLD SURFACES

Glass slides were immersed in piranha solution (H₂SO₄ 70%: H₂O₂ 30% v/v) for 1 hour, slides were then thoroughly rinsed with ultrapure water and dried in an oven (120 °C) overnight. An Edwards Auto 306 thermal evaporator was used to evaporate a layer of titania on the clean slides. After slides were placed inside the chamber was sealed and pumped to $<2 \times 10^{-6}$ mbar before ≈ 10 nm of chromium was evaporated onto the slides at a rate of 0.1 nm s^{-1} , to form an adhesion layer. Gold was then evaporated using the same conditions until the desired thickness was reached (≈ 20 nm). The slides were then removed from the evaporator and stored until required. Self-assembled monolayers were formed on the gold surface by immersing them in 6-amino-1-hexanethiol hydrochloride (10 mM in degassed ethanol) for 18 hours. Following the formation of the SAM, the samples were rinsed with degassed ethanol and stored in fresh degassed ethanol until required.

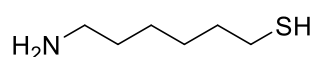


Figure 2.4.2 - Chemical structure of 6-amino-1-hexanethiol hydrochloride

2.5 CHARACTERISATION OF SELF-ASSEMBLED MONOLAYERS

2.5.1 WATER CONTACT ANGLES

A Ramé-Hart goniometer was used to determine the surface wetting properties of a substrate. First a droplet of water was applied to the surface and the angle of contact between the surface, liquid and air was recorded. Small contact angles (> 90 °C) represent a high wettability and larger contact angles (< 90 °C) represent a lower wettability. Five

measurements were taken, on different areas of the sample, so that an average contact angle could be obtained. Contact angle measurements were then compared to literature contact angles as each contact angle is different depending on the SAM being used.

2.5.2 X-RAY PHOTOELECTRON SPECTROSCOPY (XPS)

X-ray photoelectron spectroscopy (XPS) relies on the principle of photoemission where an electron is ejected from a core level by an x-ray photon with energy $h\nu$. An electron spectrometer is used to analyse the energy of the emitted photon and a graph of intensity versus electron energy is produced. This is known as the x-ray induced photoelectron spectrum. The spectrometer measures the kinetic energy of the electron and this is dependent on the photon energy of the starting x-rays. Whereas binding energy identifies the electron specifically. Binding energy can be calculated directly from the equation below, where E_B is binding energy, $h\nu$ the energy of the incident x-ray, E_K the kinetic energy and W the work function of the spectrometer.¹²⁷

$$E_B = h\nu - E_K - W \quad (2.5.1)$$

The process of photoemission can be seen in Figure 2.5.1, here an electron from the K shell is ejected. Characteristic peaks in the spectrum are produced by electrons that are excited and escape without any energy loss. Whereas electrons that undergo inelastic scattering and result in energy loss contribute to the background of the spectrum. Finally, the ionised atom must relax in some way and this is typically achieved through the emission of an x-ray photon, known as x-ray fluorescence.

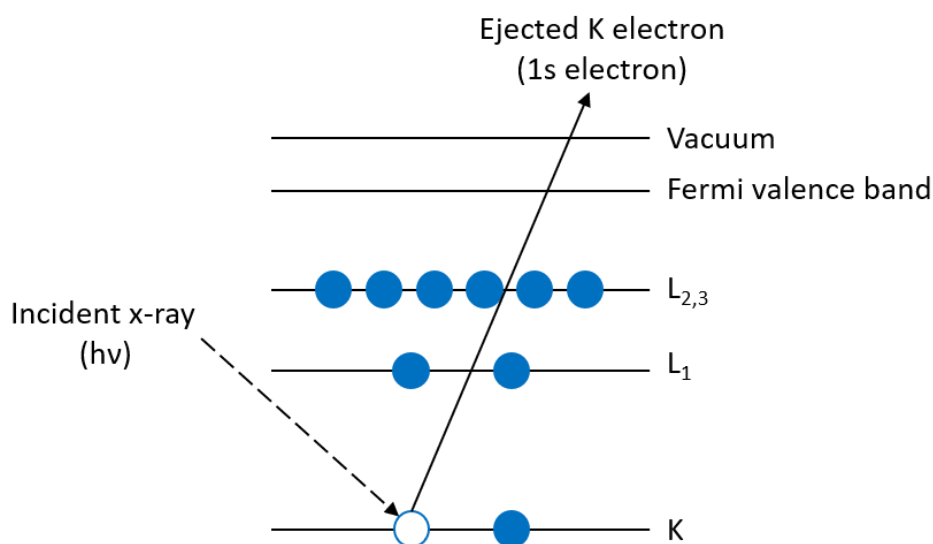


Figure 2.5.1 - Schematic of the XPS process highlighting photoionisation of an atom that occurs by ejection of a 1s electron. (Figure adapted from Figure 1.2 in reference 127).

XPS was carried out using a Kratos Supra instrument with a monochromated aluminium source and one analysis point per sample. Samples were mounted into the instrument using double sided carbon tape to attach to the sample holder. Survey scans were collected between 600 and 0 eV with 160 eV pass energy, at intervals of 1 eV. High resolution O 1s, N 1s, C 1s and Si 2p XPS spectra were also collected at 20 eV energy pass and 0.1 eV intervals. All XPS data was collected by Deborah Hammond at The University of Sheffield.

2.6 PATTERNING OF SURFACES

2.6.1 INTERFEROMETRIC LITHOGRAPHY (IL)

Interferometric lithography was carried out in collaboration with the Leggett Group at The University of Sheffield. This system was used to generate nanoscale lines on gold surfaces that had been functionalised with an amine terminated thiol SAM (section 2.4.2). The slides were then cut into $\approx 1 \text{ cm}^2$ samples using a diamond tipped scribe. After samples had been cut, they were rinsed with ethanol and dried using nitrogen. IL was carried out by exposing the surfaces to a Coherent Innova 300C frequency-doubled argon ion laser beam ($\lambda \approx 244 \text{ nm}$, maximum power 100 mW) set up in a Lloyds mirror arrangement (Figure 2.6.1).

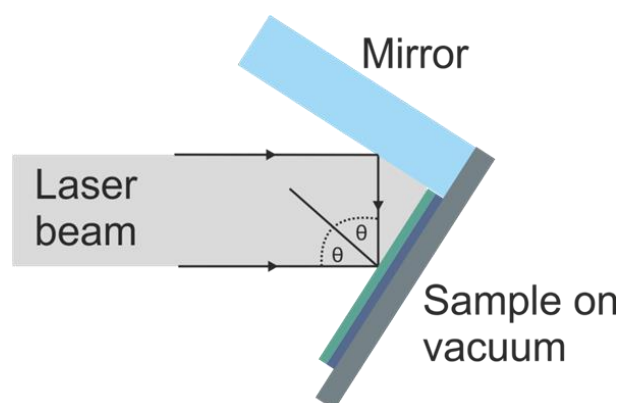


Figure 2.6.1 - Schematic showing Lloyd's mirror setup for interferometric lithography

A vacuum was used to hold the sample in place at a fixed angle of 2θ from the mirror, the laser beam was expanded so that an area of $\approx 1 \text{ cm}^2$ of the sample was covered. The laser beam was positioned so that half of the beam interacted directly with the sample whilst the other half reflected off the mirror and onto the sample. An interference pattern is produced when the reflected beam interferes with the first half of the beam and so bright and dark fringes are formed over the surface. The period of the interference pattern can be defined by the following equation:

$$period = \frac{\lambda}{2n \sin \theta} \quad (2.6.1)$$

The laser power was recorded at the sample surface before exposure so that the exposure time could be calculated. Exposure time was calculated using the formula below:

$$\text{Exposure time (s)} = \frac{\text{Dose (Jcm}^{-2}\text{)} \cdot \pi r^2}{\text{Power (W)}} \quad (2.6.2)$$

Where $r = 0.25$ cm, power is recorded by the power meter and dose is the dose required to oxidise the SAMs. The dose is a known value, depending on which SAM is used, and can be found in literature. For 6-amino-1-hexanethiol SAMs a dose of 48 J cm^{-2} was used.¹²⁸

2.7 ATTACHMENT OF PEPTIDES TO TITANIA SURFACES

2.7.1 GLUTARALDEHYDE CROSSLINKING

Self-assembled monolayers were prepared as above (section 2.4.1 and 2.4.2), both of these methods resulted in amine terminated SAMs. The amine terminated SAM is then able to interact with one of the aldehyde functional groups on glutaraldehyde (GA), resulting in the formation of an imine. GA was then attached to the SAM and the aldehyde at the free end of GA was able to react with any primary amines present in the peptide. Primary amines are present at the N-terminus of each peptide chain and also present in the side chain of lysine. This results in the formation of another imine and crosslinking of the peptide to the SAM. This process can be seen in Figure 2.7.1.

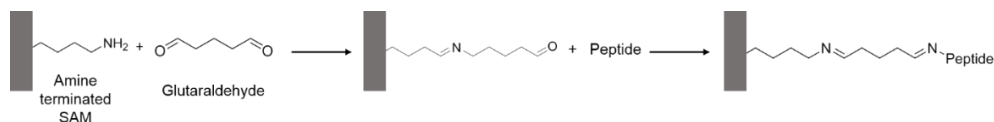


Figure 2.7.1 - Mechanism for crosslinking peptide to an amine terminated SAM using glutaraldehyde.

GA crosslinking was carried out in one step, the surface with the amine terminated SAM was incubated (room temperature) with 1% (v/v) GA solution and a 0.1 mg/ml peptide solution for 3 hours. After incubation slides were washed with ultrapure water and dried under a stream of N_2 and stored in a clean Eppendorf until required.

2.7.2 GMBS CROSSLINKING

Self-assembled monolayers were prepared as above (section 2.4.1 and 2.4.2), both of these methods resulted in amine terminated SAMs. The amine terminated SAM is able to react with the NHS ester on N- γ -maleimidobutyryl-oxysuccinimide ester (GMBS), resulting in the formation of an amide bond and GMBS attachment to the SAM. The maleimide group present in GMBS is then able to react with sulfhydryl groups resulting in the formation of a stable thioether linkage that is not reversible. Therefore, maleimide is able to react with the sulfur group present in cysteine residues and so cysteine tagged peptides have been used for GMBS cross linking. This process can be seen below in Figure 2.7.2.

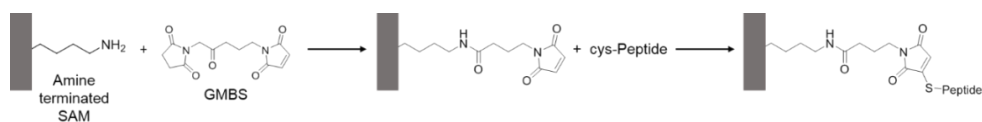


Figure 2.7.2 - Mechanism for crosslinking peptides to an amine terminated SAM using GMBS.

GMBS cross linking was carried out in two steps, the first step being incubation of the surface in GMBS solution (0.0028 g in 1 ml DMSO) for 30 minutes at room temperature. The surface was then rinsed with PBS and added to the peptide solution (0.1 mg/ml in PBS) for 30 minutes at room temperature. Finally, the surface was rinsed with PBS and ultrapure water, dried under a stream of N_2 and stored in a clean Eppendorf until needed.

2.8 MINERALISATION OF NPs ON SURFACES

Once surfaces were functionalised with a self-assembled monolayer (2.4) and peptides attached via crosslinking (2.7.1 and 2.7.2) the surfaces were then placed into a CoPt (2.3.1) NP synthesis reaction. Once the synthesis reaction had reached completion, samples were removed washed with ultrapure water and dried under a stream of N_2 . Samples were stored in an Eppendorf until needed for characterisation.

2.9 CHARACTERISATION OF NANOPARTICLES AND SURFACES

2.9.1 TRANSMISSION ELECTRON MICROSCOPY (TEM)

In TEM a focused beam of high energy electrons (100 – 400 keV) is directed at the sample and the transmitted beam intensity is collected. Using high voltages enables greater penetration of the sample and therefore gives a better resolution.¹²⁹ Traditionally electrons are generated via field emission from a tungsten filament however in modern instruments it is common to find a Schottky style field emission gun.¹²⁹ Generated electrons are then focused onto the sample by applying an electromagnetic field and by being under high vacuum. Samples for TEM must be thin as electrons need to penetrate the sample so that they can be detected underneath. Electrons that have passed through the sample are typically detected using a phosphor screen or a charged couple device that will form a 2D projection of the sample.¹²⁹

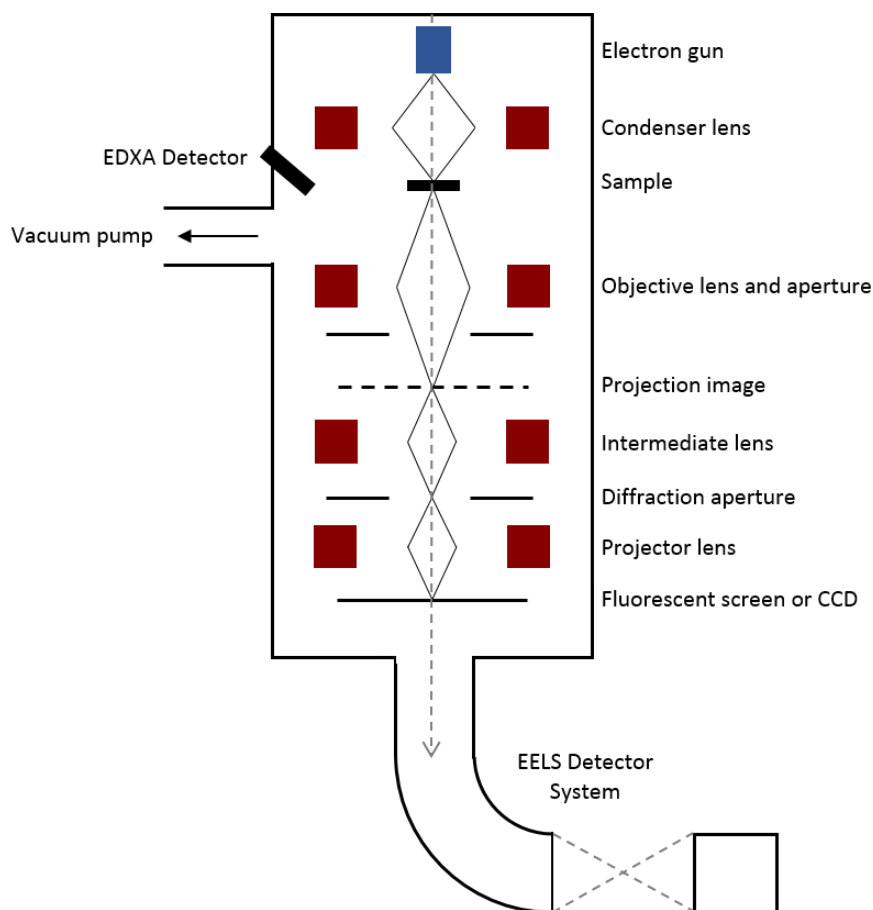


Figure 2.9.1 - Schematic of TEM (Figure adapted from figure 2.8 in reference 8)

TEM was used to image synthesised MNPs. The MNPs were collected magnetically and washed with ultrapure water at least 5 times. 10 μl of this suspension was pipetted onto carbon coated copper TEM grids (S162-3, Agar) and the grids were allowed to air dry. Micrographs were recorded with a FEI Technai G2 Spirit TEM and processed with Gatan DigitalMicrograph software.

2.9.1.1 Grain size analysis

The grain size of the NPs imaged using TEM was recorded along the longest axis using ImageJ software.¹³⁰ Approximately 200 particles per sample were measured and this data was fitted with a Gaussian distribution in GraphPad Prism software.

2.9.1.2 Staining of TEM samples

Staining was carried out for samples that did not contain dense iron, cobalt or platinum materials such as for imaging of MjHSP. This is because low electron density elements would have poor contrast with the electron beam and therefore need to be stained. The stain is made up of a heavy metal salt and electrons in the staining solution interact and deflect the beam much more than the sample. Therefore, the stain provides increased contrast between the stained sample and the background. Sample is added to the grid as described above

(2.9.1), this is then followed by the addition of heavy metal stain (2 % uranyl acetate or 0.075 % uranyl formate). The stain is then blotted off after 12 seconds and the grid is dried using a vacuum.

2.9.2 SCANNING ELECTRON MICROSCOPY (SEM)

Scanning electron microscopy (SEM) is one of the most widely used techniques for characterisation of nanomaterials. Resolution down to a few nm can be obtained using this method and not only is topographical information obtained but this technique can also provide information on chemical composition.¹²⁹

Typically, in a SEM a source of electrons is focused into a beam, with a very fine spot size of approximately 5 nm and with energies ranging from a few hundred eV to 50 keV.¹²⁹ Deflection coils are used to pass the beam of electrons over the sample. When electrons hit and penetrate the sample several interactions occur, and this results in electrons and photons being emitted from the sample. These electrons and photons are collected by a cathode ray tube and this is what generates the SEM image. There are three different types of SEM image that can be produced: secondary electron, backscattered electron and elemental x-ray maps.¹²⁹

Inelastic and elastic scattering can occur when a primary electron interacts with an atomic electron or either the atomic nucleus. An inelastic collision results in the primary electron transferring part of its energy to the other electron. If the transferred energy is large enough then the other electron will emit from the sample, this is known as a secondary electron.¹²⁹ Backscattered electrons are produced when the primary electron is elastically scattered with the atomic nucleus, this results in a backscattered electron that has the same energy as the primary electron. As the atomic number of the sample increases so does the chance of producing backscattered electrons.¹²⁹

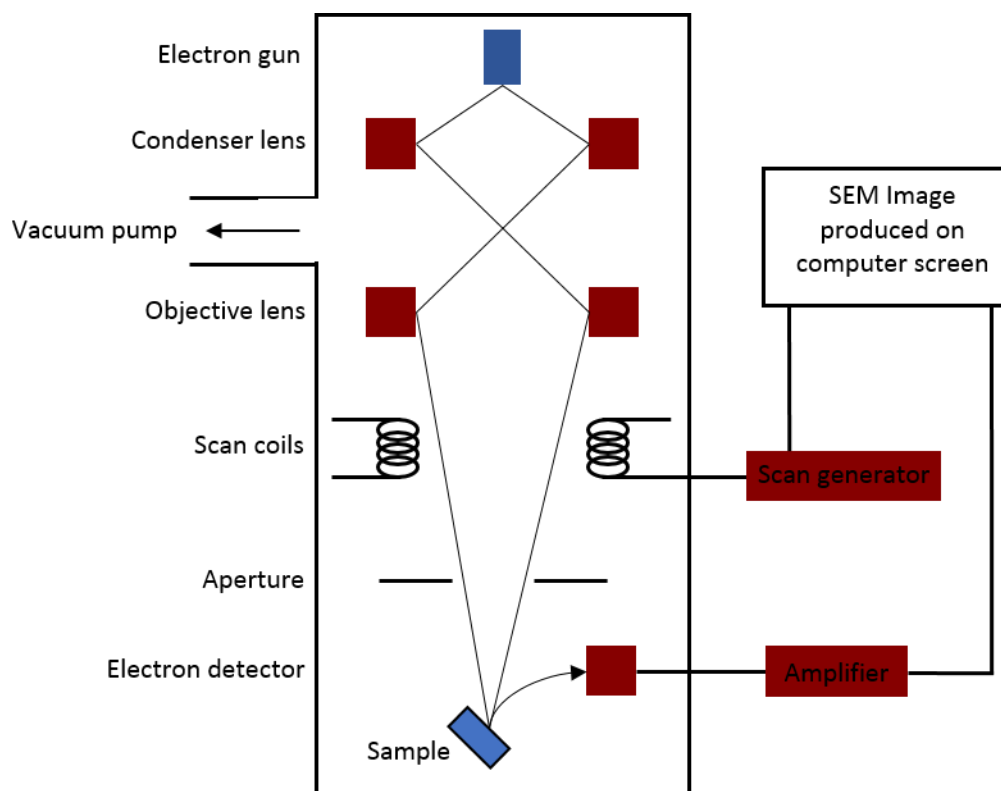


Figure 2.9.2 - Schematic showing typical set up of an SEM. (Figure adapted from figure 2.6 in reference 8).

Samples were mounted onto aluminium stubs with double sided carbon tape and silver paint was used to earth the sample. SEM images were recorded using a FEI Inspect F50 operated with xT microscope control software. The SEM chamber was first pumped to $< 5 \times 10^{-5}$ mbar, the samples were imaged at a working distance of 10 mm and at an accelerating voltage of 5 – 10 keV. An in lens secondary detector was used to detect the secondary electrons and digital micrographs produced using the xT software.

2.9.3 POWDER X-RAY DIFFRACTION (XRD)

X-ray diffraction is a technique that makes use of constructive interference of monochromated x-rays within a crystalline lattice. The crystal lattice spacing (d) is related to the scattering angle (θ) by Bragg's law:¹³¹

$$n\lambda = 2d\sin\theta \quad (2.9.1)$$

Where n is the order and λ is the wavelength of the incident ray. Crystallographic planes in the sample result in the production of characteristic peaks in the XRD spectrum at precise angles. The 2θ angle at which a peak is located can be converted to a d -spacing, it is then possible to compare the spectrum to known standards and the samples identity known.

MNPs formed during mineralisation reactions were dried under vacuum and the powder sample loaded into a glass capillary that was mounted into a Bruker D8 Advance Powder

diffractometer or a Bruker D8 Powder diffractometer. X-rays were generated at 40 keV using a Cu K α 1 source ($\lambda = 1.54056 \text{ \AA}$), with x-ray intensities collected between $2\theta = 0^\circ$ and 90° (0.020° and 1.5 seconds per step).

2.9.3.1 Using the Scherrer equation to calculate particle size

Particle size was calculated using the Debye-Scherrer equation¹³²:

$$D = \frac{k\lambda}{\beta \cos\theta} \quad (2.9.2)$$

Where k is the shape constant (0.89), β is the full width at half maximum (FWHM) at angle θ and λ is the wavelength of the electron source.

2.9.4 VIBRATING SAMPLE MAGNETOMETRY (VSM)

Vibrating sample magnetometry (VSM) is based upon Faraday's Law which states that any change in the magnetic environment of a coil of wire will cause a voltage to be induced in the coil.¹³³ Typically in VSM the sample is vibrated perpendicular to the applied field and it is the oscillating magnetic field that induces a voltage in the pick-up coils. The induced voltage is proportional to the magnetic moment of the sample. It is possible to generate a magnetic hysteresis loop by recording the magnetic moment of the sample over a range of applied magnetising fields.¹³³

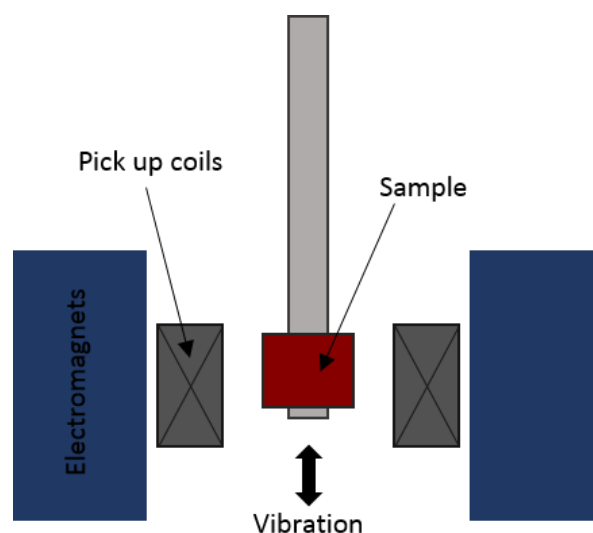


Figure 2.9.3 - Schematic of a VSM (Figure adapted from figure 1 in reference 133).

VSM was used to characterise the magnetic properties of synthesised NPs. MNPs were dried in a vacuum oven (1 hour at 40°C) before being weighed into a gelatine capsule. Gelatine capsules were mounted onto the end of a rigid carbon rod and loaded into the VSM (Oxford Instruments MagLab VSM). Samples were vibrated at 55 Hz, and the magnetic response of the material was recorded over a field range of -20 to 20 kOe at 300 K. This resulted in the

generation of a magnetic hysteresis loop at a fixed temperature, using this magnetic hysteresis loop it was possible to calculate coercivity (H_c), magnetic saturation (M_s) and remnant magnetisation (M_r).

2.9.5 INDUCTIVELY COUPLED PLASMA OPTICAL EMISSION SPECTROMETRY (ICP-OES)

Inductively coupled plasma optical emission spectrometry (ICP-OES) was used to determine the amounts of metal (Fe, Co, Pt, Ag and Bi) in the NPs synthesised. An argon plasma is used in ICP-OES and this plasma contain a significant number of argon ions. Plasma is formed by passing argon gas through a plasma torch with electrons. Electrons are accelerated and collide with argon atoms releasing more electrons and forming argon ions. When sample is introduced into the plasma, a proportion will become ionised. Electrons move from a lower to higher energy level when an atom or ion is excited within the plasma. Relaxation of these electrons back into their ground state releases energy in the form of photons. The photons emitted have wavelengths that are characteristic to the elements being emitted. This is then compared to known standards so a calibration curve can be made, and the concentration of the element determined.¹³⁴

Nanoparticle samples were dissolved in aqua regia (4:1 molar ratio HCl:HNO₃) and then diluted using ultrapure water. Samples were analysed using a Spectro-Ciros-Vision ICP-OES Spectrometer. All ICP-OES data was collected by Neil Bramall at the University of Sheffield.

2.9.6 ATOMIC FORCE MICROSCOPY (AFM)

Atomic force microscopy (AFM) is a technique that allows topographic information and measurements to be collected with good resolution and accuracy. An advantage of AFM is that it does not need to be carried out under high vacuum but can be carried out in air and almost any kind of sample can be imaged using this technique.¹³⁵

In AFM a sharp tip (100 – 200 μm long) is located at the free end of the cantilever and is used to build up topographic images. Deflection of the cantilever occurs when there are forces between the tip and the sample. A detector measures this deflection as the tip is scanned over the sample, allowing a topographic image to be produced. A laser beam is reflected off the back of the cantilever and onto a photosensitive diode and this allows the position of the cantilever to be known.¹³⁵ It is possible to detect deflections in the cantilever down to < 1 nm by detecting any shifts of the laser spot caused by deflection of the cantilever. Van der Waals forces are the main contributing force that result in deflection of the cantilever. As the tip gets very close to the surface (less than a few angstroms away) the interatomic forces between the cantilever and sample are mainly repulsive. This is caused by overlap of the

electron clouds associated with atoms of the tip and the surface, this is known as the contact regime. In the non-contact regime, the tip is further away from the surface (10 to 100 angstroms away) and so the interatomic force is attractive. This is a result of the long range attractive Van der Waals forces.¹³⁵

There are several modes of AFM that can be carried out. In contact mode the tip makes soft physical contact with the sample. This requires the tip to have a lower spring constant than the spring constant holding atoms together at the surface. Therefore, as the tip comes down towards the surface a repulsive contact force occurs causing the cantilever to bend.

For non-contact mode a stiffer cantilever is required, and this is vibrated near to the sample surface. In this case, the cantilever needs to be vibrated close to its resonant frequency.¹³⁵ When the tip approaches the surface a change in the resonant frequency is detected. This allows for sub angstrom resolution to be achieved. The detection system will monitor the resonant frequency and distance between the tip and sample to ensure that both are kept constant.

Another AFM mode is tapping mode, this is similar to non-contact mode however the tip is brought into closer contact with the surface, until it just touches. The advantages of tapping mode are less damage is likely to occur to the sample than when in contact mode and larger scans can be imaged compared to non-contact mode.

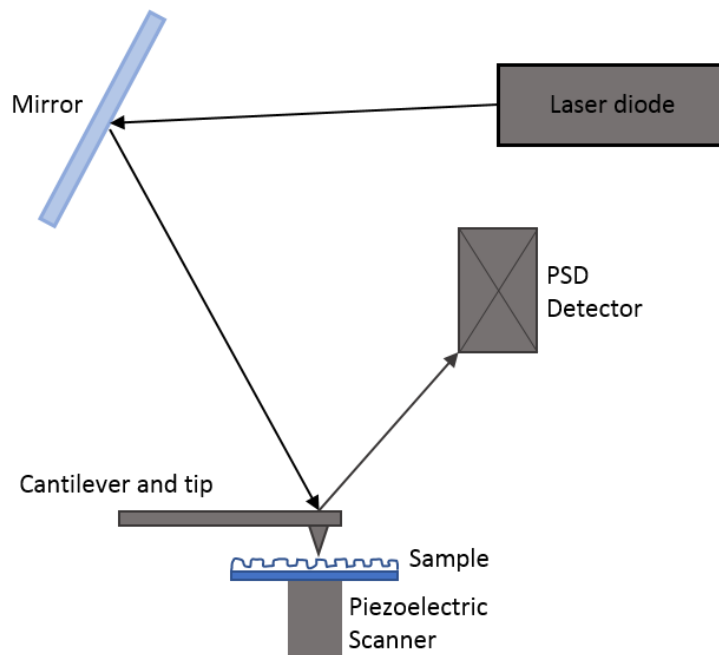


Figure 2.9.4 - Schematic showing set up of an AFM. The sample is mounted onto a scanner, and the cantilever and tip are positioned near the surface. Cantilever deflections are recorded by a photodiode that detects the position of the laser beam that is deflected off the back of the cantilever. (Figure adapted from figure 2.14 in reference 129)

In this study, a Bruker Multimode 5 in tapping mode was used to collect data. AFM tips (OTESPA-R3, Bruker) were fixed into the tip holder and attached onto the AFM head. The cantilever was then tuned to resonant frequency in air using the Nanoscope software. The cantilever was then passed over the surface, vibrating at its resonant frequency, to generate a topographic image. The amplitude set point was then adjusted until a good topographic image was obtained, the cantilever was maintained at a constant frequency by the Nanoscope software.

CHAPTER THREE: PATTERNING ON THE NANOSCALE

3 PATTERNING ON THE NANOSCALE

Previous work in the Staniland group has used micro-contact printing for the generation of patterned surfaces.^{115,123,136,137} Using μ CP it is difficult to generate nanoscale patterns due to possible distortions caused by the stamp. This occurs when the small features of the stamp are spaced apart by distances comparable to their size. This can result in features collapsing into one another during the stamping process. Therefore, the alternative patterning method of IL was investigated for this purpose.

Through the use of IL it has been possible to generate much smaller patterns than would be possible via μ CP.^{123,124} Previous work in the Staniland group has used this method to generate line patterns with a period of 357 nm on a gold surface.¹²⁴ Once these nanoscale line patterns were generated the surface was incubated in a magnetite synthesis reaction so that NPs could be mineralised on the surface. This was the first example, in literature, of combining IL and MNP mineralisation to create functional nanopatterned surfaces. Although this is an excellent step forward in the production of BPM, magnetite NPs are too magnetically soft to be used for application of data storage. Further work in the group investigated the use of CoPt NPs which are known to be magnetically hard and suitable for use in magnetic data storage. Nanoscale patterned surfaces were generated using IL and then incorporated into a CoPt NP mineralisation reaction.¹²³ However, characterisation of the NPs mineralised on the surface revealed a very low coercivity (20 – 30 Oe), this is much lower than would be expected for L1₀ phase CoPt.¹²³

Previous generation of nanoscale patterned surfaces and mineralisation of MNPs onto these surfaces is an excellent step forward towards the production of BPM. However, there are some areas that require further improvement for their use in BPM to be realised. Firstly, as CoPt NPs were mineralised onto surfaces with much lower coercivities than expected improvements to the synthesis need to be made so that higher coercivity values are achieved. Secondly, only nanoscale line patterns have so far been generated for MNP patterning. For BPM dot patterns would be required to achieve high density data storage. Therefore, work in this chapter focuses on the production of nanoscale dot patterned surfaces and work in subsequent chapters focuses on improving the synthesis and quality of Pt alloy MNPs produced.

3.1 NANOSCALE PATTERNING OF TITANIA SURFACES

3.1.1 APTES FORMATION ON TITANIA

Different concentrations and incubation times for the formation of APTES SAMs on titania surfaces was investigated. The chemical structure of APTES can be seen in Figure 3.1.1, APTES has a silane head group that is able to react with a titania surface and an end group consisting of an amine. Further functionalisation of the surface would be possible by using the amine group to react with different crosslinkers.

First the amount of APTES added was varied from 0.1 ml up to 1 ml per 20 ml reaction. Incubation time was kept constant at 1 hour for all samples. From part A of Figure 3.1.2 it can be seen that none of these concentrations resulted in a contact angle that is expected for APTES SAMs (literature value of 45°).^{138,139} A contact angle of 45° indicates that good wetting of the sample is possible using this SAM. Instead all samples had much larger contact angles (60 – 70°). As a result, the lowest and highest concentrations of APTES used were then tested against different incubation times. First 0.1 ml APTES per 20 ml was incubated in solution for 40 mins, 6 hours, 20 hours and 24 hours. The results of this can be seen in part B of Figure 3.1.2. Once again, all samples had higher contact angle values than the literature value for APTES. This is likely to suggest that the SAM has not assembled onto the surface in the same orientation as what would produce the literature contact angle value. The closest contact angle achieved to the literature value was 50° and this was from the sample that had been incubated in solution for 20 hours. As longer incubation times resulted in a lower contact angle for 0.1 ml APTES, only incubation times of 1 hour and 20 hours was tested for a higher concentration of APTES (1.0 ml of APTES per 20 ml). After incubation for only 1 hour, a contact angle of 27° was observed, significantly lower than the literature value. Whereas when an incubation time of 20 hours was used a contact angle of 45° was obtained, this is the only sample to have resulted in a contact angle that is consistent with literature. Therefore, 1.0 ml of APTES per 20 ml has been used for the formation of subsequent SAMs on titania surfaces.

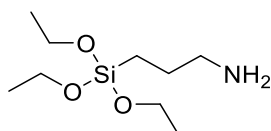


Figure 3.1.1 – Chemical structure of 3-aminopropyltriethoxysilane (APTES)

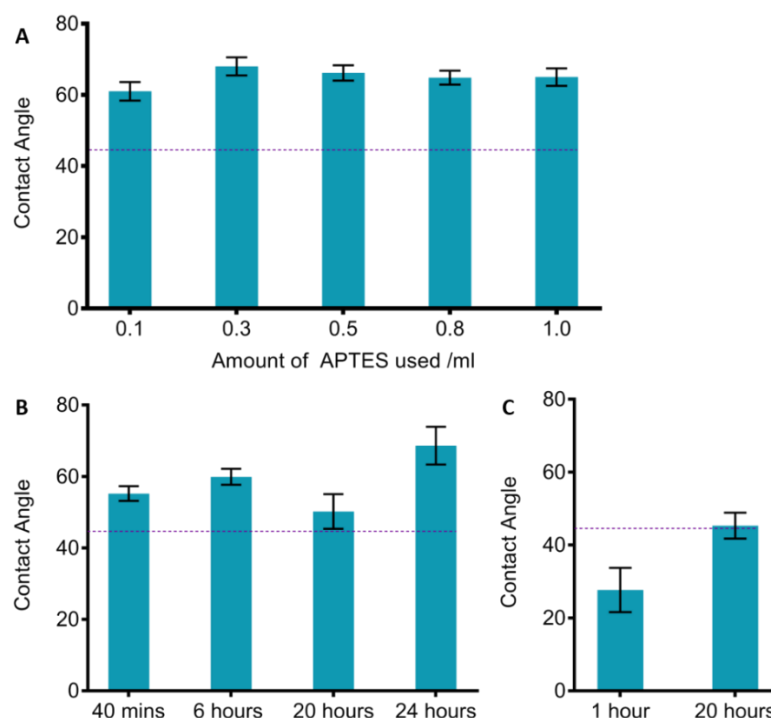


Figure 3.1.2 – Contact angle measurements for APTES formation on titania surfaces. A) Different volumes of APTES used per 20 ml and all incubated in solution for 1 hour. B) 0.1 ml APTES per 20 ml used and kept in solution for different lengths of time. C) 1.0 ml APTES used per 20 ml and kept in solution for different lengths of time. Dotted line represents literature value for contact angle.^{138,139}

Due to the problems encountered involving the contact angles for APTES SAMs on titania surfaces, a sample (1.0 ml APTES per 20 ml and incubation time of 20 hours) was investigated using x-ray photoelectron spectroscopy (XPS). XPS data highlights that the majority of the signal produced is coming from the glass substrate due to the high silicon and oxygen content identified. This indicates that only a very thin surface layer of APTES has been absorbed. From looking at the nitrogen spectrum two components are observed (Table 3.1.2). The peak at ≈ 400 eV is consistent with nitrogen within an organic environment such as an amine. As the angle between the sample and the detector increases the experiment is made more surface sensitive, as this happens the nitrogen concentration increases suggesting that the majority of the nitrogen groups are on the uppermost of the surface. It is expected that an adsorbed monolayer of APTES would have a thickness of less than 1 nm.* It is expected that $\approx 60\%$ of the XPS signal should come from the first 1 nm of the surface. From data collected at 0° the nitrogen concentration is $\approx 1.3\%$ of the atoms detected (

* APTES has a molecular mass of 221 gmol^{-1} , and a density of 0.946 gml^{-1} . 1 molecule would occupy $3.88 \times 10^{-28} \text{ m}^3$ which can be represented as a cube of side length $7.4 \times 10^{-10} \text{ m}^3$ (0.7 nm). Suggesting a monolayer would be <1 nm thick.

Table 3.1.1). Assuming all non-hydrogen atoms of APTES contributed equally then this would result in APTES generating 10.4 % of the signal. This suggests that as well as the adsorbed layer being very thin there is also poor coverage across the surface ($\approx 10\%$). The titanium concentration remained small but constant, this is consistent with a very thin layer of titanium on the surface. As the concentration of carbon increases with increasing angle, this suggests that carbon is on the surface and this could be due to some of the carbon being present from contamination of the surface.

Therefore, XPS data suggests that a thin layer of APTES has been adsorbed onto the surface with poor coverage. This could help to explain the inconsistencies with the contact angle measurements obtained. Although XPS data suggests that a thin layer of APTES was adsorbed onto the surface it is not possible to determine the exact thickness of the layer using XPS alone and is difficult to confirm whether monolayer or multilayer coverage has occurred. APTES is a multi-valent silane and as a result is known to form multilayers due to cross-linking between polymer monomers.¹⁴⁰ Ellipsometry data would be required to determine whether monolayer or multilayer coverage was obtained. However, due to problems encountered with using titania surfaces (difficulty evaporating titania slides and poor surface coverage of APTES SAM) ellipsometry data was not collected and a different surface and SAM system was sought (3.2).

Table 3.1.1 – Surface composition determined by quantifying XPS survey scans (600 to 0 eV) of an APTES SAM on a titania surface.

Sample and Angle	O	Ti	N	K	C	P	Si	Na
APTES (0 deg)	48.7	0.7	1.3	0.8	16.8	0.9	29.6	1.3
APTES (53 deg)	39.7	0.7	1.5	0.4	29.1	0.8	27.0	0.8
APTES (78 deg)	27.5	0.7	1.7	<0.1	49.5	0.7	18.5	1.6

Table 3.1.2 – Results from curve fitting of the N 1s high resolution spectra of an APTES SAM on a titania surface.

Angle (degrees)	FWHM	Binding Energy (eV)	% Atomic Concentration	Binding Energy (eV)	% Atomic Concentration
0	1.78	400.2	75.0	402.1	25.0
53	2.06	400.2	87.3	402.3	12.7

3.1.2 ATTACHMENT OF PEPTIDES AND PROTEINS TO SURFACES

Two different methods of crosslinking peptides to the amine terminated SAM on a titania surface were investigated. The first method was through the use of glutaraldehyde (2.7.1), the amine terminated SAM is able to interact with one of the aldehyde functional groups on GA and this results in the formation of an imine. GA is now attached to the SAM with a free aldehyde group that is able to react with any primary amines present in the peptide. Primary amines are present at the N-terminus of each peptide chain and are also present in the side

chain of lysine. This results in the formation of another imine and the peptide being crosslinked to the SAM. For GA crosslinking the protein that has been crosslinked to the surface is MjHSP, a cage protein that contains a peptide sequence on the interior of the cage that shows specificity for L1₀ phase CoPt.

The second method investigated was the use of N-γ-maleimidobutyl-oxysuccinimide ester (GMBS) (2.7.2) to attach peptides to the SAM. An N-hydroxysuccinimide (NHS) ester is present in GMBS and this is able to react with the amine terminated SAM forming an amide bond and attachment of GMBS to the SAM. The maleimide group present at the other end of GMBS is able to react with sulfhydryl groups, like those present in cysteine, and formation of a stable thioether linkage occurs. Therefore, for GMBS crosslinking to be carried out cysteine tagged peptides are required. Here the peptide that has been crosslinked to the surface is one that shows specificity for L1₀ phase CoPt and a cysteine tag has been incorporated at the start of the sequence (cys-KTHEHSPLLHK). The cysteine residue is able to react with the maleimide group present in GMBS and as there is only cysteine present this means that only one mode of binding is possible.

Once crosslinking of the cysteine tagged peptide and MjHSP had been carried out the surfaces were then incubated in a CoPt mineralisation reaction. As these peptides are specific for CoPt it would be expected that NPs would only bind if crosslinking was successful. A schematic of this process can be seen in Figure 3.1.3. To ensure that the correct conditions were used for crosslinking a variety of different conditions were investigated. A basic assessment of the resulting surfaces was carried out using scanning electron microscopy. Higher resolution SEM images were unable to be obtained due to burning of the sample when using higher electron voltages (≥ 5 kV) at high magnifications.

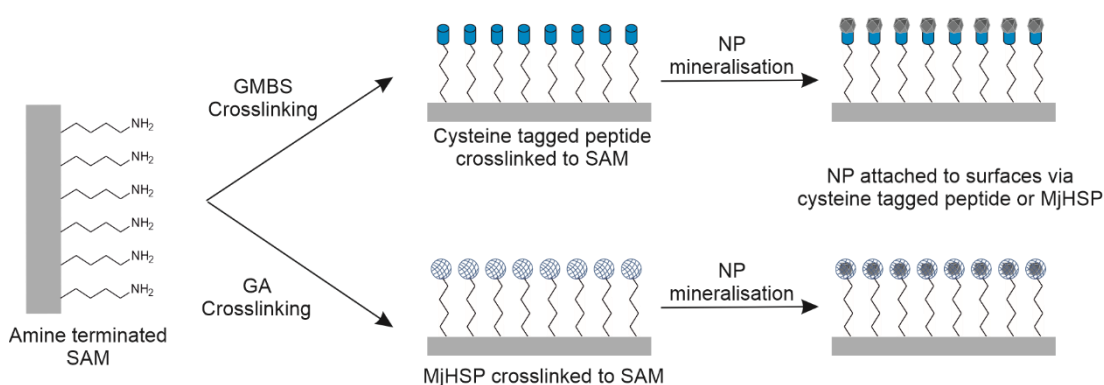


Figure 3.1.3 – Schematic showing the process of GMBS and GA crosslinking cysteine tagged peptide or MjHSP cage protein to amine terminated SAMs on titania. Followed by surfaces being put into NP mineralisation reactions. For mechanism of crosslinking process refer to Figure 2.7.1 and Figure 2.7.2.

3.1.2.1 Glutaraldehyde crosslinking

The first condition tested was the incubation time, this is how long the surface, crosslinker and MjHSP would be kept in solution together to allow the reaction to take place. Incubation times of 1.5 and 3 hours were tested. The resulting SEM images (Figure 3.1.4) show that GA crosslinking carried out using an incubation time of 3 hours has a more even coverage of NPs across the surface compared to the 1.5 hour sample. In the SEM images, NPs are represented by the brighter white regions whereas the titania surface is represented by the darker region. In the SEM image for 1.5 hours incubation time there is aggregation of the particles present on the surface and a lower overall concentration of NPs. Therefore, based on these SEM images an incubation time of 3 hours was taken forward.

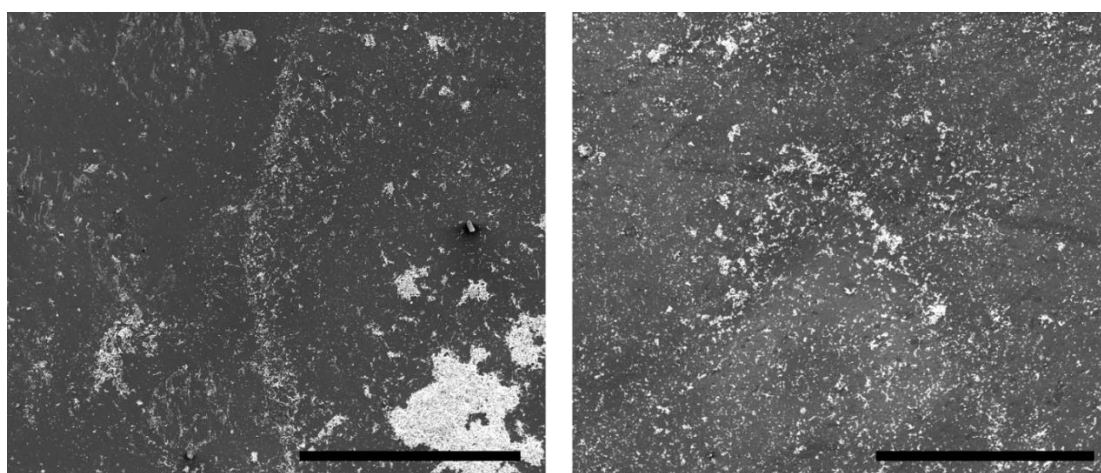


Figure 3.1.4 – SEM micrographs for glutaraldehyde crosslinking MjHSP using different incubation times of 1.5 hours (left) and 3 hours (right). Scale bars represent 300 μm and images at 400 x magnification.

The second condition investigated for GA crosslinking was whether the reaction should be carried out in one or two steps. Completing the reaction in one step involves incubating the SAM, GA and MjHSP together at the same time. Whereas completing the reaction in two steps involves first incubating GA with only the SAM, followed by incubation of MjHsp with the amine terminated SAM with GA attached to it. A total incubation time of 3 hours was used for both methods, for example when the reaction was completed in two steps both steps were incubated for 1.5 hours. SEM images for both samples show that NP attachment has taken place using both methods. However, crosslinking carried out in 1 step resulted in a higher density of NPs on the surface compared to the sample where crosslinking was carried out in 2 steps.

As amines are used to attach both the SAM and MjHSP to GA it is possible that instead of crosslinking these two different components together, the GA could instead crosslink two MjHSP molecules together or GA could couple from one amine group on the surface to

another. SEM images for crosslinking carried out in two steps show that there are less NPs present on the surface. This could be a direct result of GA coupling between two amine groups present in the SAM and effectively terminating the reaction. It is possible that this could occur during the first step of the reaction as once GA has coupled to the amine terminated SAM the only other option for binding is to another amine group present in the SAM. Whereas when the reaction is completed in one step MjHSP is accessible for binding. When the reaction is completed in one step it is possible that GA could crosslinking two MjHSP protein cages together instead of coupling to the amine terminated SAM and so this would also lower the specificity of the reaction. However, as there are more NPs present on the sample carried out in one step this is the condition that will be carried forward for future crosslinking.

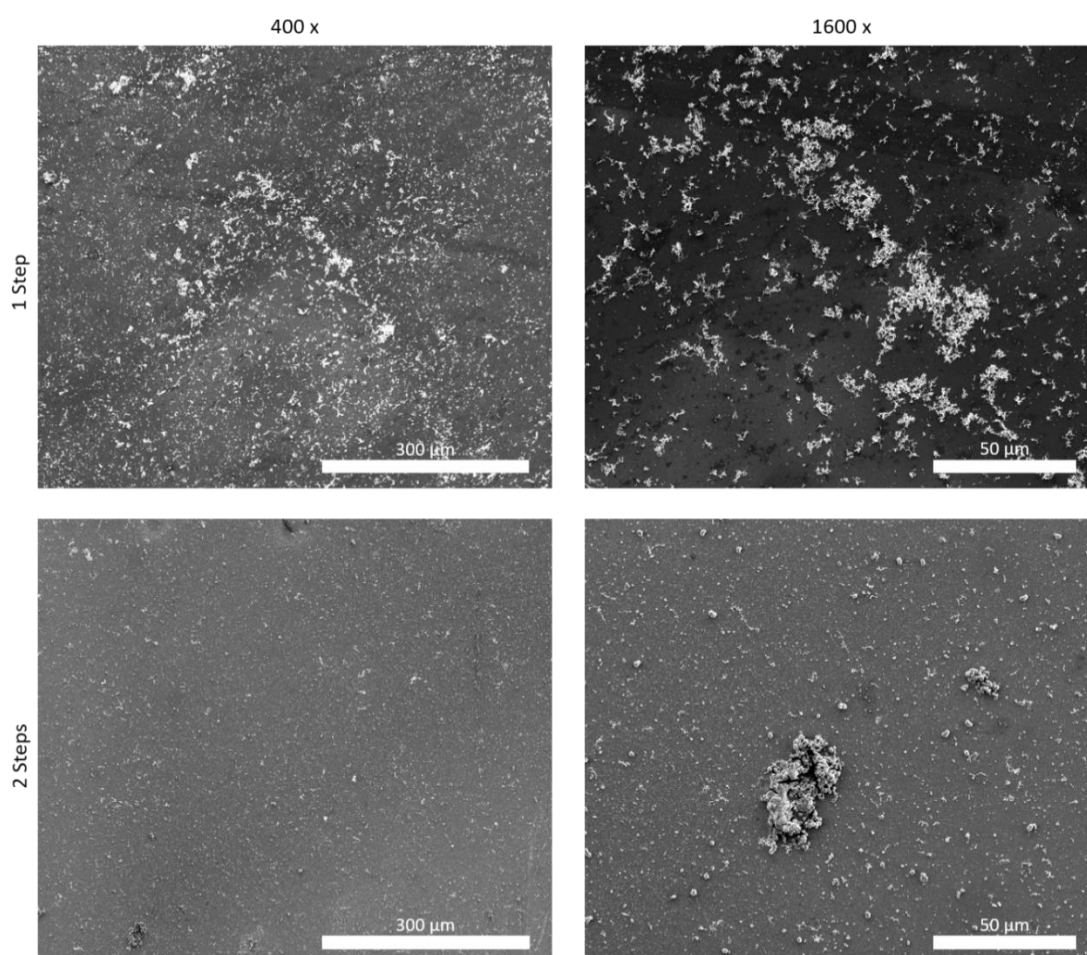


Figure 3.1.5 – SEM micrographs for GA crosslinking carried out in 1 or 2 steps. 3-hour incubation time used for both methods and a concentration of 1% v/v. Scale bars represent 300 μm on 400 x magnification image and 50 μm on 1600 x magnification image.

Finally, as a control sonication was carried out to ensure that NPs were chemisorbed to the surface and not just physisorbed (Figure 3.1.6). A control surface that had been put into a mineralisation reaction was also imaged. This control surface contained an amine terminated

SAM, but crosslinking had not been carried out, so any NPs formed on the surface should only be physisorbed. The SEM image for this sample shows that there is some NP formation on the surface however particle density and coverage is much lower than compared to when crosslinking has been carried out. After sonication a much lower particle density is observed and large aggregates on the surface have been removed. Although there is still some material present on the surface after sonication it is in a low yield and this could be due to NPs interacting with the amine terminated SAM. Later on, in this thesis (chapter 5) it is shown that lysine residues can bind with high affinity to CoPt NPs and so it is possible that the amine group present in the SAM is behaving in a similar way here.

When crosslinking has been carried out there is a much higher concentration of NPs present on the surface. This suggests that crosslinking is required so that MjHSP is attached to the surface for mineralisation of CoPt NPs to take place. After sonication of this sample a decrease in particle density is observed, suggesting that previously not all material was chemisorbed onto the surface. Sonication is likely to have removed material that was only physisorbed onto the surface. Large aggregates that were observed before sonication have now been removed suggesting that these aggregates were likely to be from NPs magnetically attracting together during mineralisation. Although a decrease in particle density is observed there is still a much higher concentration of particles present on the surface compared to the control sample where crosslinking has not taken place. Although GA crosslinking is generally thought to be irreversible it is possible to reverse this process under acidic conditions and so the imine can be hydrolysed back to the corresponding primary amine.¹⁴¹ Once crosslinking was carried out these surfaces were incubated in a solution containing Co^{2+} and Pt^{2+} metal ions, it is known that this metal salt solution has a pH of 3 (4.2) and so when the crosslinked surface is placed in this solution it is possible that the hydrolysis reaction could occur. If hydrolysis is able to take place, then this would result in a lower percentage of peptide crosslinked to the surface and as a result NP formation on the surface would also be less likely. Therefore, this could account for the formation of low-quality surfaces with uneven coverage.

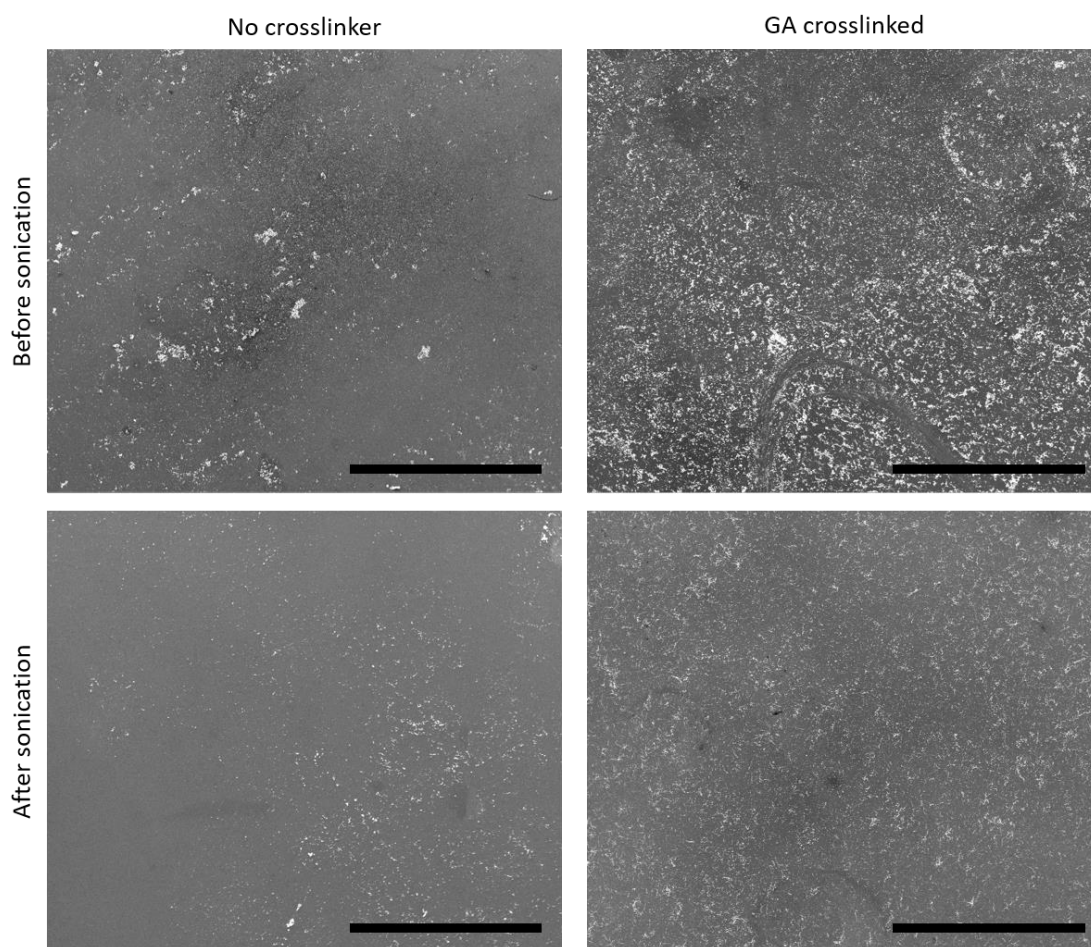


Figure 3.1.6 – SEM micrographs of GA crosslinking carried out for 3 hours followed by mineralisation of NPs and mineralisation carried out on a surface containing only the amine terminated SAM (no crosslinker). Images were recorded before and after sonication of the samples to ensure that NPs were chemisorbed and not just physisorbed. All images are at 220 x magnification and scale bars represent 500 μm .

3.1.2.2 GMBS Crosslinking

GMBS crosslinking was based on the protocol outlined by ThermoFisher.¹⁴² Modifications to the protocol were required as this protocol was based on crosslinking two peptides together rather than a SAM and a peptide. Therefore, steps that required removal of excess crosslinker by use of a desalting column were not possible and instead removal of the surface from solution followed by washing steps was carried out instead. Suggested incubation times of 30 mins and concentrations of GMBS were followed from the protocol. The surface with an amine terminated SAM present was first incubated with GMBS for 30 minutes, the sample was removed and washing steps followed, then the surface was placed into a solution containing the cysteine tagged peptide. The reaction was terminated by removing the surface from solution and followed by thorough washing.

One condition that required optimisation was the concentration of peptide used, two concentrations were tested (0.25 mg/ml and 0.5 mg/ml). From the SEM images (Figure 3.1.7)

it can be seen that NPs are present on both surfaces. There are regions where more aggregation of NPs has occurred, on both samples, this aggregation is likely to be as a result of NPs magnetically attracting to each other. Both concentrations have a similar particle density, and qualitatively it is difficult to distinguish which sample has a higher concentration of NPs. However, there is more aggregation present on the 0.5 mg/ml sample and so for future sample preparation a peptide concentration of 0.25 mg/ml would be used as this produced comparable particle density with less aggregation present.

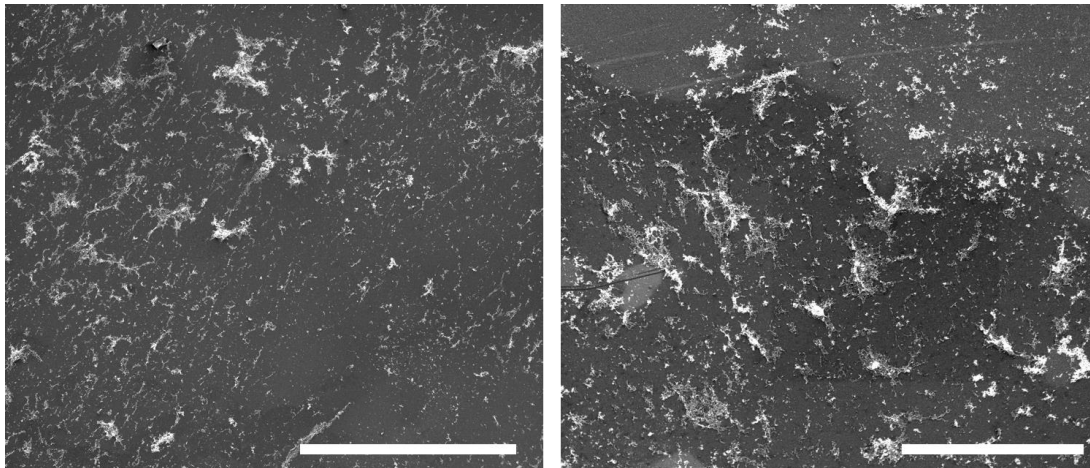


Figure 3.1.7 - SEM micrographs for GMBS crosslinking carried out using 0.25 mg/ml (left) and 0.5 mg/ml (right) peptide concentration. Scale bars represent 300 μ m and images are at 400 x magnification.

Sonication was carried out to ensure that material was chemisorbed to the surface and not just physisorbed. A control surface that had been exposed to the cysteine containing peptide (no crosslinker) and put into a mineralisation reaction was also imaged. For this control surface crosslinking of the peptide to the surface was not carried out and so any NPs formed on the surface should only be physisorbed. The SEM image (Figure 3.1.8) for this sample shows that there is some NP formation on the surface however it has a much lower particle density and coverage compared to when crosslinking has been carried out. After sonication a much lower particle density is observed and large aggregates on the surface have been removed. Comparing the control sample to the sample where GMBS crosslinking has taken place, shows that a larger number of NPs are present on the surface. Therefore, this suggests that crosslinking the peptide to the surface is crucial to ensuring that NPs can be mineralised on the surface. After sonication of this sample a reduction in particle density was observed, suggesting that previously not all NPs were chemisorbed onto the surface but may have been physisorbed. Although a reduction in particle density is observed it is still much higher than when crosslinking does not take place.

From optimisation carried out so far it can be observed that following the protocol set out by ThermoFisher and using a peptide concentration of 0.25 mg/ml, followed by sonication, is suitable for crosslinking a cysteine tagged peptide to an amine terminated SAM. Using the SEM images obtained for both GA and GMBS crosslinking it is not possible to identify whether one method would be more suitable over the other. Therefore, before crosslinking is carried out to attach peptides onto a nanoscale patterned surfaces further characterisation would be required so that a detailed analysis can be performed.

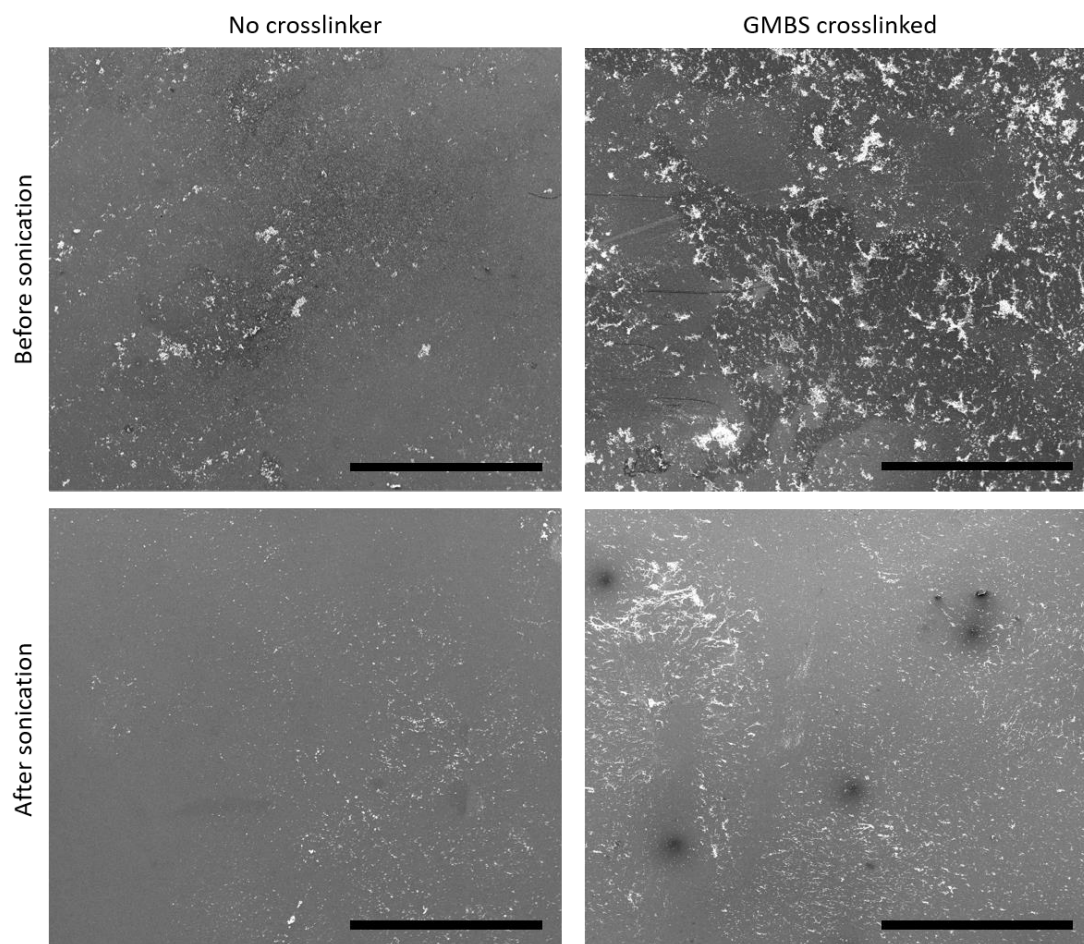


Figure 3.1.8 - SEM micrographs of GMBS crosslinking followed by mineralisation of NPs and mineralisation carried out on a surface containing only the amine terminated SAM (no crosslinker). Images were recorded before and after sonication of the samples to ensure that NPs were chemisorbed and not just physisorbed. All images are at 220 x magnification and scale bars represent 500 μm . Black spots on bottom right image are from where 'burning' of the sample has occurred during imaging.

3.1.3 INTERFEROMETRIC LITHOGRAPHY (IL)

It is known that IL is capable of forming patterns in SAMs down to 30 nm resolution and capable of patterning wide areas in one exposure.^{121,143,144} Once exposure conditions have been optimised, it is possible to reliably reproduce these patterns. Therefore, IL is able to achieve the patterning resolution that is required for BPM. IL was carried out in collaboration

with The Leggett Group at The University of Sheffield, allowing access to an IL system as well as AFM for imaging of patterned surfaces.

IL was carried out on titania surfaces with a SAM of APTES. However, due to the poor surface coverage that was identified from XPS and contact angle data, IL carried out on these surfaces resulted in the formation of very weak patterns (Figure 3.1.9). Two exposure doses were tested (1.08 and 2.81 Jcm^{-2}) and both AFM images show that line patterns were formed on the surface. However, lines of the SAM are very faint and not consistent. There is also a lot of contamination present on the samples, observed by the white marks on the AFM image, and this would need to be removed before optimising the IL procedure any further.

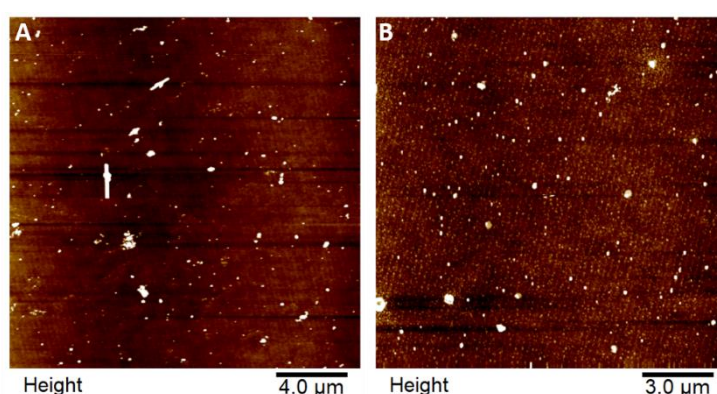


Figure 3.1.9 – AFM images of APTES SAMs on titania that were patterned using IL. A) sample exposed to dose of 2.81 Jcm^{-2} and B) sample exposed to dose of 1.08 Jcm^{-2} . Angle of exposure is 20° .

3.2 NANOSCALE PATTERNING OF GOLD SURFACES

Due to the problems encountered when carrying out IL on titania surfaces with an APTES SAM a different approach was investigated. This approach used a gold surface instead and an amine terminated thiol SAM. The interaction of thiol SAMs on gold is one of the most well studied examples as it is easy to prepare and has high stability due to the strength of the Au-S bond formed.¹¹¹ Therefore, by using a well-studied system it should be possible to optimise the conditions for SAM formation more easily so that IL can be used to generate nanoscale patterned arrays. Although crosslinking was tested using titania surfaces and an APTES SAM this should not affect the conditions already identified as an amine terminated SAM is being used on a gold surface and so the chemistry of the SAM surface should remain unchanged.

3.2.1 FORMATION OF AMINE TERMINATED SAMs ON GOLD

SAMs of 6-amino-1-hexanethiol were formed on gold surfaces. A concentration of 10 mM was used, and slides were incubated in solution for 18 hours . Following SAM formation, samples were rinsed with degassed ethanol and dried under a stream of nitrogen so that contact angle measurements could be made. A contact angle of $32.5^\circ \pm 0.96^\circ$ was obtained and this is consistent with literature values for this SAM.^{145,146} Therefore, as the contact angle

value obtained is consistent with literature the concentration and incubation conditions used here were used for all subsequent sample preparation.

Table 3.2.1 – Contact angle measurements for 6-amino-1-hexanethiol SAM on gold surface. Contact angle measurements repeated a minimum of five times on different areas of the surface.

Sample	Contact Angle /degrees
10 mM 6-amino-1-hexanethiol SAM on gold surface	32.5±0.96

3.2.2 INTERFEROMETRIC LITHOGRAPHY (IL)

Once SAMs of 6-amino-1-hexanethiol hydrochloride were formed on gold surfaces, the surfaces were then exposed to laser light setup in a Lloyd's mirror configuration. This resulted in the formation of dark and bright fringes over the surface. Where constructive interference occurred SAMs were removed from the surface and in regions where destructive interference occurred no changes to the SAM were observed. This resulted in the formation of periodic arrays with uniform lines of SAM separated by regions where the SAM had been removed. The surface was then placed into a gold etch solution to remove any gold from areas where SAM was no longer present. This resulted in regions of SAM on gold separated by the glass substrate.

3.2.2.1 Production of nanoscale line arrays

To achieve well defined nanoscale features the dose of exposure needs to be optimised. Exposure dose is proportional to the laser power and the exposure time. Therefore, before each exposure the laser power was measured at the sample surface so that exposure dose could be easily calculated. Laser power is relatively stable and as a result the exposure time can be altered so that different exposure doses were achieved. A range of different exposure times were tested so that the optimum exposure dose for a 6-amino-1-hexanethiol hydrochloride SAM was identified, samples were then characterised using AFM.

1) Interferometric Lithography

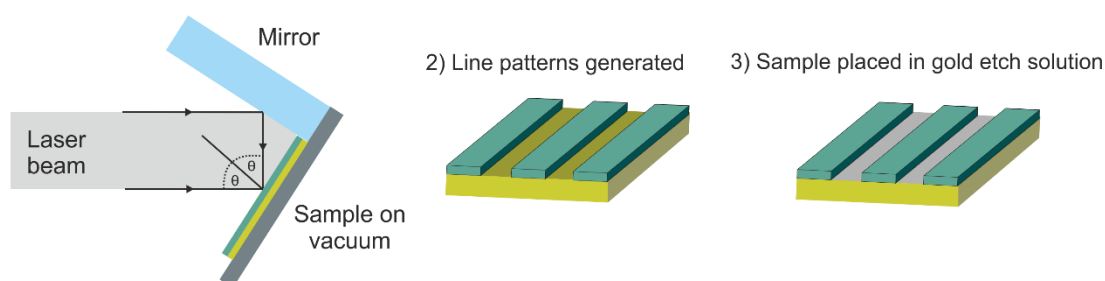


Figure 3.2.1 – Schematic showing the process used to generate line patterns on gold. 1) Gold surface with amine terminated thiol SAM was exposed to laser light in a Lloyd's mirror configuration 2) Degraded SAM was washed away to leave line array of the SAM and 3) Sample is placed in gold etch solution so that remaining gold between the regions of SAM is removed.

Initially, exposure doses of 36 Jcm^{-2} and 48 Jcm^{-2} were investigated and samples imaged using AFM (Figure 3.2.2). As can be seen from the AFM images, the features produced are well defined. Using an exposure dose of 48 Jcm^{-2} resulted in line patterns that are much more well defined than those generated from an exposure dose of 36 Jcm^{-2} . This suggests that an exposure dose of 48 Jcm^{-2} for a 6-amino-1-hexanethiol hydrochloride could be optimum. After exposure the samples were placed into gold etch solution, this removed any unprotected gold from the surface and results in a larger height difference between the SAM and the rest of the surface. Therefore, making patterns more prominent and easier to see when imaging using AFM. Another advantage of carrying out etching is that this will also help to remove any contaminants from the surfaces either as a direct result of the etch solution or from thorough washing of samples. As can be observed from the AFM images there is minimal contaminant present on the surfaces.

The angle of exposure used was 20° , using a smaller angle results in patterns with a larger period between them. Ideally for BPM, patterns would need to be generated with smaller periods between features and smaller nanoscale features on the surface. Using a smaller angle is experimentally easier and was used for the optimisation of exposure dose. Once all other parameters are known the angle of exposure can then be increased so that patterns with smaller feature sizes are generated.

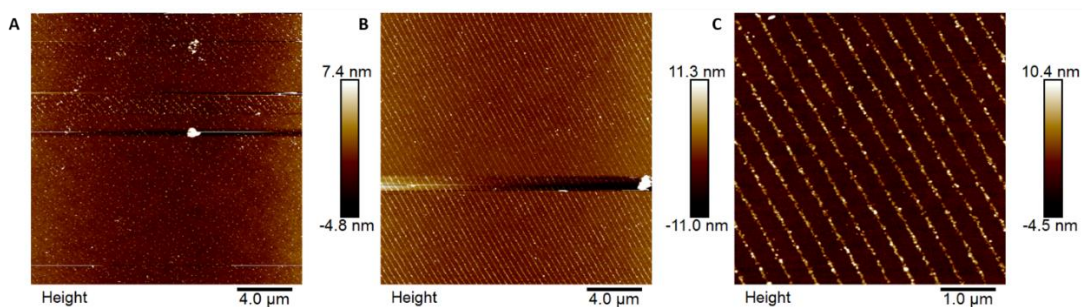


Figure 3.2.2 - AFM Images of A) Exposure dose of 36 Jcm^{-2} and B) and C) exposure dose of 48 Jcm^{-2} . All samples were placed in etch solution for 12 minutes and an exposure angle of 20° was used.

The sample that was generated from an exposure dose of 48 Jcm^{-2} was imaged in more detail and the resulting images can be seen below in Figure 3.2.3. These images have been used to collect data such as the period of the pattern as well as the height of the SAM. The average line width of the pattern was calculated to be 158 nm, this data was obtained from the highest magnification image and regions where data was collected are highlighted with dotted lines on the AFM image. An average height for regions where SAM is present was calculated to be 8.3 nm. It is expected that a SAM of 6-amino-1-hexanethiol hydrochloride

would have a monolayer thickness of ≈ 0.71 nm.* As the height obtained from AFM is 8.3 nm this would suggest that the majority of the height obtained comes from the evaporated gold and only approximately 1 nm is due to the presence of the SAM.

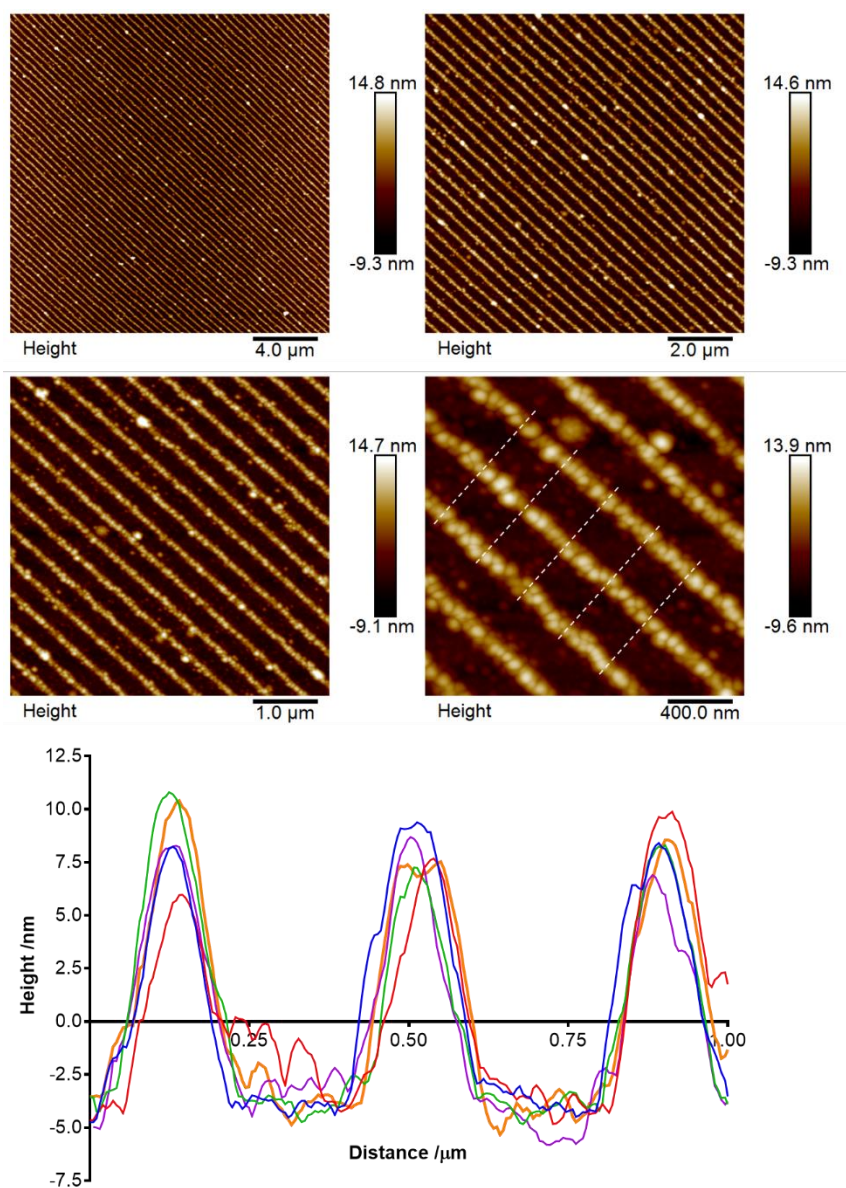


Figure 3.2.3 – AFM images collected from sample produced using an exposure dose of 48 Jcm^{-2} followed by etching for 12 minutes and at an exposure angle of 20° . Dotted lines represent regions used to calculate average period of pattern and this has been presented graphically. Average line width of 158 nm and height of 8.3 nm was calculated.

As an exposure dose of 48 Jcm^{-2} produced well defined features and good contrast, a slightly reduced exposure dose was tested to see if this would still produce well defined features. An exposure dose of 40 Jcm^{-2} was selected. AFM images were collected for this sample and these

* 6-amino-1-hexanethiol hydrochloride has a molecular mass of 170 gmol^{-1} , and a density of 0.791 gcm^{-3} . 1 molecule would occupy $3.56 \times 10^{-28} \text{ m}^3$ which can be represented as a cube of side length $7.09 \times 10^{-10} \text{ m}$ (0.71 nm). Suggesting a monolayer would be ≈ 0.71 nm thick.

can be seen in Figure 3.2.4 below. Once again well-defined nanoscale features are observed and there is good contrast between regions where SAM is present and absent. The highest magnification image has been used to calculate the period of the pattern as well as the height of the SAM. Dotted lines can be observed on the image and this is where data was collected, an average line width of 151 nm and a height of 10.7 nm was calculated. This period is very similar to the period produced from an exposure dose of 48 Jcm^{-2} (158 nm). However, the height of the SAM is lower (8.3 nm) for an exposure dose of 48 Jcm^{-2} compared to the height of the SAM for a 40 Jcm^{-2} exposure (10.7 nm). The samples were cut from the same gold substrate that had been immersed in a solution of 6-amino-1-hexanethiol hydrochloride to form a SAM, and so the difference in height could be due to using different areas of the substrate for each sample, as a slight variation in height would be expected across the whole substrate.

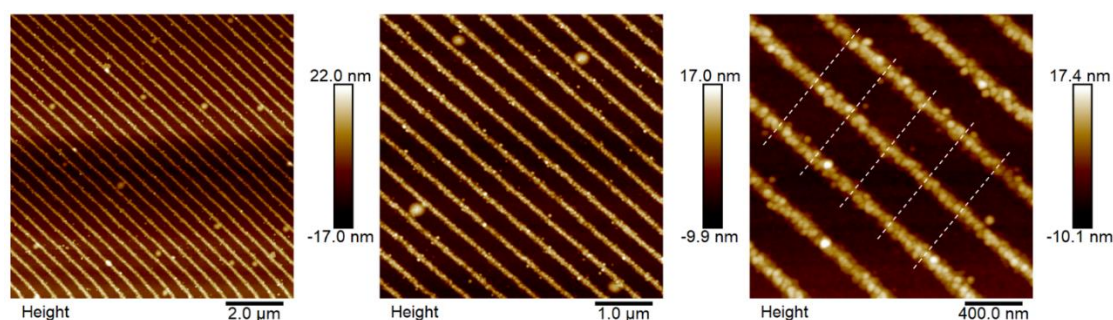


Figure 3.2.4 – Sample generated from using an exposure dose of 40 Jcm^{-2} followed by etching time for 12 mins and an exposure angle of 20° . Line width calculated as 151 nm and height of SAM as 10.7 nm. Dotted lines represent where data was collected to calculate period of pattern and height of SAM.

Exposure doses of 40 and 48 Jcm^{-2} have resulted in well-defined nanoscale line patterns with line widths of 151 and 158 nm being produced respectively. These exposure doses will be carried forward to generate nanoscale dot patterns.

3.2.2.2 Production of nanoscale dot arrays

Once the production of nanoscale patterned lines was successfully achieved (3.2.2.1), the focus then moved on to the production of nanoscale dot patterns. The formation of biomineralised dot arrays of CoPt or FePt NPs would be a significant step forward towards BPM. The first stage of this process is the production of dot arrays. Previous work in the literature has shown that IL is capable of producing nanoscale dot arrays in SAMs through the application of two exposures, with rotation of the sample through 90° between exposures (Figure 3.2.5).¹²¹

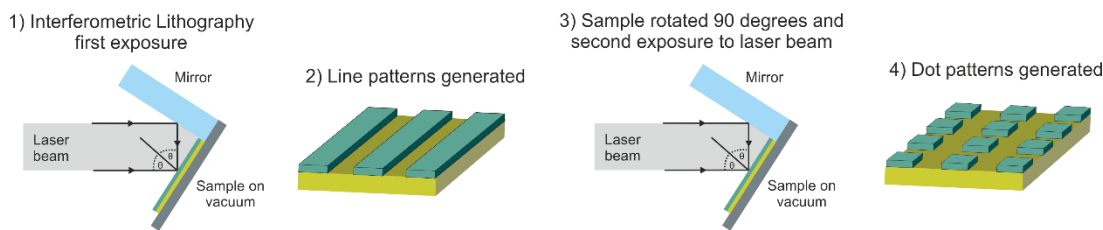


Figure 3.2.5 – Schematic showing the process used to generate dot patterns on gold surfaces. 1) Gold surface with amine terminated thiol SAM was exposed to laser light in a Lloyd's mirror configuration 2) After one exposure this would result in a line array generated 3) Sample was rotated by 90° and exposed to laser light once again and 4) Degraded SAM was washed away to leave a dot array pattern on gold.

The same approach as described in section 3.2.2.1 was followed, using the optimised conditions for the first exposure. After the first dose the sample was rotated by 90° and exposed to the laser, this time at a slightly reduced dose. A slight reduction in dose is required so that the sample is not overexposed and does not result in non-uniform dot patterns formed. As exposure doses of 40 and 48 Jcm^{-2} generated well defined line arrays, both exposures are tested here to identify whether one dose over the other resulted in more defined dot arrays.

A dose of 48 Jcm^{-2} was first used, this was followed by a second exposure of dose 38 Jcm^{-2} . AFM images obtained from this sample can be seen in Figure 3.2.6 and from these images it is possible to identify that a periodic dot array has been formed. AFM images were used to calculate the average line width of the pattern as well as height of the SAM. A line width of 204 nm and height of 7.3 nm was obtained.

A dose of 40 Jcm^{-2} was also used for the formation of dot arrays, after rotation of the sample by 90° a second exposure at dose 33 Jcm^{-2} was carried out. From these AFM images the line width of the pattern and height of the SAM was calculated, a line width of 194 nm and height of 5.3 nm was obtained. The line width fits well with the sample produced from an exposure dose of 48 Jcm^{-2} and although the height is slightly lower this could be due to using a different area of the gold substrate for the generation of this sample.

The line widths of 194 and 204 nm generated are larger than what would be required for BPM, however using a slightly larger line width allows for easier imaging and identification of attachment of peptides and subsequently NPs to the arrays. Therefore, once the whole process has been fully optimised it would then be possible to reduce feature sizes further by increasing the angle of exposure.

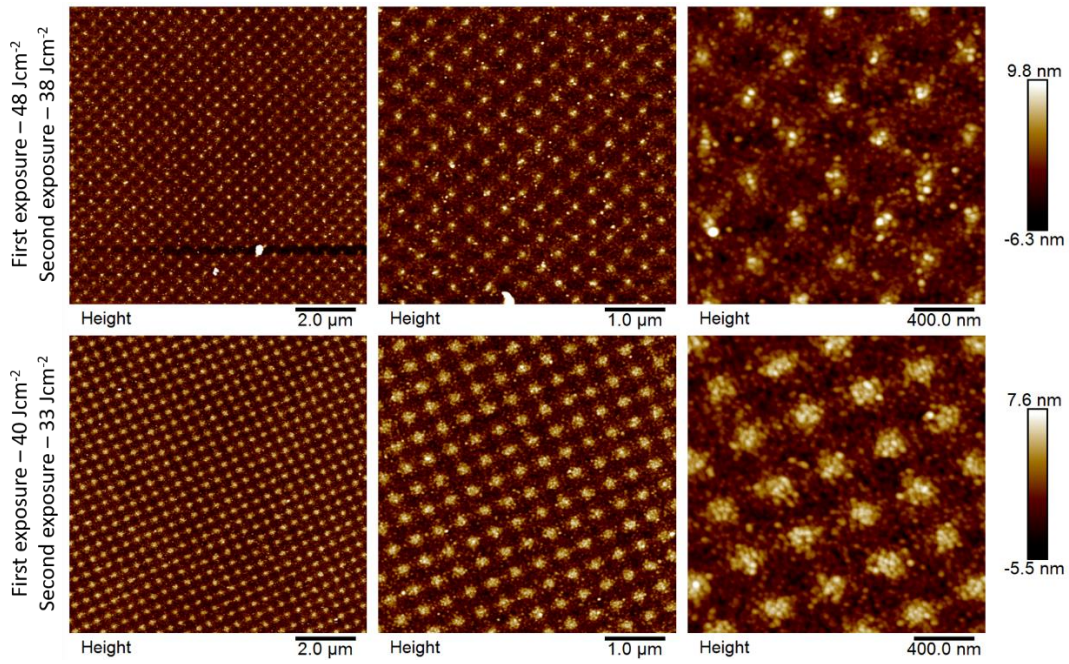


Figure 3.2.6 – **Top**: First exposure was at a dose of 48 Jcm^{-2} , sample was then rotated 90° and exposed to a dose of 38 Jcm^{-2} . A line width of 204 nm and height of 7.3 nm was calculated. **Bottom**: First exposure was at a dose of 40 Jcm^{-2} , sample was then rotated 90° and exposed to a dose of 33 Jcm^{-2} . A line width of 194 nm and height of 5.3 nm was calculated. Samples were placed into etch solution for 12 minutes and angle of exposure was set to 20° .

3.3 SUMMARY

In this chapter formation of SAMs, crosslinking of peptides/proteins to SAMs and production of nanoscale arrays using IL were investigated. Initially, an APTES SAM on a titania surface was investigated however problems with surface coverage were encountered. As a result of this it was difficult to generate well defined nanoscale patterns using IL. Further optimisation of the formation of APTES SAMs on titania would be required before this system is able to be reliably used for the generation of nanoscale patterned surfaces.

However, crosslinking using this system was investigated to attach peptides/proteins to the surface. Two types of crosslinking were used, GA and GMBS crosslinking. From the SEM images obtained it was difficult to identify whether one method over the other would be more suitable for use. However, it was possible to optimise the conditions for both reactions. The optimised conditions identified for GA crosslinking were that the reaction should be carried out in 1 step, a 3- hour incubation and a peptide concentration of 0.1 mg/ml would also be used. For GMBS crosslinking, following the protocol set out by ThermoFisher produced good results when a peptide concentration of 0.25 mg/ml was used. Only a basic assessment of crosslinking was carried out using SEM therefore before crosslinking is carried out to attach peptides/proteins to nanoscale patterned surfaces a more detailed analysis would be required. This could be achieved through the use of crystal quartz microbalance dissipation (QCM-D) to monitor attachment to the surface. Collection of higher resolution SEM images would also be beneficial so that morphological information for the NPs present on the surface can be obtained. Using energy dispersive x-ray as part of SEM imaging would allow for elemental analysis to be carried out on the surfaces.

Due to the problems encountered using APTES SAMs on titania, interferometric lithography was carried out using a system of an amine terminated thiol on a gold surface instead. It was important that an amine terminated SAM was used so that this group can be used for future attachment to the surfaces. Samples were exposed to a laser beam, set up in a Lloyds mirror configuration, at a dose of 40 – 50 Jcm⁻² and this resulted in line patterns formed with a period of \approx 150 nm. These conditions were then carried forward for the production of nanoscale dot patterned surfaces. Samples were first exposed to a laser beam at doses of 40 – 50 Jcm⁻², the sample was then rotated by 90° and a second exposure carried out (33 – 38 Jcm⁻²). This resulted in dot arrays formed on the gold surface with a period of \approx 200 nm. The production of nanoscale dot patterned surfaces is an excellent step forward to BPM becoming a reality. However, smaller nanoscale features would be required for BPM and this could be achieved by increasing the angle of exposure used in IL. Crosslinking peptides to

these surfaces would then be possible, followed by incorporation into NP mineralisation reactions for the production of a biotemplated nanoscale dot array.

CHAPTER FOUR: SYNTHESIS & DOPING
OF PT ALLOY MAGNETIC NANOPARTICLES

4 SYNTHESIS AND DOPING OF Pt ALLOY MAGNETIC NANOPARTICLES

Pt alloy NPs in the L1₀ phase have received a great deal of interest due to their possible use for future data storage as they have a high enough magnetocrystalline anisotropy to remain magnetically stable at volumes of a few nanometres.³⁷ However, current synthesis methods for L1₀ phase NPs require the use of harsh reaction conditions and solvents. In this chapter a room temperature synthesis method is investigated for the formation of Pt alloy NPs, along with the addition of additives that may promote L1₀ ordering. Hopefully, this would be a step towards achieving MNPs with a high coercivity that are produced using a green synthesis method, without the need for high temperature annealing steps and use of harsh solvents.

Two different types of additives will be investigated, first is the inclusion of dopants into the synthesis and second is the use of biological molecules such as peptides and proteins. Incorporation of impurities into Pt alloy nanoparticles has been shown to lower the annealing temperature required to transform the NPs from the disordered to the ordered phase. Elements such as silver, boron, antimony, tin, lead and bismuth have been incorporated into CoPt NPs.^{41,147–150} Whereas elements such as silver, copper, gold and zirconium have been used for FePt.^{151–153} Here, the effect of incorporating silver and bismuth into FePt and CoPt room temperature synthesis reactions was investigated. Silver and bismuth were chosen over other dopants due the large increases in coercivity observed in literature, as well as being materials that are readily available.

MjHSP is a small heat shock protein from *Methanococcus jannaschii*. It assembles into a 24 subunit hollow cage with interior and exterior diameters of 12 nm and 6 nm respectively.⁶³ A small peptide sequence that shows binding specificity for L1₀ phase CoPt has previously been incorporated at the N-terminus of each subunit of the cage.⁶³ Therefore, by carrying out particle synthesis in the presence of MjHSP it is expected that L1₀ NPs will be preferentially formed inside the cavity. Finally, silver and bismuth doping has been tested in combination with MjHSP. By combining the protein cage and doping it is predicted that the coercivity will be increased beyond that obtainable via a standard room temperature coprecipitation reaction, or with the addition of doping or the cage protein alone.

4.1 L1₀, L1₂ AND A1 PHASE Pt ALLOY NANOPARTICLES

Controlling the composition of Pt alloy NPs is crucial as different compositions can result in different chemical and physical properties as well as different crystal structures. There are three possible ordered phases of Pt alloys which are XPt₃ (L1₂), XPt (L1₀) and X₃Pt (L1₂), where X represents either Fe or Co.³⁶ Only the L1₀ phase is magnetically hard whereas FePt₃ is paramagnetic and Fe₃Pt is ferromagnetic in the ordered phase.³⁶ As well as these three ordered states it is possible that NPs are synthesised in a disordered state, known as the A1 phase. NPs in the A1 phase may also consist of different compositions such as: XPt₃, XPt and X₃Pt. There are distinct differences between the phases that can be identified from XRD, VSM and ICP-OES data that will allow for the composition of the NPs to be determined, characteristic features can be seen in Table 4.1.1 and theoretical powder XRD spectrums can be seen in Figure 4.1.1

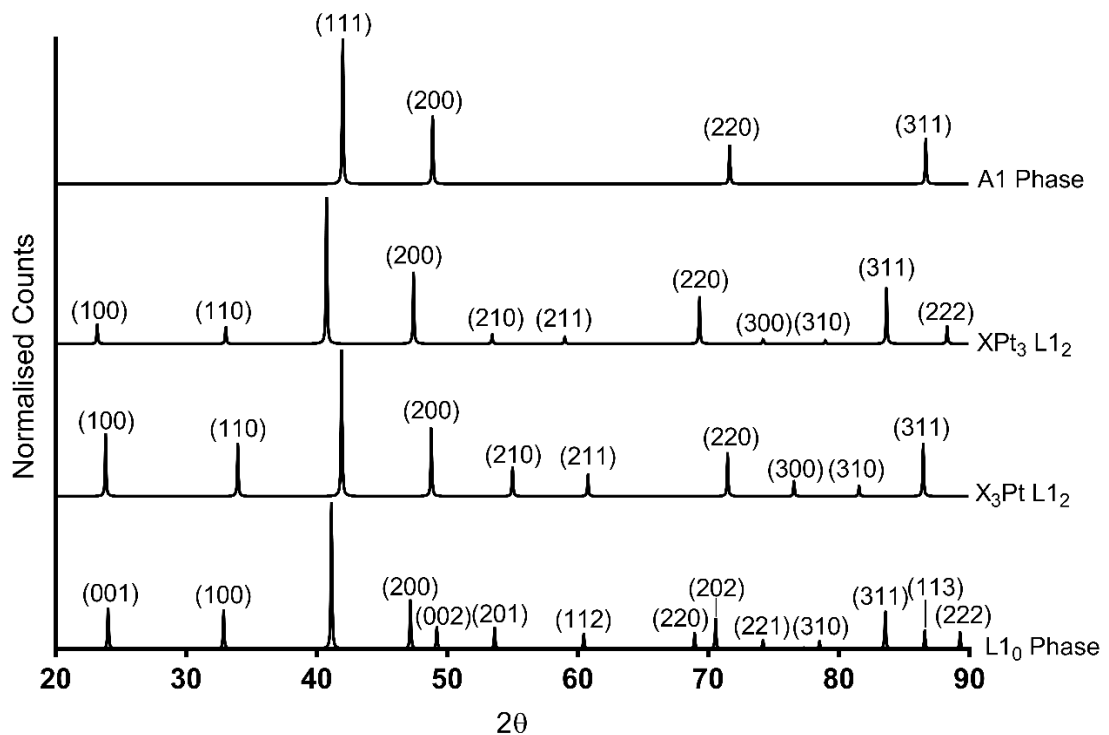


Figure 4.1.1 – Theoretical powder XRD for the A1 and L1₀ phases of Co/Fe Pt alloys with lattice planes labelled. Crystallographic data downloaded from the crystallography open database and modelled using Mercury software.

Table 4.1.1 – Table highlighting the difference in characteristic features as determined by XRD and VSM for the L1₂, L1₀ and A1 crystal phases of Pt alloy NPs. XRD peaks in black – common to all phases, red – unique to L1₀, blue – unique to L1₂ and orange – common to both L1₂ and L1₀.^{36,154}

Phase	Magnetic Properties	Crystal Structure	Particle size /nm	Composition X:Pt
L1 ₂ XPt ₃	H _c ≈ 0 – 100 Oe Paramagnetic at RT	fcc	15 – 20	25:75
L1 ₂ X ₃ Pt	H _c ≈ 100 – 200 Oe Magnetically soft Ferromagnetic	fcc	10 – 15	75:25
L1 ₀ XPt	H _c ≈ 1 – 10 kOe Magnetically hard	fct	2 – 10	50:50
A1 XPt ₃ , X ₃ Pt and XPt	Almost no H _c at room temperature	fcc	Variable	Variable

4.2 CoPt NANOPARTICLE SYNTHESIS AND CHARACTERISATION

CoPt MNPs were synthesised in a room temperature co-precipitation reaction and these particles were analysed using ICP-OES, XRD, and VSM. ICP-OES was used to investigate the effect of varying the ratios of Co to Pt and what effect this had on the overall composition of the NPs. The amount of Pt was kept constant and the amount of cobalt was varied from 1:1 up to 6:1. Increasing the molar amount of cobalt generally resulted in increased cobalt in the final sample. However, a 1:1 input ratio gave a higher amount of cobalt than expected, as a ratio of 60:40 was present in the synthesised sample. When a 3:1 input ratio was used, a ratio of 40:60 was obtained in the NP product, which is the closest sample to the ideal 50:50 ratio for CoPt. Using a 3:1 input ratio has been previously identified as giving the closest to the desired 50:50 ratio.⁶⁴

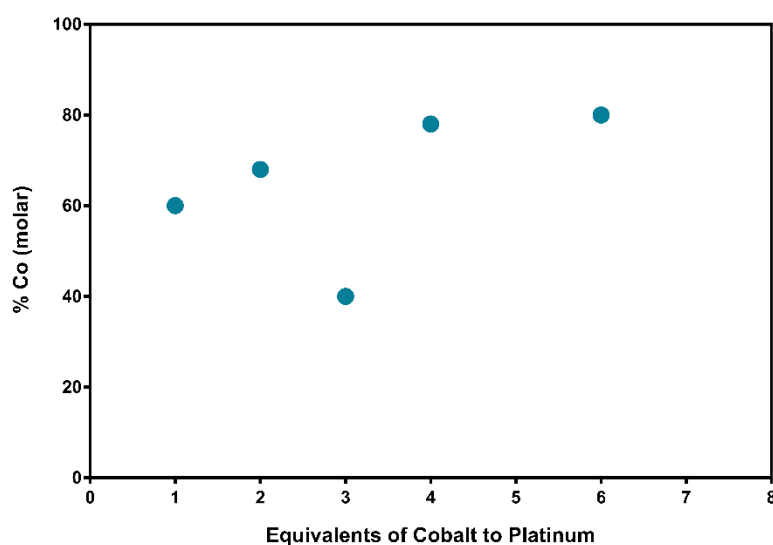


Figure 4.2.1 - ICP-OES analysis of CoPt NPs synthesised from different ratios of cobalt and platinum. Y axis – the percentage cobalt in the final product. X axis – the equivalents of cobalt and platinum used.

From ICP-OES data it is not possible to determine whether the ordered (L1₀/L1₂) or disordered phase (A1) has been synthesised. Therefore, XRD was used to determine the crystal structure of the particles. All of the observed reflections from the sample (diffraction peaks) were compared to known standards for A1, L1₂ and L1₀ CoPt. The principle diffraction peaks at $2\theta = 40.3^\circ$, 46.8° , 68.8° and 82.8° correspond to the (111), (200), (220) and (311) reflections of CoPt in the A1 phase (Figure 4.2.2). The (111) peak is the most intense and therefore was used to calculate the particle size via the Scherrer equation. This calculation suggests that the particles have an average size of ≈ 7.8 nm. In literature example CoPt NPs typically vary from 1 – 20 nm so a value of 7.8 nm would be an acceptable size for the NPs.^{42,45,63,155}

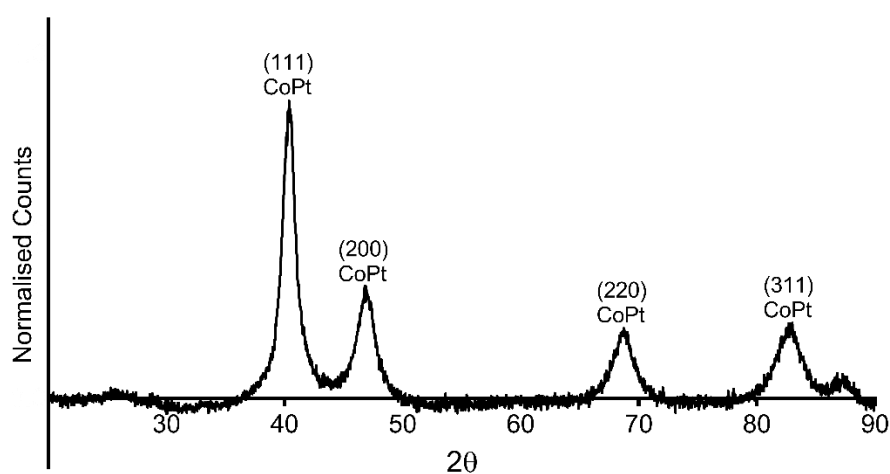


Figure 4.2.2 - XRD data for synthesised CoPt with lattice planes labelled. Particle size calculated from the Scherrer equation is 7.8 nm.

Room temperature VSM analysis shows that the particles exhibit hysteresis and have a coercivity of 15 Oe (Figure 4.2.3). In literature a coercivity of 36 Oe is reported for as-synthesised CoPt nanoparticles however, this method was not carried out at room temperature and instead the synthesis involved heating to 200°C .⁴² Therefore, achieving a coercivity of 15 Oe from a room temperature synthesis would be an acceptable value for A1 phase CoPt. From ICP-OES, XRD and VSM data it can be determined that A1 phase CoPt was successfully synthesised.

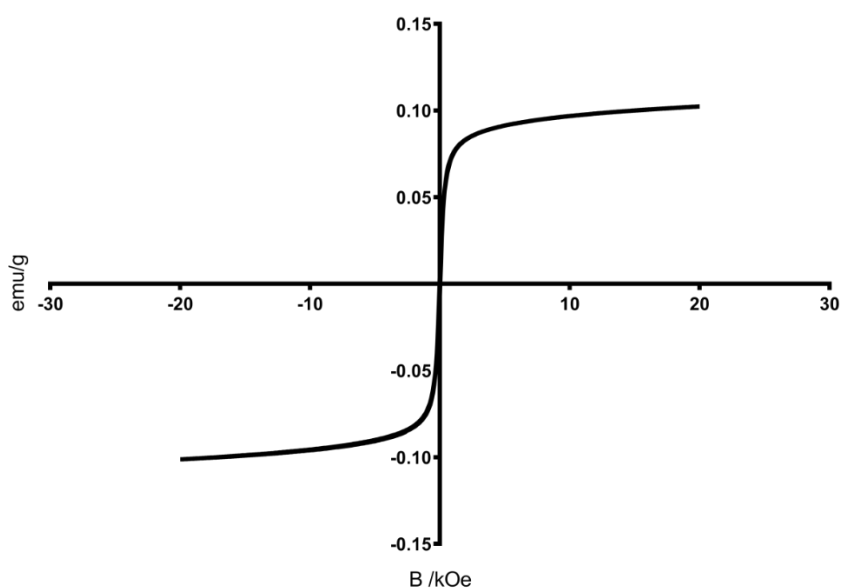


Figure 4.2.3 – Magnetic hysteresis of CoPt nanoparticles at 300 K. Y axis is magnetic moment in emu/g and X axis is magnetic field strength in kOe. Coercivity of 15 Oe.

The pH of a CoPt room temperature co-precipitation reaction has been monitored. The pH starts at $\approx 6 - 9$ due to the presence of only ultrapure water. On addition of Co^{2+} and Pt^{2+} salts the pH stabilises at $\approx \text{pH } 5$. After addition of NaBH_4 the pH decreases down to 3, overtime this pH slowly increases to $\approx \text{pH } 4$. As biological molecules, such as peptides and proteins, are likely to be used to help control the synthesis and growth of the NPs it is important that the pH of the reaction is known. Amino acid residues will behave in different ways depending on the pH, so to fully understand what is happening in the synthesis reaction the pH needs to be known.

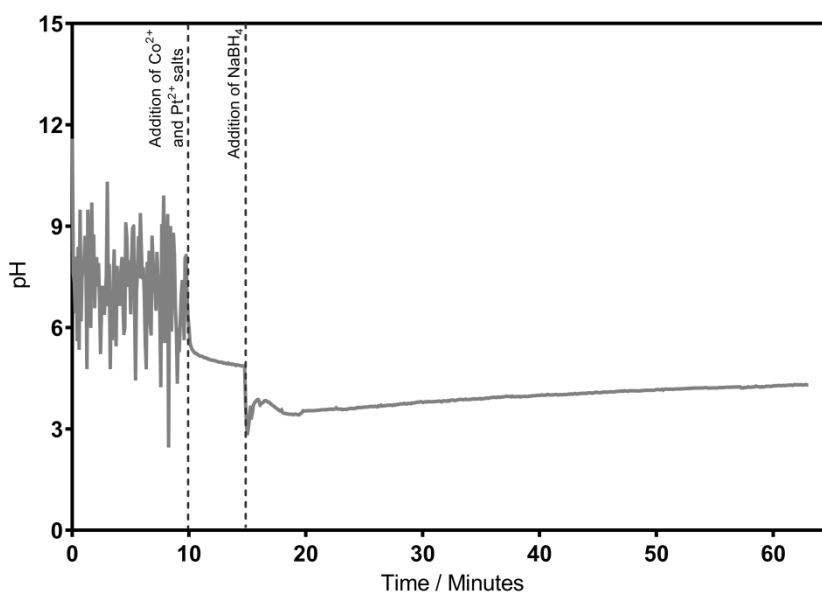


Figure 4.2.4 - pH profile for a CoPt synthesis reaction. Addition of Co^{2+} and Pt^{2+} salts after 10 minutes and addition of NaBH_4 at 15 minutes followed by incubation of the reaction for 45 minutes.

4.3 FePt NANOPARTICLE SYNTHESIS AND CHARACTERISATION

FePt MNPs were synthesised via a room temperature co-precipitation reaction and characterised using ICP-OES, XRD, VSM and TEM. The ratios of iron to platinum in the synthesis were varied to investigate the effect on the overall composition of the NPs and ascertain a ratio that could achieve a 50:50 ratio consistent with the formation of FePt. The amount of Pt was kept constant and the amount of Fe varied from 1:1 up to 5:1. The samples were dissolved in aqua regia and analysed by ICP-OES to allow iron and platinum content to be determined. The results from the ICP-OES can be seen below (Figure 4.3.1). Using a 1:1 ratio gave a very low amount of iron, only 20%. It is likely that FePt₃ has been synthesised, in this case. Increasing the amount of iron resulted in a roughly linear increase in the amount of iron in the final sample. Using a 5:1 input ratio of iron to platinum resulted in NPs that consisted of ≈ 70% iron, this data would be consistent with Fe₃Pt being formed. The closest ratio to 50:50 was observed when an input ratio of 3:1 was used, this gave a 41:59 ratio. Further optimisation was carried out to try to achieve a closer 50:50 ratio by using input ratios of 3.2:1 and 3.5:1 but this resulted in 60% iron and 40% platinum. Therefore, a 3:1 input ratio was selected for all subsequent synthesis reactions and is consistent with literature examples.⁶¹ However, ICP-OES data cannot reveal whether the ordered phase (L1₀/L1₂) or the disordered phase (A1) has been synthesised. Therefore, XRD was used to characterise the crystal structure of the NPs.

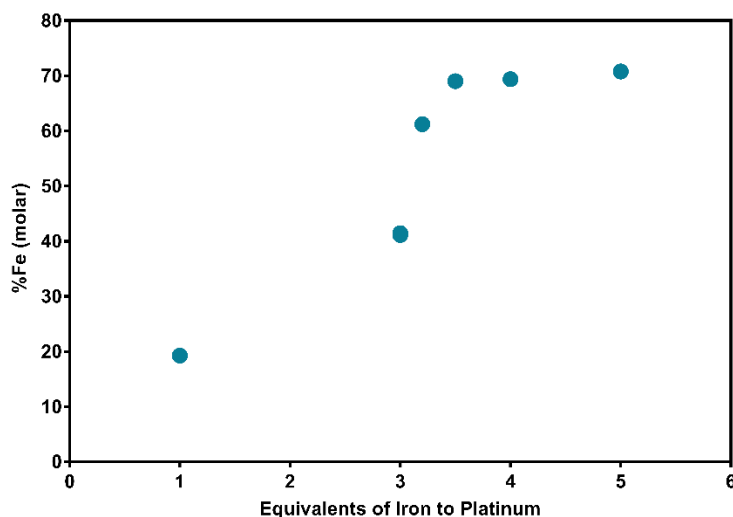


Figure 4.3.1 – ICP-OES analysis of FePt NPs synthesised from different ratios of cobalt and platinum. Y axis is the percentage iron in the final product. X axis is the equivalents of iron and platinum used.

Crystallographic analysis of the particles was performed using powder XRD and the peaks in the spectrum were compared to known standards for A1, L1₂ and L1₀ phase FePt. The XRD data shows peaks at $2\theta = 40.3^\circ, 46.9^\circ, 68.2^\circ, 82.4^\circ$ and 87.1° which correspond to the (111), (200), (220), (311) and (222) reflections of FePt in the A1 phase. It is expected that the

particles would be in the A1 phase as this reaction has been carried out at room temperature and higher temperatures are usually required for the formation of the L1₀ phase.¹⁵⁵ The (111) peak is the most intense and this peak was used to calculate particle diameter via the Scherrer equation. This calculation suggests that the particles have a diameter of ≈ 8.5 nm. In literature FePt NPs typically vary in size from 2 – 10 nm, depending on the synthesis method, therefore a value of 8.5 nm would be an appropriate size for the NPs.^{44,46,61,80}

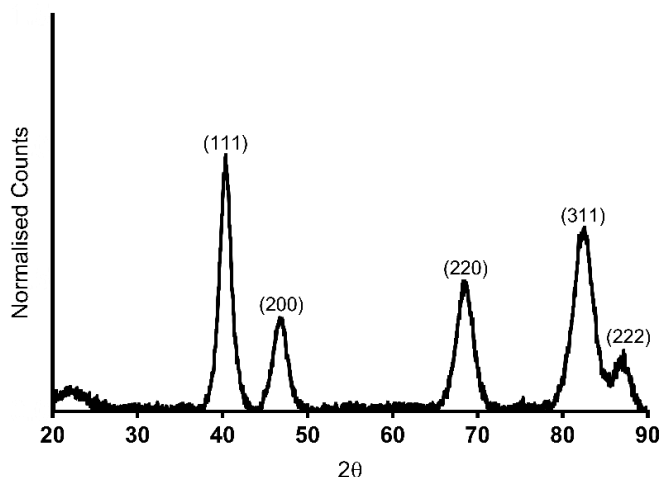


Figure 4.3.2 - XRD data collected for FePt nanoparticles with lattice planes labelled. Diameter calculated from the Scherrer equation is 8.5 nm. Broad peak at $\approx 20^\circ$ is from glass capillary.

Room temperature VSM analysis shows that the particles exhibit hysteresis and have a coercivity of 11 Oe (Figure 4.3.3). Typically, in literature very low or almost no coercivity is observed for as-synthesised FePt NPs at room temperature.^{30,44,82} Therefore, achieving a coercivity of 11 Oe from a room temperature synthesis would be an acceptable value of A1 phase FePt NPs. Combining ICP-OES, XRD and VSM data confirms that A1 phase FePt was successfully synthesised using this method.

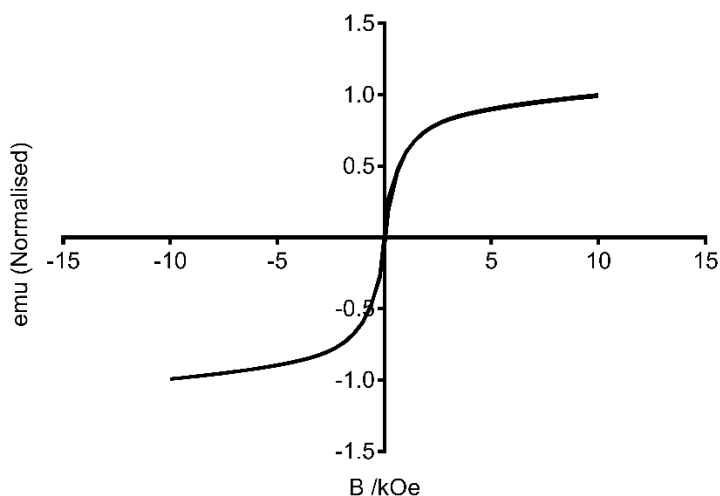


Figure 4.3.3 – Magnetic hysteresis of FePt NPs carried out at 300 K. X axis is magnetic field strength in kOe and Y axis is normalised magnetic moment. Coercivity of 11 Oe.

Transmission electron microscopy has been used to image the NPs produced (Figure 4.3.4), grainsize analysis was performed by measuring the particles in ImageJ. The data was plotted in GraphPad Prism and a Gaussian distribution fitted. This analysis reveals that the particles have a mean diameter of $\approx 19 \pm 6$ nm. Compared to literature values this is at the higher end of values observed for FePt NPs. However, this could be due to the particles aggregating through magnetic interactions and the high electron density of platinum alloys, making it difficult to grainsize individual particles by TEM. The particle diameter observed by TEM is much larger than that determined from XRD (8.5 nm). When estimating particle diameter from XRD data the Debye-Scherrer equation is used, this equation assumes that the particles have a spherical morphology due to the shape constant (β) being set to 0.89. Therefore, the particle diameter estimated from XRD is accurate assuming the particles have a spherical morphology. However, as can be observed from TEM the particles do not have a perfectly spherical morphology and as a result this could be why such a large difference in particle size is observed between TEM and XRD data.

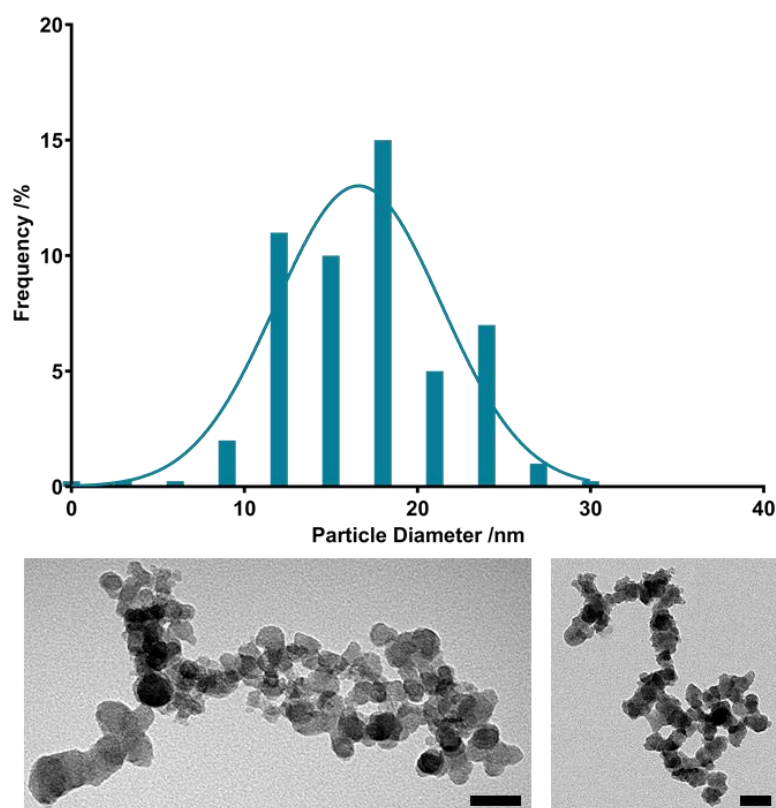


Figure 4.3.4 - TEM micrographs of FePt nanoparticles and histogram showing particle size distribution. Scale bars represent 50 nm.

The pH of a FePt synthesis reaction has been monitored throughout. The reaction starts at \approx pH 7 when only deoxygenated ultrapure water is present, this decreases down to \approx pH 3 when Fe^{2+} and Pt^{2+} salts are added. After 10 minutes the NaBH_4 was added, and the pH

returned to neutral, indicating that iron and platinum were precipitating out of solution. The pH of the reaction is important if it is to be combined with proteins or peptides that offer control and specificity for the L1₀ phase.

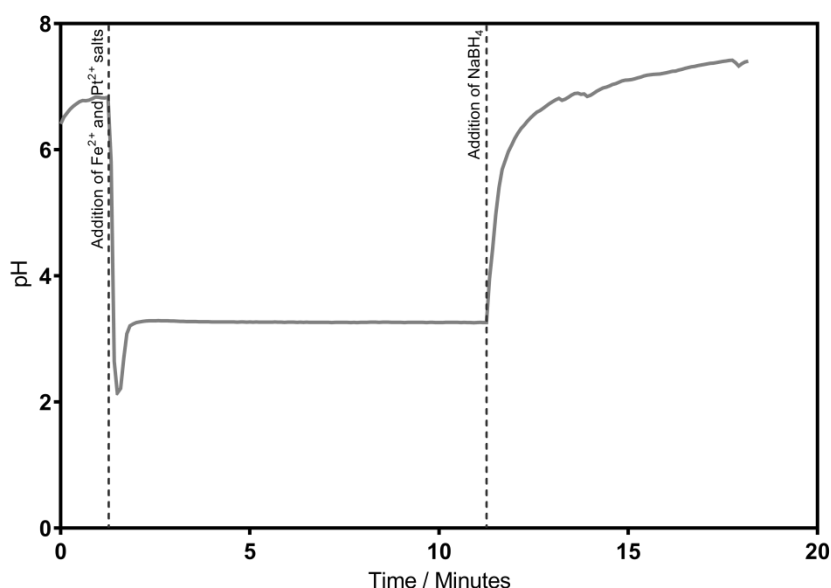


Figure 4.3.5 - pH profile of a FePt synthesis reaction, addition of Fe²⁺ and Pt²⁺ occurs after 1 minute and addition of NaBH₄ at 11 minutes.

4.3.1 SYNTHESIS OF ANNEALED FePt

Annealing of FePt was carried out under an argon atmosphere and by heating the sample to 825 °C for 1 hour. Annealing at this temperature is known to cause the NPs to undergo the transition from the A1 to L1₀ phase.¹⁵⁵ XRD confirmed that the L1₀ phase was synthesised due to the presence of the (001) and (110) peaks. These peaks are not present in the diffraction data of the pre-annealed NP. Annealing has clearly caused the sample to undergo the transition from the disordered to ordered phase. Splitting of the (200) peak is also present in the annealed sample which is characteristic of the L1₀ phase. The Scherrer equation has been used to calculate crystallite diameter before and after annealing, in each case the (111) peak was used as it is the most prominent. Prior to annealing the sample had a crystallite size of 8.5 nm and after annealing the size increased to 33.96 nm. This increase in size is to be expected as the particles will have agglomerated together during the annealing process. Room temperature VSM was performed on this sample and from this a coercivity of 10.8 kOe was observed. This is a very large coercivity and is consistent with literature coercivity values for L1₀ phase FePt.^{44,81} Therefore, XRD and VSM data both confirm that L1₀ phase FePt has successfully been synthesised using this method.

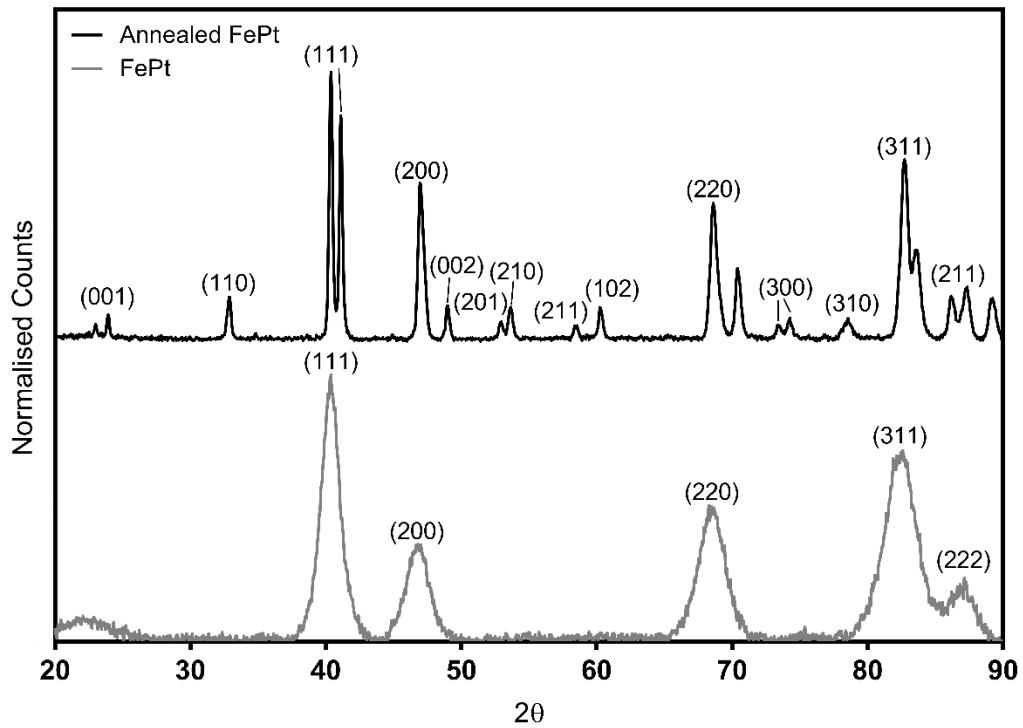


Figure 4.3.6 – XRD spectrum of FePt pre (grey) and post annealing (black). Lattice planes for A1 and L₁₀ phase FePt have been labelled. Broad peak at $\approx 20^\circ$ is from glass capillary.

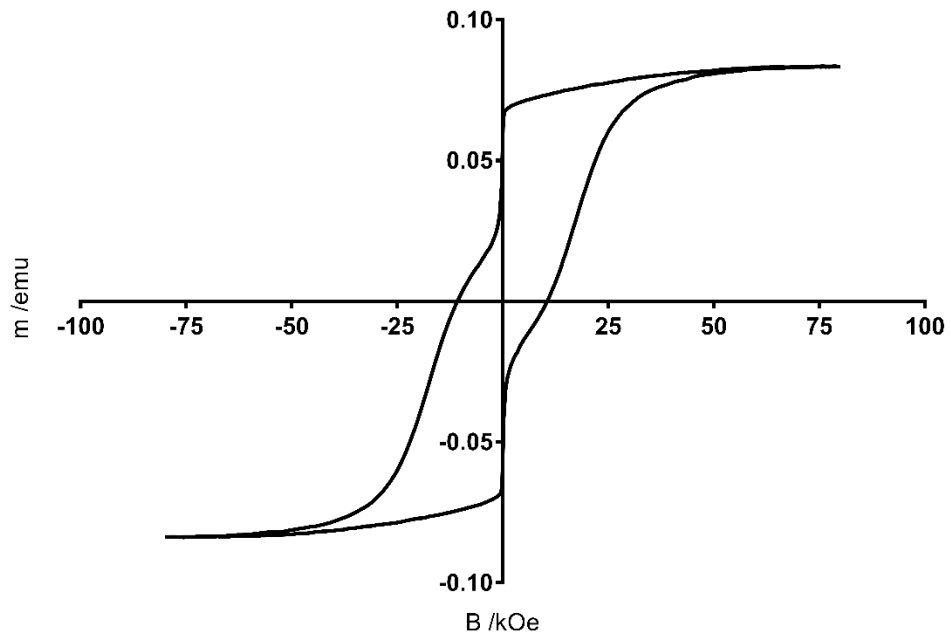


Figure 4.3.7 – Room temperature (300 K) VSM of annealed FePt. Y axis is magnetic moment in emu/g. X axis is magnetic field strength in kOe. Coercivity of 10.8 kOe.

4.4 DOPING THE NANOPARTICLE REACTIONS

4.4.1 SILVER DOPING

Incorporating silver (Ag) into FePt or CoPt NPs is known to reduce the temperature required for the formation of the ordered L1₀ phase.^{149,152} Addition of Ag into CoPt is thought to promote L1₀ ordering and (001) orientation, this orientation is crucial to obtain the large perpendicular magnetocrystalline anisotropy.¹⁴⁹ Therefore, silver doping has been carried out to investigate whether silver can promote L1₀ ordering and increase the coercivity in room temperature synthesis reactions. The levels of silver doping investigated were 0, 2, 5, 7 and 10 %. The XRD data for 0, 2 and 10% Ag shows peaks at $2\theta = 40.4^\circ$, 46.9° , 68.6° and 82.9° which correspond to the (111), (200), (220) and (311) planes of CoPt. These peaks are consistent with A1 phase CoPt. The characteristic peaks at $2\theta = 25^\circ$ and 35° for L1₀ CoPt are absent, again suggesting that the A1 phase has been synthesised. An extra peak at $2\theta = 65.3^\circ$ is observed in the spectrum for 10% Ag doping which does not correlate to any *d*-spacings that are consistent with CoPt or Ag. In the 5% Ag spectra an extra peak is observed at $2\theta = 25^\circ$, this is consistent with the *d*-spacings for the (001) plane which is typical of L1₀ phase CoPt. However, this is not usually observed alone, as the (110) peak at 35° would usually be present to indicate the L1₀ phase. Therefore, it is likely that there could be some partial L1₀ character in the sample. Particle diameter has been calculated from the (111) peak using the Scherrer equation. This calculation suggests that particles have a diameter of ≈ 7.8 nm for CoPt, 9.3 nm for 2% Ag doping and 5.9 nm for 10% Ag doping (Table 4.4.1). These calculated particle sizes are within the literature range for CoPt.

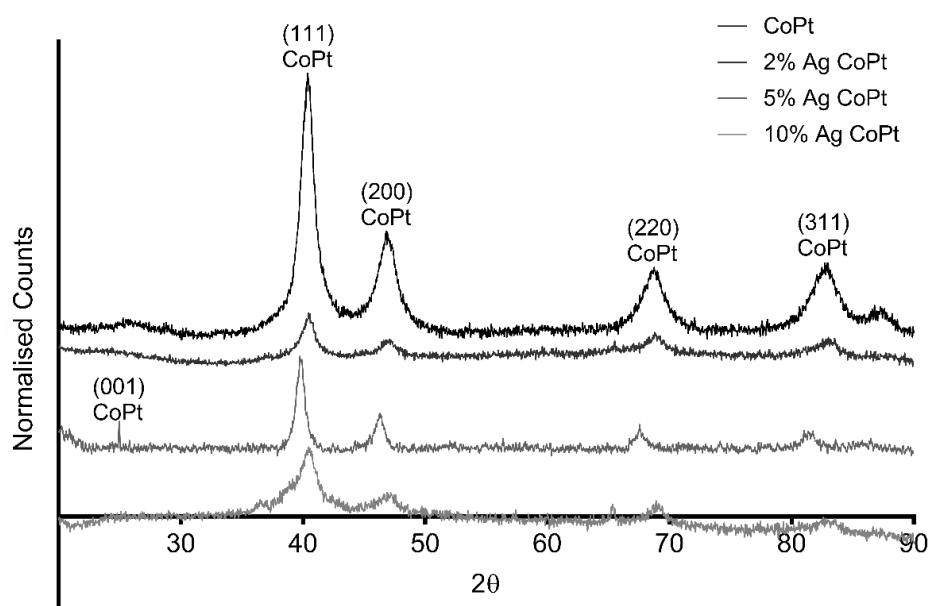


Figure 4.4.1 - XRD spectrum of CoPt (black line), 2% Ag doped CoPt (dark grey) and 10% Ag doped CoPt (light grey).

Table 4.4.1 - Particle size for CoPt, 2 and 5 % Ag doped CoPt calculated from XRD using the Scherrer equation.

Sample	Calculated particle size from Scherrer equation /nm
CoPt	7.8
2% Ag CoPt	9.3
5% Ag CoPt	12.7
10% Ag CoPt	5.9

Room temperature VSM data shows maximum coercivity is achieved at 5% Ag doping (130 Oe), this is 8.5 times greater than the Ag free NP. Whilst 7 and 10% Ag doped samples have coercivity values that are half that of CoPt, suggesting that addition of too much Ag can have an adverse effect on the formation of CoPt. The increase in coercivity observed for 5% Ag doping could be due to the slightly increased particle size calculated from XRD. It is known that coercivity increases with NP size until the NPs reach a critical size limit, this is where the NPs will no longer be single domain but become multi domain.⁴⁶ Due to the presence of the (001) peak in the XRD for 5% Ag doping, it is possible the increase in coercivity resulted from a combination of partial L1₀ character and increased NP size. However, the coercivity values are lower than expected for L1₀ phase CoPt and therefore suggests that the A1 phase has been synthesised, this is consistent with XRD data as only one characteristic peak of L1₀ phase is present. However, compared to literature values an increase in coercivity is observed. In the majority of literature annealing at high temperatures is required for the production of the L1₀ phase and large coercivity values are achieved. Synthesis of CoPt in the small heatshock protein cage (MjHSP) results in a coercivity of 150 Oe prior to annealing, using a reverse micelle method can produce coercivities between 0 – 25 Oe and a high temperature chemical reduction synthesis can produce coercivities between 0 – 36 Oe.^{42,51,63,155} Therefore, the incorporation of silver into a room temperature co-precipitation reaction has produced comparable coercivity values without the need for harsh solvents and temperatures.

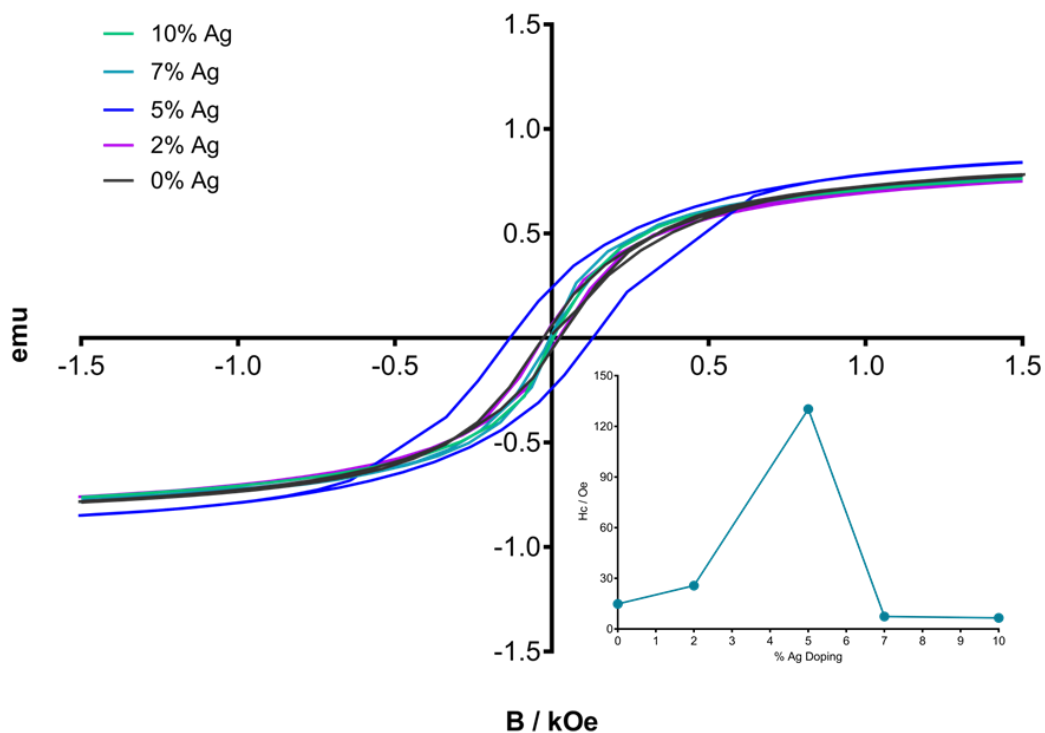


Figure 4.4.2 - VSM data collected at 300 K for 0, 2, 5, 7 and 10% Ag doped CoPt. Inset figure shows coercivity values for each sample.

Finally, silver doped CoPt NPs were characterised using ICP-OES to identify the chemical composition of the NPs. The results from ICP-MS can be seen below in Figure 4.4.3. The amount of silver in the final NP is always less than the starting percentage of doping put into the reaction. Therefore, adding more than 7% Ag to the synthesis does not further increase the amount of Ag incorporated into the final NP composition as an increase by only 0.2% is observed but 3% more Ag was added into the synthesis. The increase in coercivity observed is actually from a 4% Ag doped sample, even though 5% Ag was added to the reaction. From all data obtained it suggests that A1 phase CoPt NPs were produced, however through using silver doping higher coercivities were able to be achieved compared to control CoPt NPs.

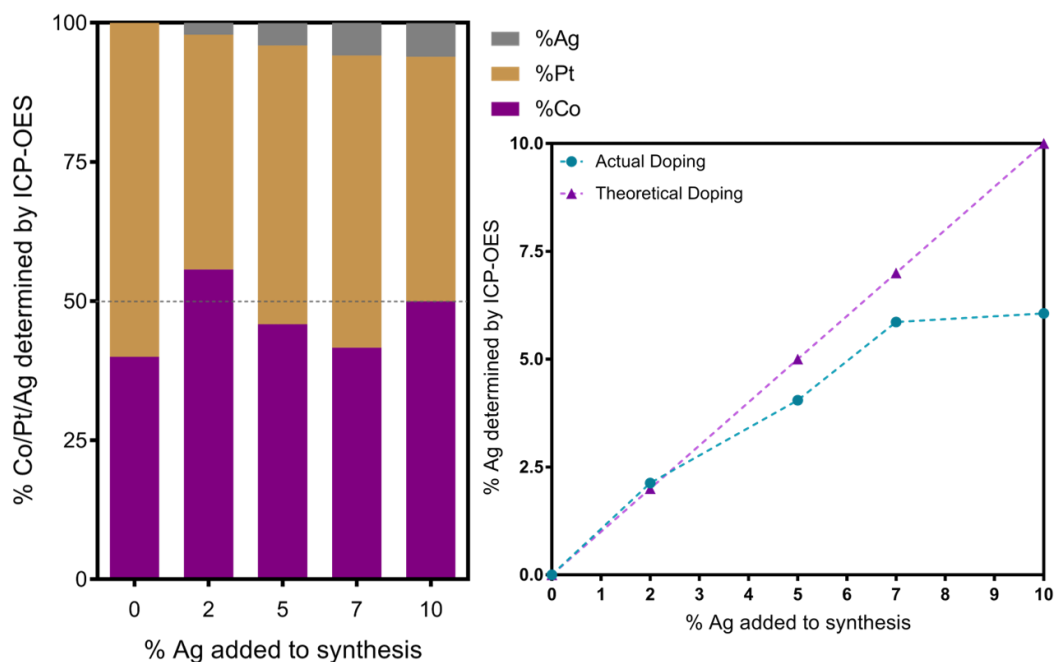


Figure 4.4.3 – ICP-OES data for Ag doped CoPt samples. **Left:** Purple – molar percentage of Co present, yellow – molar percentage of Pt present and grey – molar percentage of Ag present. **Right:** Molar percentage of Ag present in samples plotted against theoretical percentage Ag doping.

Silver doping was also carried out in an FePt synthesis reaction at the optimised doping level obtained from the CoPt experiment. This was to reduce the volume of samples that would need to be characterised, and as FePt and CoPt are chemically very similar the amount of dopant needed is likely to be similar. The XRD data shows peaks at $2\theta = 40.4^\circ, 46.9^\circ, 68.3^\circ, 82.4^\circ$ and 87.1° which correspond to the (111), (200), (220), (311) and (222) planes. All of these planes are consistent with A1 phase FePt, the peaks characteristic for L1₀ phase NPs would be expected at $2\theta = 25^\circ$ and 35° . Therefore, as these peaks are not present this suggests that A1 phase FePt has been synthesised. The diffraction data indicates an absence of silver species, and the peaks are indistinguishable to pure FePt, suggesting that silver does not alter the lattice parameters of FePt at this level of doping. The Scherrer equation has been used to calculate particle diameter for both samples, in each case the (111) peak was used. For as synthesised FePt a particle diameter of 6.79 nm was obtained and 5% Ag doped FePt had a diameter of 6.37 nm. Although there is a slight decrease in particle size on addition of silver it is not significant, this suggests that the addition of silver has not had an adverse effect on the synthesis reaction.

Room temperature VSM data shows an increase in coercivity when using 5% Ag in the reaction. As synthesised FePt has a coercivity of 11 Oe and this is consistent with literature values.⁶¹ Whilst adding 5% Ag into the reaction results in NPs that have a coercivity of 240 Oe. Therefore, an increase of 229 Oe has been obtained by adding silver into the reaction.

However, these coercivity values are much lower than what would be expected for L1₀ phase FePt suggesting that A1 phase FePt has been synthesised. Though compared to literature values for FePt NPs synthesised under ambient conditions an increase in coercivity is observed. Therefore, addition of silver allows FePt NPs with a higher coercivity to be synthesised under ambient conditions and without the need for harsh solvents and temperatures.

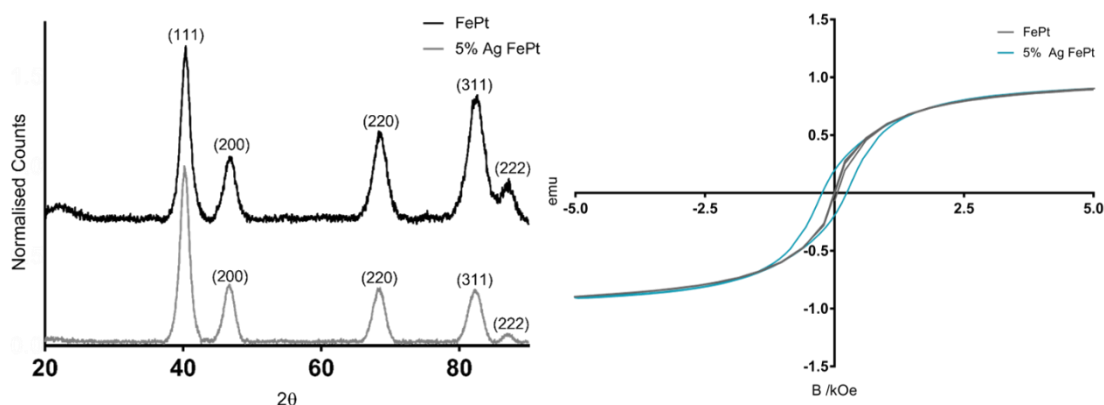


Figure 4.4.4 - XRD for FePt (black) and 5% Ag doped FePt (grey). Lattice planes that are typical of FePt have been labelled. Room temperature VSM data for FePt (black) and 5% Ag doped FePt (blue) with coercivity values of 11 Oe and 240 Oe respectively. X axis is magnetic field strength in kOe and Y axis is normalised magnetic moment. Broad peak at $\approx 20^\circ$ is from glass capillary.

ICP-OES was used to identify the chemical composition of the doped FePt NPs and the results can be seen in Table 4.4.2. Compared to control FePt NPs the NPs doped with Ag result in the molar ratio of Fe to Pt becoming slightly closer to the ideal 50:50 ratio. There is slightly less silver present in the sample than expected as 5% (by volume) was added to the reaction but overall 4% has been incorporated into the final NP product. However, this is the same incorporation as what was observed for silver doping with CoPt NPs.

Table 4.4.2 – ICP-OES data for 0 and 5 % Ag doped FePt NPs.

% Initial Ag Doping	% Fe	% Pt	% Ag
0	41.13	58.87	0.00
5	43.88	52.53	3.59

4.4.2 BISMUTH DOPING

Incorporation of bismuth into the synthesis of CoPt NPs has been shown to lower the annealing temperature required for the formation of the L1₀ phase and increase coercivity.¹⁵⁶ It is thought that bismuth promotes L1₀ ordering and does this by being distributed onto the surface of the as-made nanoparticles, because of its reduced surface energy, and it is then released after annealing. This results in increased interdiffusion of Co and Pt atoms causing the L1₀ phase to form at lower temperatures.¹⁵⁶ Therefore, bismuth doping was carried out

to investigate whether the addition of bismuth can promote $L1_0$ ordering and increase coercivity in room temperature synthesis reactions. The levels of Bi doping investigated were 1, 1.5, 2, 2.5, 3 and 5%. Synthesised NPs have been characterised using XRD, VSM and ICP-OES. The XRD data for 0, 2% and 5% doping shows peaks at $2\theta = 40.4^\circ$, 46.8° , 68.4° and 82.4° corresponding to the (111), (200), (220) and (311) planes. The XRD data suggests that the NPs are in the $A1$ phase due to the lack of the (001) and (110) crystal planes and no shift is observed in the (111) plane which is expected for the $L1_0$ phase. There are also no peaks present for bismuth; however, it is possible that these peaks could be very small and may be within the background noise of the spectrum. The Scherrer equation has been used to determine particle diameter and from this calculation a diameter of 7.8 nm was given for both CoPt and 5% Bi doped CoPt. An increase in diameter was observed for 2% Bi doped CoPt, from 7.8 nm up to 11.3 nm. However, this is still comparable to literature values for particle size. Therefore, suggesting that the presence of bismuth has not had an adverse effect on the synthesis reaction, this is also demonstrated through the quality of the XRD spectrum and how well it overlays with the control.

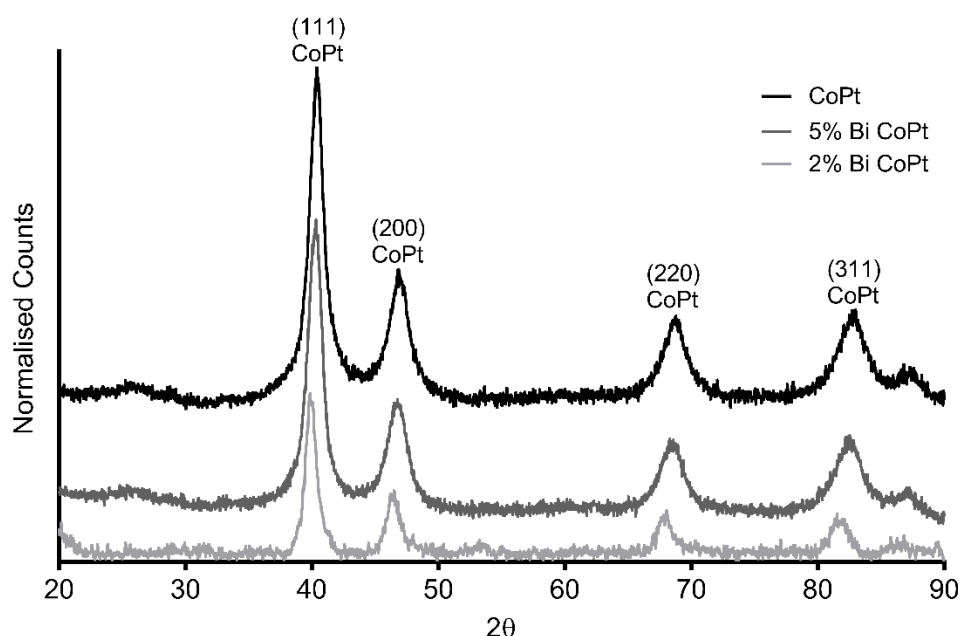


Figure 4.4.5 - XRD spectrum of CoPt and 5% Bi doped CoPt with lattice planes labelled that are typical of CoPt.

Table 4.4.3 - Particle size for CoPt and 5 % Bi doped CoPt calculated from XRD using the Scherrer equation.

Sample	Calculated particle size from Scherrer equation /nm
CoPt	7.8
2% Bi CoPt	11.3
5% Bi CoPt	7.8

Room temperature VSM data was collected for bismuth doped samples and a maximum in coercivity was observed for 2% (148 Oe), this is a ten-fold increase in coercivity compared to the control. Using 1% doping results in an increase in coercivity up to 73 Oe. After 2% doping the coercivity decreases back down towards the control value, however using 5% bismuth still gives a coercivity of 55 Oe. 1.5% and 2.5% bismuth doping were carried out to ensure that 2% doping achieved the maximum coercivity and that this could not be improved upon. As was observed with silver doping it is possible that the increase in coercivity arises from the slight increase in particle size, as there are no peaks present in the XRD consistent with $L1_0$ phase this is likely to be the case. Incorporation of bismuth into the synthesis reaction resulted in NPs with a higher coercivity than those synthesised without bismuth. However, although an increase in coercivity has been achieved much higher coercivity values are required for the application of bit patterned media.

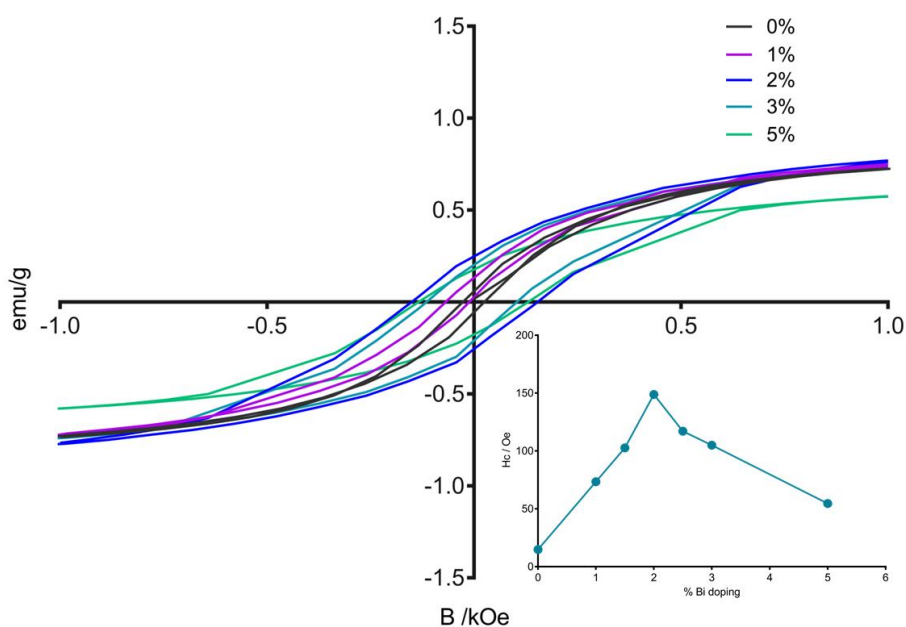


Figure 4.4.6 - Room temperature (300 K) VSM data for 0, 1, 2, 3 and 5% Bi doped CoPt. Inset figure shows coercivity values for each sample.

ICP-OES data for bismuth doped samples shows that the amount of bismuth that has been incorporated into the final NP composition is very close to the amount of bismuth added to the reaction. However, the ratios of Co and Pt vary between samples, for example 1.5% bismuth has 14.6% Pt content and 84.3% Co which suggests that Co_3Pt was synthesised. Whereas 1% bismuth doping has a 48.5:50.6 ratio, suggesting the CoPt was synthesised. This is also true for 2, 3 and 5% doping. Doping carried out at 2.5% is also starting to approach the formation of Co_3Pt rather than CoPt. Compared to control CoPt the incorporation of bismuth into the synthesis has resulted in ratios of Co to Pt that are closer to the 50:50 ratio expected for CoPt.

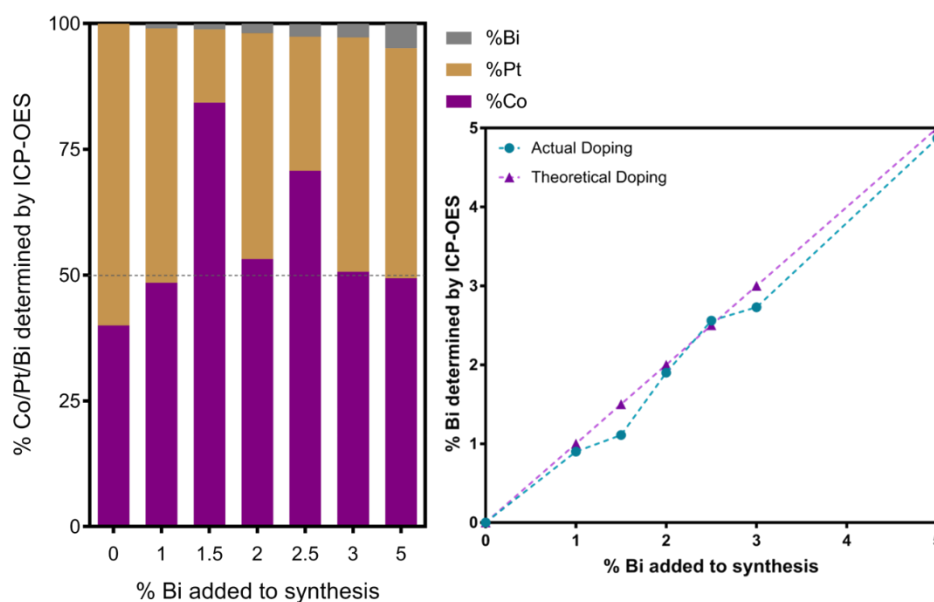


Figure 4.4.7 – ICP-OES data for bismuth doped CoPt samples. **Left:** purple – molar percentage Co, yellow – molar percentage Pt and grey – molar percentage Bi. **Right:** Difference between actual and theoretical doping in final NP.

Bismuth doping was also incorporated into an FePt synthesis reaction, again only the level of doping that gave the highest coercivity for CoPt was tested. The NPs were characterised using XRD, VSM and ICP. XRD data for FePt and 2% Bi doped FePt both contain peaks at $2\theta = 40.4^\circ, 46.6^\circ, 68.3^\circ$ and 87.1° which correspond to the (111), (200), (220), (311) and (222) planes. These planes are consistent with the A1 phase of FePt and the characteristic peaks for $L1_0$ phase FePt are not present, suggesting that A1 phase FePt was synthesised. In the bismuth doped sample there are peaks at $42.4^\circ, 43.4^\circ$ and 49.1° these peaks do not correlate to any d -spacings of bismuth alone, A1 phase or $L1_0$ phase FePt and are likely to be caused by the presence of BiPt in the sample.¹⁵⁷ The Scherrer equation has been used to estimate the particle diameter, the (111) peak has been used for this as it is the most prominent. Particles synthesised in the absence of bismuth have a diameter of 6.79 nm whereas particles synthesised in the presence of bismuth have a diameter of 6.37 nm. The bismuth doped particles are slightly smaller in size but not significantly. Therefore, this suggests that the addition of bismuth does not have a detrimental effect on the synthesis reaction.

Room temperature VSM was performed on both samples and a coercivity value of 11 Oe was obtained for as synthesised FePt NPs. When 2% bismuth was added into the synthesis a coercivity of 278 Oe was observed, this is an increase in coercivity of 267 Oe. Although an increase in coercivity is observed it is still much lower than what is expected for $L1_0$ phase FePt NPs. However, compared to literature values of coercivity, for NPs synthesised under ambient conditions, 278 Oe is increased. The majority of as synthesised NPs have very low coercivity values, generally close to zero.^{44,81,82} Therefore, the addition of bismuth into a

room temperature co-reduction reaction results in NPs that have an increased value of coercivity than to those previously synthesised in this way.

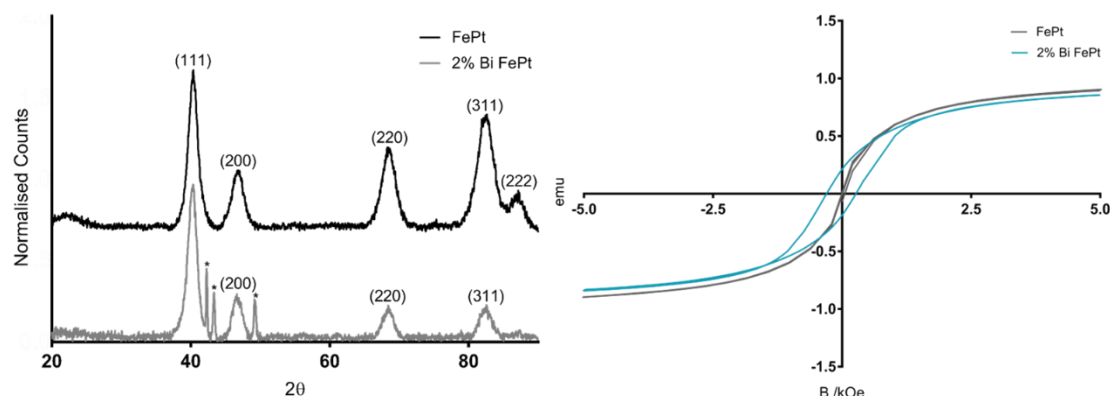


Figure 4.4.8 - XRD for FePt (black) and 2% Bi FePt (grey) with lattice planes labelled that are typical of FePt. * represents peaks caused by the presence of Bi or BiPt in the sample.¹⁵⁷ Room temperature VSM of FePt (black) and 2% Bi doped FePt blue with coercivity values of 11 Oe and 278 Oe respectively. X axis represents magnetic field strength in kOe and Y axis is normalised magnetic moment. Broad peak at $\approx 20^\circ$ is from glass capillary.

Finally, ICP-OES was used to identify the chemical composition in the final doped NPs (Table 4.4.4). Incorporation of bismuth into the NPs has resulted in NPs that have a ratio that is closer to the ideal 50:50 compared to control FePt NPs. Slightly less bismuth was incorporated than what was originally added to the synthesis, so the increase in coercivity is actually from doping at 1.1% bismuth.

Table 4.4.4 – ICP-OES data for 0 and 2% bismuth doped samples.

% Initial Bi Doping	% Fe	% Pt	% Bi
0	41.13	58.87	0.00
2	43.82	55.08	1.10

4.5 CoPt SYNTHESISED IN THE PRESENCE OF MJHSP

MjHSP is a small heat shock protein that assembles into a 24-subunit cage with an interior and exterior diameter of 6 and 12 nm respectively. Large 3 nm pores at the 3 fold axes allow exchange between the interior of the cage and the bulk solution.¹⁵⁸ The protein cage has internal and external surfaces that can be chemically or genetically modified. A small binding CoPt binding peptide (KTIEIHSPLLHK) has previously been incorporated on the interior of the protein cage, at the N-terminus.⁶³

MjHSP was purified as described in chapter 2.1. Isolated protein was then analysed using SDS-PAGE to determine the molecular weight and purity. MjHSP has a molecular weight of 16.5 kDa per subunit and is composed of 147 amino acids.⁶³ Subjecting the protein to size exclusion chromatography results in separation of three species. Samples with a larger molecular weight will elute first from the column as they are unable to enter the pores in the

matrix and so will stay in the mobile phase. In contrast to this samples with lower molecular weights will elute last from the column as they are able to enter the pores and will move through the column by a longer path, through the pores of the matrix. Relating this to the presence of three peaks suggests that molecules with different molecular weights are being eluted. Each of these three peaks was analysed using SDS-PAGE (Figure 4.5.1) and it can be seen that peaks A and B have the same molecular weight of 15 kDa, this corresponds to the expected molecular weight of MjHSP. By combining the results from SDS-PAGE and gel filtration it can be deduced that peak A is likely to contain the fully assembled protein cage whereas peak B is likely to consist of unassembled protein cage. It is not possible to identify this from SDS-PAGE alone as proteins are denatured before being run on the gel and therefore only a band for a single subunit of MjHSP is observed. MjHSP was not detected in peak C due to no bands of the expected molecular weight being observed and so this fraction was discarded.

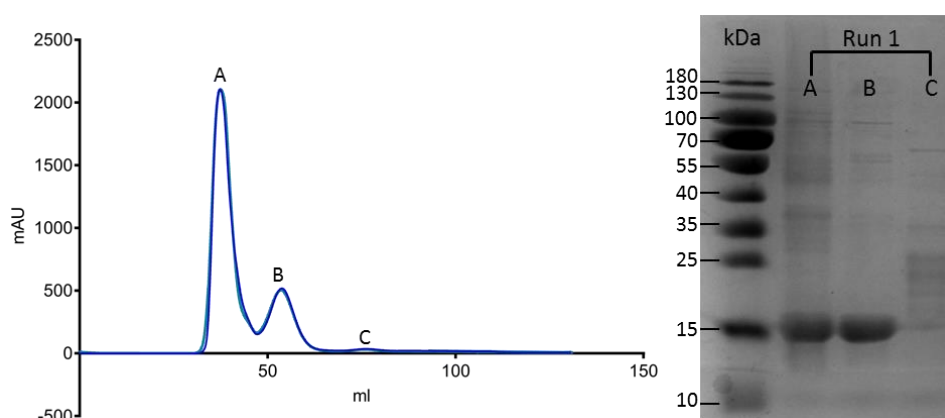


Figure 4.5.1 - Gel filtration curves for the purification of MjHSP and SDS-PAGE gel for the corresponding gel filtration runs.

TEM has been used to measure the size of the protein cage. For the protein cage to be visualised on TEM the sample needed to be negatively stained. In negative staining the background is stained with heavy metals to improve contrast at the edges of the sample which shows up as bright areas.¹⁵⁹ A histogram produced from grain sizing shows the size distribution of the cages with a mean diameter of 12.4 nm. This value fits well with literature values as the protein cage is known to have an exterior diameter of 12 nm based on crystal structure.⁶³ This shows that the isolated protein is assuming the correct quaternary structure, allowing the cage to function as a nanoreactor for later NP synthesis experiments.

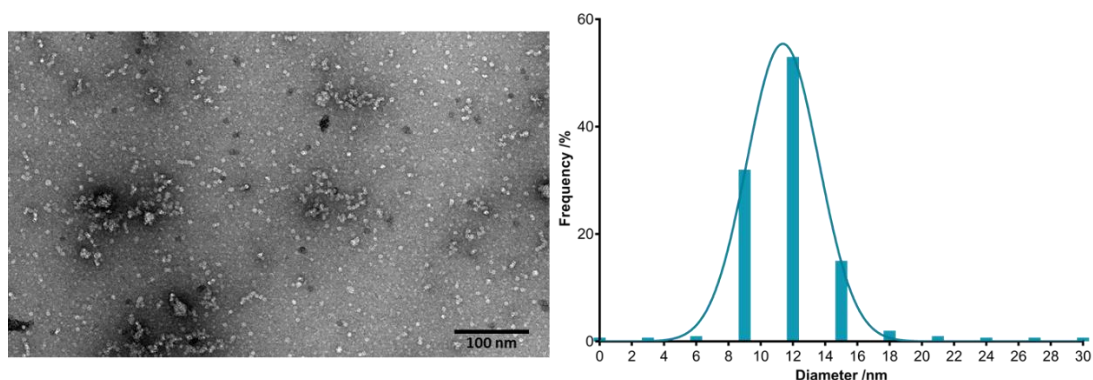


Figure 4.5.2 - TEM micrograph of MjHSP stained with 0.75 % uranyl acetate, scale bar represents 100 nm. Histogram showing size distribution of the protein cages.

CoPt NPs have been synthesised in the presence of MjHSP. The presence of the (111), (200), (220) and (311) planes in XRD experiments confirm that A1 phase CoPt has been synthesised. The (001) and (110) planes that are specific to L1₀ phase CoPt are not present suggesting L1₀ CoPt has not been produced. VSM data for NPs synthesised in the presence of MjHSP has also been collected and a coercivity of 41 Oe was recorded. Literature values for NPs synthesised via the protein cage are 150 Oe.⁶³ However, this value is higher than protein free control CoPt NPs that have a coercivity of 15 Oe.

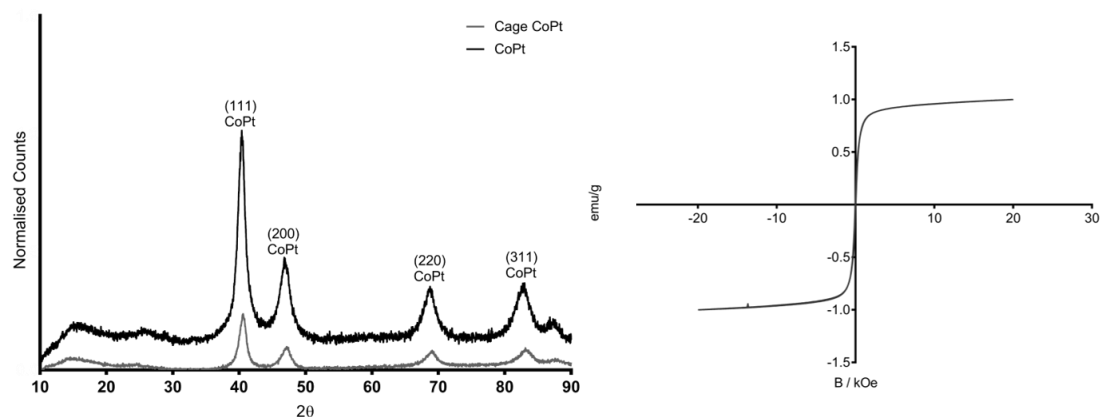


Figure 4.5.3 – XRD spectrum of CoPt (black) and CoPt synthesised in the presence of MjHSP (grey) with lattice planes typical of CoPt labelled. Room temperature (300 K) VSM data for CoPt synthesised in the presence of MjHSP. Coercivity value of 41 Oe.

Table 4.5.1 - Particle sizes calculated for CoPt and CoPt synthesised in the presence of MjHSP from XRD using the Scherrer equation.

Sample	Calculated particle size from Scherrer equation /nm
CoPt	7.8
Cage CoPt	6.0

Finally, ICP-OES analysis of particles synthesised in the presence of MjHSP indicate that the NPs have a composition of 60% Co and 40% Pt. Combination of ICP-OES, XRD and VSM data suggests that A1 phase CoPt was synthesised in the presence of MjHSP and not L1₀ phase.

Annealing of cage particles

NPs synthesised in the presence of MjHSP have been annealed at 825 °C for 1 hour under an argon atmosphere. Annealing at this temperature is thought to induce the transition from A1 to L1₀ phase.⁴⁵ XRD confirmed that L1₀ CoPt had been synthesised after annealing due to the presence of (001) and (110) planes in XRD data and the shifting of the (111) plane. Splitting of the (200) peak was also observed. Particle size has been calculated using the Scherrer equation. Prior to annealing the particle diameter was 7.8 nm, after annealing this increased to 12.9 nm. This is to be expected as the particles will agglomerate together during the annealing process.

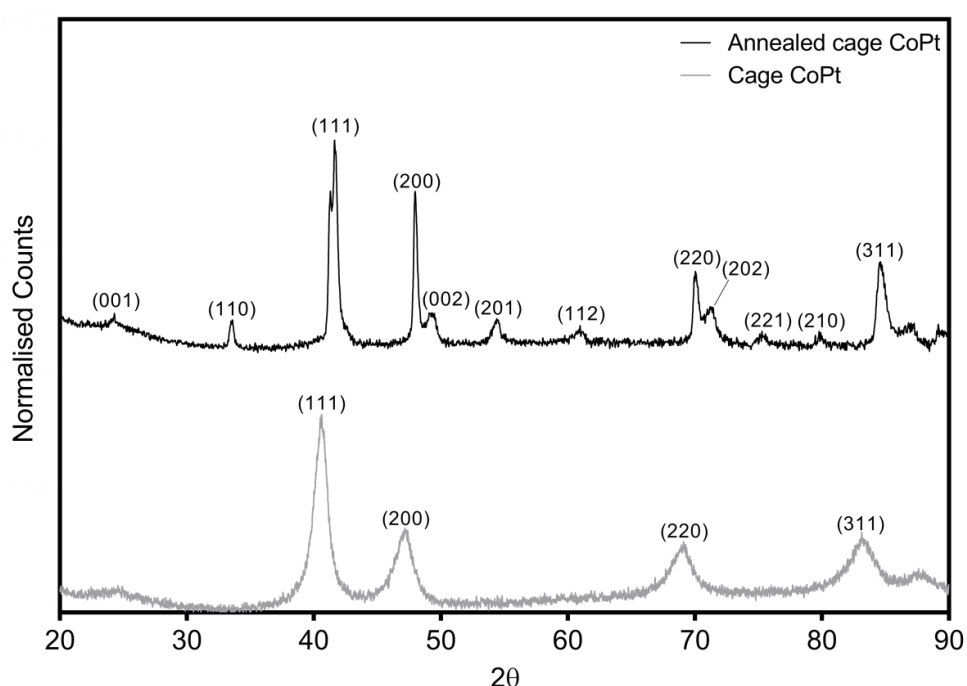


Figure 4.5.4 - XRD of CoPt synthesised in the presence of MjHSP before (grey) and after (black) annealing at 825 °C under an argon atmosphere for 1 hour. Lattice planes for A1 and L1₀ phase CoPt have been labelled. Broad peak at $\approx 20^\circ$ is from glass capillary.

Table 4.5.2 - Particle size for CoPt and annealed CoPt determined from XRD using the Scherrer equation.

Sample	Calculated particle size from Scherrer equation /nm
CoPt	7.8
Annealed CoPt	12.9

To understand the magnetic properties of the cage synthesised NPs, and the effect of annealing, the samples were subjected to room temperature VSM analysis. A coercivity of 225 Oe was observed for the annealed sample, this is much lower than expected for L1₀ phase CoPt. The presence of the (210) and (211) peaks in the XRD spectrum are typical of the L1₂ phase, therefore it is possible that a mixture of ordered phases L1₀ and L1₂ were

synthesised. As the L_{12} phase has lower coercivities than the L_{10} phase this could explain the reduced coercivity observed for this sample.

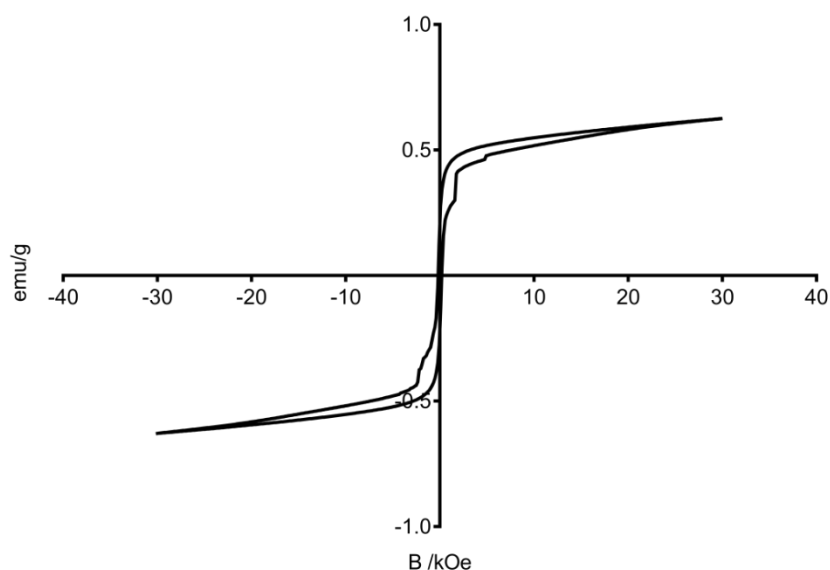


Figure 4.5.5 - Room temperature (300 K) VSM data for annealed CoPt particles. Coercivity of 225 Oe.

4.5.1 SILVER DOPED CoPt SYNTHESISED IN THE PRESENCE OF MjHSP

Synthesis in the presence of MjHSP has been combined with silver doping to investigate whether the combination of the two can increase coercivities even further. Silver doping was carried out at 2, 5, 7 and 10%, although 5% Ag doping in NPs synthesised in the absence of MjHSP showed a maximum in coercivity it is possible that the synthesis conditions may vary from this in the presence of MjHSP. Therefore, a range of silver doping levels were investigated. Samples were first characterised using TEM to determine particle size and morphology. Grain size analysis was performed and a histogram showing particle size distribution was plotted. The mean diameter for silver doped CoPt NPs synthesised in the presence and absence of MjHSP are similar, between 3 and 4 nm. These values are consistent with literature values of 4.32 nm.⁶³ The interior diameter of the protein cage is 6 nm, if the NPs are synthesised inside the cage they would need to be slightly smaller than the interior dimensions. Therefore, NP sizes of 3 – 4 nm would suggest that the particles are synthesised within the cage. All levels of silver doping produce NPs with a similar spherical morphology, consistent with the NPs being synthesised inside the protein cage.

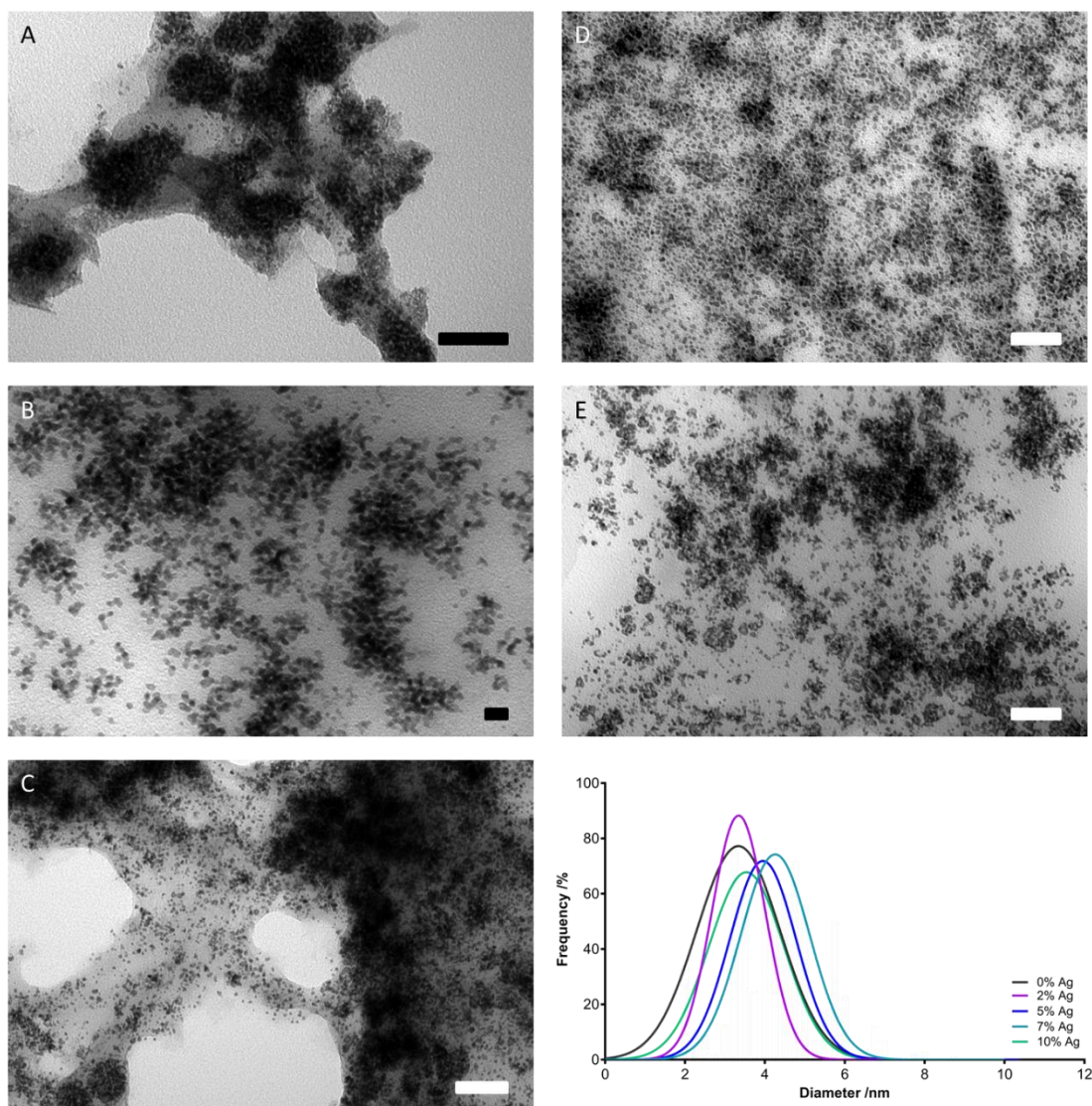


Figure 4.5.6 - TEM micrographs of a) 0% Ag doped b) 2 % Ag doped c) 5 % Ag doped d) 7 % Ag doped and e) 10 % Ag doped all synthesised in the presence of MjHSP. Scale bars represent 50 nm (a, c, d and e) and 10 nm (b). Histogram showing particle size distribution for Ag doped samples.

The doped NPs were also analysed using SDS-PAGE to determine if the protein cage was still present after synthesis and washing of the NPs. A sample of purified protein cage was loaded onto the gel as a control and a band is observed at 15 kDa for MjHSP (lane labelled MjHSP in Figure 4.5.7). The NPs were boiled in SDS loading dye to remove any bound protein. In each of the lanes for the silver doped samples a band can be seen at approximately 15 kDa indicating the presence of MjHSP after synthesis. This confirms that MjHSP is still interacting with CoPt NPs after synthesis. Other bands are observed in the lane for MjHSP however these impurities are not present in the silver doped samples. Suggesting that they do not play a role in the synthesis and that washing steps carried out after synthesis have removed any material that is not attached to the NPs.

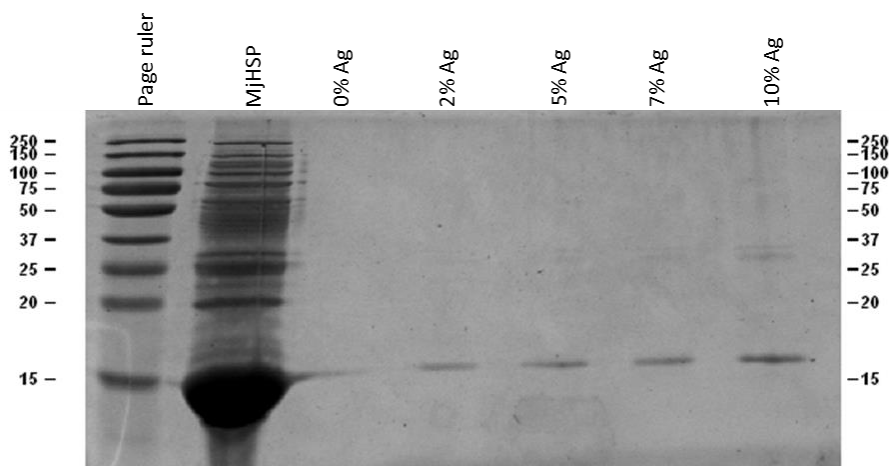


Figure 4.5.7 - SDS-PAGE of CoPt nanoparticles synthesised in the presence of MjHSP and containing different amounts of Ag doping. Units of molecular weight are kDa.

ICP-OES was used to determine the ratios of Co, Pt and Ag in the NPs synthesised. This data is summarised below in Table 4.5.3 and the ratios vary widely between samples. In each case more Ag has been incorporated into the final sample than expected, for 7 and 10 % doping the amount of Ag present is approximately 2.5 times higher. The amount of Co in each sample also varies widely. This could suggest that there is competition between Co and Ag to incorporate into the protein cage. Cobalt ions are smaller than silver due to their position on the periodic table, whilst silver and platinum are of comparable size. Therefore, one possibility is that the Pt and Ag ions are preferentially making their way into the protein cage due to their similar size or that the Pt and Ag ions are displacing Co ions from the interior of the protein cage. Further optimisation of the synthesis would be required so that ratios closer to the ideal 50:50 could be achieved.

Table 4.5.3 – Elemental composition of Ag doped samples synthesised in the presence of MjHSP.

% Ag doping	% Co	% Pt	% Ag
0	60.41	39.59	0.00
2	53.27	41.88	3.96
5	60.43	33.44	6.13
7	38.48	44.70	16.82
10	25.99	47.18	26.83

Taken together the analysis of CoPt NPs synthesised in the presence of MjHSP indicates that the NPs are monodisperse in size and are therefore likely to have been synthesised in the interior of the protein cage. As MjHSP contains a small peptide sequence that is thought to be specific to L1₀ phase it was expected that the formation of L1₀ particles would be favoured. However, from crystallographic analysis there are none of the expected peaks present to indicate that the L1₀ phase has been synthesised (Figure 4.5.8). The presence of the (111), (200), (220) and (311) planes indicate that A1 phase CoPt has been synthesised. XRD of the

doped samples produces a much noisier signal, possibly due to a much lower amount of sample. The presence of silver is observed in the sample by the peaks marked with a *. Particle size was calculated from XRD data using the Scherrer equation. In each case the (111) peak was used. NPs synthesised in the cage in the absence of silver have the largest particle size of 7.85 nm, and 2 and 5% silver doping have particle sizes of around ≈ 6 nm. Therefore, a slight reduction in particle size is produced by incorporating silver.

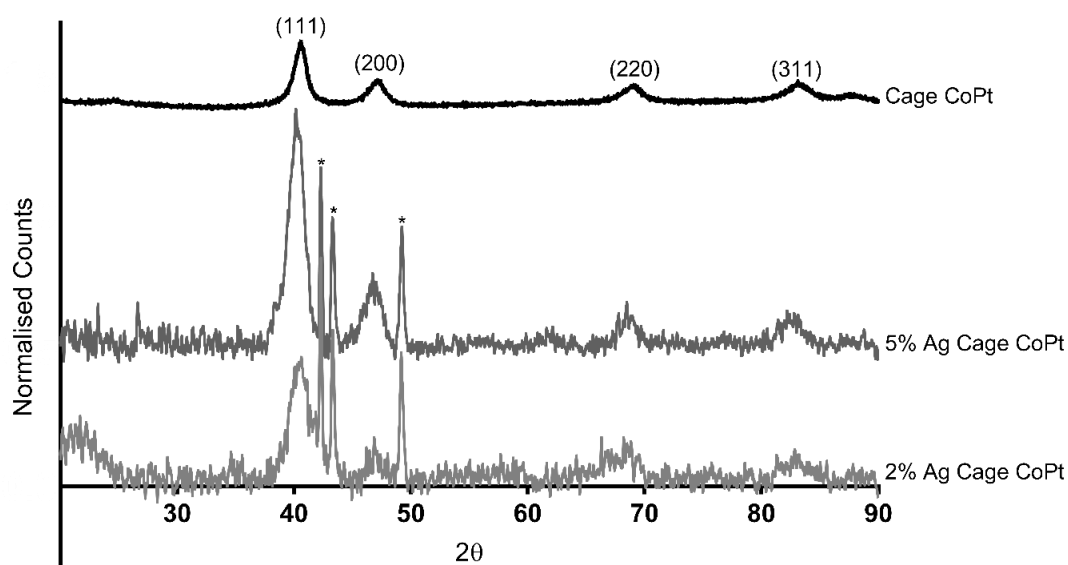


Figure 4.5.8 - XRD of CoPt synthesised in the presence of MjHSP (black), with 5% (grey) and 2% (light grey) Ag doping. Peaks characteristic of CoPt have been labelled. * represent peaks that relate to Ag. Broad peak at $\approx 20^\circ$ is from glass capillary.

Table 4.5.4 - Particle size for cage CoPt, 2% Ag doped cage CoPt and 5% Ag doped cage CoPt as determined by the Scherrer equation from XRD.

Sample	Particle size calculated from Scherrer equation /nm
Cage CoPt	7.8
2% Ag cage CoPt	6.0
5% Ag cage CoPt	6.3

Room temperature VSM was carried out on the silver doped cage samples. The 2% silver doped sample has the largest increase in coercivity, up to 60 Oe. ICP analysis shows that the 2% doped sample actually has 5% silver present in the final NP composition, this is consistent with silver doping levels carried out in the absence of MjHSP. 5% silver doping results in a decrease in coercivity down to 15 Oe, this is consistent with as synthesised CoPt. Finally, 7% silver doping has a coercivity of 47 Oe this is very similar to MjHSP CoPt which has a value of 41 Oe. Therefore, coercivity values suggest that A1 phase CoPt has been synthesised here and the incorporation of silver has only increased on addition of 2% Ag into the synthesis, resulting in a coercivity of 60 Oe. From the coercivity values obtained from the different silver doping levels it is difficult to identify any trends. Synthesis was only carried out once for each

doping level and as a result only one VSM measurement collected, access to a VSM system was limited and so collecting repeats of each sample was difficult. Therefore, if synthesis was repeated and VSM measurements collected it could be that coercivity values are within error of each other and a significant change from the control sample (0 % Ag with MjHSP) may not be observed. Therefore, before any conclusions can be made on the effect incorporating silver into the synthesis, in the presence of MjHSP, has on the coercivity further repeats would be required.

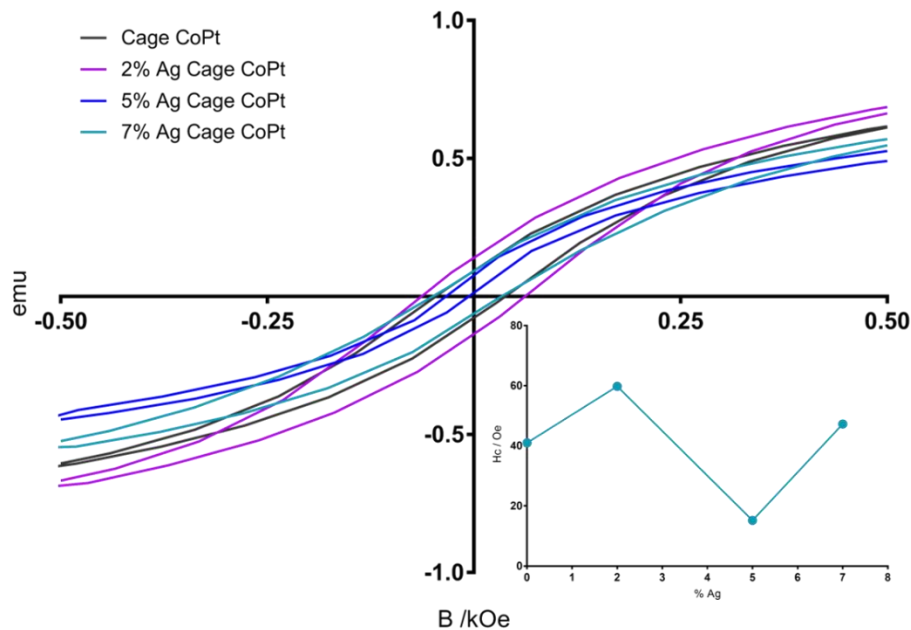


Figure 4.5.9 - Room temperature (300 K) VSM of Ag doped CoPt synthesised in the presence of MjHSP. Inset figure shows coercivity values for each sample.

4.5.2 BISMUTH DOPED CoPt SYNTHESISED IN THE PRESENCE OF MJHSP

Bismuth doping has been carried out at 1, 1.5, 2 and 2.5% for CoPt synthesised in the presence of MjHSP. A maximum in coercivity was observed for 2% Bi doped CoPt (148 Oe) and so bismuth doping around 2% was investigated for synthesis with MjHSP present. The presence of the (111), (200), (220) and (311) planes in the XRD spectrum indicate that CoPt has been synthesised in the A1 phase. The absence of the (100) and (110) planes and shifting of the (111) peak that are characteristic of L1₀ phase also indicate that A1 phase has been produced. In the 2% Bi doped sample there is an extra peak present at 2θ = 51° which *d*-spacing corresponds to the (002) peak for CoPt. This peak is consistent with the L1₀ phase, however as there are none of the other characteristic peaks present it is unlikely that the L1₀ phase has been synthesised.

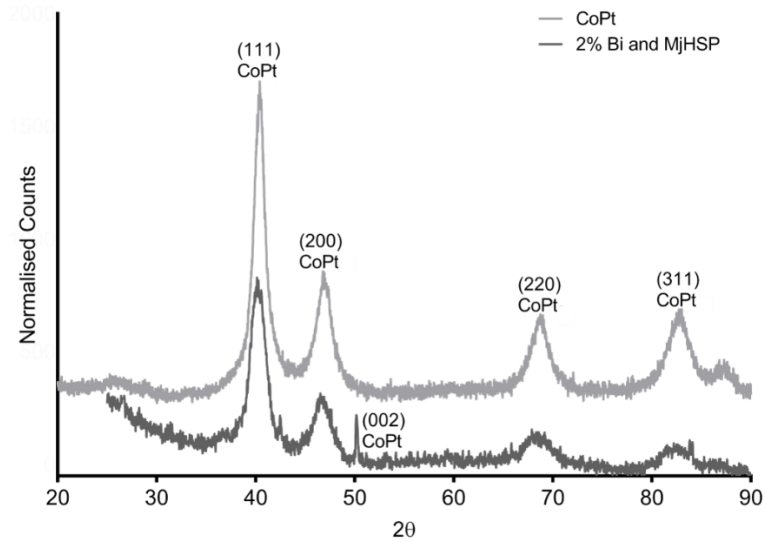


Figure 4.5.10 - XRD data for CoPt and 2% Bi doped CoPt both synthesised in the presence of MjHSP. Room temperature VSM data shows that the presence of bismuth in the samples results in a reduction in coercivity compared to CoPt synthesised in MjHSP. However, the values are similar to that of as synthesised CoPt, approximately 15 Oe. Therefore, this suggests that CoPt has been synthesised, but it is in the A1 disordered phase.

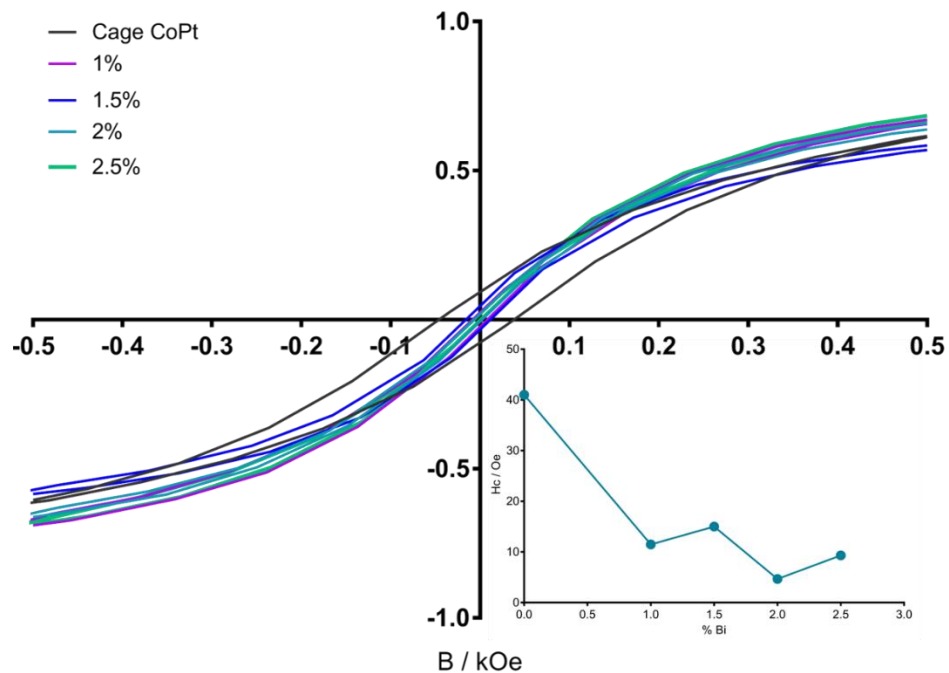


Figure 4.5.11 - Room temperature (300 K) VSM data for Bi doped CoPt synthesised in the presence of MjHSP. Inset figure showing coercivity values for each sample.

ICP-OES data shows that the amount of bismuth present in the sample varies greatly from what is the expected percentage of bismuth doping. The ratios of Co and Pt also vary between each sample and in some cases are far away from the ideal 50:50 ratio. This could

suggest why such a large reduction in coercivity is seen when bismuth doping is incorporated into MjHSP.

All the data collected for bismuth doping in the presence of MjHSP suggests that further optimisation of the synthesis is required. This could involve using different starting ratios of Co:Pt:Bi to achieve the optimum ratios inside the protein cage.

Table 4.5.5 – Elemental composition of Bi doped samples synthesised in the presence of MjHSP.

% Bi doping	% Co	% Pt	% Bi
0.0	44.54	55.46	0.00
1.0	9.86	89.66	0.49
1.5	43.69	51.80	4.51
2.0	67.56	28.71	3.73
2.5	37.23	58.88	3.89

4.6 SUMMARY

CoPt and FePt NPs were successfully synthesised in the A1 phase. A 3:1 starting ratio is required for both CoPt and FePt NPs to achieve a final NP composition that is closest to the ideal 50:50 ratio. CoPt and FePt have coercivity values of 15 and 11 Oe respectively which are both consistent with literature values for a room temperature synthesis method. XRD analysis reveals neither particles possess any L1₀ character and this is to be expected from a room temperature synthesis reaction. L1₀ FePt was successfully synthesised after annealing at 825 °C, this was confirmed by characteristic peaks in XRD and the presence of a large coercivity (10.8 kOe) from VSM.

CoPt NPs were produced in the presence of MjHSP. An increase in coercivity was observed, going from 15 Oe up to 41 Oe, this was lower than expected compared to literature values for this synthesis method. Although MjHSP has a peptide sequence on the interior of the cage that shows specificity for L1₀ phase CoPt it did not result in NP with any L1₀ phase character. Only after annealing at 825 °C for 1 hour were the characteristic peaks for the L1₀ phase observable by XRD and a higher coercivity obtained.

Silver and bismuth doping were incorporated into both CoPt and FePt synthesis reactions. 5% silver doping gave the largest increase in coercivity for CoPt (130 Oe) and an increase was also seen for FePt (240 Oe). XRD analysis of CoPt indicated that there was some L1₀ character present in the NPs due to the presence of the (001) plane, however there were no other characteristic peaks for the L1₀ phase present. Doping with bismuth also resulted in an increased coercivity for both CoPt and FePt, 2% Bi doping gave the largest increase in

coercivity. Coercivities of 150 Oe and 278 Oe were obtained for CoPt and FePt respectively. However, from XRD analysis of both samples there was no L1₀ character present.

Bismuth and silver doping were also incorporated into CoPt reactions carried out in the presence of MjHSP. All levels of bismuth doping resulted in samples having a much lower coercivity than MjHSP synthesised NPs. No L1₀ character was observed in XRD, this is to be expected due to the very low coercivity values measured by VSM. From ICP-OES the ratios of Co:Pt:Bi were determined and for all samples these were not close to the ideal 50:50 ratio, therefore suggesting that the reaction needs to be further optimised. 2% silver doping in the presence of MjHSP resulted in a slight increase in coercivity from 41 Oe to 60 Oe, all other samples had very similar or lower coercivity values than MjHSP CoPt.

In conclusion, it is possible to increase coercivity of CoPt and FePt NPs synthesised in a room temperature co-reduction synthesis by the incorporation of bismuth and silver, with bismuth giving higher values. The use of biological templates, such as MjHSP, produces CoPt NPs that have a higher coercivity also which can be increased further by incorporating silver into the synthesis. However, for use in BPM much larger coercivities are required and so further work in this thesis will investigate the role biological templates play and the affect they have on the synthesis of CoPt and FePt NPs.

Table 4.6.1 – Summary of different synthesis methods used for CoPt and FePt and properties of resultant NPs formed.

Sample	XRD Planes	Particle size /nm	Coercivity /Oe	Ratio X:Pt (X = Co/Fe)	Crystal Phase
CoPt	(111) (200) (220) (311)	7.8	15	40:60	A1
CoPt and MjHSP	(111) (200) (220) (311)	6.0	41	60:40	A1
Annealed CoPt and MjHSP	(001) (110) (111) (200) (002) (201) (112) (220) (002) (221) (210) (311)	12.9	225	-	L1 ₀ /L1 ₂
5% Ag CoPt	(111) (200) (220) (311)	12.7	130	46:50:4	A1
2% Bi CoPt	(111) (200) (220) (311)	11.3	148	53:45:2	A1
FePt	(111) (200) (220) (311) (222)	8.5	11	41:59	A1
Annealed FePt	(001) (110) (111) (200) (002) (201) (210) (211) (102) (220) (300) (310) (311) (211)	33.9	10800	-	L1 ₀
5% Ag FePt	(111) (200) (220) (311) (222)	6.37	240	44:52:4	A1
2% Bi FePt	(111) (200) (220) (311) (222)	6.37	278	44:55:1	A1

CHAPTER FIVE: SPOT PEPTIDE ARRAYS

5 SPOT PEPTIDE ARRAY DESIGN AND OPTIMISATION

The SPOT synthesis method was first published in 1992 by Frank *et al* and has allowed for the synthesis and screening of large numbers of synthetic peptides.⁸³ Each peptide spot is arranged into an array on a nitrocellulose membrane and each spot is treated as an individual reaction vessel. Here SPOT peptide array technology has been used to investigate peptides, identified from literature, that show specificity for L1₀ phase CoPt and FePt nanoparticles and thin films to further understand how these peptides work and identify key regions and residues present in the sequences.^{61,63}

5.1 LEAD SEQUENCES

Peptides that show specificity for L1₀ phase CoPt and FePt NPs (previously identified in literature) were identified through the use of phage display technology, where a large library of peptide sequences are displayed on a phage.^{61,63} The phage is exposed to the target material and sequences that bind with the highest affinity are identified. Work by Klem *et al* identified a peptide that shows specificity for L1₀ phase CoPt. A library containing 10¹⁰ unique peptide sequences of 12 amino acids long was screened against thin films of L1₀ phase CoPt. After five rounds of selection one dominant sequence was identified: KTHEIHSPLLHK. This peptide was then incorporated into the protein cage of the small heat shock protein, MJHSP, and was used to template the size and direct phase specific nucleation of CoPt NPs.⁶³ The NPs synthesised were 6.5 nm in diameter (consistent with the interior of the protein cage) with a coercivity of \approx 150 Oe, whereas NPs synthesised in the presence of wild-type MJHSP exhibited no hysteresis at room temperature.⁶³ Phage display technology was also used to identify peptides that show specificity for L1₀ phase FePt and four dominant sequences were identified: HNKHLPSTQPLA, SVSVGMPKSPRP, VISNHRESSRPL and KSLSRHDHIIHHH.⁶¹ HNKHLPSTQPLA was isolated from selection performed on thin films and L1₀ phase NPs, whereas the other three peptides were only identified from screening against thin films of L1₀ phase FePt. HNKHLPSTQPLA was used in mineralisation experiments. NPs synthesised using this peptide were characterised using TEM, electron diffraction, STEM and XRD indicate that FePt NPs synthesised using this method have some degree of chemical ordering. However, peptide mediated room temperature synthesis of both CoPt and FePt has not resulted in a high degree of magnetocrystallinity that is comparable to that achieved by using annealing (150 Oe compared to 1-10 kOe achieved after annealing).^{44,45,47,51,52} Here these peptides will be the lead sequences, and by using SPOT peptide array technology a variety of

different screens will be performed to understand how these peptides interact with CoPt and FePt NPs.

Phage display is a very powerful technique, but it can only identify sequences that bind with a high affinity to the target material. This means that a systematic analysis of the sequences identified cannot be undertaken. The conditions in which each panning round is performed can alter the outcome of the sequences selected and so the protocol must be carefully designed to ensure that the resulting peptides are the most relevant. SPOT peptide array technology is a complementary screening method to phage display and has many advantages: experimental procedures are relatively simple, inexpensive reagents and equipment are used and a wide choice of library design is available. Most importantly, each SPOT can be designed and probed individually, meaning that each sequence can be analysed allowing for a deeper understanding of the binding process.

As synthesis and nucleation of NPs can depend on many factors, screening has been carried out against all steps involved in a synthesis reaction, which are: screening against precursor metal ions (Fe^{2+} , Co^{2+} and Pt^{2+}), a synthesis reaction and already synthesised NPs. This process can be seen schematically in Figure 5.1.1.

Ideally screening should be carried out against L1_0 phase NPs however this was not possible due to problems with particle aggregation. As L1_0 NPs have been annealed at $825\text{ }^\circ\text{C}$ as part of their synthesis it was difficult to fully disperse the NPs in solution. The particles accumulated together during screening and as such made it very difficult to obtain useful data. The majority of the NP binding data was collected whilst on a research placement in Japan and due to the problems encountered with screening against L1_0 NPs, screening was only carried out against A1 phase NPs due to the limited time available to collect data. Although screening was not carried out against L1_0 phase NPs it is still possible to obtain useful data from screening against A1 phase NPs. Regions of the peptide that are important and detrimental for binding to CoPt and FePt NPs can be highlighted as well as any specific amino acid residues. Any similarities or differences between the peptide sequences for the two materials can be identified. It is also possible to determine specificity of the lead sequences for one material over the other. From using NP binding data alone, it would not be possible to suggest peptide sequences that may be suitable for the formation of the L1_0 phase. However, by using the NP binding data in combination with metal ion binding and

particle synthesis data this allows a bigger picture to be built up and identification of peptides that are suitable for the synthesis of Pt alloy NPs selected.

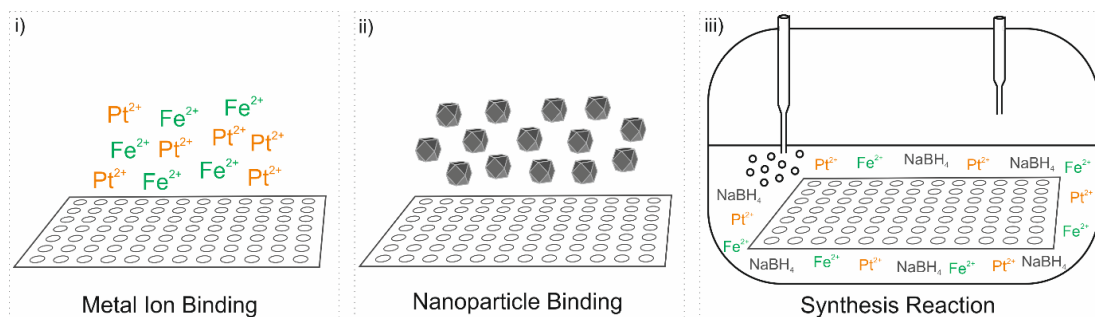


Figure 5.1.1 – Schematic showing the binding assays carried out for CoPt and FePt nanoparticles i) metal ion binding ii) nanoparticle binding and iii) synthesis reaction.

As the pH will be different in each screening method it is important to consider how pH will affect the peptides. The isoelectric point (pI) is the pH at which an amino acid is neutral and carries no net charges. All five peptides have relatively high (8 – 11) isoelectric points, therefore at pHs between 8 and 11 these peptides will be neutral. At pH values less than the pI the side chains will be protonated so any lysine, histidine and arginine residues will carry a positive charge. NP binding experiments are carried out at pH 7 and metal ion binding experiments at pH 3. Screening carried out in a synthesis reaction starts at pH 3 and increases to pH 7 on addition of reducing agent. Therefore, throughout all types of screening lysine, arginine and histidine will possess positive charges.

Table 5.1.1 – The isoelectric point (pI) and amino acid composition were analysed for the five lead peptide sequences using the ProtParam tool in ExPASy.

Sequence	Specificity	Isoelectric point (pI)	Amino acid composition
HNKHL PSTQPLA (1)	FePt	8.76	16.7% H 16.7% L 16.7% P
KTHEIH SPLLHK (2)	CoPt	8.61	25.0% H 16.7% L 16.7% K
KSLSRHDH IHHH (3)	FePt	8.78	41.7% H 16.7% S
SVSVG MKPSRP (4)	FePt	11.00	25.0% P 25.0% S 16.7% V
VISHNRESSRPL (5)	FePt	9.58	16.7% R 25.0% S

5.2 PEPTIDE ARRAY DESIGN

5.2.1 ALANINE SCANNING

Alanine scanning was carried out on each of the lead sequences and this is where each amino acid in turn is replaced with alanine. Alanine does not have a side chain and so has lower functionality compared to other amino acids. Therefore, by replacing amino acids with alanine it should allow for any key binding residues to be identified. This would be observed by a reduction in binding suggesting that the replaced amino acid was required for binding. Using this technique, it would also be possible to observe increases in binding intensity which would suggest that the original amino acid was unfavourable for binding to the NPs or metal ions. Alanine scanning was carried out on all five lead peptide sequences and resulted in a total of 60 different peptide sequences being screened.

5.2.2 TRUNCATION

Truncation of the peptides was used to identify the shortest amino acid sequence that is needed to retain peptide activity. Furthermore, by shortening the peptides, it should be possible to identify key binding regions, this would be observed by having the same binding intensity as the lead sequence or possibly a higher binding intensity. If any decreases in binding intensity are observed compared to the lead sequence, then this would suggest that these regions of the peptide alone are not able to bind to the NPs or metal ions. Truncation was performed on all five lead peptide sequences and the peptides were truncated from 9 down to 5 amino acids in length. This resulted in a total of 150 different peptide sequences.

5.2.3 POSITIONAL SCANNING

Positional scanning was carried out based on the results of the alanine scanning. In this case residues which showed poor binding were substituted with other amino acids in turn to investigate whether binding could be improved. The amino acids used to replace the original residue were leucine, proline, serine, threonine, histidine, lysine, methionine, glycine, valine, glutamic acid and isoleucine. These amino acids were chosen as they were prevalent in all five original lead sequences. The positions altered in each peptide are highlighted in red below. In total 93 different peptide sequences were screened using this method.

KTHEIHSPL**LHK**
SVSVGM**KPSRP**
VISN**HRESSRPL**
KSLS**RHD**HIHHH

Figure - Lead peptide sequences with amino acid positions (red) highlighted that were altered for different amino acid residues.

5.2.4 HIGH FREQUENCY

The amino acid composition of the five lead sequences were analysed (Table 5.1.1). From this analysis it was observed that there was a large proportion of histidine, lysine, proline, leucine, serine and arginine residues. Therefore, based on this observation a peptide was designed that contained these amino acids in a weighted ratio, depending on how frequently they appeared in the lead sequences. The peptide designed was: HHSSPKLR and each amino acid was altered in turn, being replaced with histidine, serine, proline, lysine, leucine and arginine. This resulted in a total of 41 different peptide sequences.

5.2.5 REVERSAL AND SCRAMBLING OF SEQUENCES

When the peptides are synthesised on membranes one end of the peptide will always be attached to the membrane whilst the other end is free. Therefore, reversal of the lead sequences was carried out so that both ends of the peptide would be able to act as the free end. Allowing for identification of what effect immobilisation would have on binding intensity. Scrambling was carried out to identify whether the order of the amino acids in the peptide was crucial or if randomisation of the sequence still resulted in binding. All five lead peptide sequences were screened using this method and this resulted in 10 different peptide sequences.

5.2.6 CYCLISATION

Cyclisation was used to constrain the peptides in a loop structure by using cysteines to form a disulphide bond as an anchor. This would allow the topology of the peptide to be investigated, as constrained in a loop the peptide would be in a fixed orientation whereas when the peptide is anchored at one end there are many different conformations the peptide can adopt. The peptides were anchored to the membrane via a short linker sequence (GGG) followed by the first cysteine residue, the desired peptide sequence was then inserted followed by a second cysteine residue. As a control of the same length serine was used in place of cysteine, serine has the same structure as cysteine but the sulfur atom is replaced with oxygen, therefore the peptides with serine present would not be able to form a disulphide bridge. This would allow comparison with the original peptide sequence to ensure that the presence of the linker does not affect binding intensity. All five lead peptides were constrained into a loop, in total 5 peptides were cyclised and with the corresponding controls 10 peptides were screened.

5.2.7 OVERALL ARRAY DESIGN

Once peptides were designed, they were arranged into an array using Microsoft Excel software. The peptides were synthesised in triplicate on the array so that repeats can be

collected and screening against only one array is necessary. In total 364 peptides were designed for screening against. It is possible to generate arrays with up to 600 peptide spots on, this results in 200 unique peptide spots in triplicate on the array. As there are more than 200 unique peptides that need to be screened against this has been separated into different arrays. The first array contained alanine scanning of all five LS, truncation for LS1, LS2 and LS5 as well as the high frequency peptides. The second array contained truncation of LS3 and LS4 and positional scanning. A third smaller array was generated for the reversal and scrambling of peptides as well as cyclisation.

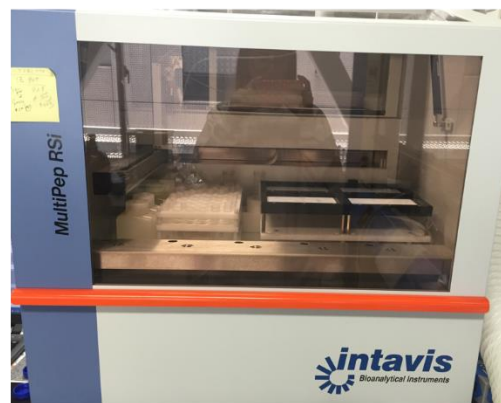
Once layout of the arrays was designed using Microsoft Excel this data was then transferred to the Intavis software so that a programme for synthesis of the arrays could be selected. Once a programme is selected the software then generates a report that details all reagents and solvents required for synthesis. Using this information, it is possible to make up all amino acid solutions required for synthesis, as well as coupling reagents and solvents used for deprotection and washing steps. Once all reagents and membranes are prepared and loaded into the auto peptide-spotter it is then possible to start the peptide synthesis reaction. Depending on the number and length of peptides to be synthesised this can take between 24 and 120 hours. Throughout this time reagent levels are monitored and topped up if required. An overview of this process can be seen schematically in Figure 5.2.1.

1. Peptide array layout designed using Microsoft Excel

Report of derivative requirements
User: Admin, Date: 31.05.2016

sequence: Sequence\Rosie\CoPt and FePt peptide array.txt
method: Method\Yuan\416229_yuan_glned.MFM
configuration: Tray\ResPepSL_600Spots\ana.MPC

2. Peptide array layout transferred to auto-peptide spotter software, programme for synthesis selected and report detailing reagents generated



3. Reagents and membranes loaded into auto-peptide spotter ready for peptide synthesis

Figure 5.2.1 – Overview of the process used for peptide array design and synthesis.

5.3 OPTIMISATION OF BINDING CONDITIONS FOR NANOPARTICLE BINDING

Small test membranes were synthesised so that binding conditions could be optimised before screening was carried out on the larger membranes. These test membranes contained the five lead sequences and one negative control sequence (AAAAA), the peptides were generated in triplicate and each membrane contained 18 peptide spots in total (Figure 5.3.1). The concentration of NPs, binding time and the use of blocking buffer needed to be optimised before carrying out larger scale binding experiments. After binding experiments the membranes needed to be washed to reduce any background noise and therefore different buffers and washing times were tested.

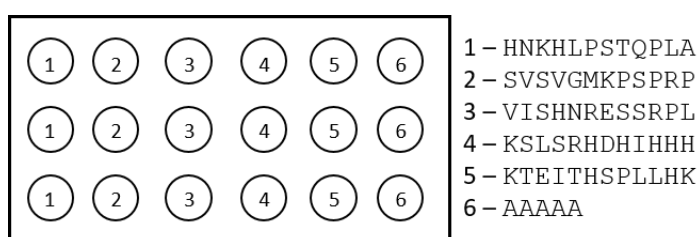


Figure 5.3.1 - Schematic to show the layout of test peptide arrays

5.3.1 CONCENTRATION OF NPs AND BINDING TIME

The first binding condition that was tested was the concentration of NPs and binding time. To begin with four different concentrations were tested, from 0.036 mg/ml up to 4 mg/ml. Initially the membranes were incubated in NP solution for 1 hour, however if binding was not observed after 1 hour the membrane was incubated for longer. If binding was observed after 1 hour then the membrane was taken out of the NP solution and imaged. Binding was observed for 0.036 mg/ml and 0.18 mg/ml after 1 hour, however the background noise is high which suggests that a blocking buffer may be needed. 0.4 mg/ml and 4 mg/ml solutions were incubated for 3 hours however binding was still very poor after this time and therefore these concentrations were not carried forward for further screening. 0.18 mg/ml was the only concentration carried forward as it showed the highest amount of contrast between the background and peptide spot although further optimisation was required due to the high background noise.

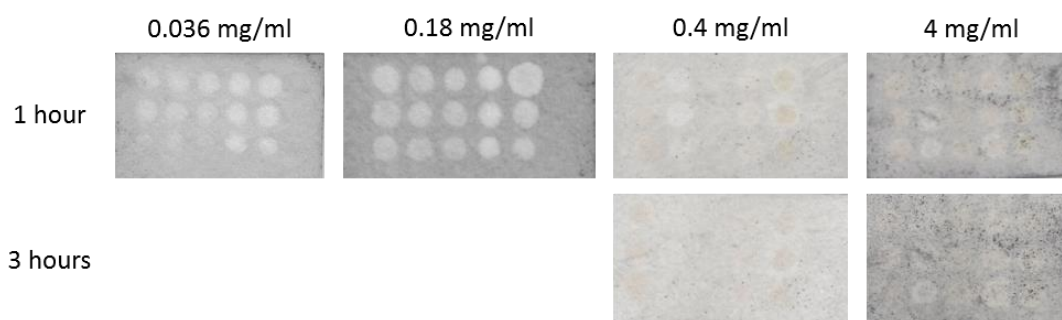


Figure 5.3.2 - Test arrays after binding CoPt NPs for 1 and 3 hours at concentrations of 0.036, 0.18, 0.4 and 4 mg/ml.

5.3.2 USE OF BLOCKING BUFFERS

A blocking buffer is used to prevent non-specific binding to unoccupied sites on the membrane.¹²⁵ Blocking can help to improve the signal to noise ratio of the assay by reducing background noise.¹⁶⁰ If blocking is not carried out for long enough then this can result in excessively high background noise conversely excessive concentrations of blocking buffer may mask any binding interactions. Therefore, to detect only binding to peptide spots the blocking conditions need to be optimised.

Two different blocking buffers were tested: bovine serum albumin (BSA) and skim milk. BSA was tested at two concentrations (1 % and 3 %) whilst skim milk was only tested at 3 %. The membrane was incubated in the blocking buffer solution for 1 hour prior to binding being carried out, washes with ultra-pure water were carried out before the NP solution was added to the membrane. NP binding was monitored and imaged over 24 hours; membranes were taken out of the NP solution when distinct binding to peptide spots was observed. Only 3 hours binding was required for the membrane that had been blocked using 1 % BSA, whereas when using 3 % BSA 20 hours was required. For 3 % skim milk 24 hours incubation was required for distinct binding to be observed. However, the background noise is still high in some cases and therefore it is important that washing conditions were tested on each blocking buffer before deciding which blocking buffer to use.

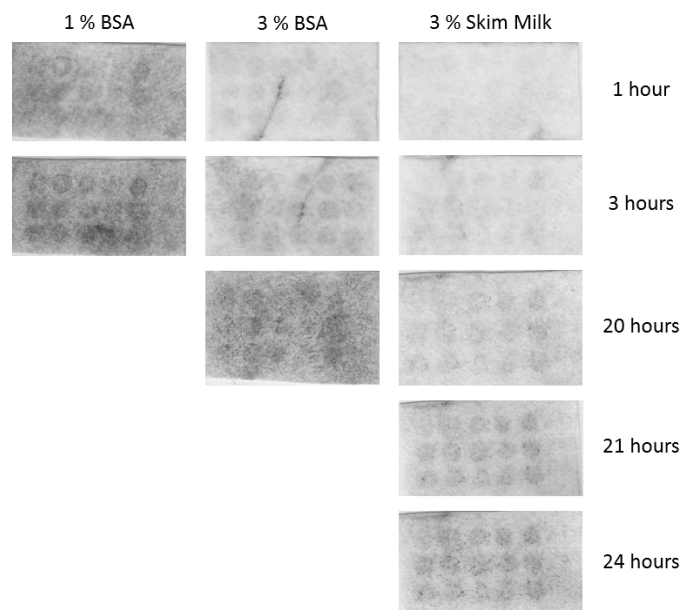


Figure 5.3.3 - Test arrays used to investigate the effects of different blocking buffers on NP binding. All binding was carried out at 0.18 mg/ml.

5.3.3 WASHING CONDITIONS

Each of the membranes from section 5.3.2 was then subjected to a range of different washing conditions, ultra-pure water and tween (0.5 % and 1 %) were tested. Washing was monitored and imaged throughout, when using 1 % BSA much longer washing times are required compared to 3 % BSA and 3 % skim milk. Therefore, 1 % BSA was not taken forward for use on larger membranes. 3 % BSA only required a 1-hour wash with 0.5 % tween present, whereas 3 % skim milk required a 2-hour wash to achieve the same result. Therefore, optimum binding conditions identified were a NP concentration of 0.18 mg/ml, blocking for 1 hour in 3 % BSA solution, binding over 20 hours followed by washing for 1 hour in 0.5 % tween.

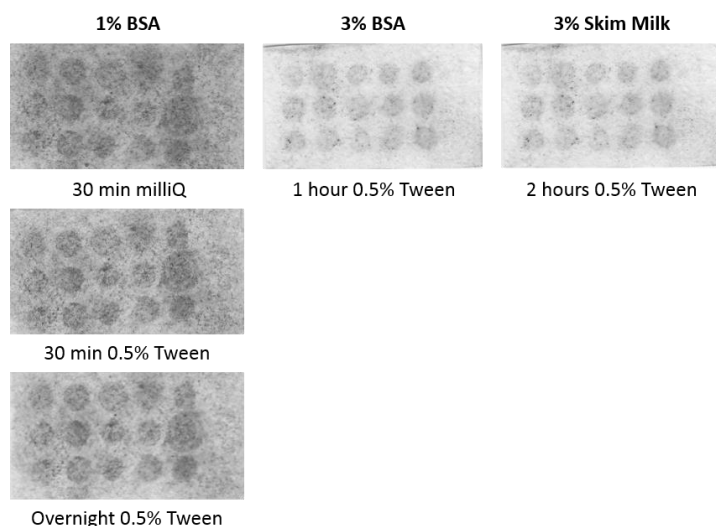


Figure 5.3.4 - Test arrays used to investigate different washing conditions after particles have been bound. All particle binding was carried out at 0.18 mg/ml.

5.4 BINDING CONDITIONS FOR METAL ION BINDING

The conditions used for screening the peptide arrays against different metal ions were kept similar to those used for NP binding as this process had already been optimised well. As BSA is known to bind to metal ions the blocking buffer for metal ion screening was changed to skimmed milk.^{161,162} This was done to ensure that background noise was kept to a minimum and the metal ions would only bind to peptide spots and not the rest of the membrane.

Blocking was carried out for 1 hour in 3% skim milk; however, this was followed by a 1-hour wash step in EDTA. An EDTA wash was carried out to remove any traces of metal that may be contained in the blocking buffer so that this would not interfere with detection of Fe^{2+} , Pt^{2+} and Co^{2+} metal ions. Metal ion binding was carried out at the same concentration that would be used in a synthesis reaction, as the free peptides could be used in a synthesis reaction it is essential that the conditions of a synthesis reaction were closely followed. Binding was carried out for 20 hours, as had been identified from NP binding, followed by washing with ultrapure water. As only a faint coloured spot was observed after 20 hours binding, tween washing was not required as this would have been too stringent.

5.5 BINDING CONDITIONS FOR SYNTHESIS REACTIONS

For screening carried out against FePt and CoPt synthesis reactions the conditions were kept as similar as possible to the conditions used in the NP synthesis reactions. This would allow for a more direct comparison to be made. However, membranes still needed to undergo blocking and so membrane preparation was carried out in the same way as for metal ion binding. This involved 1 hour in 3% skim milk blocking buffer followed by a 1-hour EDTA wash. The membrane was then immersed into the metal ion solutions, either a mixture of Co^{2+} and

Pt²⁺ or Fe²⁺ and Pt²⁺ for 1 hour before reducing agent was added. The reaction was then incubated for 40 minutes, after this time the membrane was removed from the reaction vessel and washed with ultra-pure water.

5.6 COMPARISON OF DETECTION AND IMAGING SOFTWARE

As the majority of this work was carried out in collaboration with the Okochi Lab at The Tokyo Institute of Technology, I had access to the ImageQuant TL software. However, this software was not available at The University of Sheffield, so ImageLab was used instead. All arrays screened against NPs have been detected using ImageQuantTL, whilst arrays used for metal ion binding and screening against synthesis reactions have been detected using ImageLab.

To ensure that comparison could be made between arrays imaged using the two different software packages, the detection was carried out on a small test membrane to ensure that both pieces of software identify the levels of binding intensity as the same. As can be seen from Figure 5.6.1 the peptides have been identified in the same order from highest to lowest intensity (LS4 > LS5 > LS1 > LS3 > LS2) from detection using both software packages. However, detection using ImageLab resulted in overall higher SNR values being obtained and, in some cases, larger error bars are present compared to detection using ImageQuantTL. Although there is some deviation between the two software packages this should not affect data analysis as direct comparison will only be made between arrays of the same screening type. All arrays of the same screening type were screened using the same software package. Therefore, the use of two different software packages should not have an overall effect on data analysis.

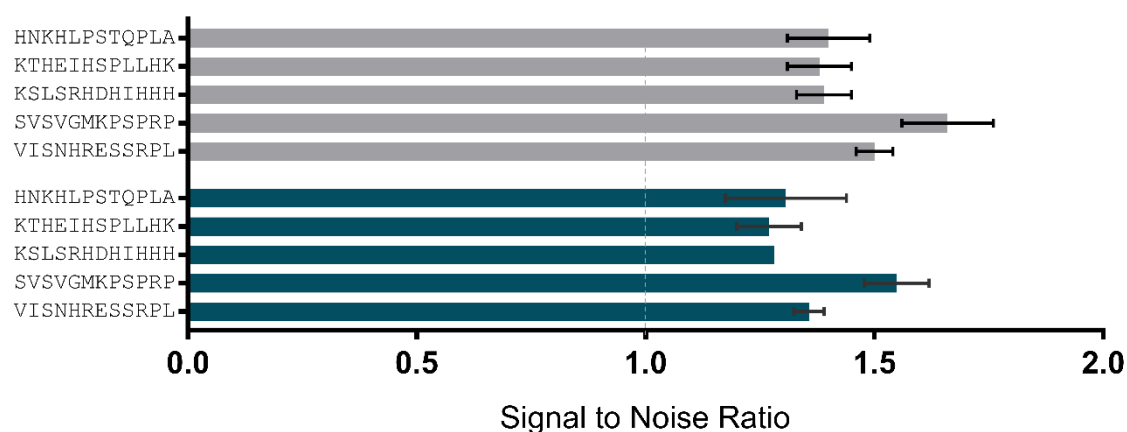


Figure 5.6.1 – SNR data for all five lead sequences that have been screened against CoPt NPs. Dark green – ImageQuantTL software used for detection and grey – ImageLab software used for detection. Dotted grey line represents background noise. Signal to Noise Ratio (SNR)

5.7 SIGNAL TO NOISE RATIO

Signal to noise ratio (SNR) compares the level of a desired signal (intensity of peptide spot) to the level of background noise. Background was the intensity of the membrane in regions where no peptide spots were present. Therefore, a SNR value of 1.0 would indicate binding to the peptide spots that is of similar intensity to the background noise suggesting that negligible binding is occurring. The larger the SNR suggests a much greater difference between background noise and binding intensity and so binding to this peptide sequence is higher. Sequences that have SNR values of less than 1.0 suggest that other factors may be playing a role for example the material could be being repelled by the peptide.

Typical SNR values for NP binding and screening against a synthesis reaction are between 1.0 and 2.0, with higher values suggesting higher binding. Higher SNR values are observed for metal binding, this is due to the reagents used for detection and imaging of the arrays. Therefore, this makes it difficult to quantitatively compare between the different sets of data (NP binding and metal binding) but it is still possible to draw conclusions from both sets of data qualitatively. As the highest binding peptides for each material will still have the highest SNR values, however it is not possible to say that a particular sequence binds with higher intensity to either FePt NPs or Fe²⁺ for example.

5.7.1 SOURCES OF ERROR AND RANDOM VARIATION

Using SPOT peptide arrays for screening against MNPs is likely to result in some random variation and sources of error, as the NPs do not fully disperse in solution and also aggregate together through magnetic interactions. Because the NPs do not fully disperse in solution it is possible that NPs can drop out of solution and so this would result in a higher proportion of NPs being on one area of the membrane. This could cause certain areas of the membrane to become darker in colour and would suggest that these peptide spots bind with a higher intensity, when it is in fact a result of these peptide spots being in contact with a higher concentration of NPs for a prolonged time. Care was taken to try and minimise this effect by sonication of the NPs before their first application to the membrane, a rotor speed for the mixer was also selected that would ensure NPs were kept in solution as best as possible. NP binding was monitored throughout and if aggregation was observed, the NP solution was sonicated again and reapplied to the membrane. Although care was taken to minimise this effect screening was carried out overnight, so it was not possible to monitor the entire length of the screening and as a result there are some peptide spots that have larger error bars due to this. When screening against metal ions this area was no longer a concern as all metal salts used fully dissolved in solution. However, as binding of the metal ions to the peptides did not

result in a colour change being observed colorimetric detection was not possible. Therefore, a detection reagent was required for imaging. It is possible that the detection reagent may not have been applied evenly across the membrane and so this would result in areas of the membrane having a higher binding intensity. The same volume of detection reagent was used each time and pipetted evenly across the membrane however it is still possible that there could be variation between repeats of each peptide spot, resulting in some peptide spots having large error bars.

Screening carried out against a synthesis reaction was susceptible to the largest amount of error due to the fact that a membrane was placed into a synthesis reaction. Therefore, this made it very hard to control the screening process and so stringent washing steps were instead required to try and remove any sources of error and variation.

CHAPTER SIX: CoPt PEPTIDE ARRAYS

6 CoPt PEPTIDE ARRAY SCREENING

6.1 NANOPARTICLE BINDING

Peptide arrays were first screened against pre-made CoPt NPs. These particles were in the A1 phase and the final peptide arrays obtained from this screening can be seen in Figure 6.1.1.

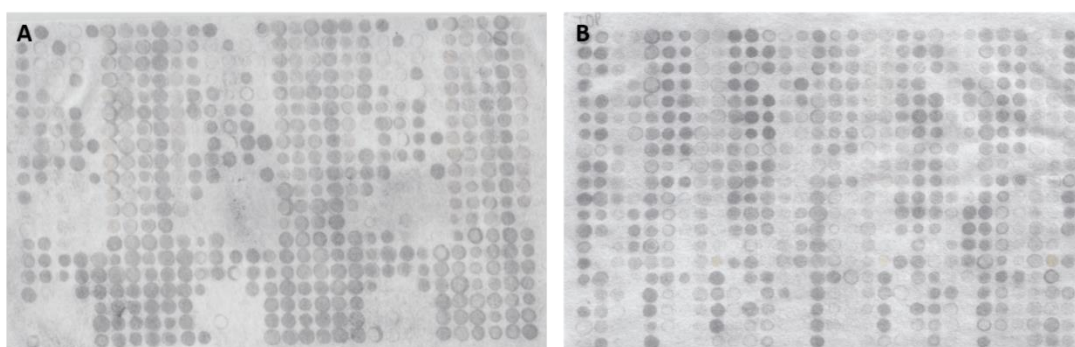


Figure 6.1.1 - Peptide arrays after NP binding has been carried out A) 1st generation array and B) 2nd generation array.

6.1.1 LEAD SEQUENCES

All five lead sequences were screened against CoPt NPs and the results can be seen in Figure 6.1.2. In general, all five sequences are of similar intensity but LS4 has the highest overall. LS1, LS3, LS4 and LS5 were all identified from screening carried out against L1₀ phase thin films and NPs of FePt and so it is interesting that they bind with such high affinity to CoPt NPs.⁶¹ LS2 was identified from screening against L1₀ thin films of CoPt and so it would be expected that this sequence would have the highest affinity for binding to CoPt NPs. However, this does not seem to be the case here.

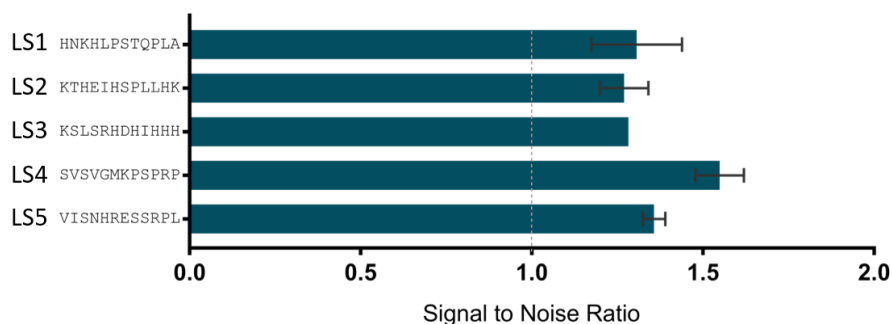


Figure 6.1.2 – SNR data for all five lead sequences screened against CoPt nanoparticles. Dotted grey line represents background noise.

6.1.2 ALANINE SCANNING

Alanine scanning was carried out on all five lead peptide sequences to identify individual key amino acids. Unfortunately, when each of the amino acids were replaced with alanine there

were no significant increases or decreases in binding intensity for all five LS. Only changing one amino acid at a time leaves the majority of the peptide unchanged. Therefore, this suggests that not one single amino acid is responsible for binding but that it is a combination of several amino acids in the peptide sequence.

6.1.3 TRUNCATION

Truncation was performed on all five lead peptides, the 12 amino acid peptides were shortened systematically from 9 amino acids in length all the way down to 5 amino acids, screening against a range of peptide lengths. Allowing for the identification of any key regions for binding and the shortest length of peptide that can retain peptide activity.

Truncation of LS1 resulted in sequences that had both significantly reduced and increased SNR compared to the lead sequence. The key trend that is observed from the truncation data is that removal of lysine from sequences results in decreased binding. When lysine was removed sequences have a significantly reduced SNR value and this is highlighted in part B of Figure 6.1.3. For sequences that do not contain lysine, binding is reduced down to the same level as background noise ($SNR \approx 1$), this suggests that almost no binding is occurring. Sequences that contain lysine have increased or similar binding compared to LS1, this true for shorter peptide sequences (pentamers) and longer peptide sequences, up to 9 amino acids in length. Peptide sequences, containing lysine, that are either 5, 6 and 7 amino acids in length have a slight increase in SNR compared to those that are 8 or 9 amino acids in length. This could suggest that CoPt NPs have a slight preference for shorter peptide sequences.

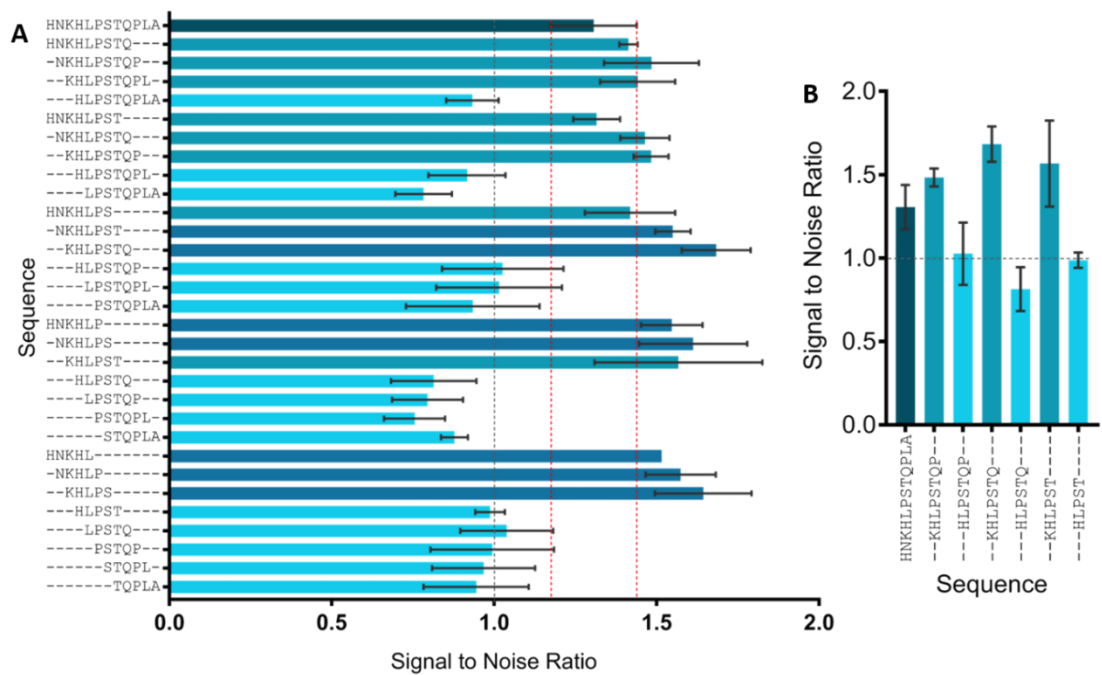


Figure 6.1.3 – A) Truncation data for LS1. Dark green – LS1, teal – sequence with similar intensity to lead, dark blue – increased binding and light blue – decreased binding B) Truncation data highlighting the importance of lysine. Dark green - lead peptide, teal - sequence containing lysine and light blue - sequence with lysine removed. Dotted grey line represents background noise.

Truncation data for LS2 also highlights the importance of lysine and this can be seen in Figure 6.1.4. All sequences that have increased SNR values, compared to LS2, contain lysine. Sequences that do not contain lysine have significantly reduced binding. However, peptides that are six amino acids in length and do not contain lysine have slightly reduced SNR values compared to LS2. The most dramatic difference in SNR values is observed for pentamers, only sequences KTHEI and PLLHK have increased binding compared to LS2 and all middle sections of the peptide are significantly reduced, so much so that they have SNR values of less than 1 and this suggests that no binding is occurring.

In LS2 there are two lysine residues, one at either end of the peptide, removal of lysine from either end results in a significant reduction in binding. A similar reduction in binding is observed regardless of which lysine residue has been removed and so no preference for one lysine residue over the other is detected. The lysine at the start of the sequence is anchored to the peptide array whereas the one at the end is able to move freely, it might be expected that the free lysine would be able to interact with NPs more easily. However, this does not seem to be the case as similar binding is observed for lysine that is anchored to the array.

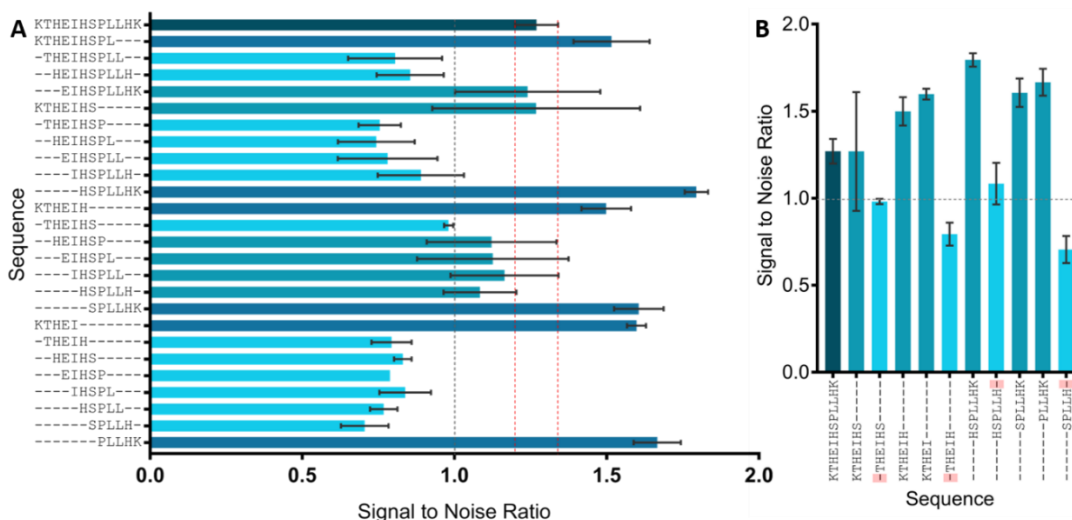


Figure 6.1.4 - A) Truncation data for LS2. Dark green – LS2, teal – sequence with similar intensity to lead, dark blue – increased binding and light blue – decreased binding B) Truncation data highlighting the importance of lysine. Dark green - lead peptide, teal - sequence containing lysine and light blue - sequence with lysine removed. Dotted grey line represents background noise.

From truncation of LS3 it is harder to identify any key trends or regions of the peptide as the majority of truncated sequences have similar binding intensity to LS3. This could suggest that the entire peptide sequence is required for binding to CoPt NPs, however the lead sequence itself has a signal to noise ratio of ≈ 1.1 , this is not much higher than background noise. This peptide was originally identified from literature for specificity to the L1₀ phase of FePt therefore the fact it shows poorer binding to CoPt is understandable.⁶¹ Although the majority of sequences show similar binding there are three sequences that have significantly increased binding and three sequences that have significantly reduced binding compared to LS3, these sequences can be seen in Figure 6.1.5.

The sequences that have increased binding are the only sequences that do not contain aspartic acid. All other sequences that contain aspartic acid have either a similar or decreased SNR values compared to LS3. Therefore, this suggests that aspartic acid is unfavourable for binding to CoPt NPs. The three sequences that have increased SNR contain a large proportion of basic residues such as lysine, arginine and histidine. Basic residues are present at either end of the peptide and this could make the side chains more accessible for binding to NPs. Sequences KLSLRH and KLSLR show a much larger increase in SNR than any truncated sequences identified from LS1 and LS2.

The sequences that have decreased binding also contain a large number of other basic residues, mainly histidine, the decrease in binding could be observed due to too many positively charged residues being next to each other and this may be unfavourable for

binding to NPs. However, it is likely to be the presence of aspartic acid that also results in decreased binding.

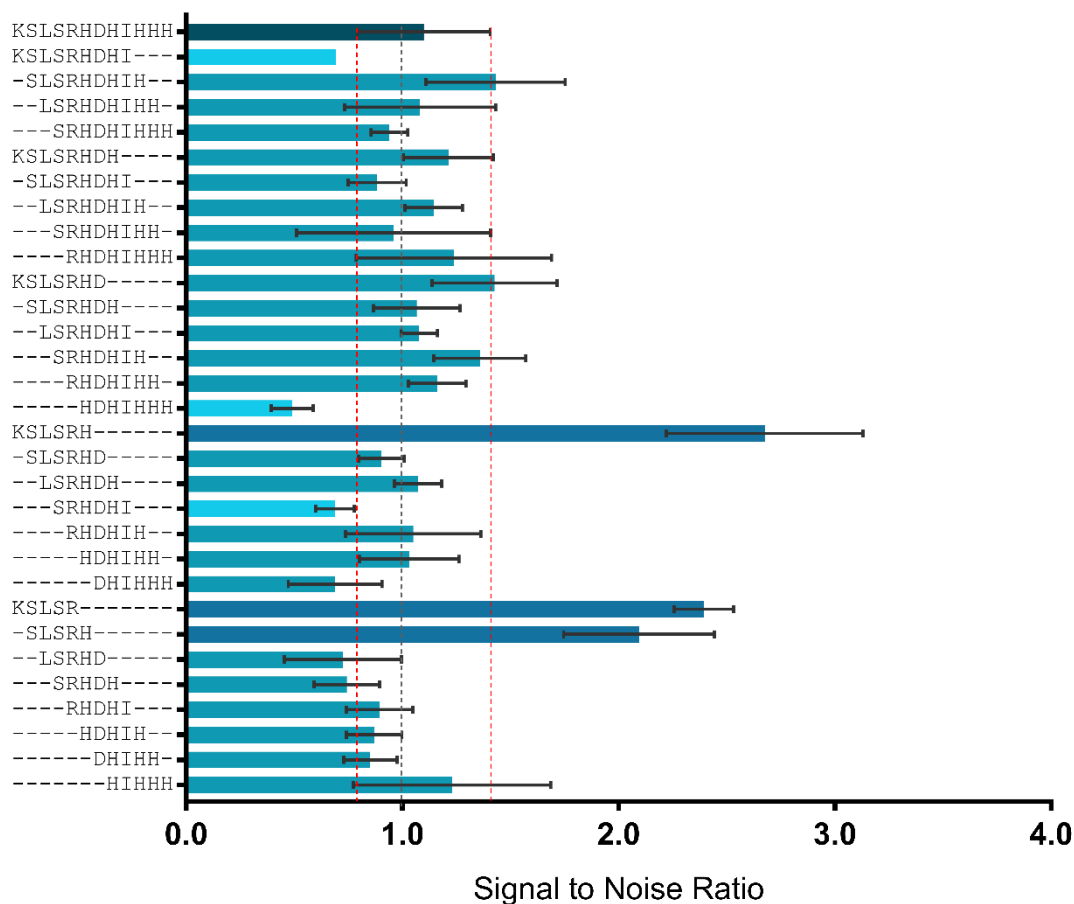


Figure 6.1.5 – Truncation data for LS3. Dark green – LS3, teal – sequence with similar intensity, dark blue – increased binding and light blue – decreased binding. Dotted grey line represents background noise.

Truncation data for LS4 highlighted the importance of basic residues, such as arginine and lysine. Removal of arginine and lysine from the end of the peptide sequence resulted in a significant decrease in SNR, this suggests that these residues are important for binding to CoPt NPs. Sequences that have had arginine or lysine removed from the end of the peptide sequence have SNR values of less than 1. Sequences that contain lysine in the centre of the peptide sequence (VGMKPSP, GMKPSP and MKPSP) have reduced binding even though lysine is present, this suggests that the position of lysine in the sequence is important and presence at the end of peptides is favoured. This is in contrast to LS1 where the presence of lysine, either at the end or buried in the sequence, resulted in increased binding. The sequence that has the highest SNR is SVSVGK, this sequence contains a lysine residue at the end which could account for the increased binding observed. This sequence has the highest SNR compared to truncated sequences from LS1, LS2 and LS3 showing its importance for binding to CoPt NPs.

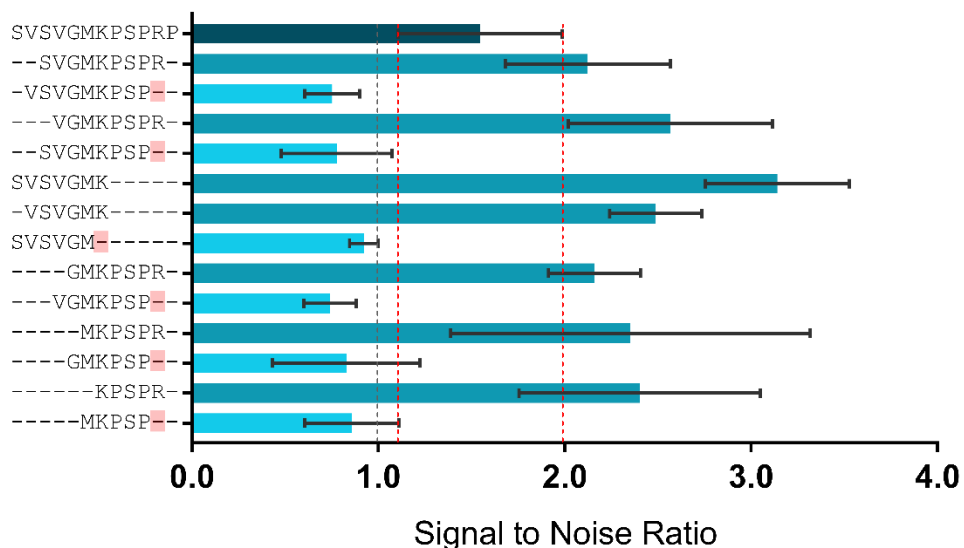


Figure 6.1.6 - Truncation data for LS4 highlighting the importance of basic residues, lysine and arginine. Dark green – LS4, Teal - sequences containing either lysine or arginine and light blue - sequences with lysine or arginine removed. Dotted grey line represents background noise.

Finally, truncation was carried out on LS5, there are three sequences that have increased binding compared to the lead and the majority of truncated sequences show decreased or similar binding to LS5. The sequences that have increased SNR are: VISNHR, ISNHR, SNHRESSR and SSRPL. It is possible that sequences VISNHR, ISNHR and SSRPL could have an increased SNR as they no longer contain glutamic acid at the end of the peptide (Figure 6.1.7). However, SNHRESSR contains glutamic acid but it also contains three basic residues so overall the peptide would have a charge of +2. Sequences VISNHR and ISNHR also have an overall charge of +2 and there is a higher concentration of positive charge on ISNHR due to the peptide being shorter than VISNHR and SNHRESSR and so this could suggest why the highest SNR value is observed for this sequence. There are four other sequences that have an overall charge of +2 (HRESSR, HRESSRP, NHRESSR and LS5) and these sequences are of similar intensity to the lead sequence, this suggests that an overall charge of +2 on the peptide is favourable for binding to CoPt NPs. Sequences that have decreased SNR values compared to LS5 have an overall charge of +1 or are neutral (ESSRP and ESSRPL). Therefore, this suggests that for LS5 a higher overall positive charge is favourable for binding to CoPt NPs compared to lower positive charges or peptides that are neutral.

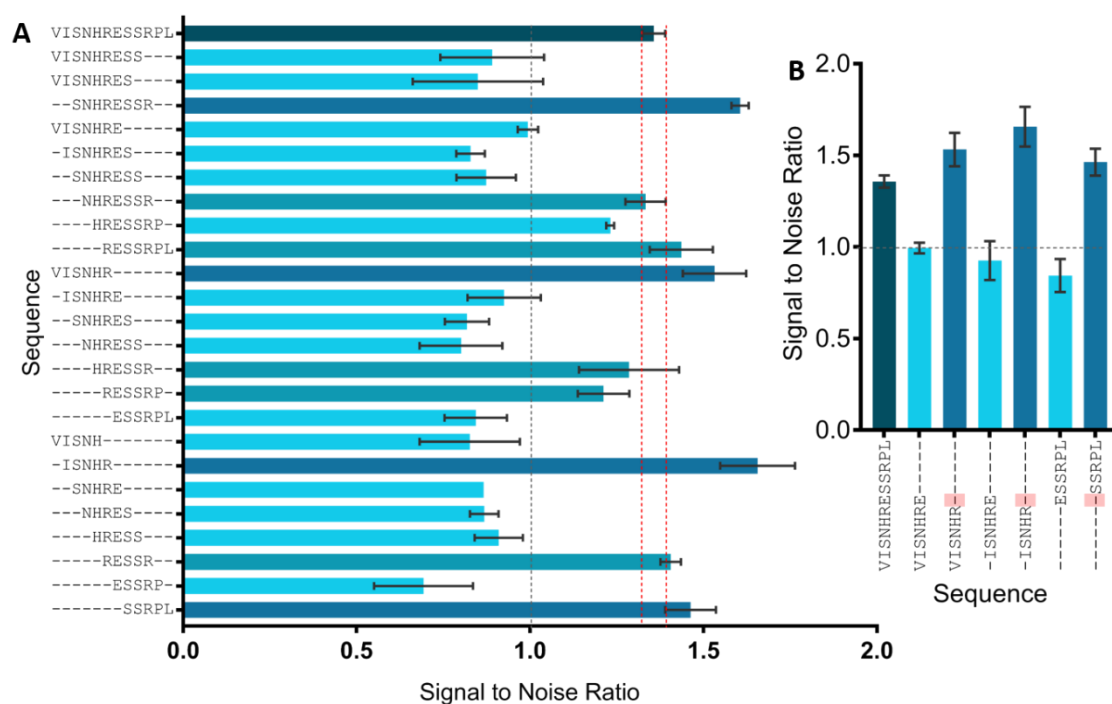


Figure 6.1.7 - A) Truncation data for LS5. Dark green – LS5, teal – sequence with similar intensity to lead, dark blue – increased binding intensity and light blue – decreased binding B) Truncation data showing glutamic acid is unfavourable. Dark green - lead peptide, light blue - sequence containing glutamic acid and dark blue - sequence with glutamic acid removed. Dotted grey line represents background noise.

6.1.4 POSITIONAL SCANNING

Only replacement with amino acids that showed a significant increase or decrease are presented graphically and discussed here. Positional scanning data for LS2 involved replacement of leucine and histidine at positions 10 and 11 respectively. Replacement of histidine with isoleucine and serine gave similar binding to LS2. Histidine was identified as being important for binding to CoPt NPs from truncation data, therefore it is surprising that replacement with a hydrophobic and polar amino acid gave similar binding. However, as there are two lysine residues at either end of the peptide as well as two other histidine residues present in the sequence this could suggest that removal of one basic residue may not have a significantly adverse effect due to the presence of other basic residues.

However, replacement of histidine with glutamic acid results in decreased binding, this is to be expected as a basic positively charged residue is being replaced by an acidic and negatively charged residue. Replacement of leucine with glutamic acid also resulted in decreased binding. Glutamic acid was also identified as being unfavourable for binding from truncation data and so the positional scanning data matches this well. Replacement of leucine with histidine also resulted in decreased binding, leucine is hydrophobic and so by introducing a basic residue it was thought that binding would increase. This decrease in binding could be accounted for by the presence of two other basic residues next to the histidine that has been

introduced, giving a sequence of HHK. It is possible that having three positively charged residues next to each other is unfavourable as the repulsion between the three side chains could change the conformation of the peptide.

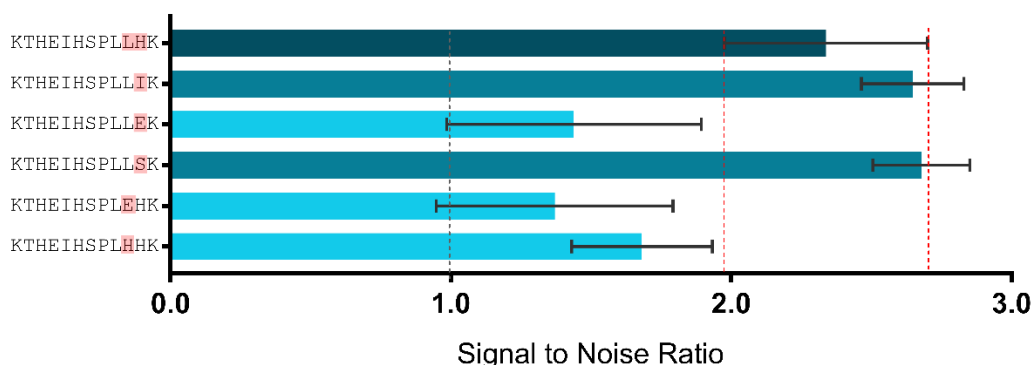


Figure 6.1.8 - Positional scanning data for LS2. Dark green – LS2, teal – similar intensity to LS2, light blue – decreased binding. Red boxes highlighted the amino acid residues that have been substituted. Dotted grey line represents background noise.

Positional scanning for LS3 involved replacement of arginine, histidine and aspartic acid at positions 5, 6 and 7 respectively. The largest increase in binding intensity was observed when arginine was replaced with methionine. Replacement of histidine with threonine resulted in increased binding, it was expected that replacing a basic residue with a hydrophobic, polar or acidic residue would decrease binding, but here this is not the case. However, as there are already many basic residues present within the peptide it is possible that removal of one would not have a significant effect on the overall binding ability of the peptide. Threonine has a less bulky side chain compared to histidine so it is possible that sterics could play a role in the increased binding intensity observed, by having a less bulky side chain it could make the surrounding side chains more accessible for binding.

When aspartic acid was replaced with proline and leucine an increase in binding was observed. From truncation data acidic residues were shown to be unfavourable for binding to CoPt NPs and so it is expected that substitutions of aspartic acid with other amino acids would result in increased binding. Leucine is a neutral hydrophobic acid, so incorporation of this residue results in a higher overall positive charge for the peptide compared to when aspartic acid is present. Therefore, this could account for the increase in binding observed. Replacement with proline also increased the overall positive charge of the peptide. However, when aspartic acid is replaced with histidine a decrease in binding is observed. There are now six histidine residues in the sequence and overall eight basic residues giving the region RHHIH^{red}HH^{red}. This region may be unfavourable as there a large number of basic residues

together and repulsion can occur between the side chains, resulting in the conformation of the peptide changing.

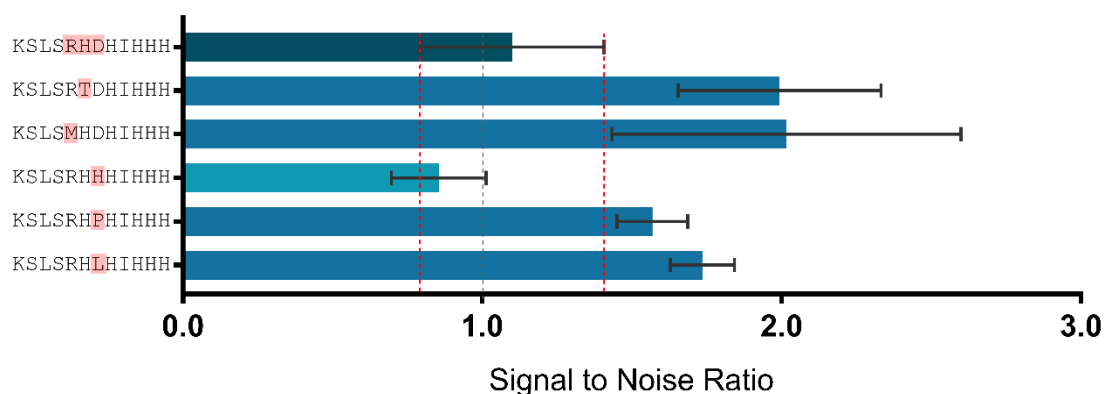


Figure 6.1.9 – Positional scanning data for LS3. Dark green – LS3, dark blue – increased intensity to LS3, light blue – decreased binding and teal – similar intensity to LS3. Red boxes highlighted the amino acid residues that have been substituted. Dotted grey line represents background noise.

Positional scanning was carried out for LS4 and in this case lysine and arginine at positions 7 and 11 respectively were substituted. Substitution of lysine resulted in the majority of sequences having similar binding intensity compared to LS4. Lysine was identified as an important residue for binding to CoPt NPs from truncation data and so it would be expected that replacement of this residue would result in decreased binding. However, truncation data for LS4 found that the presence of lysine at the end of the peptide sequence resulted in increased binding compared to when lysine was 'buried' in the peptide sequence. As lysine is present in LS4 in the middle of the peptide this could explain why substitutions resulted in similar SNR values to the LS4. The only substitution of lysine that resulted in decreased SNR was replacement with glutamic acid. This was to be expected as a basic positively charged residue is being replaced by an acidic negatively charged residue and would therefore change the overall charge of the peptide sequence. Replacement of arginine with glutamic acid also resulted in decreased binding intensity.

A decrease in binding intensity was observed when arginine was replaced with valine, serine and histidine. By replacing arginine with valine, a basic positively charged residue has been replaced with a hydrophobic residue and it is likely that valine will not interact as well with CoPt NPs as the side chain for valine only consists of hydrocarbons which are not known to have a strong interaction with MNPs. Although serine has an -OH group at the end of its side chain it is likely to result in reduced binding for a similar reason as valine. Replacement of histidine with isoleucine in LS2, resulted in similar SNR values to LS2 however there are more basic residues overall in LS2 than LS4, so removal of one does not greatly affect the overall binding ability of the peptide. Whereas in LS4 there are only two basic residues in the

sequence so removal of one is likely to have a more significant effect on the peptides binding ability. The decrease observed for histidine is unexpected as in this case like is being replaced for like (both basic residues) and so this would suggest that it is to do with the structure of histidine rather than the charge. Histidine has an imidazole side chain whereas arginine has an aliphatic carbon chain ending in a guanidino group. Therefore, histidine has a more sterically bulky side chain compared to arginine and this could be why a decrease in binding intensity is observed.

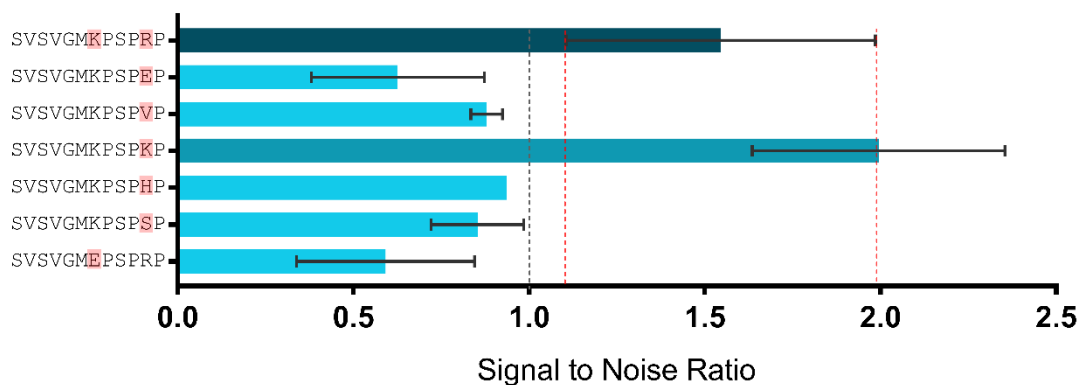


Figure 6.1.10 - Positional scanning data for LS4. Dark green – LS4, teal - similar intensity to LS4, light blue – decreased binding. Red boxes highlighted the amino acid residues that have been substituted. Dotted grey line represents background noise.

In LS5 histidine and arginine at positions 5 and 10 were substituted in turn for different amino acids. The majority of substitutions carried out for arginine resulted in sequences that had a similar intensity to LS5. The only significant decrease observed was when arginine was replaced with valine. This is likely to be because a basic positively charged amino acid has been replaced with a hydrophobic amino acid and is less likely to interact with the NPs. A significant increase is observed when arginine is replaced with lysine and a preference for lysine was observed from truncation data. This same trend is observed when histidine is replaced with lysine. Although histidine and arginine are both basic positively charged residues, they have very different side chains compared to lysine. Lysine has an aliphatic carbon chain ending in an amino group whereas histidine has an imidazole side chain and arginine also contains an aliphatic carbon chain but ending in a guanidino group. Therefore, lysine has the least sterically bulky side chain, and this explains why an increase in binding is observed when lysine is used.

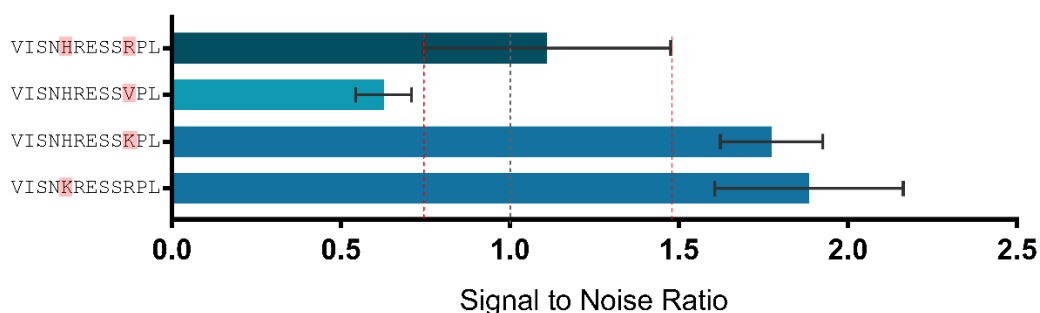


Figure 6.1.11 - Positional scanning data for LS5. Dark green – LS5, teal - similar intensity to LS5, light blue – decreased binding. Red boxes highlighted the amino acid residues that have been substituted. Dotted grey line represents background noise.

6.1.5 HIGH FREQUENCY

Signal to noise ratio data can be seen in Table 6.1.1, for all variations of the high frequency peptide. There are only six variations to the peptide that show an increase in SNR and nine that show a decrease. Peptides that showed an increase or decrease in SNR were then plotted graphically so that those that have a significant change in SNR can be identified, this can be seen in Figure 6.1.12. This results in only two peptides having a significant increase in SNR and four peptides with a significant decrease. Those that show an increase are the replacement of histidine (position 1) with leucine and serine (position 3) with proline.

Table 6.1.1 – Change in signal to noise ratio compared to the original high frequency peptide HHSSPKLR. Green - increase in SNR greater than 0.1, red - decrease in SNR greater than 0.1 and grey - no significant change in SNR.

	H	H	S	S	P	K	L	R
H	-	-	-0.03	-0.16	-0.24	0.08	0.03	0.01
S	0.07	0.19	-	-	-0.18	0.07	0.08	0.08
P	0.04	0.14	0.18	0.03	-	0.02	0.13	-0.01
L	0.17	0.05	-0.10	0.10	-0.02	-0.03	-	-0.11
K	0.06	0.03	0.06	0.05	-0.29	-	-0.04	-0.03
R	0.04	-0.05	-0.19	0.00	0.00	-0.12	-0.28	-

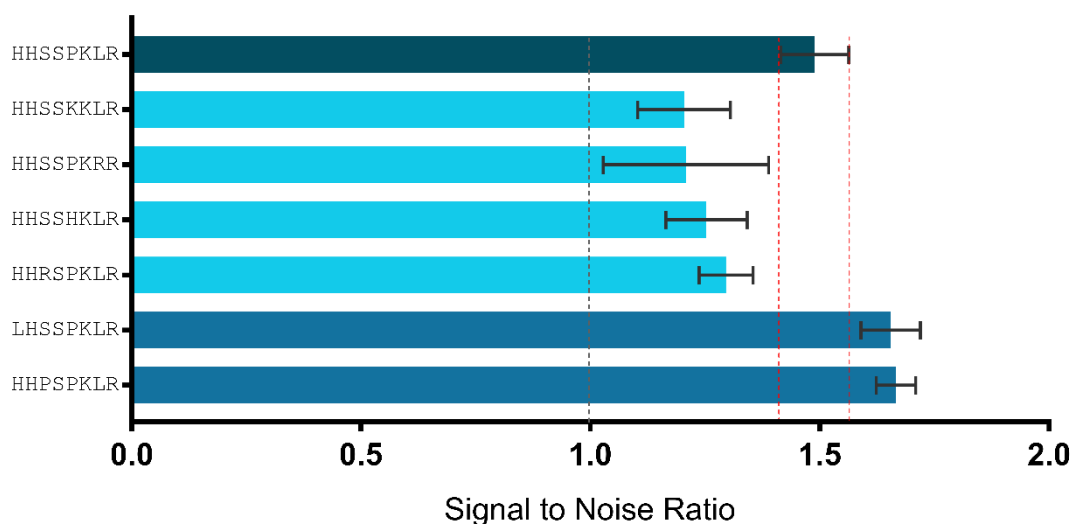


Figure 6.1.12 – High frequency binding intensity data compared to the original high frequency sequence (HHSSPKLR), highlighting sequences that have a reduction binding intensity (light blue) and those with an increased binding intensity (dark blue). Dotted grey line represents background noise.

The two peptides that show an increase in SNR have been compared to the five lead peptide sequences (Figure 6.1.13). Both peptides show an increase compared to all five lead peptides however variations of the lead sequences from truncation and positional scanning show larger increases in SNR compared to the high frequency peptides.

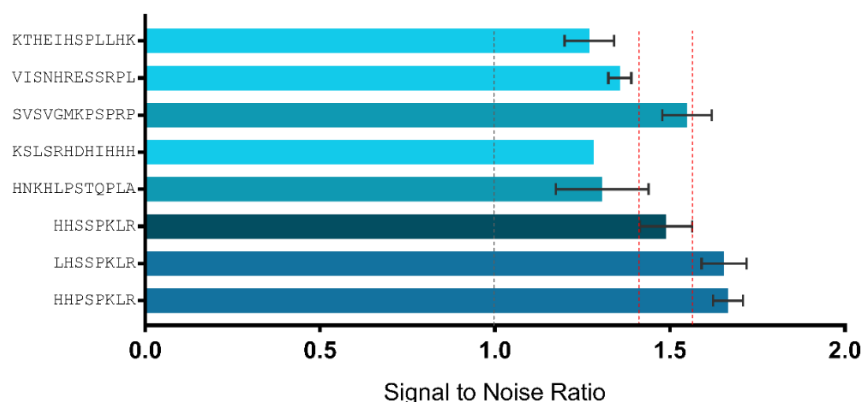


Figure 6.1.13 - Sequences with the highest binding intensity from the high frequency array compared to the original lead peptide sequences. Light blue - reduced binding intensity and dark blue - increased binding intensity. Dotted grey line represents background noise.

6.1.6 REVERSAL AND SCRAMBLING

Reversal and scrambling of all five lead sequences was carried out. By reversing the peptide sequence, it is possible to investigate whether the orientation of the peptide has an effect on its binding ability. The start of the peptide is anchored to the membrane and the end is free, therefore by reversing the sequence it will be possible to see what effect there is when one end of the peptide is anchored, and one end is free. The peptides are synthesised from the c-terminus to the n-terminus and so there will always be a free amino group at the end of the peptide even when sequences have been reversed. For the majority of the lead

sequences there is little variation in SNR between the original sequence and the reversed sequence. Only LS1 has a significant difference between the two sequences, the reversed sequence has a higher SNR than the original sequence. This could be because histidine and lysine are now at the free end of the peptide rather than anchored to the membrane, basic positively charged residues were identified as important for binding to CoPt NPs from truncation and positional scanning data, suggesting why the reversed sequence has a higher SNR value.

Scrambling of the peptides was also performed to identify whether the exact sequence of the peptide was important or just the presence of the amino acids and the overall charge was enough to retain the peptides binding ability. Only one scrambled peptide per lead sequence has been chosen at random as every variation of scrambling each peptide would result in a very large number of combinations and screening against such a large number would be impractical, time consuming and costly. For the majority of the lead peptides there is very little difference between the original and scrambled sequences this would suggest that the presence of the specific amino acids is more important than their order in the peptide sequence.

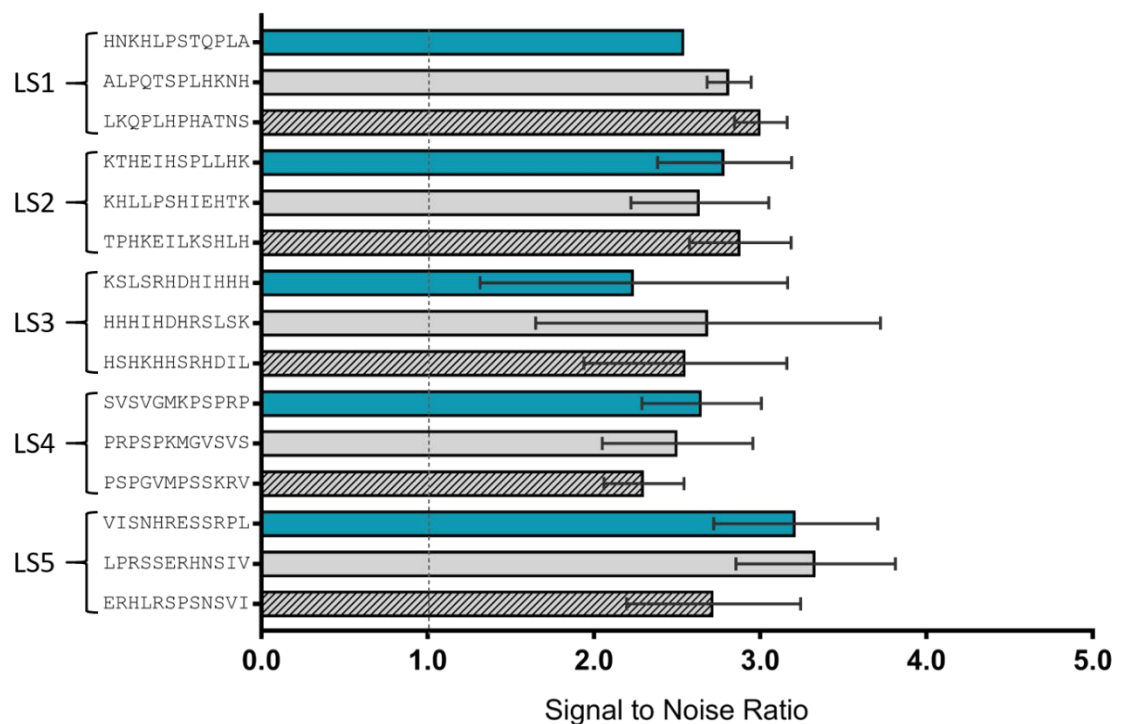


Figure 6.1.14 - Scrambling and reversal of lead peptide sequences. Teal - lead peptide sequences, grey - reversed sequence and diagonal striped - scrambled sequence. Dotted grey line represents background noise.

6.1.7 CYCLIC

The lead peptide sequences have been constrained into a loop by the incorporation of cysteine residues at either end of the peptide to form a disulphide bond that can act as an anchor. A control peptide containing serine residues instead of cysteine has been included, serine has the same structure as cysteine except that the sulfur atom is replaced with oxygen, meaning that a disulphide bond is not able to form. For all of the lead peptides the original linear peptide has a larger SNR value compared to the cyclic peptide. This suggests that the linear peptide conformation is preferred compared to when constrained in a loop for binding to CoPt NPs. It is possible that the linear peptide can adopt many different conformations compared to the cyclic peptide and that this wide variety of conformations makes the peptide more accessible for binding.

Comparison of the peptides containing serine instead of cysteine results in SNR values that are similar to that of the cyclic peptide. It would be expected that the serine containing peptides have similar values to the original LS, however this does not seem to be the case. This suggests that the presence of the glycine linker region or the serine residues has adversely affected the peptides ability to bind to NPs. Glycine does not have a side chain and so incorporation of GGG at the start of the peptide sequence is unlikely to cause this effect and so it is likely to be the presence of the serine residues that is responsible. Only for LS4 is the serine containing peptide of similar value to the original lead sequence.

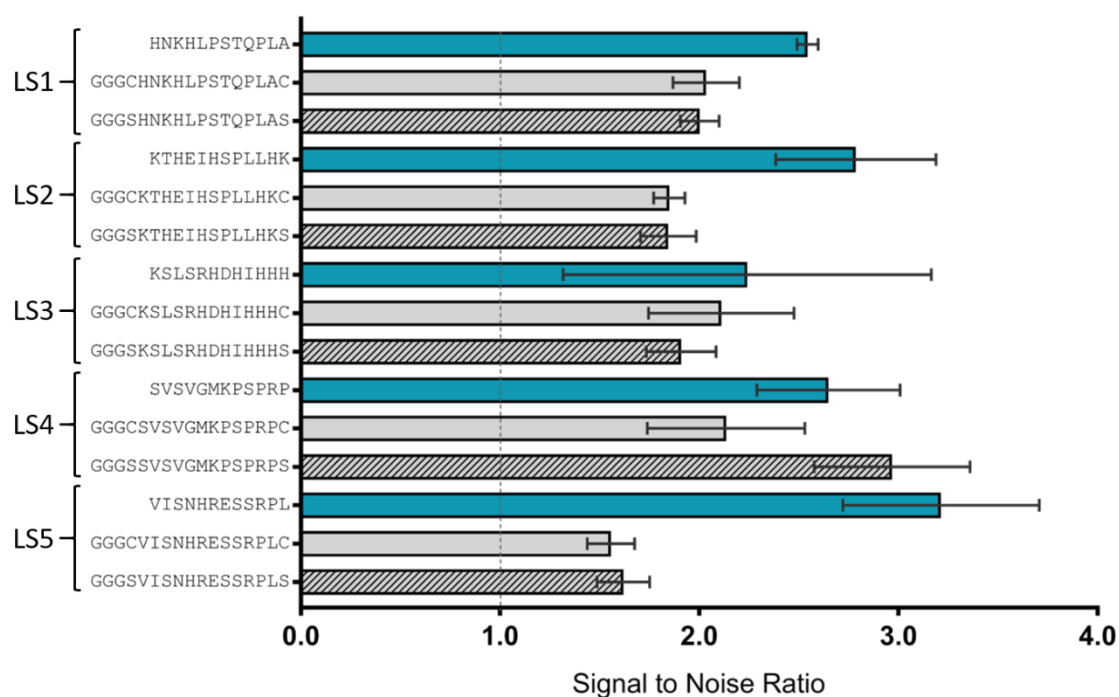


Figure 6.1.15 - Comparison of cyclic and linear lead peptide sequences. Teal - lead peptide sequence, diagonal striped - constrained in a loop and grey – corresponding sequence with cysteines replaced with serine. Dotted grey line represents background noise.

Scrambling, reversal and cyclisation of peptides has only been carried out for nanoparticle binding; this is because the results obtained from particle binding indicate that these transformations have not had a significant effect on the peptides ability to bind NPs. It is also difficult to confirm whether peptides have successfully cyclised and not just formed a disulphide bridge with another peptide.

6.2 METAL ION BINDING

Co^{2+} and Pt^{2+} solutions were used to screen against peptide arrays containing alanine scanning, truncation, positional scanning and high frequency peptide sequences. However, screening against Co^{2+} did not yield any results as after incubating the membrane in Co^{2+} solution overnight and imaging, all spots had an intensity less than background noise, as can be seen in Figure 6.2.1. The dark spots on the membrane come from the sequence EQKLISEEDL, this sequence was used as a negative control for NP binding as it should not bind to CoPt NPs. On all previous screening carried out this sequence has had a SNR value of around 1 suggesting that it binds as well as background noise and so has low affinity to CoPt NPs. It is unexpected that the majority of peptides would not bind to Co^{2+} and so different Co^{2+} salts were screened. Cobalt (II) sulphate was originally used to screen against the membrane as this is the Co complex that is used in the synthesis of CoPt NPs. However, to ensure that this was not causing issues with the membrane cobalt (II) chloride was used but this gave the same result as seen for cobalt (II) sulphate. Following this, the pH of the Co^{2+} solutions were checked and a pH of ≈ 3 was observed. This is typical for Co^{2+} and is the same pH observed in a synthesis reaction before reducing agent is added and ideally this is the pH screening should be carried out at. As the majority of spots have a much lighter intensity than the background this suggests that the Co^{2+} is being repelled away from the peptides and surface of the membrane. Whereas if Co^{2+} was binding poorly to the peptides, then this would result in peptide spots appearing with similar intensity to the background. As a result of this only binding data for Pt^{2+} is discussed in detail here.

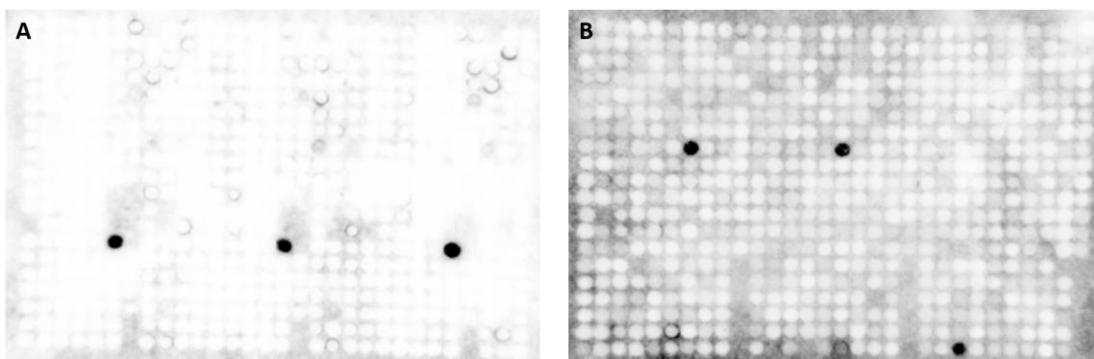


Figure 6.2.1 - Peptide arrays that have been incubated in Co^{2+} solution overnight to assess binding. A) Cobalt (II) sulphate used and B) Cobalt (II) chloride used.

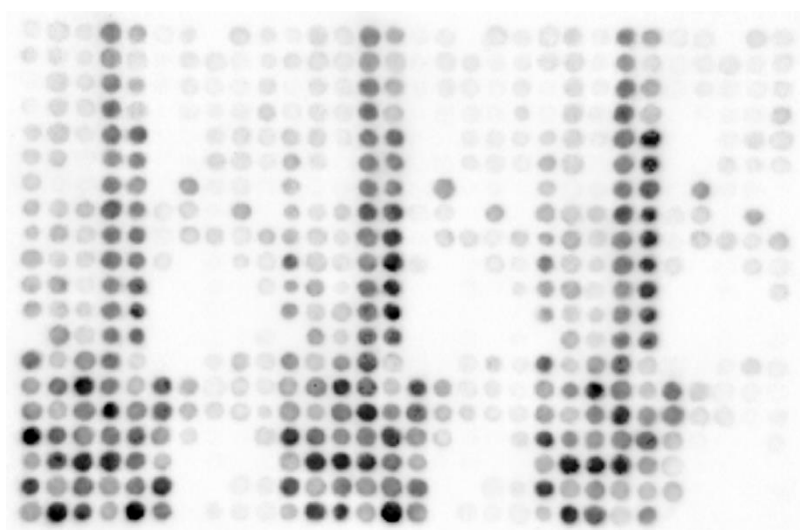


Figure 6.2.2 – Peptide array that was incubated in Pt^{2+} solution overnight to assess binding.

6.2.1 LEAD SEQUENCES

All five lead sequences were screened against Pt^{2+} and the results can be seen in Figure 6.2.3. LS3 has the highest intensity when binding to Pt^{2+} , followed by LS1. LS2 has the third highest intensity but is almost three times less than LS3. LS4, which had the highest intensity when binding to NPs, is now fourth and LS5 has the lowest intensity of all five sequences. This suggests that this sequence is not favourable for binding to Pt^{2+} compared to the other four sequences.

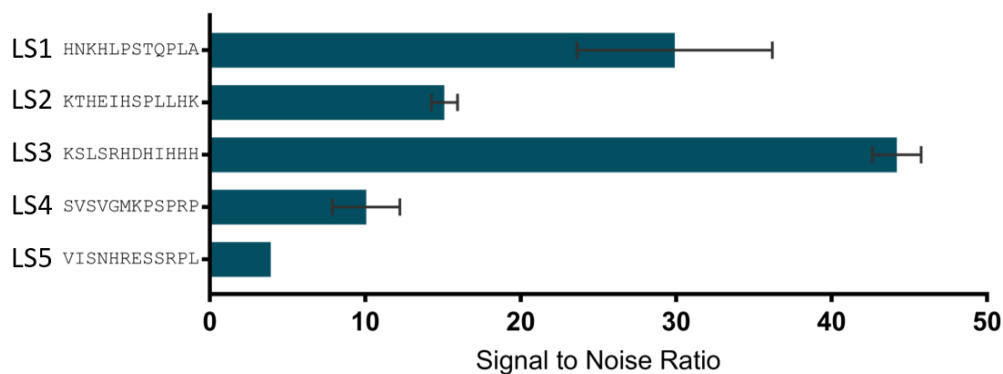


Figure 6.2.3 – SNR data for all five lead sequences screened against Pt²⁺.

6.2.2 ALANINE SCANNING

Data for LS1 shows that there are six sequences where a reduction in SNR is observed, the most significant of these is when lysine is replaced for alanine. Replacement of both histidine residues with alanine also resulted in reduced binding. As well as replacement of asparagine, leucine and serine with alanine. Therefore, these residues are important for binding to Pt²⁺. Basic residues such as lysine and histidine were identified from screening against NPs and so this data matches well.

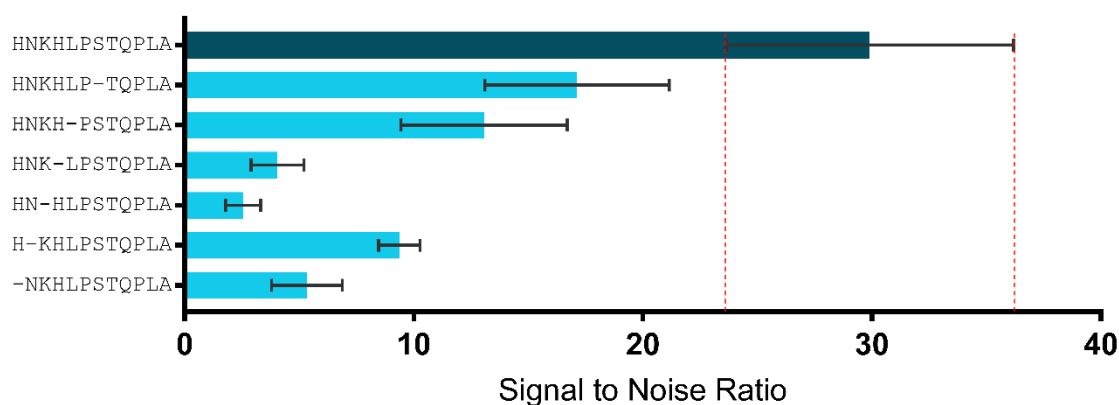


Figure 6.2.4 - Alanine scanning data for LS1. Dark green - lead peptide sequence and light blue - sequences that have decreased SNR.

Alanine scanning for LS2 results in eight sequences that have increased SNR values and one that shows a significant decrease. The significant decrease is observed when lysine (position 1) is substituted with alanine. However, when lysine (position 12) is substituted with alanine an increase in binding is observed and this is unexpected as lysine was previously highlighted as important from screening against NPs. Replacement of E, I, S, P, L, L and H also resulted in an increase in SNR however as the error bars on these residues are very large it is difficult to say how significant this increase is. Therefore, the alanine scanning data will need to be considered in combination with truncation and positional scanning data to see if the trends observed here are true.

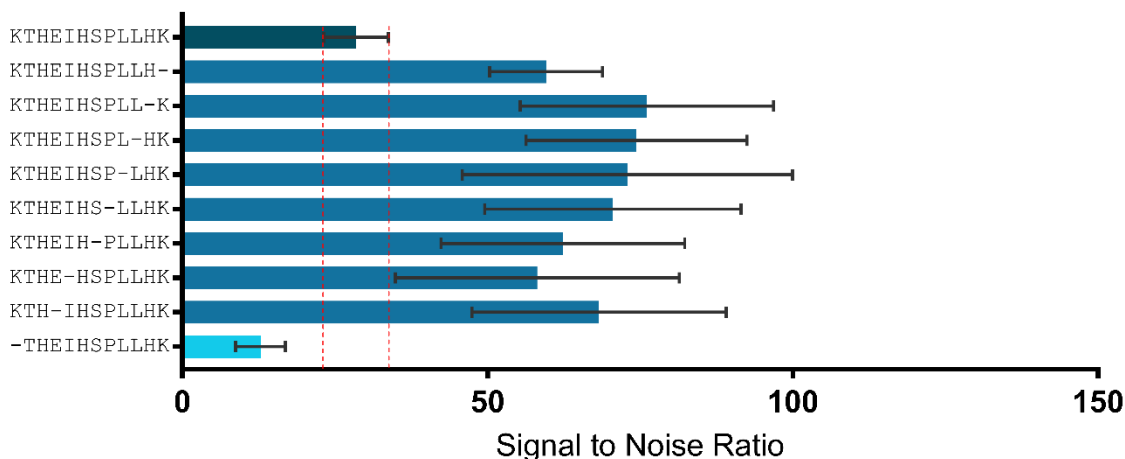


Figure 6.2.5 - Alanine scanning data for LS2. Dark green – LS2, dark blue - increased SNR and light blue - decreased SNR.

Alanine scanning carried out for LS3 resulted in all substitutions having SNR values that were similar to LS3. Therefore, this suggests that swapping out one amino acid did not have a dramatic effect on the peptides ability to bind to Pt^{2+} and that there is not one amino acid in particular that is responsible for binding and so a combination of amino acids is responsible for binding. Further analysis is required to identify which regions of LS3 are important for binding to Pt^{2+} .

Data for LS4 resulted in three sequences that show an increase in SNR and one with decreased SNR compared to LS4. The significant decrease was observed from substitution of methionine with alanine and so this suggests that methionine is important for binding to Pt^{2+} . The three sequences that show an increase in binding involve substitution of proline with alanine, as every time proline is removed an increase in SNR is observed this suggests that proline is unfavourable for binding to Pt^{2+} .

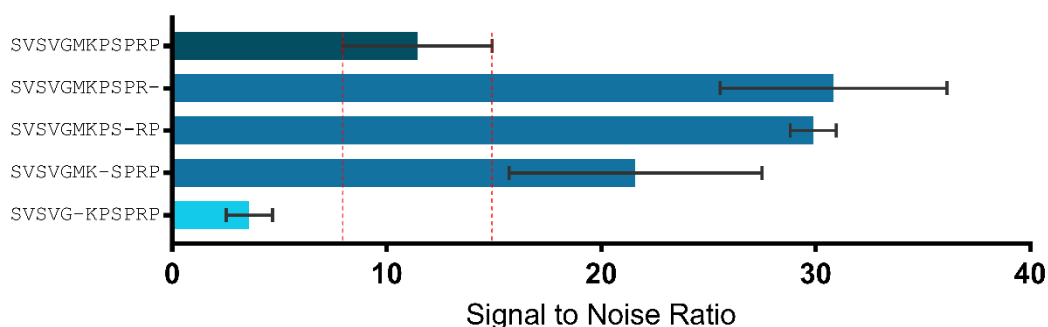


Figure 6.2.6 - Alanine scanning data for LS4. Dark green – LS4, dark blue - increased SNR and light blue - decreased SNR.

Finally, alanine scanning data for LS5 has identified five replacements that result in increased SNR and only one that has reduced SNR. This reduction in SNR is observed when histidine is replaced with alanine, the amine present in the side chain of histidine is likely to be

responsible for binding to Pt^{2+} and so removal of this results in decreased binding. Increases in SNR are observed when E, S, S, P and L are substituted with alanine. The most significant increase is when glutamic acid is substituted for alanine, this suggests that glutamic acid is not favourable for binding to Pt^{2+} . As glutamic acid is a hard ligand it is unlikely to interact strongly with a soft metal centre such as Pt^{2+} and this explains why removal of glutamic acid results in increased binding.

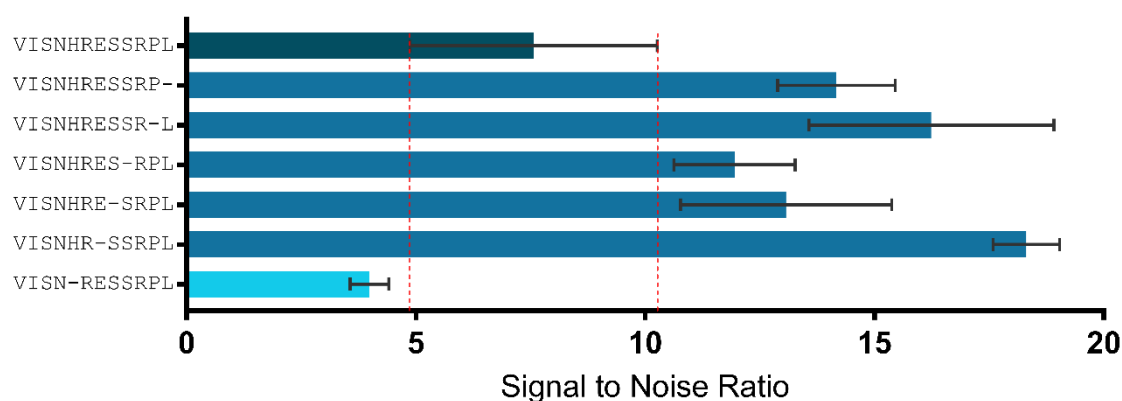


Figure 6.2.7 - Alanine scanning data for LS5. Dark green - lead peptide sequence, dark blue - increased SNR and light blue - decreased SNR.

6.2.3 TRUNCATION

Truncations were performed on all five lead peptide sequences to identify if there are any particular regions of the peptides that are important for binding to Pt^{2+} . In general, truncation of all five lead peptide sequences led to sequences that had significantly reduced binding compared to the lead. However, there are some sequences that show similar or increased binding to the lead and the data has also allowed for trends in each of the peptides to be identified.

Starting with LS1 it can be observed that three sequences have similar binding compared to LS1 and all others are significantly reduced. The sequences HNKHLPS, HNKHLP and HNKHL all have a similar intensity to LS1, as there are similarities between these three sequences this could suggest that this region of the peptide is important for binding to Pt^{2+} . The sequences that have the least reduced SNR values compared to LS1 are highlighted in red in Figure 6.2.8. All of these sequences have a lysine residue present whereas sequences that do not contain lysine have a significant reduction in SNR and so the presence of lysine in the sequence is important for binding to Pt^{2+} . This trend was also identified from truncation data collected from screening against CoPt NPs. As all three sequences that have similar intensity to LS1 contain histidine at the start of the sequence, when this histidine residue is removed a significant reduction in SNR is observed. This could suggest that histidine at the start of the peptide sequence is important for binding to Pt^{2+} . However, sequences such as HLPSTQPLA,

HLPSTQPL, HLPSTQ and HLPST all contain histidine at the start of the sequence and have significantly reduced SNR values compared to LS1. This reduction in SNR is likely to be caused by a decrease in charge density. Sequences HNKHLPS, HNKLP and HNKHL all have an overall charge on the peptide of +3 whereas sequences HLPSTQPLA, HLPSTQPL, HLPSTQ and HLPST all have an overall charge of +1. The overall charge is then divided by the length of the peptide resulting in charge density which can be seen in Table 6.2.1. From this data it is observed that sequences with a higher charge density have a much higher SNR value and so result in increased binding to Pt²⁺.

Table 6.2.1 – Calculated charge densities for truncated peptides related to their SNR values.

Sequence	Overall Charge	Peptide Length	Charge Density	SNR
HNKHLPS	+3	7	0.43	27.1
HNKHL P	+3	6	0.50	23.3
HNKHL	+3	5	0.60	34.2
HLPSTQPLA	+1	9	0.11	1.36
HLPSTQPL	+1	8	0.13	1.65
HLPSTQ	+1	6	0.17	1.52
HLPST	+1	5	0.20	0.96

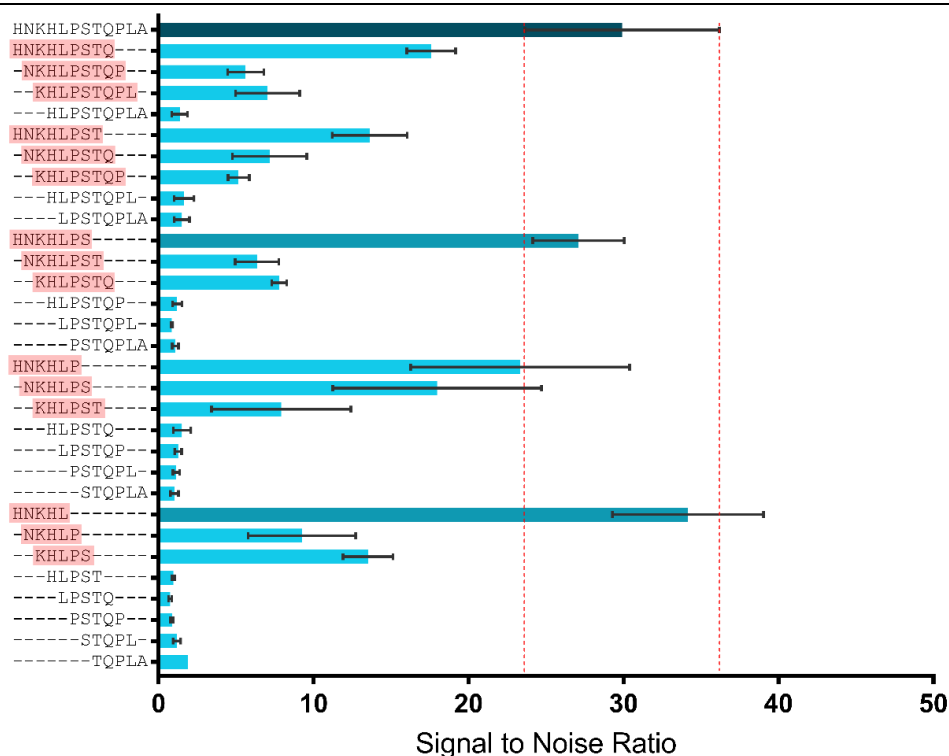


Figure 6.2.8 – Truncation data for LS1. Dark green – LS1, teal - similar SNR to lead sequence and light blue - decreased SNR.

Truncation of LS2 resulted in all truncated sequences having significantly reduced SNR compared to LS2. Therefore, suggesting that the full-length peptide sequence is preferred for binding to Pt²⁺. However, there are a few notable sequences which have been highlighted in red in Figure 6.2.9, these highlighted sequences have the least reduced SNR compared to

the lead. In each of these sequences' lysine is present at one end of the peptide, when this lysine residue is removed a significant reduction in SNR is observed suggesting that lysine is important for binding to Pt^{2+} . This trend was observed from NP screening data. Sequences HSPLLH, THEIH and HEIHS have a similar intensity to sequences SPLLHK and KTHEI. It is possible that although these sequences do not contain lysine, they have a similar intensity due to the presence of two histidine residues and either end of the sequence. As lysine and histidine are both basic residues this could account for the similar intensity observed. It is possible that the reason LS2 has a much higher SNR value compared to all truncated sequences is due to the presence of two lysine residues at either end of the peptide which is not achieved in any of the truncated peptides.

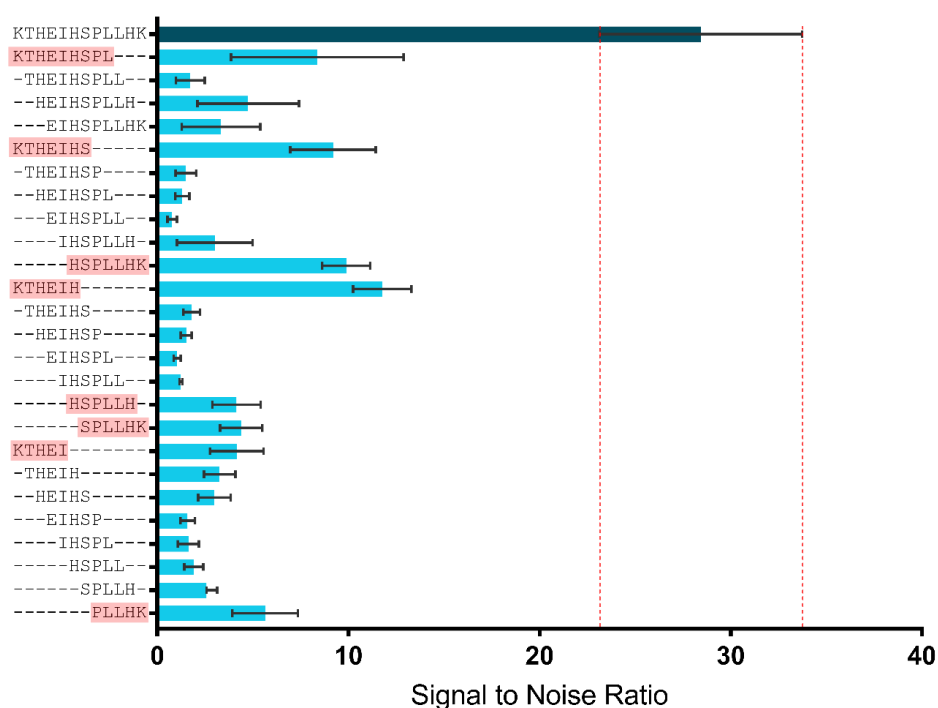


Figure 6.2.9 - Truncation data for LS2. Dark green – LS2 and light blue - decreased SNR.

Truncation of LS3 resulted in all but two sequences having decreased SNR compared to the lead. The two sequences that have increased or similar SNR to the lead are SRHDHIIHH and RHDHIIHH. Both of these sequences contain five histidine residues suggesting these residues are be important for binding to Pt^{2+} . Sequences that do not contain a large number of histidine residues are more significantly reduced compared to LS3 and so histidine could be responsible for the peptides binding ability to Pt^{2+} .

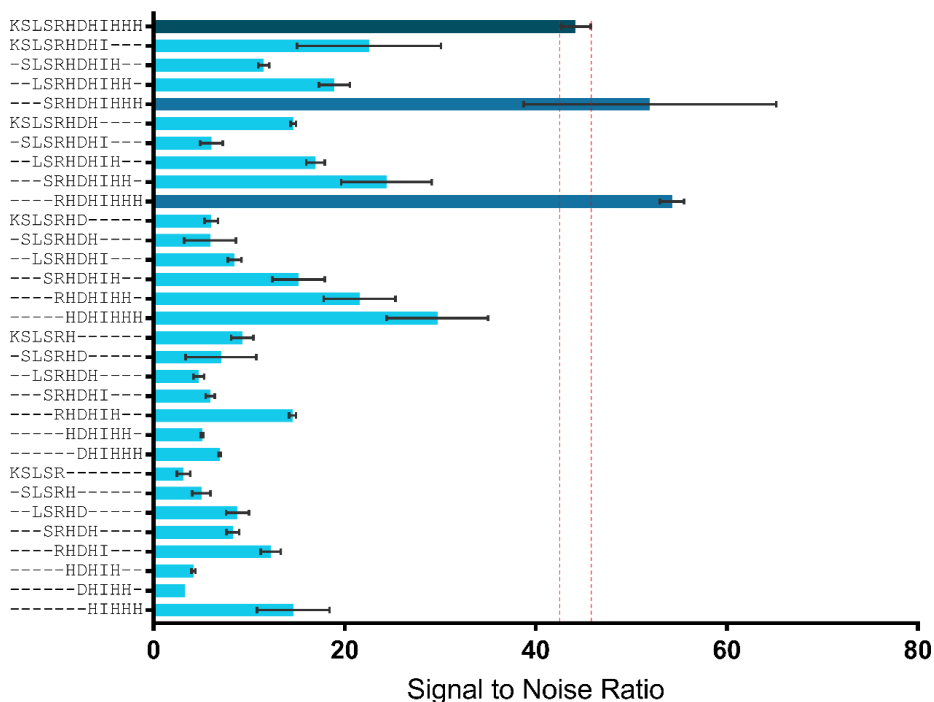


Figure 6.2.10 - Truncation data for LS3. Dark green – LS3, dark blue - increased SNR and light blue - decreased SNR.

Truncation of LS4 resulted in most sequences having an increased SNR compared to LS4. The increased sequences all contained the region of the peptide, SVGMKP or SVGMK, these sequences are highlighted in red in Figure 6.2.11 below. This suggests that this region of the peptide is important for binding to Pt²⁺. Another key trend that can be identified from the truncation data is the importance of methionine. In part b of Figure 6.2.11, it can be seen that removal of methionine from the peptide sequence results in a significant decrease in binding, this is the case when methionine is removed from either end of the peptide. Alanine scanning of this lead peptide also identified methionine as being important for binding as well as positional scanning data collected from screening against CoPt NPs.

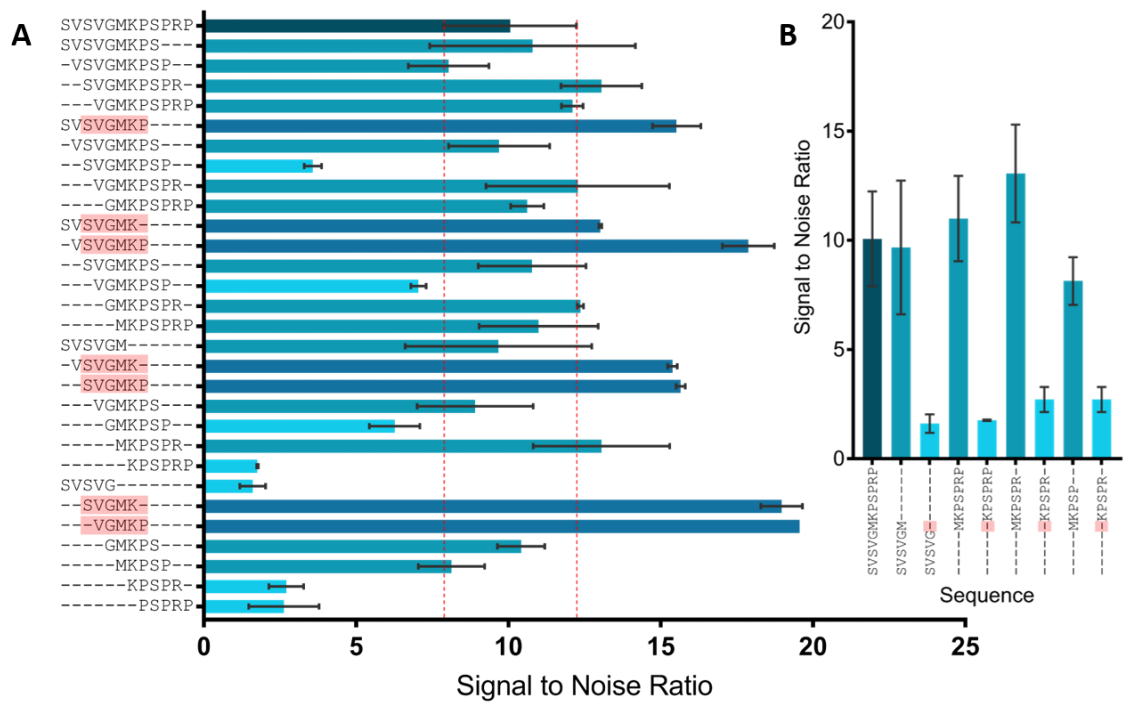


Figure 6.2.11 - A) Truncation data for LS4 and B) Truncation data highlighting the importance of methionine. Dark green – LS4, teal - similar SNR to lead, dark blue - increased SNR and light blue - decreased SNR.

Truncation data for LS5 resulted in a large proportion of sequences that have a similar SNR to LS5. LS5 has the lowest SNR compared to the other lead sequences for binding to Pt^{2+} and the error bars are very large for some of the sequences. Therefore, this makes it difficult to draw many conclusions from the truncation data for LS5.

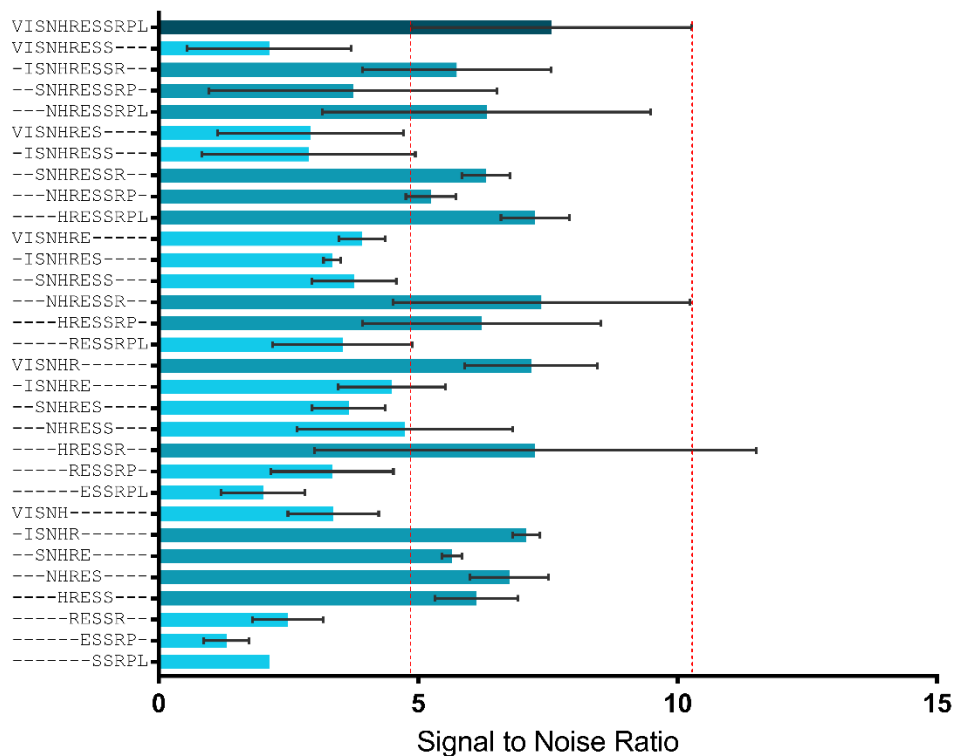


Figure 6.2.12 - Truncation data for LS5. Dark green – LS5, teal - similar SNR to lead and light blue - decreased SNR.

6.2.4 POSITIONAL SCANNING

Positional scanning was carried out for four of the lead peptides and the data is summarised here based on the overall effects that have been observed. The first trend that was observed from positional scanning is the incorporation of methionine into the lead sequences and this can be seen in Figure 6.2.13. This was observed for all four LS and a very significant increase in SNR is observed when methionine is substituted into the sequences. This increase is observed no matter what amino acid is being replaced as acidic, basic and hydrophobic residues are replaced and a large increase in SNR is observed for all.

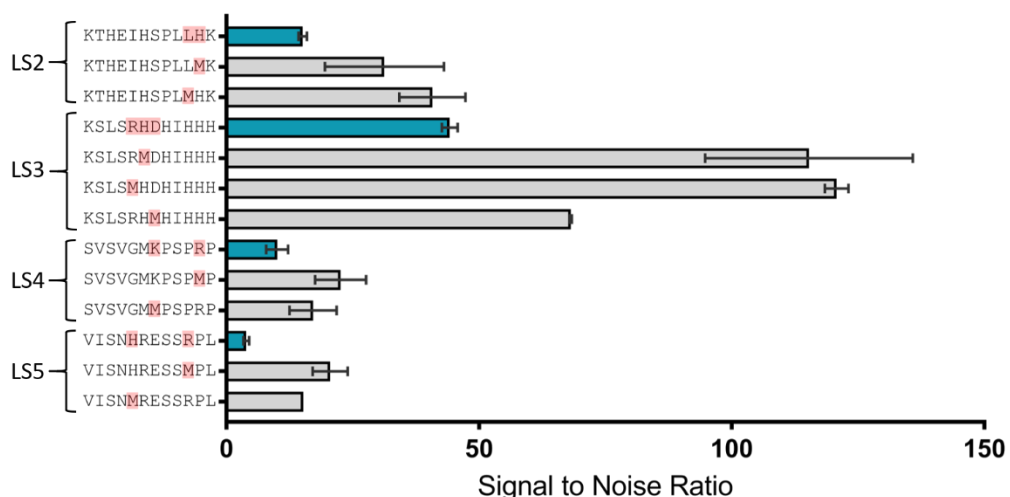


Figure 6.2.13 - Positional scanning data highlighting the importance of methionine for binding to Pt^{2+} . Teal - lead peptide sequences, grey - sequences where methionine has been incorporated. Red boxes highlighted the amino acid residues that have been substituted.

The second trend that was observed is the incorporation of lysine and histidine residues into the sequence. Again, this trend was observed from all four lead peptide sequences and the data can be seen in Figure 6.2.14. For LS2 leucine and histidine (positions 10 and 11) were substituted with lysine and histidine. The largest increase was observed when hydrophobic leucine was substituted for basic lysine, the amine group that is present in lysines side chain is more likely to interact with Pt^{2+} than the aliphatic carbon chain present in leucine. A similar increase is seen when leucine is substituted for histidine. Histidine has an imidazole ring as part of its side chain and so this is likely to act as a soft donor ligand and interact with the soft Pt^{2+} . Replacement of histidine in LS2 with lysine results in a slight increase in SNR, from previous screening (NP binding) lysine has been identified as the most important residue for binding whereas histidine is important for binding when there are multiple residues together. Therefore, this could account for the increase observed when histidine is replaced with lysine.

In LS3 arginine, histidine and aspartic acid (positions 5, 6 and 7) were replaced with lysine and histidine residues. Replacement of arginine and histidine with lysine resulted in a significant increase in SNR. Although all three are basic residues, a preference for lysine is observed and this could be due to lysine having a simpler side chain. Lysine has an amine group at the end of its side chain, whereas histidine has an imidazole ring and arginine a guanidino group, both of which are more sterically bulky than the side chain of lysine. It is possible that this would then make lysines side chain more accessible for binding to Pt^{2+} . When aspartic acid, a negatively charged residue, was replaced with lysine and histidine a significant increase in SNR was observed. Pt^{2+} is a soft acid and so will prefer to react with

soft or intermediate ligands, the carboxylic acid group present in glutamic acids side chain is likely to act as a hard ligand. Whereas the amine groups present in lysine and histidine will act as an intermediate ligand. This could suggest why an increase in SNR is observed when replacing glutamic acid for lysine or histidine.

Only one substitution that involved lysine and histidine, and gave a significant change in SNR, was observed for LS4. Substitution of lysine with histidine resulted in a slight increase in SNR, as only the structure of the side chains is different here, but functionality of the side chains remains the same so a dramatic increase would not be expected. Only one significant substitution is observed for LS5 and this was that replacement of arginine with histidine resulted in increased binding.

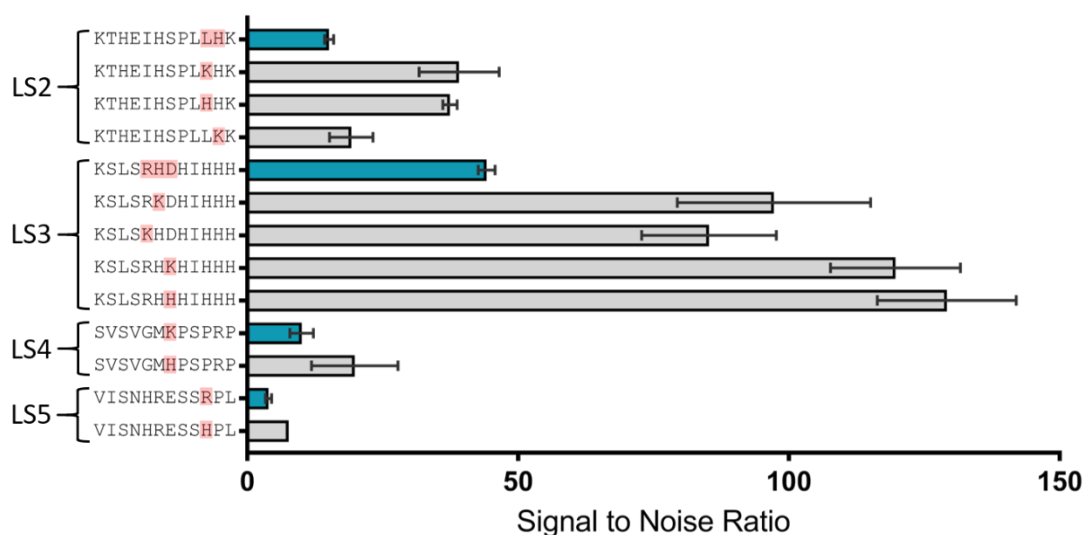


Figure 6.2.14 - Positional scanning data highlighting the importance of lysine and histidine. Teal - lead peptide sequences, grey - sequences where lysine and histidine has been incorporated. Red boxes highlighted the amino acid residues that have been substituted.

The final trend observed from the positional scanning data was the adverse effect of glutamic acid. However, this trend was only observed for LS2 and LS3 and can be seen in Figure 6.2.15. In LS2 leucine and histidine (positions 10 and 11) were replaced for glutamic acid and in both cases a significant reduction in binding was observed. Replacement of histidine with glutamic acid involves going from a positive charge to a negative charge and so it is likely that this swapping in charge had an adverse effect on binding. Leucine is a hydrophobic amino acid and so is unlikely to be involved directly with binding. It is possible that leucine could act as a spacer residue and removal of this results in the conformation of the peptide changing. However, it is more likely that the dramatic decrease observed is from the incorporation of glutamic acid.

In LS3 arginine, histidine and aspartic acid (positions 5, 6 and 7) were substituted with glutamic acid. Replacement of arginine and histidine resulted in a significant decrease in SNR. However, when aspartic acid was replaced with glutamic acid an increase in SNR was observed. This could suggest that, although acidic amino acids seem to be unfavourable for binding, if one is already present in the sequence it could be favourable to swap this for glutamic acid rather than aspartic acid for binding to Pt^{2+} . However, further testing would be required to ensure this is the case as aspartic acid is only present in one of the five lead peptide sequences.

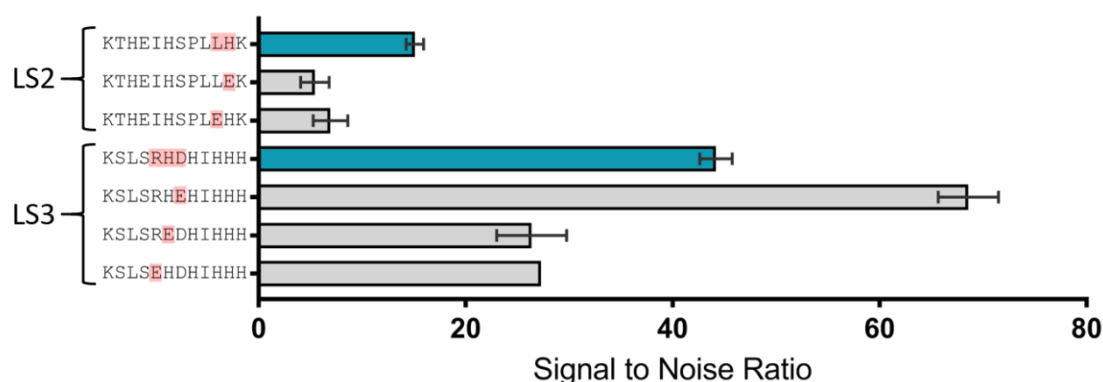


Figure 6.2.15 - Positional scanning data for the incorporation of glutamic acid. Teal - lead peptide sequences, grey - sequences where glutamic acid has been incorporated. Red boxes highlighted the amino acid residues that have been substituted.

6.2.5 HIGH FREQUENCY

Signal to noise ratio data for the high frequency screening can be seen in Table 6.2.2. There are 17 sequences that show decreased SNR compared to the lead high frequency peptide (HHSSPKLR) and 15 sequences that show an increase in SNR. Sequences that showed an increase or decrease in SNR were plotted graphically (Figure 6.2.16) so only those that show a significant change in SNR can be identified. This resulted in nine sequences with a significant increase in SNR and thirteen sequences with a significant decrease. Those that show an increase in binding are where lysine has been substituted in place of the original amino acids and those that show a decrease in binding are where substitution for proline or leucine has taken place. Lysine was identified as being important from truncation and positional scanning data from screening against Pt^{2+} as well screening carried out against NPs. Proline and leucine are both hydrophobic residues and therefore less likely to be involved in binding. The overall charge on the peptide has been calculated and plotted against the SNR values and can be seen in the inset graph in Figure 6.2.16. Generally, it can be noted that sequences with a higher SNR have a higher overall peptide charge, and those with lower SNR values have a lower overall peptide charge. This suggests that a higher overall

charge on the peptide results in increased binding to Pt^{2+} and could also explain why the incorporation of lysine, histidine and arginine into the sequence results in increased binding.

All nine increased sequences also have a much higher SNR values compared to the original five lead sequences, this suggests that they bind to Pt^{2+} with very high affinity and that this combination of amino acids is important. However, the overall increase in SNR is not as large as some of the increases observed from positional scanning data especially from the incorporation of methionine and lysine.

Table 6.2.2 - Signal to noise ratio compared to the lead high frequency peptide (HHSSPKLR). Green represents SNR increased by more than 10, red represents SNR decreased by more than 10 and grey represents sequences that have similar intensity to the lead.

	H	H	S	S	P	K	L	R
H	-	-	31.8	-0.6	10.6	-16.4	18.3	5.5
S	-20.0	-26.8	-	-	3.7	-27.2	-2.0	-18.8
P	-14.5	-31.7	-21.6	-10.2	-	-36.9	35.0	-30.4
K	32.7	-3.3	37.7	37.4	38.5	-	38.5	-0.3
L	-21.5	-26.5	-11.4	-21.5	0.1	-29.2	-	-21.2
R	21.0	1.8	37.7	19.0	33.5	-8.6	10.0	-

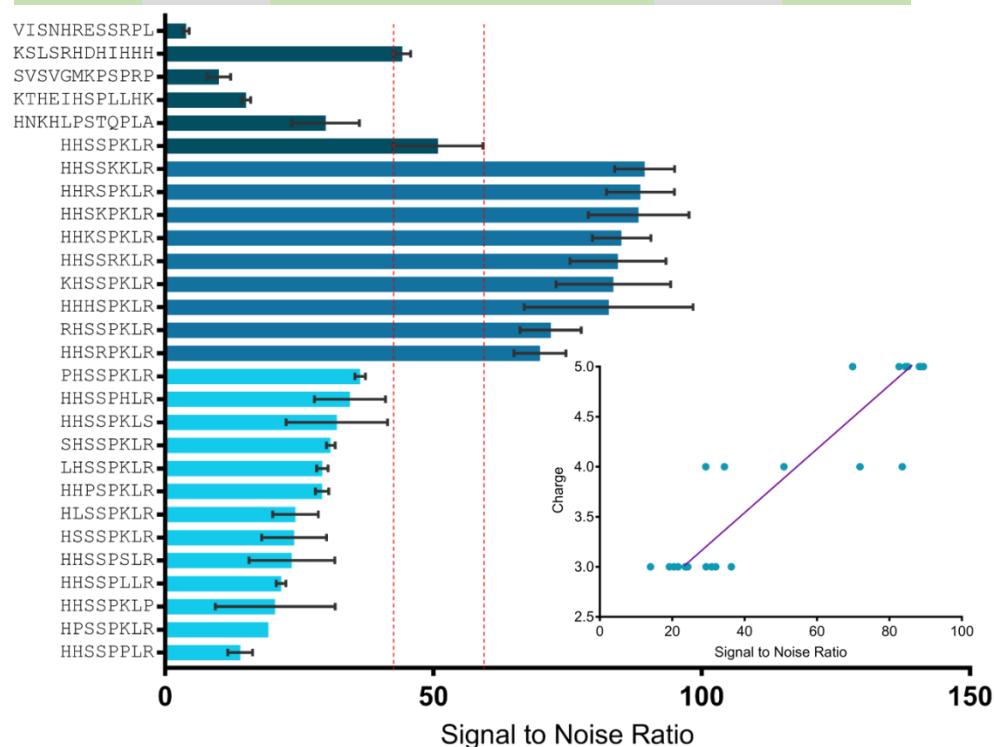


Figure 6.2.16 - Signal to noise ratio for high frequency screening. Dark green - lead peptide sequences, dark blue - increased SNR and light blue - decreased SNR. Inset figure highlights charge plotted against SNR values, purple line highlights increasing SNR relates to higher overall charge.

6.3 SCREENING AGAINST A SYNTHESIS REACTION

The final stage of the screening process was to screen the peptide arrays against a CoPt synthesis reaction. As the lead sequences were designed for use in the synthesis of CoPt NPs

this is an important stage of the screening and will allow identification of any differences in sequences compared to particle binding and metal ion binding. However, incorporation of the peptide arrays into a synthesis reaction was difficult to ensure that NP binding and synthesis was consistent across the array.

There were some areas of the arrays that had more background noise, even with different washing procedures this was hard to eliminate and as such some sets of data have large error bars. The resulting arrays produced from this screening can be seen in Figure 6.3.1. Due to the problems with high background noise no conclusions could be drawn from the alanine scanning, the high frequency array and only some of the lead sequences are discussed for truncation and positional scanning.

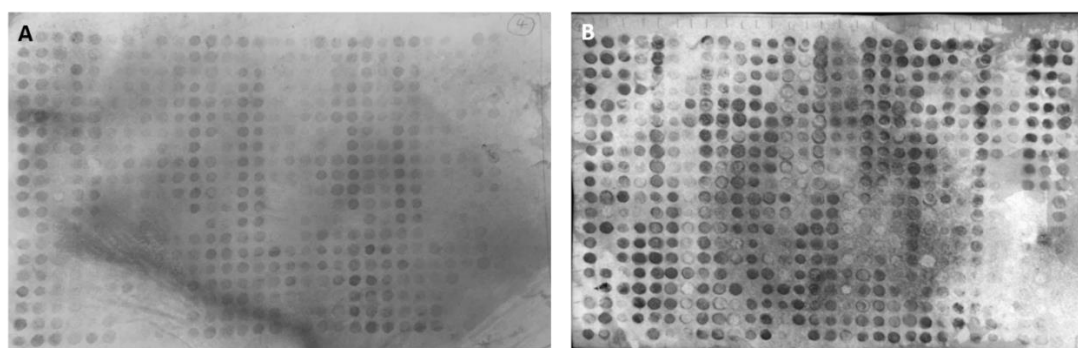


Figure 6.3.1 - Synthesis arrays for screening against a CoPt synthesis reaction. A) 1st generation peptide array and B) 2nd generation peptide array

6.3.1 LEAD SEQUENCES

All five lead sequences were screened against an CoPt synthesis reaction (Figure 6.3.2). LS1, LS2, LS3 and LS4 all have very similar intensities from this screening although error bars for LS3 and LS4 are large. LS5 has the lowest intensity and a value close to 1, suggesting that a similar level of binding to background noise is occurring. This sequence was also unfavourable for Pt²⁺ binding suggesting that this sequence may not be ideal to use in an CoPt synthesis reaction.

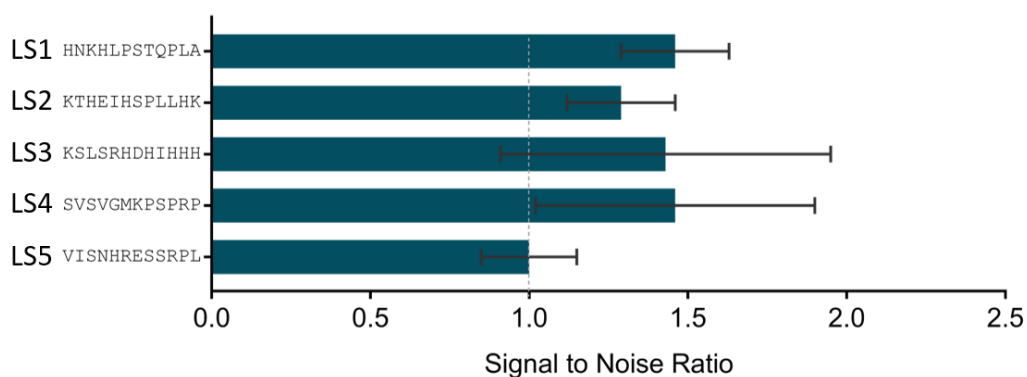


Figure 6.3.2 – SNR data for all five lead sequences screened against a CoPt synthesis reaction. Dotted grey line represents background noise.

6.3.2 TRUNCATION

Truncation was carried out for all five lead peptide sequences, however due to the nature of the screening method the majority of sequences had very large error bars or similar SNR to the lead peptide. This was the case for LS1, LS2, LS4 and LS5 as all sequences had a similar intensity to the original sequence, and they all had SNR values of ≈ 1 which suggests that peptide spots were of similar intensity to background noise.

Truncation of LS3 resulted in five sequences having similar SNR values to the original peptide, all of these sequences contain the region KLSLRHD, which is the start of the peptide. These sequences also have the highest SNR values carried out from screening against a CoPt synthesis reaction suggesting that this region could play an important role in a synthesis reaction. Sequences that have decreased SNR compared to the original sequences contain the region, DHIH, which is at the opposite end of the peptide. Therefore, it is likely that this region is not essential during the synthesis of CoPt NPs. Previously, for metal binding the presence of more histidine residues resulted in higher binding ability of the peptides. However, these regions were also found to be unfavourable from truncation data for binding to CoPt NPs.

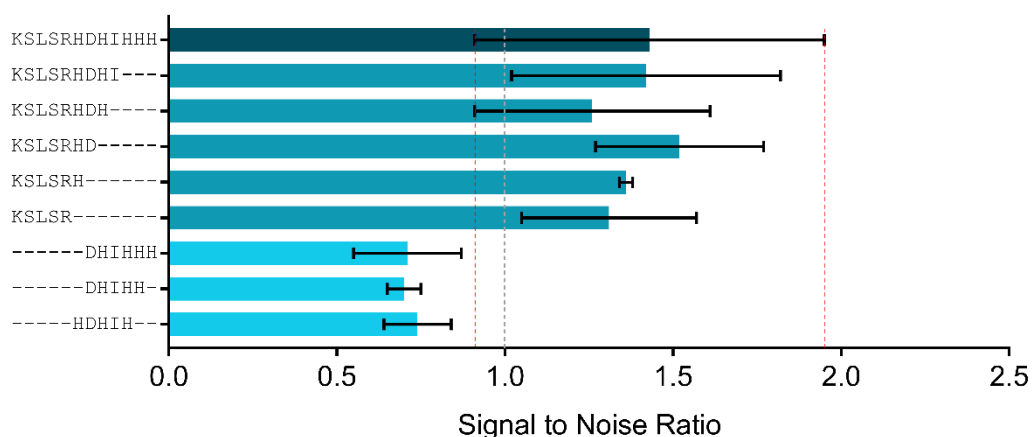


Figure 6.3.3 - Truncation data for LS3. Dark green - lead peptide sequence, teal - similar SNR to the lead and light blue - reduced SNR. Grey dotted line represents background noise.

6.3.3 POSITIONAL SCANNING

For LS3 and LS4 the same trend was observed that replacement of basic residues (arginine and lysine) with an acidic residue (glutamic acid) resulted in decreased SNR values. This trend has been observed from screening carried out against NPs and Pt²⁺. The same trend is now identified from screening against a synthesis reaction and it strongly suggests that glutamic acid is unfavourable in all aspects involved in the synthesis of CoPt NPs.

For LS5 several reductions in SNR were observed and these occurred when arginine was substituted with methionine, serine, proline and leucine and when histidine was replaced with isoleucine. The majority of these reductions in binding are to be expected as histidine and arginine are being replaced with hydrophobic or polar residues (serine, proline, leucine and isoleucine). Arginine and histidine have been highlighted as important residues from previous screening (NP and metal ion binding). It is unexpected that replacement of arginine with methionine results in decreased binding as from previous screening carried out incorporation of methionine has resulted in a significant increase in SNR. The only increase in SNR that is observed is when histidine is substituted for lysine, this increase is not significantly large and is to be expected when swapping between similar amino acids.

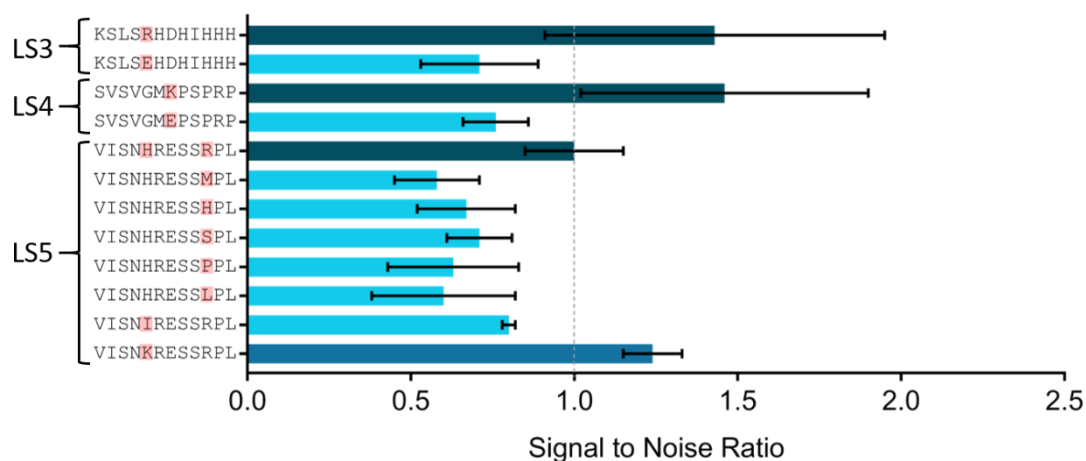


Figure 6.3.4 - Positional scanning data for LS3, LS4 and LS5. Dark green - lead peptide sequence, dark blue - increased SNR and light blue - decreased SNR.

6.3.4 HIGH FREQUENCY

The same high frequency array as used in previous screening has been screened against a CoPt synthesis reaction. Although the high frequency sequences have shown promising results from screening against CoPt NPs and Pt²⁺ this was not the case when screening against a synthesis reaction. All sequences have SNR values of less than 1, and therefore the peptide spots relating to these sequences have intensities similar to that of background noise which suggests that these sequences may not be suitable for use in a synthesis reaction.

6.4 SUMMARY AND DISCUSSION

Screening against CoPt NPs, Pt²⁺ and a CoPt synthesis reaction has resulted in a large amount of data generated and from this it is possible to identify key trends, and these are: the importance of basic residues, overall charge on the peptide, importance of methionine, the effect of proline, the impact of acidic residues and peptide length.

Basic residues

The first key trend identified was the importance of basic residues. Throughout all three types of screening the presence of basic residues, such as lysine, arginine and histidine have been highlighted as important residues. Truncation data collected from screening against NPs for LS1, LS2 and LS4 identified the importance of lysine. Truncated sequences that did not contain lysine had significantly reduced SNR values compared to the LS. For LS1 and LS2 this was the case regardless of the position of lysine in the peptide sequence, but for LS4 when lysine was in the middle of the peptide sequence a reduced SNR was observed. Only when lysine was present at the end of the sequence, for LS4, were increased SNR values achieved. Truncation of LS4 also highlighted the importance of arginine, when arginine was removed from the end of the peptide sequence a significant reduction in SNR was observed.

Positional scanning data for LS5 also highlighted the importance of lysine, as replacement of arginine and histidine with lysine resulted in increased SNR. This could suggest that lysine is preferred for binding to CoPt NPs over arginine and histidine. The preference for lysine is likely to arise from the different side chain properties of the three residues. Histidine contains an imidazole ring; arginine has an aliphatic carbon chain ending in a guanidino group and lysine has an aliphatic carbon chain ending in an amine group. Lysine has the least sterically bulky side chain and it is possible that this results in increased interaction between the NPs and the side chain of lysine.

Data collected from screening peptide arrays against Pt^{2+} also highlighted the importance of lysine. For LS1 and LS2 only truncated sequences that contained lysine had a similar intensity to the LS. Truncation of LS3 highlighted the importance of histidine as only truncated sequences containing a large number of histidine residues had similar or increased intensity compared to LS3. Positional scanning also highlighted the importance of lysine, when lysine was substituted for any amino acid a significant increase in SNR was observed. This was the case for LS2, LS3, LS4 and LS5.

Data collected from screening against a synthesis reaction also highlighted the importance of basic residues. Positional scanning carried out for LS3 and LS4 highlighted that when a basic residue was swapped for an acidic residue a significant decrease in SNR was observed. For LS5 when any basic residues were replaced a significant decrease in binding intensity was observed.

From literature it is known that amino acids that have a positively charged side chain bind well to magnetite NPs with a higher affinity than uncharged residues.¹⁶³ Although this screening was carried out for magnetite NPs it could explain why a preference for basic residues is observed when binding to CoPt NPs. Another factor is that lysine is known to be an excellent ligand for Pt complexes due to the role it plays in binding HMG domain proteins to Pt/DNA complexes in cisplatin.¹⁶⁴ Histidine is also known to play a role in the action of cisplatin, cisplatin preferentially binds to the nitrogen atom of the imidazole ring in histidine.^{165,166} Histidine has also been used for many years in protein purification by the incorporation of a polyhistidine affinity tag into the protein being purified. The polyhistidine tag can then bind to a resin of either Ni^{2+} or Co^{2+} for simple purification of the desired protein.¹⁶⁷ As there are many known examples of basic residues interacting with MNPs, Co and Pt in literature this could help to explain why a preference for these residues has been identified through screening carried out here.

Overall charge

The overall charge on the peptide seems to play a role when binding to Pt²⁺, this has been identified from the high frequency screening. Where it was observed that, in general, the higher the overall peptide charge, the higher the binding. This could suggest that highly charged peptides are favourable for binding to Pt²⁺. Positive charge on the peptide is obtained via the inclusion of basic residues and so this suggests another reason why a preference for basic residues is observed. As well as the side chains of basic residues being favourable for binding it is possible that the increased overall charge could increase the peptides binding ability also.

Importance of methionine

Methionine was also identified as a key residue from screening against CoPt NPs and Pt²⁺. Positional scanning data, collected from screening against CoPt NPs, for LS3 highlighted the importance of incorporation of methionine into the sequence. An increase in SNR was observed when arginine was replaced with methionine. However, this is the only case of incorporation of methionine resulting in a significant increase in SNR for NP binding. Pt²⁺ data highlights the importance of methionine, from alanine scanning of LS4. Replacement of methionine with alanine results in a significant reduction in SNR suggesting that methionine is an important residue for binding to Pt²⁺. Truncation data for LS4 also supported this, when sequences were truncated so that methionine was removed a significant reduction in binding was observed. Positional scanning data for LS2, LS3, LS4 and LS5 showed that incorporation of methionine into these sequences resulted in a significant increase in SNR. This increase was observed no matter what amino acid was replaced as acidic, basic and hydrophobic residues were replaced and a large increase in SNR was still observed.

As platinum is a soft donor it is known to react well with sulfur in the side chain of methionine, which acts as a soft acceptor. Sulfur is also known to bind well to Pt from its role played in the mechanism of Pt anticancer drugs. Binding of Pt anticancer drugs interact with sulfur containing peptides and proteins to form a Pt(II)-S adduct which is then transformed into the desired Pt(II)-DNA adduct.¹⁶⁸ Another non-biological example of the strength of this interaction is that sulfur is known to be an excellent poison for Pt catalysts.^{169,170} As the interaction between platinum and sulfur is known to be very strong this could explain why a preference for methionine residues has been observed.

Proline residues

Another residue that has been prevalent throughout screening is proline. Although it has not been identified as a key residue it is important to consider due its unique side chain structure and the effect that this may have. Proline is known to break alpha helical structure by causing a kink in the peptide/protein to form.¹⁷¹ Therefore, removal or incorporation of proline could result in different peptide conformations and this could affect how the peptide interacts with NPs, Pt²⁺ and how it behaves in a synthesis reaction. From screening against NPs replacement of aspartic acid in LS3 with proline resulted in an increase in binding. By replacing aspartic acid with proline, the overall charge of the peptide will have increased as well as insertion of proline at the centre of the peptide. Therefore, the increase observed could be due to the increase in charge and incorporation of proline that could cause the conformation of the peptide to change. This could allow other basic residues to become more accessible for binding to CoPt NPs. From Pt²⁺ binding, replacement of proline residues in LS4 with alanine increased binding. It is possible that the three proline residues caused kinks in the peptide sequence. Removal of proline would then remove these kinks which could result in a very different peptide conformation and possibly make other residues more accessible for binding to Pt²⁺.

Acidic residues

As well as identifying trends that are essential and help to improve binding, residues that are unfavourable for binding have also been identified. The first example of this is that the presence of acidic residues results in reduced binding. This has been identified from all three types of screening. From NP binding data truncation of LS5 identified that removal of glutamic acid from sequences resulted in an increased SNR. From truncation of LS3 it was identified that sequences where aspartic acid had been removed were the only sequences that had increased binding compared to the original lead sequence. These observations were further highlighted from positional scanning data as when glutamic acid was incorporated into LS2 and LS4 a significant reduction in binding was observed. Alanine scanning data for Pt²⁺ binding saw that substitution of glutamic acid in LS4 for alanine resulted in increased binding. When glutamic acid was incorporated into LS2 and LS3 a significant reduction in binding intensity was observed. However, replacement of aspartic acid in LS3 with glutamic acid resulted in a significant increase in binding. This could suggest that, although acidic amino acids seem to be unfavourable for binding, if one is already present in the sequence it could be favourable to swap this to glutamic acid for binding to Pt²⁺. Finally, from synthesis

data it was observed that substitution of basic residues with glutamic acid also resulted in decreased binding. Therefore, all of these observations suggest that the presence of glutamic acid and aspartic acid is unfavourable for binding to CoPt NPs, Pt²⁺ and use in a synthesis reaction.

Peptide length

Overall shorter peptide sequences have been identified as being favourable for binding to CoPt NPs and when used in a synthesis reaction. The first example of this is from truncation of LS1 where shorter peptide sequences had increased or similar SNR values to LS1. This trend was also identified from truncation of LS2 and LS3. For LS2 pentamers that contained lysine residues had some of the highest SNR values compared to LS2. Truncated sequences KLSRHH and KLSRH had the highest SNR values of all sequences compared to LS3, these sequences also had the highest SNR compared to sequences from LS1 and LS2. Therefore, this data suggests that it is possible to use shorter peptides for binding to CoPt NPs. Truncation data for screening against a CoPt synthesis reaction identified sequence KLSRHH as having the highest intensity compared to LS3. This peptide also had one of the highest intensities for all peptides that were screened against a CoPt synthesis reaction.

All of the trends identified here will be used for the selection and design of peptides that may be suitable for use in CoPt synthesis reactions, this will be discussed in detail in chapter 8 of this thesis.

CHAPTER SEVEN: FePt PEPTIDE
ARRAYS

7 FePt PEPTIDE ARRAY SCREENING

7.1 NANOPARTICLE BINDING

Peptide arrays have been screened using pre-made FePt NPs, these NPs were in the A1 (disordered) phase. Results from this screening can be seen in Figure 7.1.1.

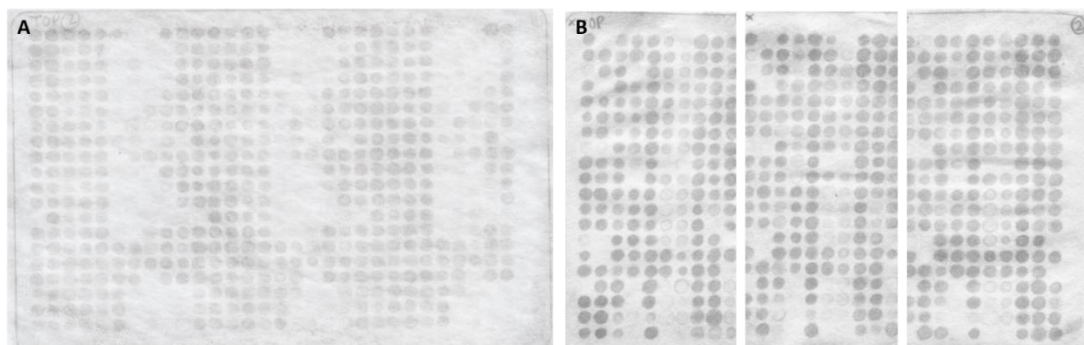


Figure 7.1.1 – Peptide arrays after NP binding has been carried out for 16 hours A) 1st generation array and B) 2nd generation array.

7.1.1 LEAD SEQUENCES

All five lead sequences were screened against FePt NPs and the results from this can be seen in Figure 7.1.2. LS3, LS4 and LS5 all have very similar SNR values and are the highest of the five sequences. However, due to the presence of large error bars further screening may be required. LS1 then has the next highest SNR value and as this sequence was identified from selection against FePt L₁₀ thin films and NPs it was expected that this sequence would bind well.⁶¹ Finally, LS2 has the lowest SNR value, this sequence was originally identified from screening against L₁₀ phase thin films of CoPt and as screening here is carried out against FePt it is understandable that a lower binding intensity is observed.

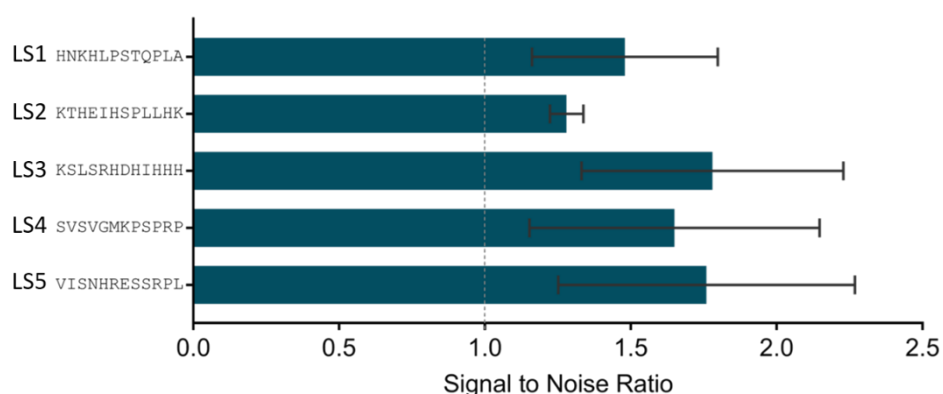


Figure 7.1.2 – SNR data for all five lead sequences screened against FePt nanoparticles. Dotted grey line represents background noise.

7.1.2 ALANINE SCANNING

To identify any key amino acids alanine scanning was carried out on all five lead sequences. Unfortunately, the majority of LS2, LS3 and LS5 had a similar intensity to the lead sequence

and the presence of large error bars made it difficult to draw any conclusions for these peptides.

Data for LS1 shows that there are four sequences where a decrease in SNR is observed (Figure 7.1.3), and these relate to when amino acids asparagine, lysine, histidine and proline are replaced with alanine. This suggests that these amino acids are important for binding to FePt NPs. Asparagine, lysine and histidine contain nitrogen groups in their side chain that would be able to interact with NPs and so this could be why a decrease in SNR is observed.

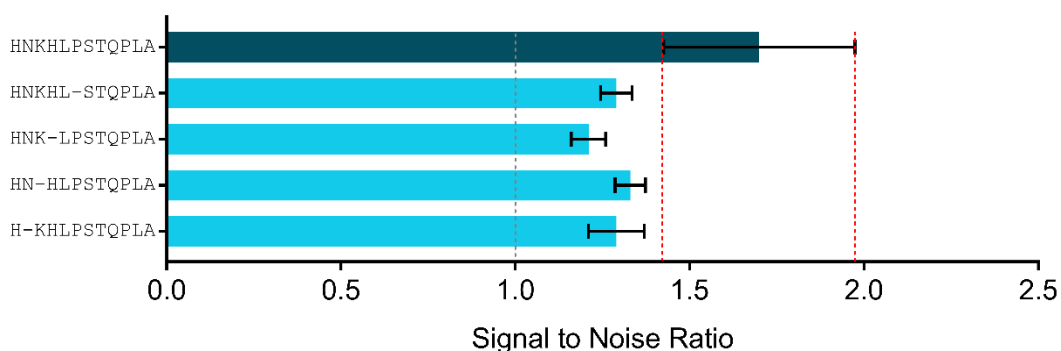


Figure 7.1.3 – Alanine scanning data for LS1. Dark green – LS1 and light blue – sequences with decreased SNR. Dotted grey line represents background noise.

Alanine scanning data for LS4 identified four sequences with decreased SNR values. These decreases relate to when serine and valine (positions 1 – 4) are replaced with alanine. Serine is a polar amino acid with an -OH group in its side chain, it is possible that this group could bind to NPs with high affinity and as a result removal from the sequence results in decreased binding. Whereas valine is a hydrophobic amino acid and is unlikely that this would interact greatly with FePt NPs, the decrease could be due to changing the overall structure of the peptide and how other amino acid side chains present and interact with NPs.

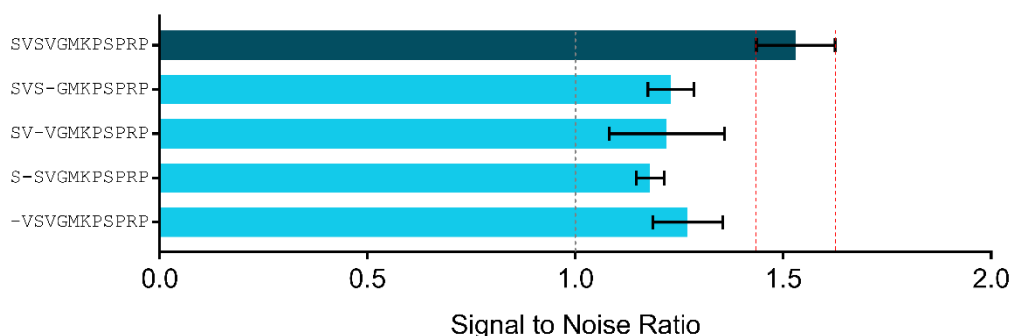


Figure 7.1.4 – Alanine scanning data for LS4. Dark green – LS4 and light blue – sequences with decreased SNR. Dotted grey line represents background noise.

7.1.3 TRUNCATION

Truncation of LS1 resulted in the majority of sequences having a similar intensity and only some sequences having reduced SNR. Although error bars present are quite large it is

possible to qualitatively identify trends from the data. In general, shorter peptide sequences are unfavourable for binding to FePt NPs. This can be seen from the low SNR values that pentamers have, with the majority having an SNR value of ≈ 1 , which suggests that almost no binding is occurring. Another trend that can be noted is sequences that contain the start of the peptide, especially histidine, asparagine and lysine, have an increased SNR compared to sequences that do not contain this region. It is seen that HNKHL, NKHLP and KHLPS have a higher SNR compared to the rest of the pentamers. Sequences LPSTQPLA, PSTQPLA and STQPLA have the most significantly reduced SNR, so much so that it is below 1 for LPSTQPLA and STQPLA. This suggests that this combination of amino acids is unfavourable for binding to FePt NPs and this could be due to the lack of basic residues present in the sequence. However, no sequences show an increase in binding compared to LS1 and so combination of HNKHLP and STQPLA results in increased binding compared to when these peptides are used separately. This suggests that longer peptides are preferred for binding to FePt NPs.

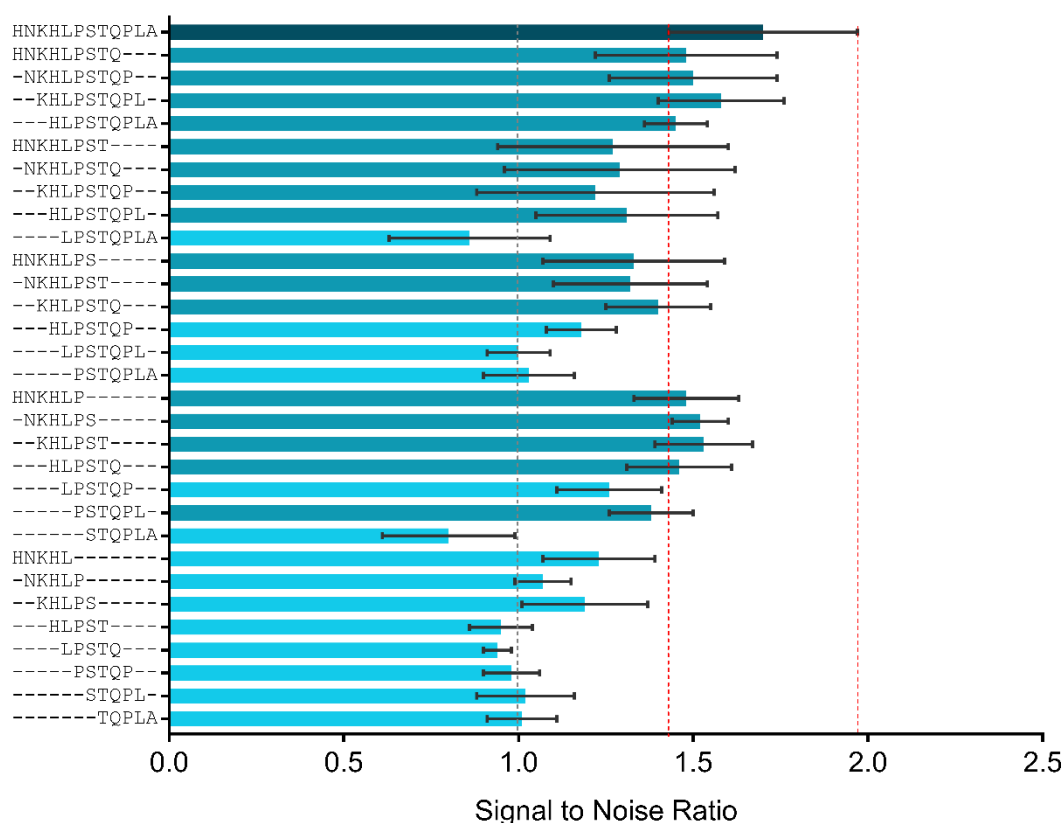


Figure 7.1.5 – Truncation data for LS1. Dark green – LS1, teal – similar SNR to LS1 and light blue – decreased SNR. Dotted grey line represents background noise.

Truncation of LS2 resulted in four sequences with increased SNR whilst the rest of the sequences had either similar or decreased SNR to LS2. The four increased sequences are: KTHEIHSPL, KTHEIS, HSPLLHK and SPLLHK. It is possible that these sequences show increased binding due to the presence of basic residues, lysine and histidine. These sequences make

up either end of the peptide and this could suggest that these regions are important for binding to FePt NPs. Whereas when the middle region of the peptide is used for NP binding much lower intensities are observed, these sequences have fewer basic residues and as a result a lower overall peptide charge. For example, EIHSPL contains one histidine residue and as glutamic acid is present this makes the peptide neutral overall. Longer peptide sequences that contain the middle of the peptide (HEIHSPL and HEIHSPLLH) have higher intensities and this is a direct result of the presence of more basic residues and an increased overall charge. There is also a link between peptide length and SNR as can be seen from part B of Figure 7.1.6. Sequences that have lysine present at one end of the peptide and are longer in length have higher SNR values. The only exception to this is EIHSPLLHK as it has a lower SNR than HSPLLHK. Although this peptide is longer the presence of glutamic acid counteracts this and so binding is reduced. In general, shorter peptide sequences are unfavourable for binding to FePt NPs, this trend was observed from truncation of LS1 also. This is confirmed by all pentamer sequences having SNR values of ≈ 1 suggesting that almost no binding is occurring.

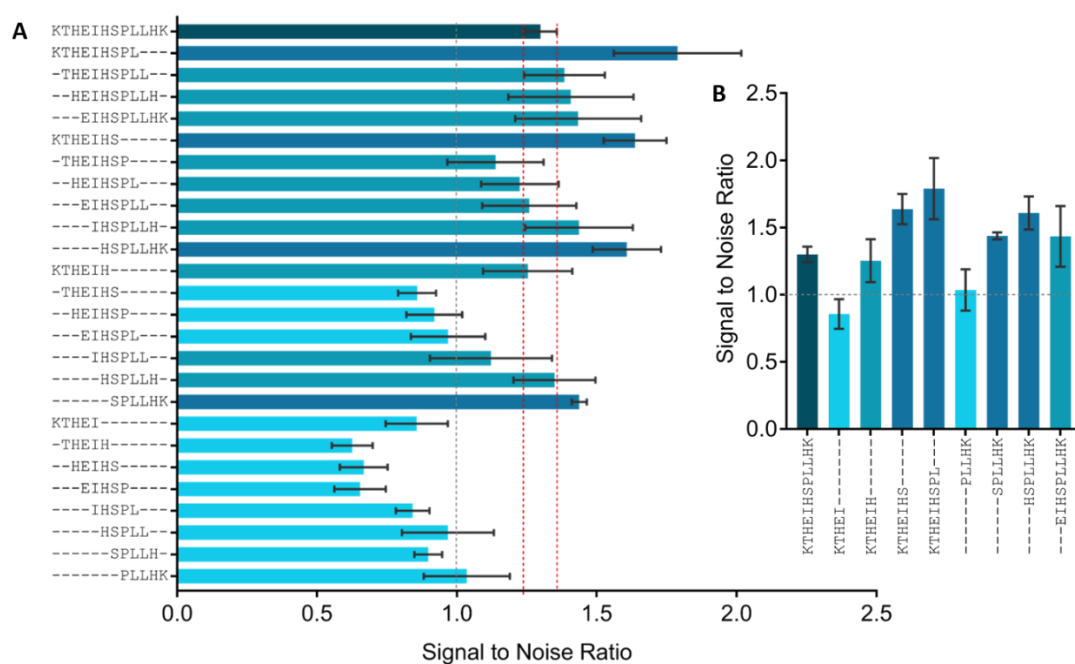


Figure 7.1.6 – A) Truncation data for LS2 and B) Data highlighting the importance of peptide length. Dark green – LS2, dark blue – increased SNR, teal – similar SNR and light blue – decreased SNR all compared to LS2. Dotted grey line represents background noise.

Truncation of LS3 resulted in all sequences having a similar intensity to LS3 as well as the presence of large error bars. Therefore, it was not possible to draw any conclusions from truncation data for LS3.

Truncation data for LS4 highlighted the importance of basic residues, arginine and lysine, as removal of these residues resulted in a significant reduction in SNR. For these sequences SNR

values of ≈ 0.5 were observed, this is much lower than background noise and suggests that no binding is occurring. Sequences that contain arginine and lysine have similar SNR values to LS4, suggesting that the reduction observed by removing these residues is significant. Therefore, this highlights the importance of basic residues for this peptides ability to bind to FePt NPs.

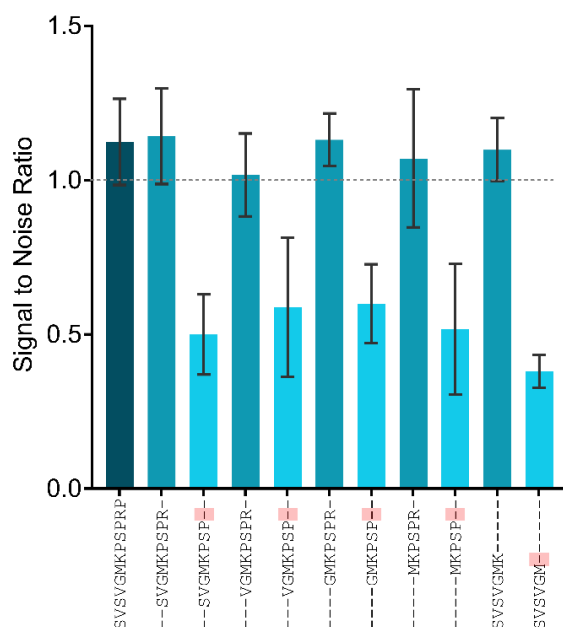


Figure 7.1.7 – Truncation data for LS4. Dark green – LS4, teal – similar SNR and light blue – decreased SNR all compared to LS4. Dotted grey line represents background noise. Red boxes highlight where arginine/lysine has been removed from sequence.

Finally, truncation data for LS5 (Figure 7.1.8) also suggested that longer peptide sequences are favourable for binding to FePt NPs. Here only peptides that are eight or nine amino acids in length have similar binding intensity compared to LS5. Shorter peptide sequences have SNR values of ≤ 1 suggesting that minimal binding is occurring. This trend has been identified from truncation of LS2, LS4 and now LS5 for binding to FePt NPs.

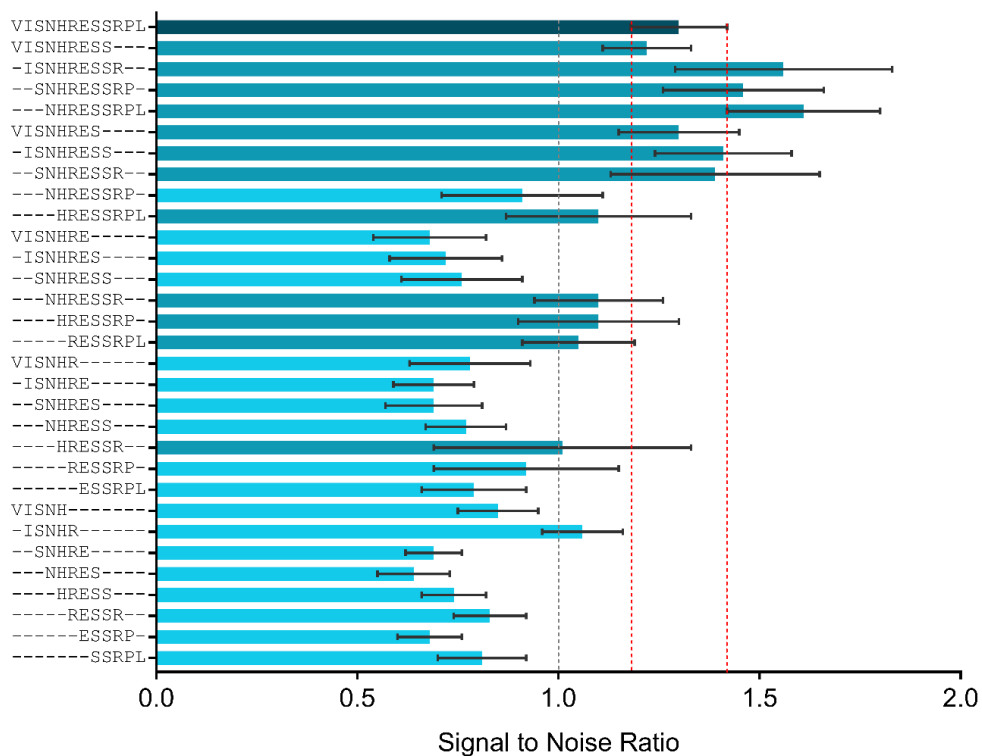


Figure 7.1.8 - Truncation data for LS5. Dark green – LS5, teal – similar SNR and light blue – decreased SNR all compared to LS5. Dotted grey line represents background noise.

7.1.4 POSITIONAL SCANNING

Positional scanning carried out for LS2 and LS3 resulted in all sequences having a similar intensity to the lead sequence. Large error bars were present for LS2, and for LS3 all sequences had an SNR value of ≈ 1 suggesting that almost no binding was occurring. Therefore, only significant changes in SNR for LS4 and LS5 are discussed here.

Positional scanning for LS4 involved substitution of lysine and arginine (positions 7 and 11). Replacement of arginine with threonine, serine, proline and leucine resulted in decreased SNR values. This replacement involved changing a basic positively charged residue for either a polar or hydrophobic residue and a decrease in SNR is to be expected as these residues are less likely to interact with FePt NPs. Replacement of lysine with valine, glycine and leucine also resulted in a significant decrease. Here a basic positively charged amino acid is being replaced with hydrophobic amino acids and so this suggests that these residues are unfavourable for binding to FePt NPs.

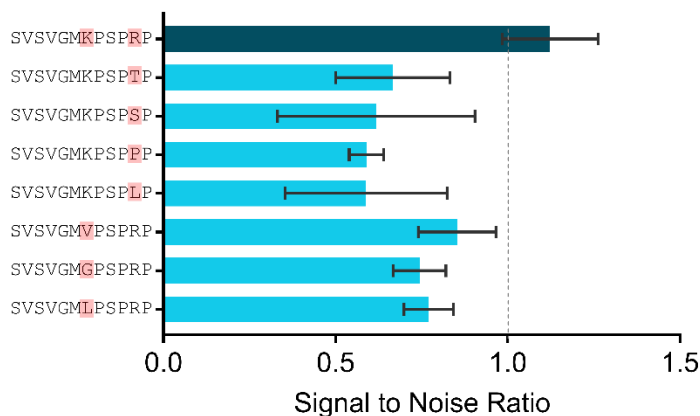


Figure 7.1.9 – Positional scanning data for LS4. Dark green – LS4 and light blue – decreased SNR compared to LS4. Dotted grey line represents background noise. Red boxes highlight positions at which substitutions have been made.

Positional scanning for LS5 involved substitution of histidine and arginine (positions 5 and 10). Replacement of arginine with valine, threonine, serine, proline and leucine resulted in decreased SNR values, as expected. Suggesting that arginine is important for binding to FePt NPs. Valine, proline and leucine are hydrophobic amino acids and as such the carbon side chain may not interact strongly with FePt NPs compared to side chains with greater functionality. However, a decrease is also observed when arginine is replaced with threonine and serine, both of which are polar amino acids. This suggests that the -OH group present in the side chain of threonine and serine is not as good at binding to FePt NPs compared to the amine group present in arginine.

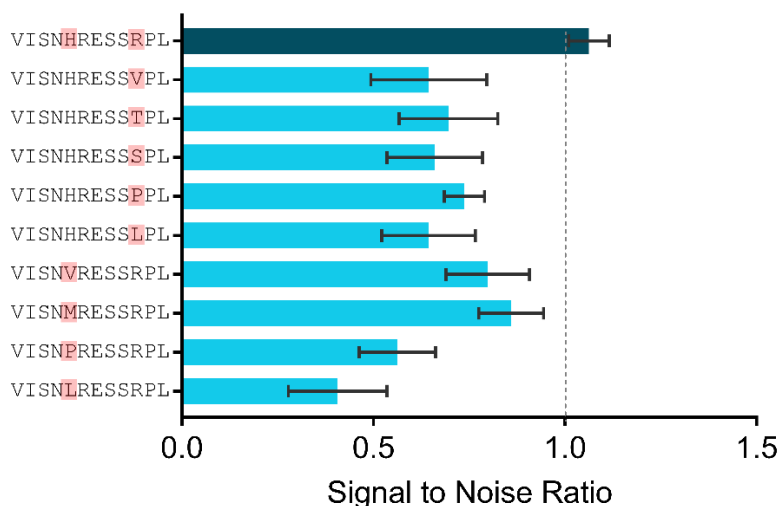


Figure 7.1.10 – Positional scanning data for LS5. Dark green – LS5 and light blue – decreased SNR compared to LS5. Dotted grey line represents background noise. Red boxes highlight positions at which substitutions have been made.

Two trends were identified from positional scanning of LS4 and LS5. The first trend is that incorporation of glutamic acid into the sequence is unfavourable for binding (Figure 7.1.11). This was highlighted by replacement of lysine and arginine, in LS4, with glutamic acid and a

significant reduction in binding was observed. SNR values of ≈ 0.5 were obtained suggesting very poor binding for these sequences. This same trend is observed when histidine and arginine in LS5 were replaced with glutamic acid. The dramatic reduction in binding observed could be due to the opposite charge of the residues. Arginine, histidine and lysine are all basic positively charged residues and glutamic acid is an acidic negatively charged residue. Therefore, suggesting that positively charged residues are preferred for binding to FePt NPs and negatively charged residues are unfavourable.

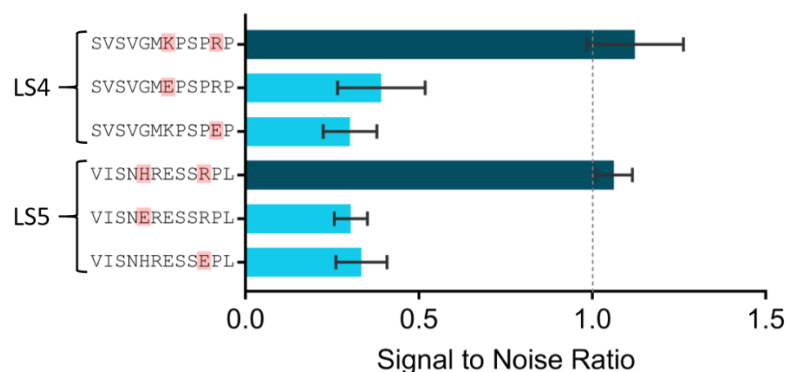


Figure 7.1.11 – Positional scanning data for LS4 and LS5 highlighting the effect of glutamic acid. Dark green – lead sequences and light blue – decreased SNR compared to LS. Dotted grey line represents background noise. Red boxes highlight positions at which substitutions have been made.

The second trend observed from positional scanning data is that substitution of basic residues with other basic residues results in binding that is of similar intensity to the original sequence, this can be seen in Figure 7.1.12. In both cases arginine is being replaced with lysine and histidine, this suggests that binding to FePt NPs does not prefer one basic residue over another and that the preference for binding is likely to be due to the positive charge.

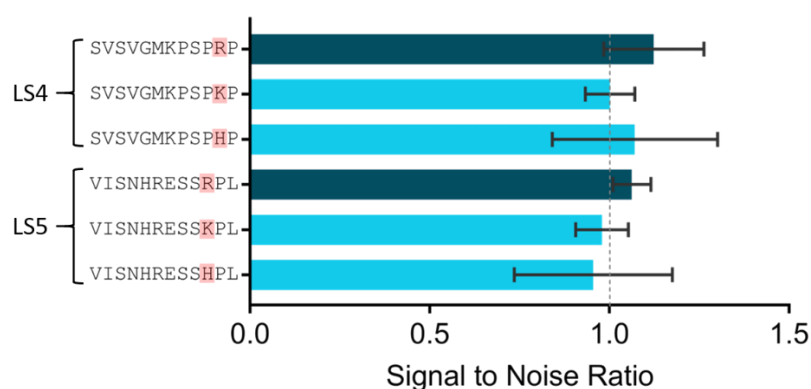


Figure 7.1.12 – Positional scanning data for LS4 and LS5 highlighting the effect of different basic residues. Dark green – lead sequences and light blue – decreased SNR compared to LS. Dotted grey line represents background noise. Red boxes highlight positions at which substitutions have been made.

7.1.5 HIGH FREQUENCY

Signal to noise ratio data for all the variations of the high frequency peptide can be seen in Table 7.1.1. There is only one variation of the peptide that has an increase in SNR and the rest of peptides had SNR values that were decreased or of similar intensity to the lead high frequency peptide. The peptide that resulted in an increase was when histidine (position 2) was substituted for serine. This is unexpected as from truncation data basic residues were identified as favourable.

The original and increased high frequency peptides have been plotted graphically, along with the five original lead sequences (Figure 7.1.13). The two high frequency peptides have significantly higher SNR values than LS2, LS3, LS4 and LS5 suggesting that this combination of amino acids could be more suitable for binding to FePt NPs. This increase is much larger than any increases observed from alanine scanning, truncation and positional scanning of the five lead sequences. Therefore, HSSSPKLR has the highest binding affinity for FePt NPs compared to all peptides screened so far.

Table 7.1.1 – Change in signal to noise ratio compared to the original high frequency peptide HHSSPKLR. Green – increase in SNR greater than 0.1, red – decrease in SNR greater than 0.1 and grey – no significant change in SNR.

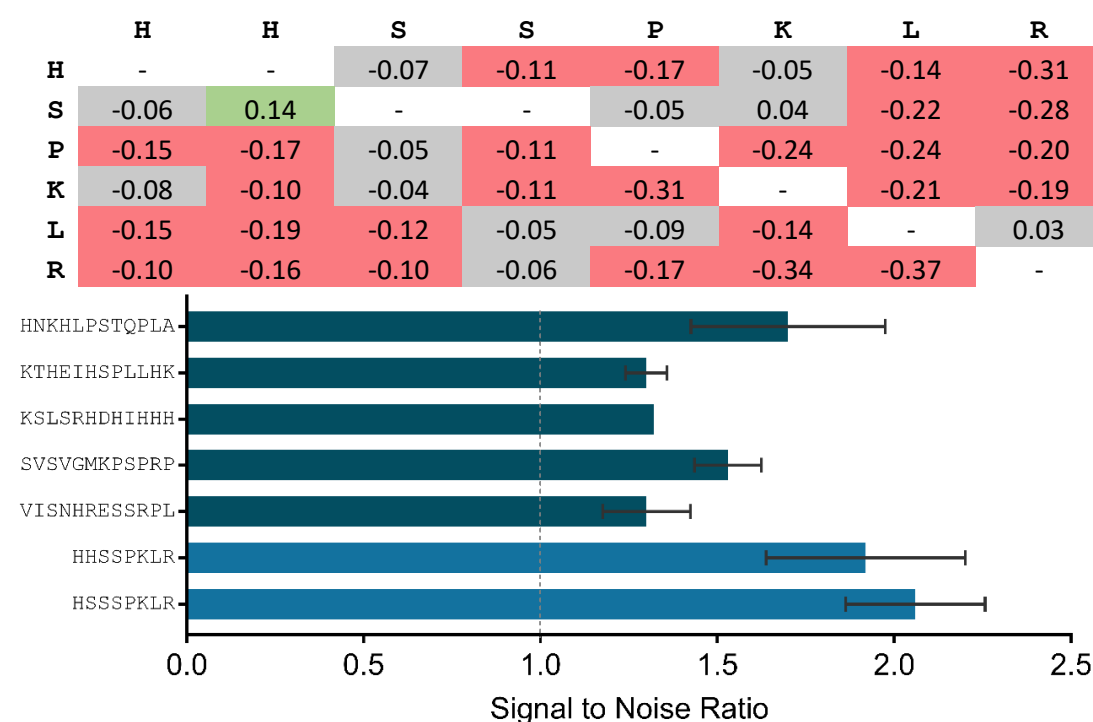


Figure 7.1.13 – High frequency binding intensity data compared to the five original sequences and the two high frequency peptides that show an increase in SNR. Dark green – lead sequences and dark blue – high frequency peptides. Dotted grey line represents background noise.

7.1.6 REVERSAL AND SCRAMBLING

Reversal and scrambling were carried out for all five lead sequences, as was done for screening against CoPt NPs. For all of the peptides the original and reversed sequence have very similar SNR values suggesting that reversal of the sequence does not greatly affect the peptides binding ability. For the majority of the peptides there is very little difference between the original and scrambled sequence, this suggests that the presence of the particular amino acids is more important than the order they are placed in. The only peptide that shows a difference between the two is for LS2, where the scrambled peptide has a higher binding intensity.

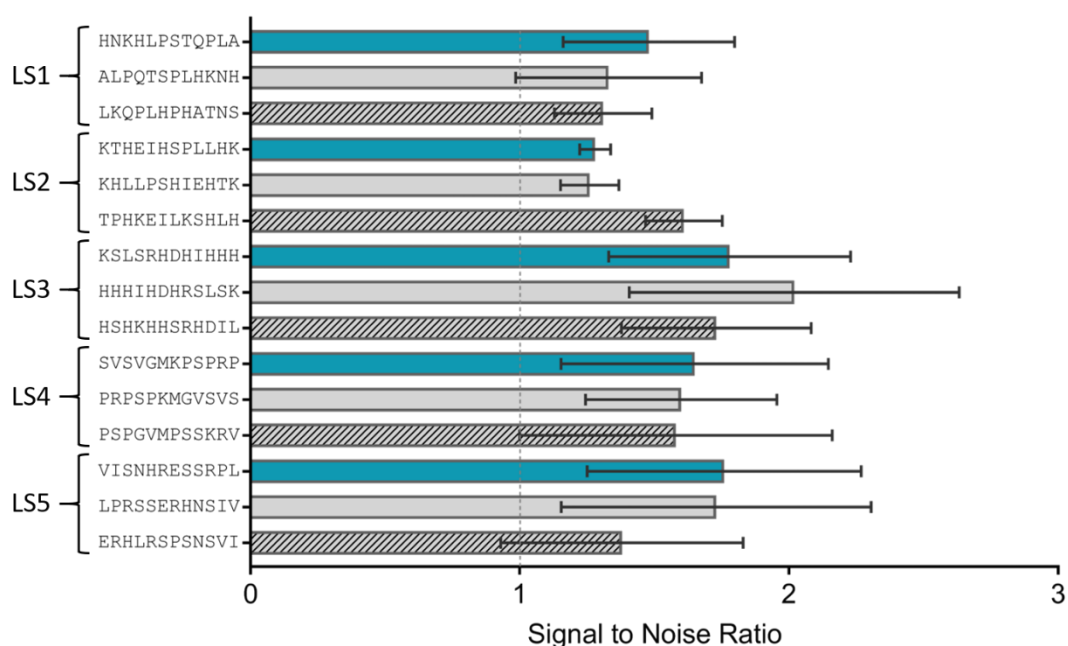


Figure 7.1.14 – Scrambling and reversal of lead peptide sequences. Teal – lead peptide, grey – reversed sequence and diagonal striped – scrambled sequence. Dotted grey line represents background noise.

7.1.7 CYCLIC

The lead peptide sequences have been constrained into a loop in the same way as previously described (chapter 6.1.7). Although error bars present are very large it is still possible to qualitatively identify trends from the data. For LS1, LS3 and LS5 there is little variation between the original sequence and the sequence constrained in a loop, suggesting that constraining the peptide has little effect on binding ability. Whereas for LS2 and LS4 an increase in binding is observed when the sequence is constrained in a loop. By constraining LS4 it is possible that the lysine and methionine present in the centre of the sequence are now more accessible for binding to NPs and this could explain the increase observed. For LS2 it is possible that the three histidine residues are now more accessible for binding compared to when the peptide is free.

It is expected that the serine containing peptides would have similar values to the original peptide sequence and as this is the case for the majority of the lead sequences this suggests that the glycine linker present does not greatly affect the peptides binding ability. The only exception to this is for LS2 where the serine containing peptide has a higher SNR value than the original sequence. This shows that the extra glycine and serine residues might have had an effect and increased the peptides binding ability.

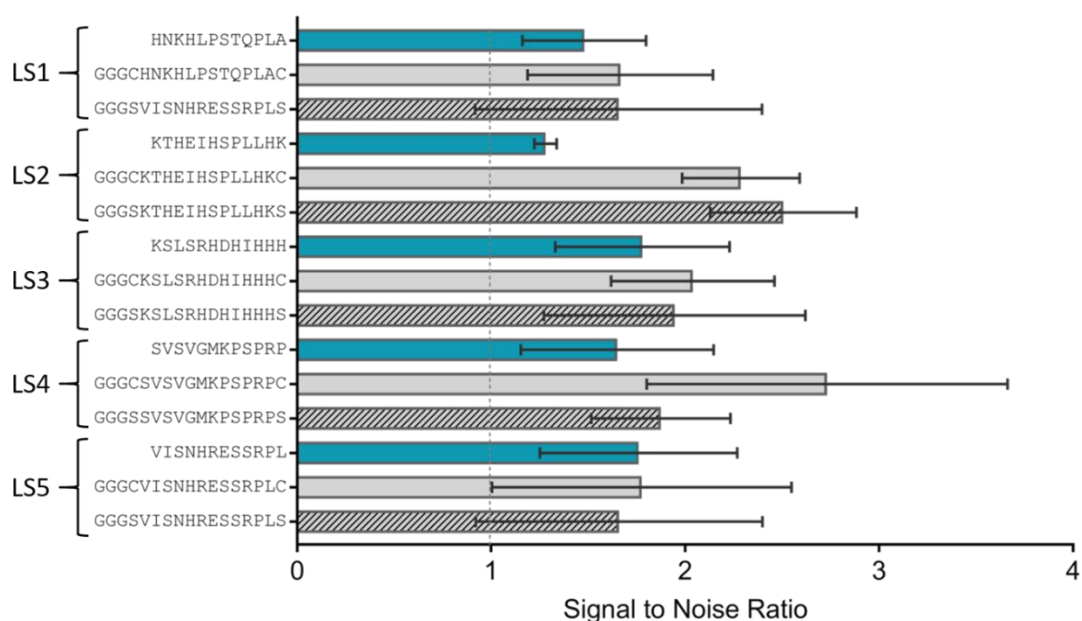


Figure 7.1.15 – Comparison of cyclic and linear lead peptide sequences. Teal – lead sequence, grey – constrained in a loop and diagonal striped – corresponding sequence with cysteines replaced with serine. Dotted grey line represents background noise.

7.2 METAL ION BINDING

Fe^{2+} and Pt^{2+} solutions were used to screen against peptide arrays containing alanine scanning, truncation, positional scanning and high frequency peptide sequences (2.2.3). Screening against Pt^{2+} was carried out using the same solution for both FePt and CoPt and so the results of Pt^{2+} binding have already been discussed in section 6.2. However, for convenience these results are summarised in Table 7.2.1. Overall the importance of lysine and histidine was identified, as can be seen through truncation of LS1 and LS2 as well as positional scanning for LS2, LS3, LS4 and LS5. Methionine was also identified as an important residue and alanine scanning and truncation data for LS4 confirm this. Positional scanning data for LS2, LS3, LS4 and LS5 also highlight the importance of methionine. Glutamic acid was identified as an unfavourable residue through alanine scanning for LS5 and positional scanning of LS2 and LS3. Some of these trends have also been observed from NP binding data. Truncation data for LS1, LS2 and LS4 shows the importance of basic residues. Positional

scanning for LS4 and LS5 also highlights this, as well as showing the detrimental effect glutamic acid has on binding to FePt NPs.

Table 7.2.1 – Summary of screening carried out against Pt²⁺. Green highlights represent important residues and red highlights represent unfavourable residues. Full data and graphs can be found in chapter 6.2.

	Alanine Scanning	Truncation	Positional Scanning
LS1	Replacement of HNKHLS all decreased	Importance of lysine , sequences where lysine has been removed have significant reduction in SNR.	N/A
LS2	Lysine (position 1) shows decrease. Large error bars present for rest of substitutions	Importance of lysine , sequences where lysine has been removed have significant reduction in SNR.	Methionine, lysine and histidine important Glutamic acid unfavourable
LS3	All substitutions similar to LS3.	Regions SRHDHIIHH and RHDHIIHH show the only increase.	Methionine, lysine and histidine important Glutamic acid unfavourable
LS4	Replacement of methionine is decreased Replacement of proline residues increased	Removal of methionine from sequences results in decreased SNR.	Methionine, lysine and histidine important
LS5	Replacement of histidine is decreased Replacement of ESSPL residues are increased	Very large error bars present, and majority of sequences similar to LS5.	Methionine, lysine and histidine important

The resulting peptide arrays from screening against Fe²⁺ can be seen in Figure 7.2.1. From the data collected there are some results with large error bars making it difficult to identify any trends from the data, this is the case for truncated peptides. These large error bars could be due to the use of a detection reagent used to image the peptide arrays, if coverage of the detection reagent was not consistent across the entire array then this is likely to result in areas of higher and lower intensity. However, it is still possible to identify key trends from the Fe²⁺ data.

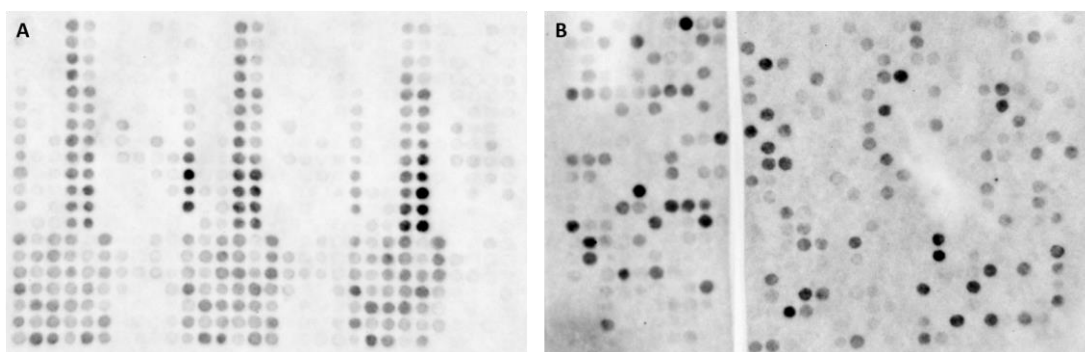


Figure 7.2.1 – Peptide arrays that have been incubated in Fe^{2+} solution overnight to assess binding. A) 1st generation array and B) second generation array.

7.2.1 LEAD SEQUENCES

All five lead sequences were screened against Fe^{2+} and Pt^{2+} metal solutions. Although the intensities are much lower for binding to Fe^{2+} the same general trends are observed between the two metals. LS1 and LS3 both have the highest intensities, LS2 is then the third highest sequence and LS4 and LS5 have the lowest intensities of all five peptides. LS1 and LS3 also bind with high affinity to FePt NPs suggesting that these sequences are important for binding to NPs and metal ions.

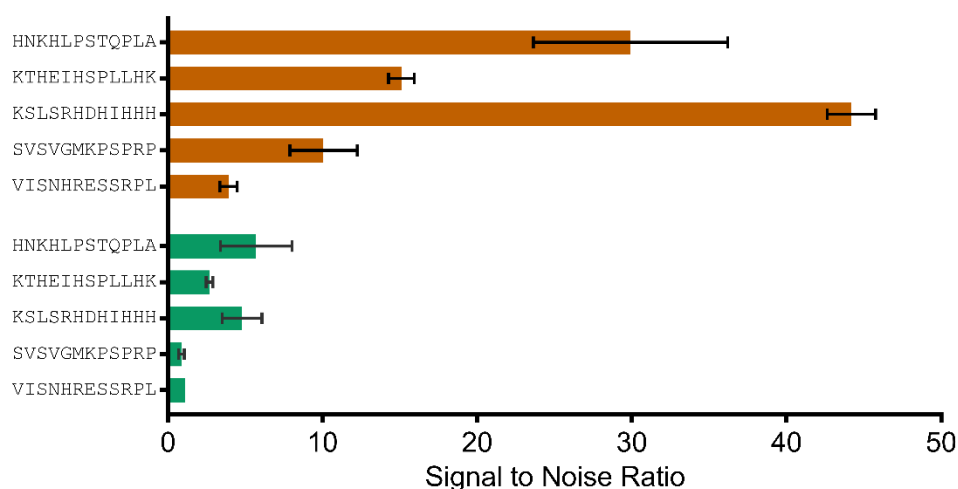


Figure 7.2.2 – SNR data for all five lead sequences screened against Fe^{2+} (green) and Pt^{2+} (orange).

7.2.2 ALANINE SCANNING

Alanine scanning data for LS1 identifies seven sequences with reduced SNR, the most significant of these is when lysine is replaced with alanine. Replacement of histidine, asparagine, leucine, proline and serine also resulted in decreased SNR values. This suggests that these residues are important for binding to Fe^{2+} . Data obtained from screening against Pt^{2+} and FePt NPs identified basic residues as being important and so the decrease observed when replacing lysine and histidine with alanine is consistent with previous data collected.

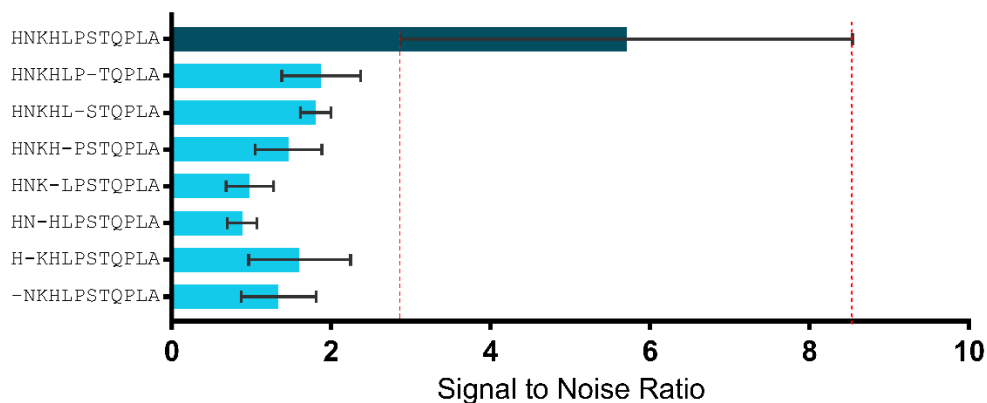


Figure 7.2.3 – Alanine scanning data for LS1. Dark green – LS1 and light blue – decreased SNR compared to LS1.

Alanine scanning for LS2 resulted in six sequences that have increased SNR and one that was decreased. The significant decrease observed is when lysine (position 1) is replaced with alanine. However, when lysine (position 12) is replaced with alanine an unexpected increase in binding is observed. This increase was unexpected as from previous screening carried out against FePt NPs basic residues were identified as important. As the error bar present is large it is possible that this increase may not be as large as first thought.

Replacement of glutamic acid, proline, leucine and histidine resulted in increased SNR. Although error bars are very large the increase is still greater than LS2. Leucine is a hydrophobic amino acid and so may not be directly involved with binding. Leucine has a much larger side chain than alanine and so it possible that this substitution results in increased binding by making other residues more accessible, now that the bulky side chain of leucine is removed.

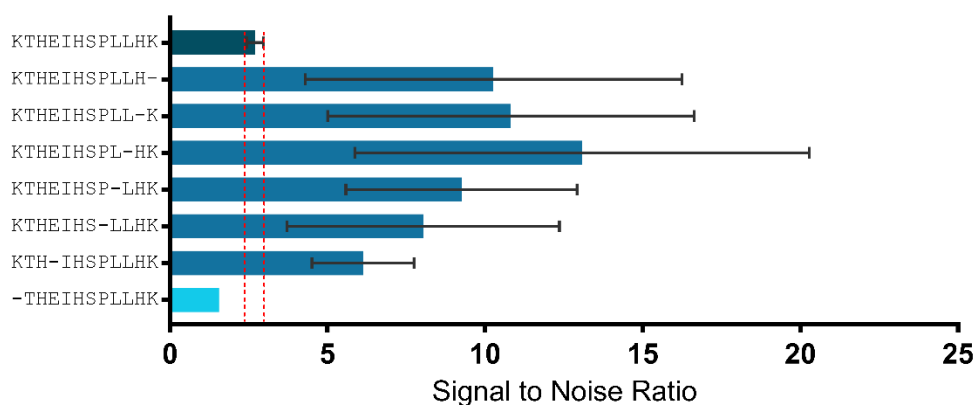


Figure 7.2.4 – Alanine scanning for LS2. Dark green – LS2, dark blue – increased SNR and light blue – decreased SNR both compared to LS2.

Alanine scanning data for LS3 resulted in all substitutions having similar SNR values to LS3 as well as the presence of large error bars. Therefore, this suggests that swapping out one amino acid did not have a dramatic effect on the peptides ability to bind to Fe²⁺ and not one

single amino acid in particular is responsible for binding, suggesting that it is a cooperative effect. Further analysis is required to identify which regions of LS3 are important for binding to Fe²⁺.

Data for LS4 highlighted only two sequences with an increased SNR. These increases relate to the replacement of proline (positions 10 and 12) with alanine. This would suggest that proline is unfavourable for binding to Fe²⁺. Data collected from screening against Pt²⁺ also identified proline as an unfavourable residue. Therefore, this data suggests that proline may not be required for binding to precursor metal ions in the synthesis of FePt NPs.

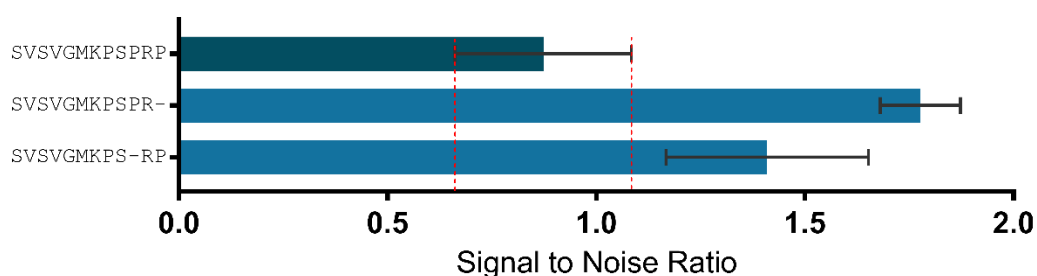


Figure 7.2.5 – Alanine scanning for LS4. Dark green – LS4 and dark blue – increased SNR compared to LS4.

Alanine scanning data for LS5 resulted in only two sequences with increased SNR, these increases were due to the replacement of proline and leucine with alanine. Proline has already been identified as unfavourable from alanine scanning of LS4 and so this further solidifies this. Removal of leucine has also been previously identified from alanine scanning of LS2. It is possible that removing the larger side chain of leucine could result in other residues becoming more accessible for binding and so an increase in SNR is observed.

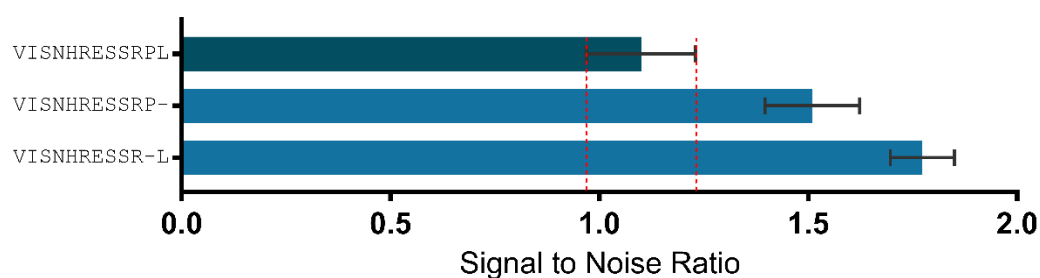


Figure 7.2.6 – Alanine scanning for LS5. Dark green – LS5 and dark blue – increased SNR compared to LS5.

7.2.3 TRUNCATION

Truncation data collected from screening against Fe²⁺ resulted in the majority of sequences having reduced binding intensity compared to the original lead sequence. Large error bars were also present for all five lead sequences making it difficult to identify any trends from the data. Truncated sequences of LS4 and LS5 had SNR values of ≈ 1 , suggesting that binding

was similar to background noise. As a result, it has not been possible to identify any key regions of the peptides for binding to Fe²⁺. Due to truncated sequences having reduced SNR suggests that shorter peptide sequences are unfavourable for binding to Fe²⁺. This trend was also identified from screening against FePt NPs.

7.2.4 POSITIONAL SCANNING

Positional scanning was carried out on four of the five lead sequences. However, only positional scanning data for LS2 is discussed here. Data for LS3, LS4 and LS5 resulted in sequences that had a similar intensity to the original lead sequence as well as having large error bars that made it difficult to identify any trends. For LS4 and LS5 all sequences had SNR values ≈ 1 suggesting that binding is very poor.

Data for LS2 resulted in two substitutions that increased SNR, and this was from replacement of leucine with lysine and histidine (Figure 7.2.7). Basic amino acid residues were highlighted as important from NP binding and so by incorporating them into the sequence here an increase in binding was observed. A larger increase is observed for lysine and this could suggest that lysine is preferred for binding to Fe²⁺. From alanine scanning of LS2 leucine was identified as a residue that does not bind well to Fe²⁺. All other substitutions of leucine resulted in similar SNR values to LS2 and so leucine can easily be replaced for other amino acids without compromising the peptides binding ability.

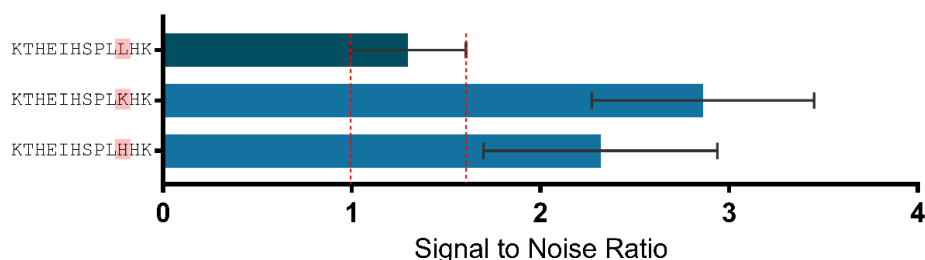


Figure 7.2.7 – Positional scanning data for LS2. Dark green – LS2 and dark blue – increased SNR compared to LS2. Red boxes highlight positions at which substitutions have taken place.

7.2.5 HIGH FREQUENCY

Signal to noise ratio data for the high frequency screening can be seen in Table 7.2.2. There are sixteen sequences with increased SNR and seventeen sequences with decreased SNR, both compared to the original high frequency peptide. All sequences where lysine was replaced with other amino acids show a reduction in binding, this is also the case for histidine (position 2). When histidine (position 1) is replaced with serine, proline and leucine a reduction in binding is observed but when replaced with lysine and arginine an increase in SNR is observed. This suggests that there could be a preference for lysine and arginine over histidine residues. Another trend that can be noted from the high frequency data is that

proline is unfavourable for binding to Fe²⁺. Substitution of proline with other amino acids resulted in increased binding whereas substituting other amino acids with proline resulted in decreased binding. This suggests that proline is unfavourable anywhere in the sequence.

Sequences that showed an increase or decrease in SNR were plotted graphically (Figure 7.2.8) so that only those that show a significant change in SNR can be identified. This resulted in eleven sequences with decreased SNR and eight sequences with increased SNR. Sequences that show an increase have similar or increased SNR values compared to LS1 suggesting that these sequences are favourable for binding to Fe²⁺. Sequences that show increased binding contain more basic residues than those that have decreased binding. Therefore, this changes the overall charge of the peptide and as a result the peptides with higher SNR values generally have a higher overall charge, this can be seen in Figure 7.2.8. This suggests that a higher overall positive charge on the peptide is preferred for binding to Fe²⁺. This trend was also observed from screening carried out against Pt²⁺.

Table 7.2.2 – Change in signal to noise ratio compared to the original high frequency peptide HHSSPKLR. Green – increase in SNR greater than 0.5, red – decrease in SNR greater than 0.5 and grey – no significant change in SNR.

	H	H	S	S	P	K	L	R
H	-	-	2.50	0.61	1.65	-1.07	2.55	1.82
S	-1.51	-1.95	-	-	0.44	-2.18	-0.05	-0.84
P	-0.54	-2.06	-1.28	-0.75	-	-2.30	-1.20	-2.28
K	3.16	-0.44	3.35	1.55	1.87	-	0.78	-0.22
L	-1.56	-1.86	0.15	-0.05	0.56	-1.90	-	-1.62
R	1.19	-1.08	2.12	1.74	1.54	-0.22	1.33	-

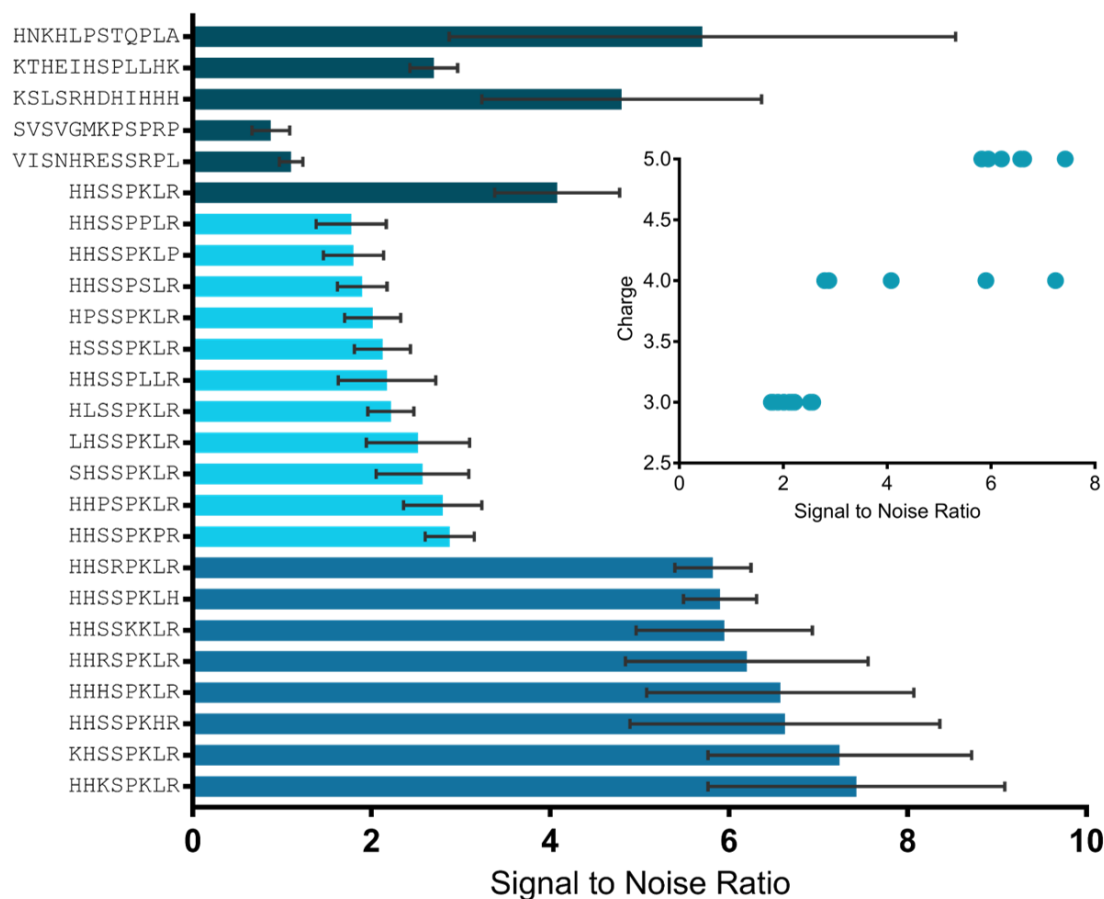


Figure 7.2.8 – High frequency binding intensity data compared to original lead sequences. Dark green – lead sequences, light blue – decreased SNR and dark blue – increased SNR. Inset figure highlights overall charge on peptide plotted against SNR values.

7.3 SCREENING AGAINST A SYNTHESIS REACTION

Incorporation of peptide arrays into a synthesis reaction was difficult to ensure that NP binding and synthesis was consistent across the array. As a result, there are some areas of the arrays that have more intense peptide spots, even with different washing procedures this was hard to eliminate, and as such some sets of data have large error bars. The resulting arrays produced from this screening can be seen in Figure 7.3.1. Due to this no conclusions could be drawn the high frequency array and only some of the lead sequences are discussed for alanine scanning, truncation and positional scanning.

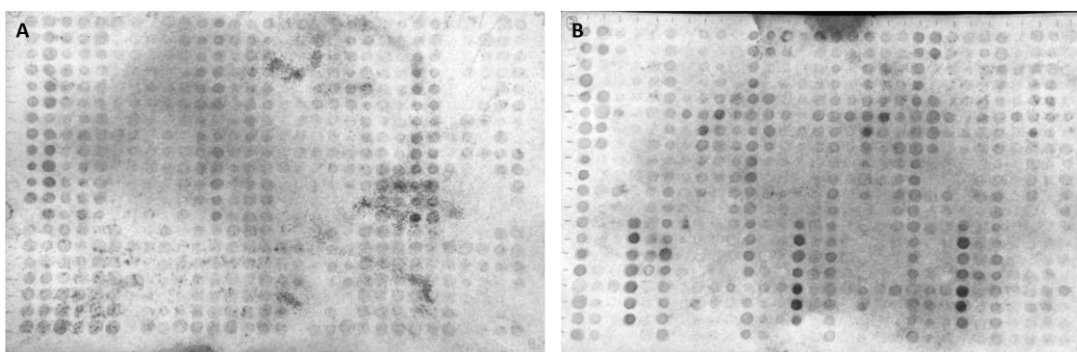


Figure 7.3.1 – Outcome of arrays used for screening against an FePt synthesis reaction. A) 1st generation array and B) 2nd generation array.

7.3.1 LEAD SEQUENCES

All five lead sequences were screened against an FePt synthesis reaction and the results can be seen in Figure 7.3.2. Now LS1, LS2 and LS4 all have similar intensities to each other. LS5 has a slightly higher intensity than background noise and LS3 has the lowest intensity that is below 1. Previously, for NP and metal ion binding LS3 was one of the highest intensity sequences however this is not the case when used in a synthesis reaction. This could suggest that this sequence prefers binding to the precursor metal ions and also to the synthesised NPs but may not be involved directly with synthesis. However, variations on this sequence may behave differently.

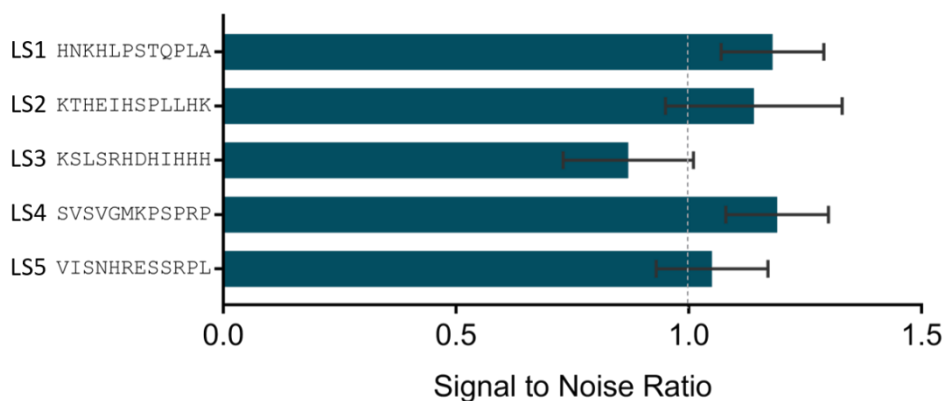


Figure 7.3.2 – SNR data for all five lead sequences screened against an FePt synthesis reaction. Dotted grey line represents background noise.

7.3.2 ALANINE SCANNING

From alanine scanning data the majority of sequences had a similar intensity to the lead sequence or very large error bars were present that made it difficult to identify any trends. This was the case for LS2, LS3, LS4 and LS5 and the only observation that can be made for LS1 can be seen in Figure 7.3.3. Substitution of lysine for alanine in LS1 resulted in a significant decrease in binding. Lysine was previously identified as important for binding to

FePt NPs as well as metal ion binding and so this data fits well, suggesting that lysine is also important in the synthesis of FePt NPs.

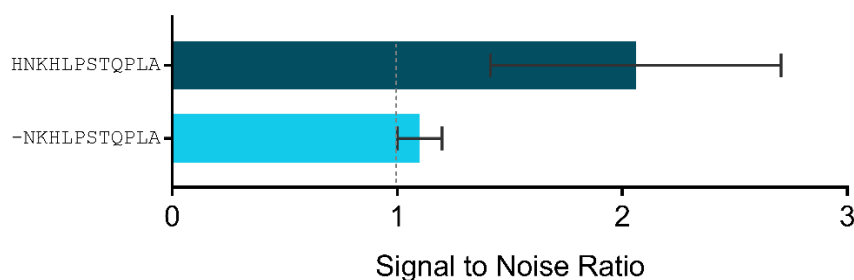


Figure 7.3.3 – Alanine scanning data for LS1. Dark green – lead sequence and light blue – decreased SNR. Dotted grey line represents background noise.

7.3.3 TRUNCATION

Truncation was carried out for all five lead peptide sequences, however due to the nature of the screening method the majority of sequences had very large error bars or a similar SNR to the lead peptide. This was the case for LS1, LS2, and LS5 as well as this they all had SNR values of ≈ 1 suggesting that peptide spots were of similar intensity to background noise.

Data from the truncation of LS3 highlighted five sequences that have significantly increased SNR values and two that show a decrease. The sequences that show an increase generally contain the start or middle section of the peptide and these sequences are: KLSLRHDH, KLSLRHD, SLSRHDH and LSRHDHI. All four of these sequences contain a large number of basic residues (lysine, arginine and histidine) and this could explain why an increase is observed. However, sequences HDHIHH and DHIIHH both have reduced SNR values but also contain a large number of basic residues. This suggests that although basic residues have been identified as favourable it is possible that when there are multiple basic residues next to each other, in this case histidine, it can become unfavourable. Repulsion between the positively charged side chains could result in the overall conformation of the peptide changing and result in the reduced SNR observed. There is one sequence that is an exception to this and that is DHIIHH as this sequence has increased SNR. This sequence has one less histidine residue compared to HDHIHH and DHIIHH so it is possible that removal of histidine could result in a different peptide conformation that is more favourable. Overall, truncation of this peptide suggests that it is a combination of the presence of basic residues and the peptides conformation that is important for binding.

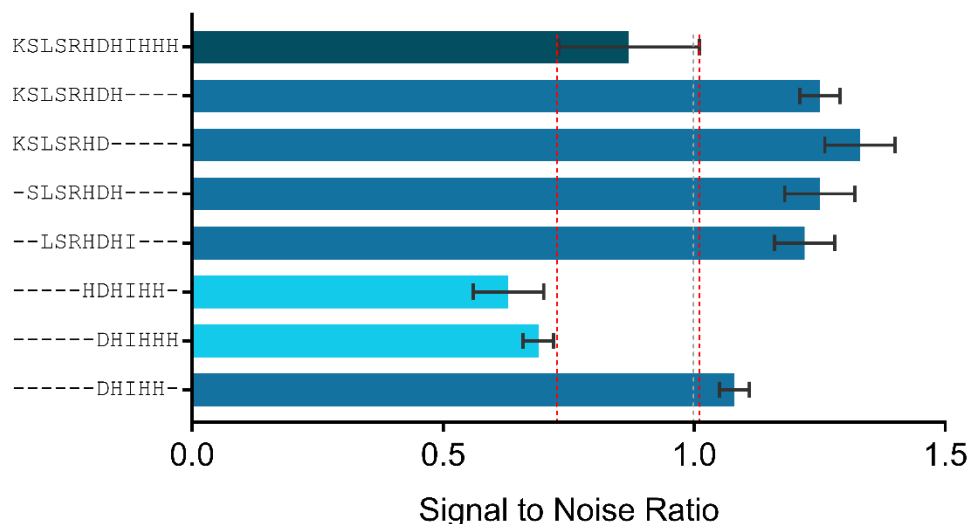


Figure 7.3.4 – Truncation data for LS3. Dark green – LS3, dark blue – increased SNR and light blue – decreased SNR compared to LS3. Dotted grey line represents background noise.

Truncation of LS4 resulted in eleven sequences with increased SNR values and only two with decreased. The two sequences that show decreased binding are sequences that no longer contain methionine in the sequence. This dramatic reduction in binding is strongly suggested to be due to the removal of methionine and this is highlighted in part B of Figure 7.3.5. Methionine was identified as important for binding to Pt^{2+} and so this could suggest why it is an important residue in the synthesis of FePt NPs. The sequences that show an increase in binding include either the start or end region of the peptide along with methionine and lysine that are present in the centre. Having both methionine and lysine together appears to be favourable for binding as when only lysine is present in the sequence a reduction in binding is observed (e.g. MKPSRP and KPSRP). The region that is unique to nearly all of the peptides that show increased binding is GMKPS and so this region could be important in a synthesis reaction. Further truncation of this sequence would allow for identification of which amino acids are crucial for use in a synthesis reaction. Truncation of other LS has resulted in shorter peptides being unfavourable for binding to FePt NPs, Fe^{2+} and Pt^{2+} , LS4 is an exception to this rule as shorter sequences such as GMKPS and MKPSRP have comparable intensities to longer peptide sequences.

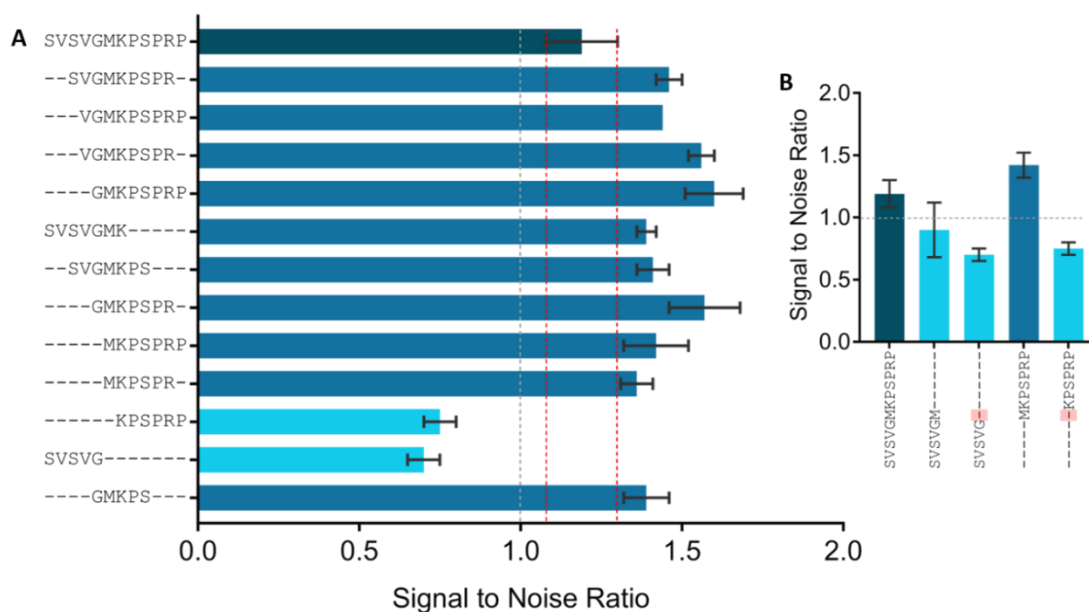


Figure 7.3.5 – A) Truncation data for LS4 B) highlighting the importance of methionine. Dark green – LS4, dark blue – increased SNR and light blue – decreased SNR both compared to LS4. Dotted grey line represents background noise. Red boxes highlight positions at which methionine has been removed.

7.3.4 POSITIONAL SCANNING

Positional scanning was performed on four of the five lead sequences and from this it has been possible to identify some significant changes in SNR from the data. Positional scanning data for LS2 resulted in two sequences with a significant decrease in SNR and one with a significant increase. Replacement of histidine with isoleucine resulted in a significant decrease as well as the replacement of leucine with serine. Therefore, suggesting that these residues may be unfavourable in the synthesis of FePt NPs. The only increase observed was from the replacement of histidine with methionine. Methionine was also shown to be important for binding to Pt^{2+} and so this could suggest that methionine is important for multiple aspects involved in the synthesis of FePt NPs.

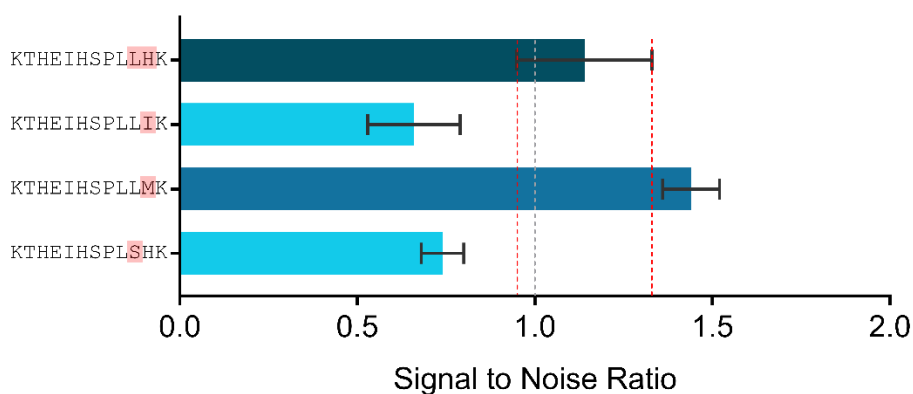


Figure 7.3.6 – Positional scanning data for LS2. Dark green – LS2, dark blue – increased SNR and light blue – decreased SNR both compared to LS2. Dotted grey line represents background noise. Red boxes highlight positions at which substitutions have taken place.

Data for LS3 resulted in three replacements that had a significant increase. These involved the replacement of histidine and aspartic acid with methionine, and aspartic acid with histidine. Incorporation of methionine was also important for LS2 and the fact that it is highlighted for LS3 further solidifies that this residue is important during the synthesis of FePt NPs. Replacement of aspartic acid with histidine results in increased SNR values and this is to be expected as an acidic negatively charged residue is being replaced with a basic positively charged residue. Basic residues were identified as important from NP binding and metal ion binding. Therefore, suggesting that they are involved in all aspects of the synthesis of FePt NPs.

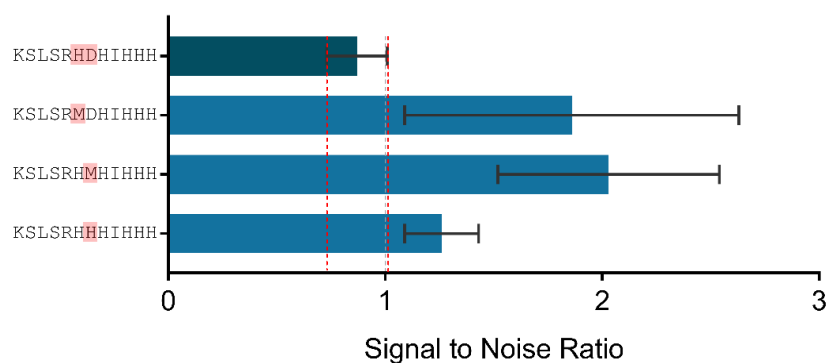


Figure 7.3.7 – Positional scanning data for LS3. Dark green – LS3, dark blue – increased SNR and light blue – decreased SNR both compared to LS3. Dotted grey line represents background noise. Red boxes highlight positions at which substitutions have taken place.

Positional scanning data for LS4 had very large error bars that made it difficult to identify any trends and the majority of sequences had similar intensity to LS4.

Finally, data for LS5 resulted in one sequence showing an increase and one showing a decrease in SNR. The increase observed was from the incorporation of methionine into the sequence and this further highlights the importance of methionine and suggests it may play a role in the synthesis of FePt NPs. The only decrease was observed from replacement of arginine with glutamic acid. Glutamic acid was identified as unfavourable for binding to FePt NPs and Pt^{2+} , therefore this suggests that glutamic acid is unfavourable for all aspects involved in the synthesis of FePt NPs.

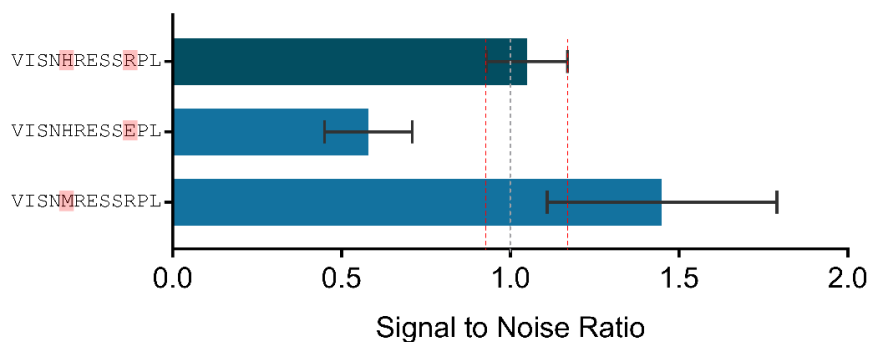


Figure 7.3.8 – Positional scanning data for LS5. Dark green – LS5, dark blue – increased SNR and light blue – decreased SNR both compared to LS5. Dotted grey line represents background noise. Red boxes highlight positions at which substitutions have taken place.

7.3.5 HIGH FREQUENCY

The same high frequency array as used in previous screening has been screened against an FePt synthesis reaction. Although the high frequency sequences have shown increased SNR values from screening against FePt NPs, Pt²⁺ and Fe²⁺ this was not the case when screening against a synthesis reaction. All sequences have SNR values of less than 1, and therefore the peptide spots relating to these sequences have intensities similar to that of background noise which suggests that these sequences may not be suitable for use in a synthesis reaction. Error bars for high frequency data were also large, which made it difficult to identify any other trends that may be occurring.

7.4 SUMMARY AND DISCUSSION

Screening against FePt NPs, Fe²⁺, Pt²⁺ and a FePt synthesis reaction has resulted in a large amount of data generated and from this it is possible to identify key trends and these are: importance of basic residues, the overall peptide charge, the importance of methionine, the adverse effect of acidic residues and peptide length.

Basic residues

The first key trend identified was the importance of basic residues. Throughout all types of screening residues such as lysine, histidine and arginine have been identified as important. Truncation data collected from screening against FePt NPs, for LS2 and LS4, highlighted the importance of basic residues. Positional scanning data for LS4 and LS5 identified that substitution of one basic residue with another basic residue resulted in binding of similar intensity. This suggested that there is not a preference for one basic residue over another. From Fe²⁺ binding data, positional scanning of LS2 indicated that substitution of leucine with lysine and histidine resulted in a significant increase in binding, further confirming the importance of basic residues. Basic residues were even more prevalent in Pt²⁺ data as truncation of LS1 and LS2 identified lysine as an important residue. Positional scanning of

LS2, LS3, LS4 and LS5 also displayed this as well as the importance of histidine. From screening against a synthesis reaction, truncation of LS3 resulted in sequences (KLSLRHDH, KLSLRHD and SLSRHDH) that contained a large number of basic residues having increased SNR values compared to LS3.

As previously mentioned (6.4), it is known that amino acids that have a positively charged side chain bind well to magnetite NPs with a higher affinity than uncharged residues.¹⁶³ Although this was carried out for magnetite NPs it could explain why a preference for basic residues is observed when binding to FePt NPs. Lysine is also known to be an excellent ligand for Pt complexes due to the role it plays in binding HMG domain proteins to Pt/DNA complexes in cisplatin.¹⁶⁴ Histidine is also known to play a role in the action of cisplatin as cisplatin preferentially binds to the nitrogen atom of the imidazole ring in histidine.^{165,166} Histidine is also involved in the oxygen binding action of haemoglobin, a covalent bond is formed between the nitrogen atom of the proximal histidine and iron, which is where oxygen reversibly binds.¹⁷² There is also a second histidine residue present, known as the distal histidine, and this has two roles - preventing oxidation of iron to a higher oxidation state and reducing the amount of carbon monoxide that can bind to haem.¹⁷² As basic residues are already known to play a role in certain biological processes that involve Fe and Pt this could explain why a preference for these residues is observed from the screening carried out here.

Overall peptide charge

Another trend that was identified is that in general when the overall charge on the peptide is higher larger values for SNR are obtained. This was identified from the high frequency screening against FePt NPs, Fe²⁺ and Pt²⁺. The sequences that had the highest SNR values had the largest overall charge on the peptide, overall peptide charge was increased by the incorporation of basic residues. Basic residues have been identified as important across all types of screening and it is believed that the amine functionality present in the side chains is essential for binding. However, it could also be the case that incorporation of basic residues alters the overall charge and therefore increases the peptides binding ability also.

Importance of methionine

Methionine was also identified as a key residue from screening against Pt²⁺ and an FePt synthesis reaction. Truncation data for LS4, collected from screening against Pt²⁺, highlighted the importance of methionine as sequences that did not contain the residue had significantly reduced binding. Positional scanning data for LS2, LS3, LS4 and LS5 also highlighted the

importance of methionine as incorporation into sequences resulted in significantly increased binding. Data collected from screening against an FePt synthesis reaction also showed the importance of methionine. All truncated sequences of LS4 that contained methionine had increased binding, whilst those that did not contain methionine were significantly reduced. Positional scanning data for LS2, LS3 and LS5 also found that incorporation of methionine resulted in higher SNR values being achieved.

Platinum is a soft donor that is known to react well with soft acceptors such as the sulfur group present in the side chain of methionine. An example of this is that sulfur is known to bind well to Pt from its role played in the mechanism of Pt anticancer drugs.¹⁶⁸ A non-biological example of the strength of this interaction is that sulfur is known to be an excellent poison for Pt catalysts.^{169,170} All of these reasons could explain why a preference for methionine has been observed from the screening carried out here.

Acidic residues

As well as identifying residues that may be essential for binding it is also important to consider residues that may be unfavourable. One residue that has been identified as being unfavourable is glutamic acid, this was identified from screening against FePt NPs, Pt²⁺ binding and an FePt synthesis reaction. Positional scanning data, collected from screening against FePt NPs for LS4 and LS5, highlighted that incorporation of glutamic acid into the sequence resulted in decreased SNR values. Positional scanning data collected from screening against a synthesis reaction also highlighted that incorporation of glutamic acid into LS5 resulted in decreased SNR values. Therefore, suggesting that glutamic acid is an unfavourable residue for binding to NPs and use in a synthesis reaction.

Peptide length

In general, shorter peptide sequences have been identified as unfavourable for binding to FePt NPs. This was identified from truncation data for LS1, LS2 and LS5. This suggests that longer peptide sequences could be preferred for binding to FePt NPs.

The trends discussed here will be used to identify peptides that may be suitable for use in FePt synthesis reactions as well as the design of new peptides for this purpose, this will be discussed in detail in chapter 8 of this thesis.

CHAPTER EIGHT: DESIGN OF PEPTIDES

8 DESIGN AND SELECTION OF PEPTIDES FOR USE IN NANOPARTICLE SYNTHESIS REACTIONS

8.1 COMPARISON OF FePt AND CoPt PEPTIDE ARRAYS

Using SPOT peptide array technology for screening CoPt and FePt has made it possible to identify key trends in lead peptide sequences so that their interaction with these materials can be better understood. There are similarities and differences between the two materials that will be discussed. Three key similarities were identified, and these are: 1) the importance of basic residues, 2) importance of methionine and 3) the adverse effect of acidic residues. There is one key difference between the two materials and that is peptide length. As CoPt and FePt have a similar crystal structures and the only difference between the two is the presence of an extra electron for cobalt, it is not surprising that similar amino acid residues may be suitable for binding to both materials.

The presence of basic residues resulted in higher binding to CoPt and FePt NPs, Pt^{2+} and Fe^{2+} as well as playing a role in synthesis of CoPt and FePt NPs. This trend was predominantly identified from truncation and positional scanning data where either a basic residue had been removed or incorporated into the sequence. In contrast, acidic residues were found to be highly unfavourable when screened against CoPt and FePt NPs, Pt^{2+} and CoPt and FePt synthesis reactions. Methionine was another residue that was identified as important for both CoPt and FePt, this was predominantly from screening against Pt^{2+} but also from screening against CoPt NPs and an FePt synthesis reaction.

As both basic and acidic residues affect the overall charge on the peptide it is possible to relate the overall peptide charge to its ability to bind to both materials. When truncation data for NP binding is compared for both materials, CoPt and FePt, (Figure 8.1.1 and Figure 8.1.2) it is observed that sequences with a higher overall peptide charge (+2 or +3) bind well to both materials. This positive charge comes from the presence of basic residues (lysine, histidine and arginine) in the sequence. Conversely, truncated sequences that do not bind well to both materials are typically neutral or have a negative charge of -1. This is observed from truncated sequences of LS1, LS2, LS4 and LS5 as there are several truncated sequences that are unfavourable for binding to both CoPt and FePt all with neutral or an overall negative charge on the peptide. LS5 is the exception to this as there are some sequences in this region that have an overall positive charge on the peptide (+1), suggesting that higher overall positive charges on the peptide are favourable.

Another difference between the two materials is peptide length. In general, from all screening carried out it was identified that CoPt prefers shorter peptides whilst FePt prefers longer peptides. Although this was identified from all types of screening it can also be observed from comparison of truncated sequences for NP binding for both CoPt and FePt (Figure 8.1.1 and Figure 8.1.2). From LS1 and LS2 it is observed that shorter sequences prefer to bind to CoPt and longer sequences to FePt. For example, truncated sequences from LS1, NKHLP and KHLPS, bind with a high affinity to CoPt but not FePt. Whereas longer sequences, HSPTQPLA and HSPTQPL, prefer binding to FePt NPs. This trend is more noticeable for truncated sequences of LS2, as almost all sequences that prefer binding to FePt are seven amino acids in length or longer. Sequences that prefer binding to CoPt are much shorter, typically five amino acids in length. In addition to these sequences, sequences that bind well to both materials contain a mixture of lengths. This is true for truncation data of all five lead sequences. Therefore, this suggests that a combination of length and overall charge of the peptides is responsible for the peptides ability to bind to one material over the other.

Unfortunately, direct comparisons were only possible for NP binding data and not metal ion binding or synthesis reaction data. There was a large difference in values for the different metal ions screened against (Fe^{2+} and Pt^{2+}) and even with normalising would have made the peptides appear in favour of binding to Pt^{2+} . Data collected from synthesis reactions had very large error bars due to high background noise, and so as a result this made it difficult to directly compare between CoPt and FePt synthesis reactions.

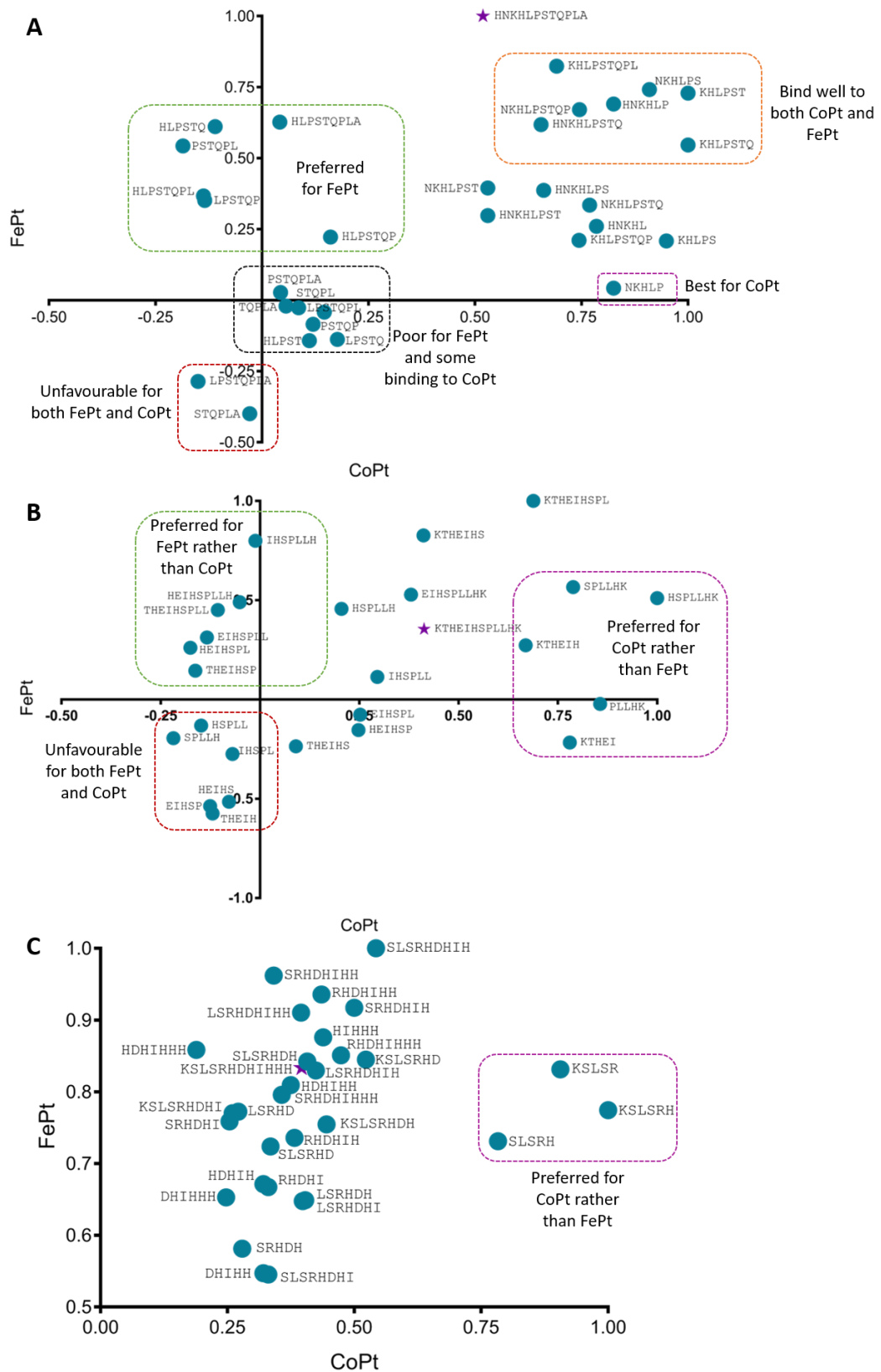


Figure 8.1.1 – Normalised nanoparticle truncation data for A) LS1, B) LS2 and C) LS3. Star represents lead sequence.

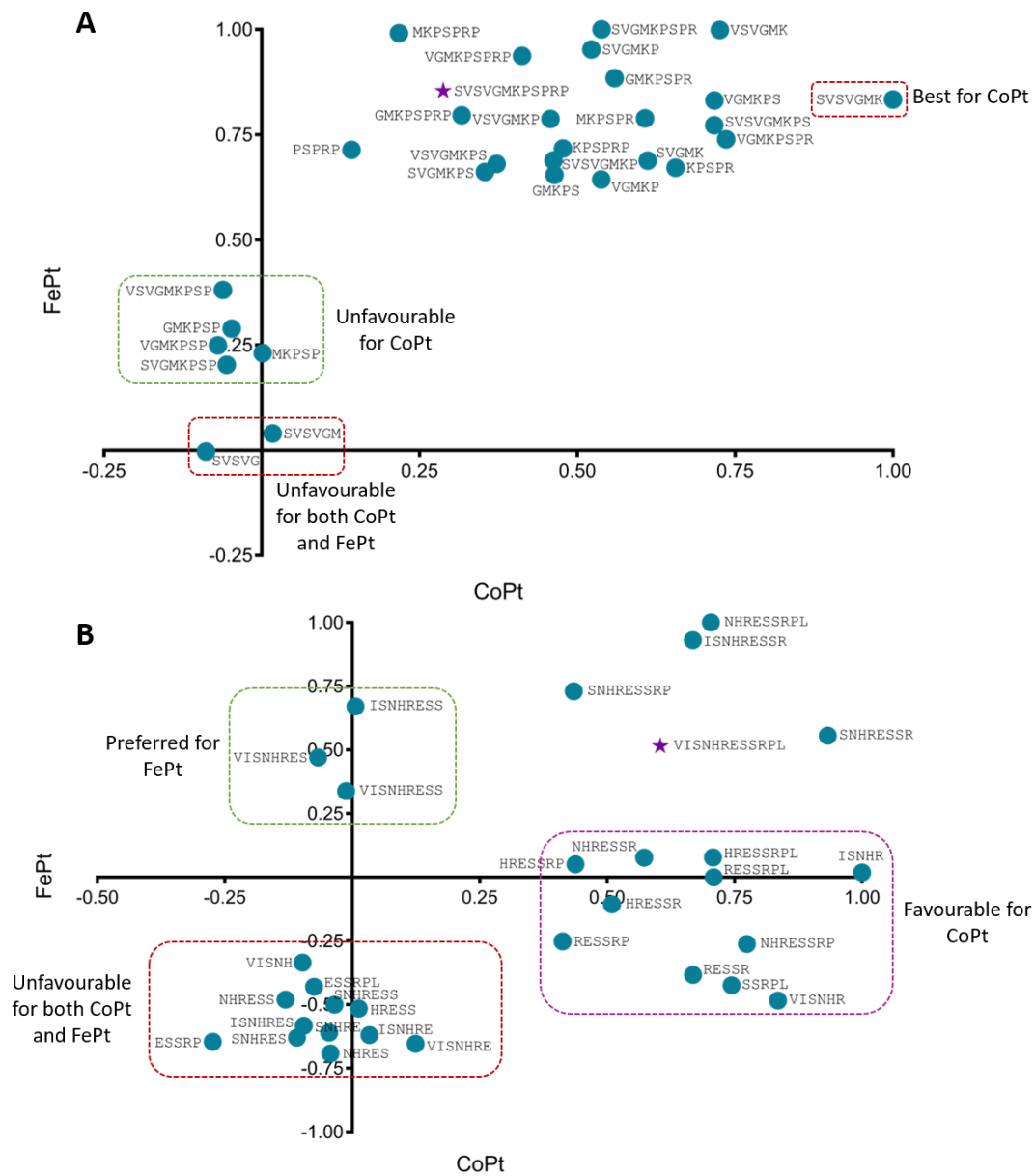


Figure 8.1.2 – Normalised nanoparticle truncation sequence data for A) LS4 and B) LS5. Star represents lead sequence

8.1.1 LEAD SEQUENCES

Using data from all types of screening carried out (NP binding, metal ion binding and synthesis reaction) has made it possible to identify if any of the lead sequences are preferred for certain aspects involved in the synthesis of NPs.

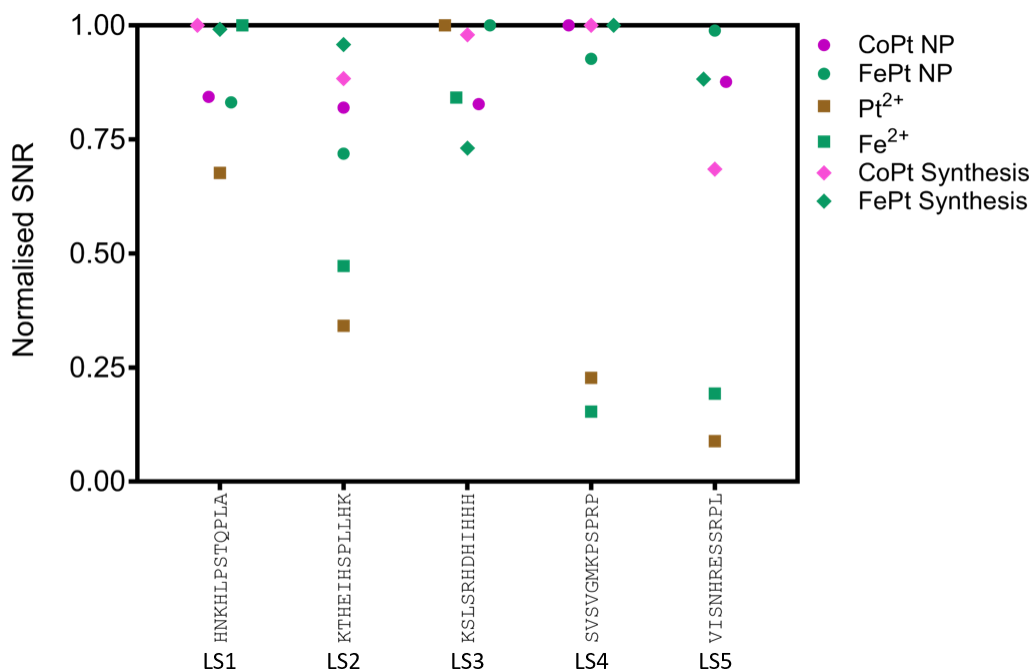


Figure 8.1.3 – Normalised SNR values for lead sequences screened against CoPt and FePt nanoparticles, Pt²⁺, Fe²⁺ and CoPt and FePt synthesis reactions.

Firstly, LS1 was identified from biopanning against thin films of L1₀ phase CoPt. LS2 was also identified from biopanning, in this case screening was carried out against thin films and NPs of L1₀ phase FePt. Therefore, it would be expected that LS1 and LS2 have the highest affinity for FePt and CoPt NPs respectively. However, this is not the case here as LS1 had one of the lowest affinities for FePt NPs and LS2 also had one of the lowest affinities for CoPt NPs. As LS2 was only identified from thin films this may suggest that the sequence behaves differently when interacting with NPs instead.

Although LS1 showed poor binding to NPs, LS1 had the second highest intensity for binding to Pt²⁺, was the top sequence for binding to Fe²⁺ and joint top when screened against an FePt synthesis reaction. It is possible that this sequence is involved in the synthesis of FePt NPs through binding to metal precursors and during initial nucleation. Of all the screening carried out no modifications made to the sequence resulted in increased binding to FePt. As no improvements can be made on this sequence it suggests that the original full-length sequence is required and a cooperative effect between all of the amino acids present in the sequence could be occurring. However, it was possible to identify a modification that

improved binding to CoPt. Truncated sequences KHPSTQ and KHPST both had increased SNR values compared to LS1 for binding to CoPt NPs, suggesting that these shorter sequences are more favourable.

LS2 was not one of the top lead sequences in any of the screening carried out for CoPt suggesting that a different sequence may be more suitable for use in a CoPt synthesis reaction. Modifications made to LS2 made it possible to improve the sequence. For example, truncated sequence HSPLLHK had the highest affinity of all sequences screened for binding to CoPt NPs. Another modification that improved binding was the incorporation of methionine. Therefore, SPOT peptide array technology has made it possible to probe this sequence further and identify where improvements can be made.

LS3 was one of the joint top sequences for binding to FePt NPs, whereas for binding to CoPt NPs it had the third highest intensity. For metal binding LS3 was the highest binder for Pt^{2+} and second highest for Fe^{2+} , this suggests that this sequence could play a role in synthesis reactions by binding to the metal precursors before nucleation begins. When screened against a synthesis reaction LS3 had the second highest SNR for CoPt but was the worst sequence for FePt. However, by truncating LS3 it is possible to improve this sequences affinity for an FePt synthesis reaction. Sequences KLSRHD and KLSRHDH both had an improved SNR compared to the original lead sequence and KLSRHD was the top sequence overall suggesting that variations of LS3 are suitable for use in an FePt synthesis reaction.

LS4 is the top sequence for binding to CoPt NPs and one of the joint top sequences for binding to FePt NPs. However, this sequence was not as good when binding to Pt^{2+} and Fe^{2+} as it came fourth for both materials. When screened against CoPt and FePt synthesis reactions LS4 performed much better and was one of the joint top sequences for both materials.

NP binding was the only screening to identify LS5 as favourable for either material, all other screening (metal ion binding and synthesis reaction) identified LS5 as unfavourable. Suggesting that this sequence is unfavourable for both CoPt and FePt. From all modifications carried out it has not been possible to make any significant improvements to this sequence. There are a few variations of this sequence that have increased SNR values compared to the lead sequence itself, but these improvements are not as great as improvements observed for the other four lead sequences. Analysis of how the lead sequences behave when screened against different aspects of the synthesis process highlight that there is no real specificity between the five LS for one material over the other.

8.1.2 HIGH AFFINITY SEQUENCES

The sequences that were identified as having the highest affinities for each of the different screening methods have been summarised in Table 8.1.1. By comparing the top peptide sequences from each type of screening it is possible to identify any differences or similarities between the peptides identified to have high affinity for either CoPt or FePt.

Table 8.1.1 – Sequences with the highest SNR values for screening carried out against CoPt NPs, FePt NPs, Pt²⁺, Fe²⁺, a CoPt synthesis reaction and an FePt synthesis reaction. Yellow – presence of lysine at end of sequence for binding to NPs and green – highlights amino acid residues that were changed from the original lead sequence.

CoPt NPs	FePt NPs	Pt ²⁺	Fe ²⁺	CoPt synthesis	FePt synthesis
HSPLLHK	KTHEIHSPL	KSLSRHMDHIHHH	KSLSRHMDHIHHH	KSLSRHD	KSLSRHD
SVSVGK	KTHEIHS	KSLSRHMDHIHHH	KSLSRHMDHIHHH	KSLSRH	GMKPSRP
PLLHK	NHRESSRPL	KSLSRHMDHIHHH	KSLSRHMDHIHHH		KSLSRMDHIHHH
KHLPSTQ	KHLPSTQPL	KSLSRHMDHIHHH	KSLSRHMDHIHHH		KSLSRMDHIHHH
ISNHR		KSLSRHMDHIHHH	KSLSRHMDHIHHH		

Nanoparticle binding

The top sequences for binding to CoPt NPs consist of shorter peptide sequences than those identified for binding to FePt. As previously mentioned, this suggests that peptide length can affect binding ability to the two different materials. Only one region is similar for binding to both CoPt and FePt NPs, this region is a truncation of LS1, KHLPTQ for CoPt and KHLPTQPL for FePt. This suggests that this region is able to bind with high affinity to both materials. Part A of Figure 8.1.1 also confirms this as sequence KHLPTQPL binds equally well to both materials (0.7 CoPt, 0.8 FePt).

Although LS1 and LS2 were shown to be unfavourable for binding to CoPt and FePt NPs, this can be seen in Figure 8.1.3, truncation of these sequences resulted in some of the highest binding peptides. For example, HSPLLHK and PLLHK, both truncations of LS2, display the highest binding to CoPt NPs. Whereas truncated sequences of LS2, KTHEIHSPL and KTHEIHS, are favourable for binding to FePt. Different regions of the peptide were identified for binding to the two different materials and so by truncating LS2 it is possible to bind to either CoPt or FePt.

One final similarity between the top sequences is that lysine and histidine are present in almost every sequence. This is to be expected as basic residues were identified as key amino acids from all types of screening carried out.

Metal ion binding

There are some similarities between the top sequences observed for binding to Pt²⁺ and Fe²⁺. These sequences are all based on variations of LS3 generated from positional scanning data. The sequences identified for Pt²⁺ contain methionine residues and those for Fe²⁺ do not. It is

known that a strong interaction occurs between the sulfur group present in methionine and the soft metal centre of Pt whereas Fe is an intermediate metal centre and so would not interact as strongly with sulfur.

Synthesis reaction

When comparing the top sequences from screening against a synthesis reaction the same peptide was identified for both CoPt and FePt, this sequence was KLSLRHD. This is the only example of where the same sequence had the highest SNR for both materials. This suggests that this sequence does not have specificity for one material over the other but could be used equally well in the synthesis of both CoPt and FePt. In contrast sequence GMKPSRP was identified from screening against an FePt synthesis and this sequence did not have high SNR values for a CoPt synthesis reaction, suggesting that this sequence prefers FePt over CoPt. Variations of LS3 that contain methionine were identified from screening against an FePt synthesis reaction and so this suggests that methionine is also likely to play a role during synthesis as well as being important for binding to metal ions.

8.2 PEPTIDE SELECTION AND DESIGN

From the findings of all screening carried out so far, candidate peptides (with high affinity) that could be suitable to promote the synthesis of CoPt and FePt when added to synthesis reactions have been selected and designed. These peptides can be seen in Table 8.2.1. Synthesis was carried out in the presence of three control peptides that are LS1, LS2 and LS3. LS1 and LS2 are the original sequences that were identified from biopanning against L1₀ thin films and NPs of FePt and CoPt respectively and so comparisons to these lead sequences and to literature can be made. A large number of the designed and selected peptides are based on this LS3 and so this peptide was used as a control to allow comparisons to be made between the original and modified sequences.

Three peptides were selected for use in CoPt synthesis reactions and these are: KLSLRHD, KLSLRHMHIHHH and KLSLRMDHIHHH. KLSLRHD was selected as it had the highest SNR of all sequences screened against a CoPt synthesis reaction. Variations of LS3 were also some of the top sequences for binding to Pt²⁺. This sequence also contains a lot of basic residues (lysine, arginine and histidine) which were identified as important from all types of screening. Although an acidic residue is present, and acidic residues were identified as unfavourable, this has been kept as it was this sequence that resulted in the highest SNR value. Sequences KLSLRHMHIHHH and KLSLRMDHIHHH were selected as these sequences were some of the highest binders for Pt²⁺. These peptides will interact with metal precursors during synthesis and so by already having a high affinity for the material it is possible this could influence the

overall synthesis and outcome of the NPs formed. One peptide for CoPt was selected based on its performance from screening against a synthesis reaction and two peptides were selected based on their performance for binding to metal precursors. Therefore, by using these peptides in a CoPt synthesis reaction it will be possible to see if one peptide results in higher quality NPs being produced to allow a fuller understanding.

The three peptides selected for CoPt synthesis were also selected for FePt. KLSLRHD was one of the top sequences identified from screening against an FePt synthesis reaction. Sequences KLSLRMDHIHHH and KLSLRHMHIHHH were identified as important from screening against an FePt and CoPt synthesis reaction and binding to Pt²⁺. It is possible that although these peptides performed well on a peptide array that they could behave differently when used as a free peptide in a synthesis reaction. By using the same peptides for CoPt and FePt it would be possible to see if there is a preference for one material over the other. As well as these three sequences being selected for use in an FePt synthesis reaction, six other peptides have been designed. These sequences can be seen in Table 8.2.1. The designed sequences consist of regions of LS3 and LS4 being combined. The start of LS3 (KLSLRH) was identified as important for both FePt and CoPt synthesis reactions and variations of LS3 were some of the top binders for Pt²⁺. The end of LS4 (GMKPSRP) was another of the top sequences from screening against an FePt synthesis reaction. Therefore, by combining these two regions and using this sequence in a synthesis reaction could result in higher quality NPs being produced. The two regions were combined in different ways so that peptides of different lengths were produced. From screening it was identified that FePt preferred longer peptides and CoPt preferred shorter peptides, so peptides in length from 6 to 13 amino acids were designed. Shorter peptides have been included so that the trends of FePt preferring longer peptides and CoPt giving best results with shorter peptides can be investigated when free peptides are used. Allowing for identification of the effect of peptide length on the quality of NPs synthesised.

All of the peptides designed and selected for use in synthesis reactions incorporate amino acid residues that were identified as important from all types of screening. For example, all of the sequences contain a large number of lysine residues and methionine is present in nearly all of the sequences. As these features were identified from all types of screening, it is important that all these features are incorporated into peptides used in synthesis reactions.

Table 8.2.1 – Designed and selected peptide sequences and which synthesis reactions they will be used in.

Peptide Sequence	Used in CoPt/FePt synthesis reaction
HNKHLPTQPLA – LS1	CoPt and FePt
KTHEIHSPLLHK – LS2	CoPt and FePt
KSLSRHDHIIHHH – LS3	CoPt and FePt
KSLSRHD	CoPt and FePt
KSLSRHMHIHHH	CoPt and FePt
KSLSRMDHIIHHH	CoPt and FePt
KSLSMK	FePt
KSLSMKH	FePt
KSLSMKP	FePt
KSLSMKPRP	FePt
KSLSMKPSRP	FePt
KSLSRHMKPSRP	FePt

8.3 SYNTHESIS OF CoPt USING DESIGNED AND SELECTED PEPTIDES

CoPt NPs were synthesised in a room temperature co-precipitation reaction, with the three selected peptides included in the synthesis as additives, the resulting NPs were analysed using ICP-OES, XRD and VSM. As there are three possible ordered phases that can be synthesised, as well as the disordered A1 phase, a table summarising the characteristic differences between all phases has been included below for reference (Table 8.3.1).

Table 8.3.1 – Table highlighting the difference in characteristic features as determined by XRD and VSM for the L1₂, L1₀ and A1 crystal phases of Pt alloy NPs. XRD peaks in black – common to all phases, red – unique to L1₀, blue – unique to L1₂ and orange – common to both L1₂ and L1₀.^{36,154}

Phase	XRD Planes	Magnetic Properties	Crystal Structure	Particle size /nm	Composition X:Pt
L1₂ XPt₃	(100) (110) (111) (200) (210) (211) (220) (311)	H _c ≈ 0 – 100 Oe Paramagnetic at RT	fcc	15 – 20	25:75
L1₂ X₃Pt	(100) (110) (111) (200) (210) (211) (220) (311)	H _c ≈ 100 – 200 Oe Magnetically soft Ferromagnetic	fcc	10 – 15	75:25
L1₀ XPt	(001) (110) (111) (200) (002) (201) (112) (220) (202) (311)	H _c ≈ 1 – 10 kOe Magnetically hard	fct	2 – 10	50:50
A1 XPt₃, X₃Pt and XPt	(111) (200) (220) (311) (222)	Almost no H _c at room temperature	fcc	Variable	Variable

ICP-OES was first used to investigate the molar ratio of cobalt and platinum in the final NP product for each sample. There is some variation between the samples, the lowest contains 39% cobalt whilst the highest has 52% cobalt. CoPt NPs synthesised in the absence of any

peptides contain 40% cobalt and so it was expected that by synthesising the NPs in the presence of peptide this could alter the ratio of Co to Pt. LS2 achieved the closest to the desired 50:50 ratio with a ratio of 48:52 suggesting that the peptide has altered the overall composition of the NPs. Here the presence of the peptide has had a positive effect on the ratio, this is also the case for sequences KLSRHD and KLSRHMHIHHH. Whereas LS1, LS3 and KLSRMDHIHHH had no real effect on the overall ratio compared to the control. It is possible that peptides with high affinity for Pt²⁺ could bind to Pt before initial nucleation of the NPs takes place. This would result in more Pt and a lower amount of Co present in the final NP composition. LS1 and LS3 both had high SNR values for binding to Pt²⁺ and so this could explain why a lower molar percentage of cobalt is present in the final synthesised NP. Whereas LS2 had a much lower binding intensity to Pt²⁺ and so it is likely that this peptide will have bound to both cobalt and platinum ions more evenly before nucleation took place, this would account for the closer ratios of cobalt to platinum. Sequence KLSRHD also had a low affinity for Pt²⁺ and this could explain why the ratio is closer to 50:50. Conversely, KLSRMDHIHHH had one of the highest affinities for binding to Pt²⁺ and there is less cobalt present in the final composition of the NP. The only peptide that does not fit this is KLSRHMHIHHH as this sequence also had one of the highest affinities for Pt²⁺, but here an increase in the amount of cobalt is observed compared to the control. It is possible that there could be an interplay between binding to Co²⁺ and Pt²⁺ during the initial step of the reaction, however as it was not possible to collect Co²⁺ binding data it is difficult to understand the peptides interaction with Co²⁺. As control NPs already had a ratio of 40:60 to begin with this is likely to be due to using a starting ratio of 3:1 suggesting that this ratio is required to synthesise NPs closer to 50:50 in composition and that inclusion of peptides with a lower binding affinity for Pt²⁺ makes it possible to alter this ratio further.

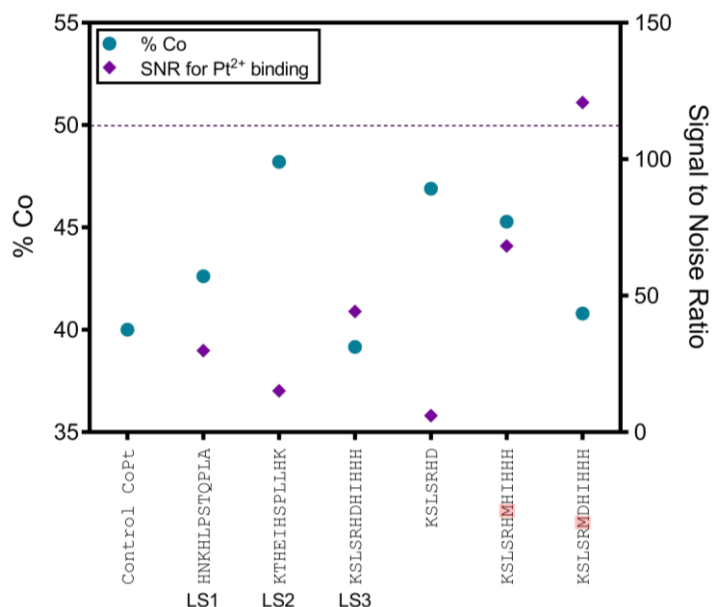


Figure 8.3.1 – ICP-OES data (circle) for CoPt NPs synthesised in the presence of different peptides plotted against signal to noise ratio data (diamond) for peptides binding ability to Pt²⁺. Purple dotted line represents ideal 50:50 ratio.

From ICP-OES data it is not possible to determine whether the ordered (L1₀/L1₂) or disordered (A1) phase was synthesised. Therefore, crystallographic analysis of the particles was performed using XRD. Peaks in the spectrum were compared to known standards for L1₀, L1₂ and A1 phase CoPt. The XRD spectrum shows peaks at 2θ = 40.2°, 46.8°, 68.4° and 82.3° which correspond to the (111), (200), (220) and (311) planes of CoPt. These planes are consistent with A1 phase CoPt, suggesting that synthesis of CoPt in the presence of the selected peptides resulted in the formation of A1 phase CoPt as the dominant product. By combining XRD and ICP-OES data it is possible to identify the phase and structure of the NPs formed. ICP-OES data suggests that NPs synthesised in the presence of LS2, KSLSRHD and KSLSRHMHIIHH are CoPt and from XRD it is known they are in the A1 phase. All other samples are also in the A1 phase but consist of a different ratio of Co to Pt and so 50:50 CoPt was not achieved. These samples typically consist of Co₄₀Pt₆₀ and the presence of LS2, KSLSRHD and KSLSRHMHIIHH is likely responsible for the formation of A1 CoPt rather A1 Co₄₀Pt₆₀.

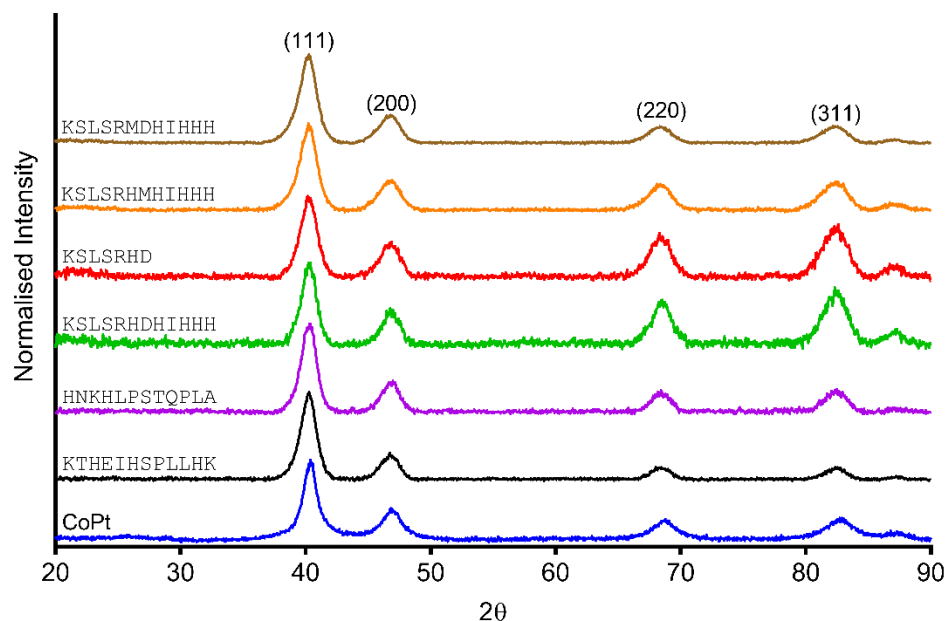


Figure 8.3.2 – X-ray diffraction data for CoPt nanoparticles synthesised in the presence of peptides. Characteristic planes of CoPt are labelled.

The Scherrer equation was used to estimate the particle size from the (111) peak (most prominent peak) and the results can be seen in Table 8.3.2. All samples have particle sizes between 6 – 8 nm which is typical for CoPt NPs. There is also little variation between samples suggesting that the presence of different peptides has not greatly affected the size of the NPs produced. It is expected that NPs with a composition of CoPt would have smaller particle sizes and those for CoPt₃ have larger particle sizes. None of the NPs synthesised here are truly CoPt₃ but have a composition of Co₄₀Pt₆₀ as this is not too far away from the 50:50 composition it is likely that similar particle sizes will be observed.

Table 8.3.2 – Particle sizes calculated using the Scherrer equation for FePt NPs synthesised in the presence of different peptides.

Sample	Particle size calculated from the Scherrer equation /nm
CoPt	7.28
HNKHLPSQTPLA – LS1	7.27
KTHEIHSPLLHK – LS2	7.27
KSLSRHDHIHHH – LS3	6.78
KSLSRHD	6.35
KSLSRHMHIHHH	5.98
KSLSRMDHIHHH	6.36

Finally, room temperature VSM was used to investigate the magnetic properties of all NPs synthesised. VSM (Figure 8.3.3) shows that all particles exhibit hysteresis, and all NPs produced in the presence of peptides have a higher coercivity than NPs synthesised in the absence of peptides.

Control CoPt NPs had a coercivity of 15 Oe and this is consistent with A1 phase CoPt₃. NPs synthesised in the presence of LS2 (KTHEIHSPLLHK) had a coercivity of 80 Oe and so an approximately 5 times increase in coercivity is observed. When LS2 was incorporated into MjHSP a coercivity of 41 Oe was obtained (chapter 3.4), therefore this suggests that by using the free peptide it is possible to achieve higher coercivities than when the peptide is constrained in a protein cage.

LS1 (HNKHLPTQPLA) gave the smallest increase in coercivity (from 15 Oe to 30 Oe). However, LS1 was identified from screening against L1₀ FePt. This result shows LS2 is specific to FePt for synthesis and this is echoed in the binding data comparison. So, using this peptide in a CoPt synthesis reaction instead could suggest why only a small increase in coercivity is observed.

LS3 (KSLSRHDHIIHH) resulted in a coercivity of 84 Oe, this is a slight increase on the coercivity obtained from LS2. LS3 was also identified from screening against L1₀ phase FePt, however throughout peptide array screening it has shown high affinity for CoPt. Incorporation of KSLSRHD, a truncated sequence of LS3, into a synthesis reaction resulted in a coercivity of 94 Oe being achieved. This is an increase in coercivity of 10 Oe compared to LS3, suggesting that a shorter peptide is superior in directing the synthesis of CoPt NPs.

Two other variations of LS3 were used in the synthesis of CoPt NPs and increased coercivities were obtained compared to control CoPt (15 Oe) and LS3 (84 Oe). Sequence KSLSRMDHIIHH resulted in the largest increase in coercivity and a value of 107 Oe was obtained and sequence KSLSRHMIIHH resulted in a coercivity of 104 Oe. The increase in coercivity for both these sequences compared to LS3 is due to the incorporation of methionine as this is the only difference between the sequences. From peptide array screening methionine was shown to be important for binding to Pt²⁺ and involved in synthesis reactions. Therefore, the increase in coercivity obtained when using peptides containing methionine confirms the trends identified from peptide array screening and suggests that methionine plays a role in the synthesis of CoPt NPs. Peptides KSLSRMDHIIHH and KSLSRHD both contain aspartic acid, although aspartic acid was identified as unfavourable from peptide array screening, these peptides had some of the highest affinities for Pt²⁺ and a CoPt synthesis reaction. Using these peptides in a synthesis reaction has not had a detrimental effect on the quality of NPs produced. This suggests that the presence of other favourable amino acids (i.e. methionine) in the sequence outweigh the negative effect of aspartic acid.

By incorporating peptides into the synthesis of CoPt NPs it was possible to increase coercivity from 15 Oe up to 107 Oe. Although larger coercivity values would be required for bit patterned media, this increase is still substantial as the majority of CoPt NPs synthesised at room temperature in literature have very low or no coercivity when measured using room temperature VSM.^{42,51,77,155}

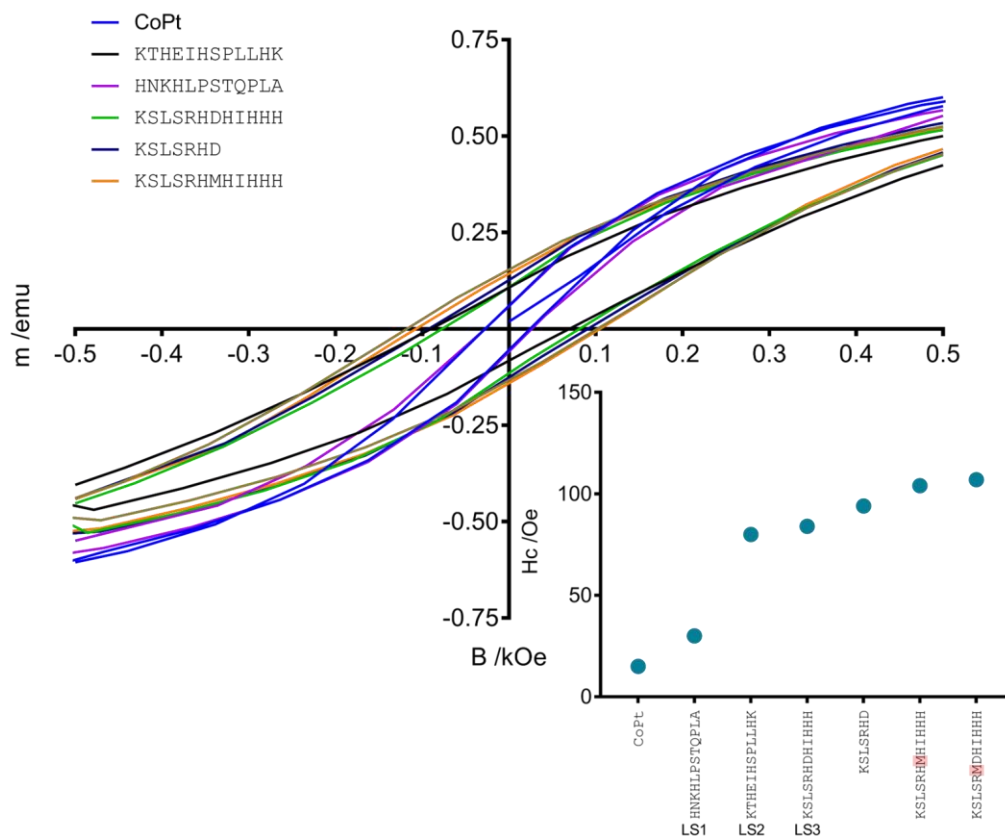


Figure 8.3.3 – Room temperature (290 K) vibrating sample magnetometry data for CoPt NPs synthesised in the presence of peptides. X axis – normalised magnetic moment and Y axis – magnetic field strength in kOe. Inset figure shows coercivity values for each sample.

8.4 SYNTHESIS OF FePt USING DESIGNED AND SELECTED PEPTIDES

Designed and selected peptides were incorporated into the synthesis of FePt NPs. NPs were synthesised using a room temperature co-precipitation method and resultant NPs were characterised using ICP-OES, XRD and VSM.

Synthesised NPs were first characterised using ICP-OES to determine the molar ratios of Fe to Pt. Control FePt (synthesised in the absence of any peptides) had a ratio of 40:60. The ratio for all samples synthesised in the presence of peptides highlighted two distinct regions, either being consistent with FePt or FePt₃. There are four samples (KLSMK, KLSMKH, KLSMKP and KLSMKPRP) that have a ratio that is much closer to the ideal 50:50. This suggests that these NPs are consistent with FePt. Whereas samples that have a ratio of approximately 20:80 are consistent with the formation of FePt₃. This is true for NPs

synthesised in the presence of LS1, LS2, L3, KLSLRHD, KLSLMKPSRP, KLSRHMKPSRP, KLSRHMHIHHH and KLSRMDHIHHH. Unlike for CoPt there is no correlation between the final amount of Pt in the sample and the peptides ability for binding to Pt^{2+} , there is also no link between the amount of Fe in the sample and the peptides ability for binding to Fe^{2+} . ICP-OES can only determine the molar ratio of iron and platinum present in the sample and cannot give information about what crystal phase the NPs are in, therefore XRD was used to determine which crystallographic phase was synthesised.

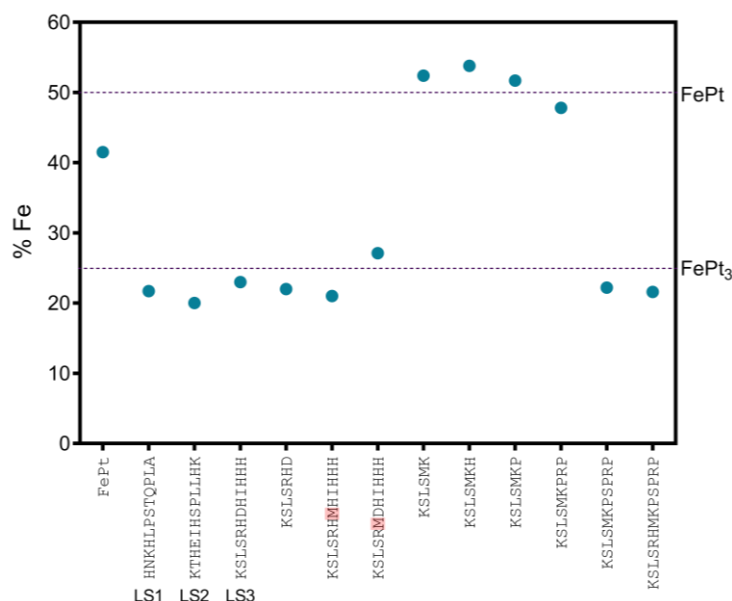


Figure 8.4.1 – ICP-OES data for FePt NPs synthesised in the presence of different peptides. Dotted line represents ratio expected for FePt and FePt₃.

Crystallographic analysis of the particles was performed using XRD. The peaks in the spectrum at $2\theta = 40.2^\circ$, 46.7° , 68.4° and 82.4° correspond to the (111), (200), (220) and (311) planes of FePt. These planes are consistent with A1 phase FePt, lack of L1₀ character is observed due to absence of peaks at 25° and 35° relating to the (001) and (110) planes. This is the case for all samples characterised suggesting that A1 phase FePt NPs were synthesised. From both XRD and ICP-OES data it was determined that a mixture of A1 FePt and A1 FePt₃ were synthesised, depending on which peptide was present. Shorter peptide sequences KLSLMK, KLSLMKH and KLSLMKP resulted in the formation of A1 CoPt NPs, from peptide array screening it was highlighted that FePt preferred longer peptide sequences. However, this may not be the case when the free peptides are used in a synthesis reaction rather than anchored to the membrane, as using these peptides a composition closer to the ideal was achieved.

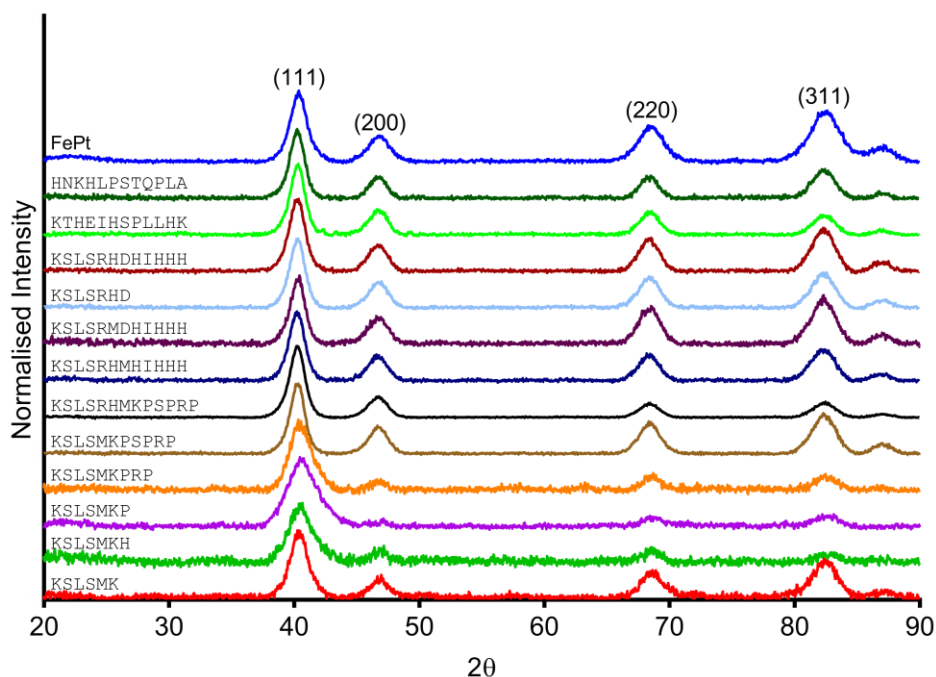


Figure 8.4.2 – X-ray diffraction data for FePt NPs synthesised in the presence of different peptides. Characteristic planes of FePt are labelled.

The Scherrer equation has been used to calculate particle size using the (111) peak, results from this can be seen in Table 8.4.1. Control FePt NPs synthesised in the absence of peptide have a calculated particle size of 5.36 nm and this is consistent with literature values for FePt NPs. There is variation in the calculated particle size with some samples having diameters up to ≈ 25 nm, with the majority having a diameter of ≈ 20.3 nm. These particle sizes are larger than would be expected for FePt NPs, typically diameters in the range 4 – 10 nm are observed. Larger NP sizes are consistent with the formation of FePt₃ rather than FePt. From ICP-OES data all samples that have a diameter of ≈ 20 nm were identified as FePt₃, therefore the presence of larger particle sizes further confirms this. In contrast, smaller diameters (4 – 6 nm) indicate that FePt was synthesised. Peptides KLSLSMK, KLSLSMKH, KLSLSMKP and KLSLSMKPRP all have diameters between 4 – 6 nm and from ICP were determined to be FePt. Composition of the NPs determined from calculated particle sizes matches well with the composition determined using ICP-OES and so confirming that a mixture of FePt₃ and FePt NPs were synthesised.

Table 8.4.1 – Particle sizes calculated using the Scherrer equation for FePt NPs synthesised in the presence of different peptides, their suggested composition based on particle size and composition determined by ICP-OES.

Sample	Calculated particle size from Scherrer equation /nm	Suggested composition from particle size	Composition determined by ICP-OES
FePt	5.36	FePt	40:60
HNKHLPSTQPLA – LS1	16.93	FePt ₃	22:78
KTHEIHSPLLHK – LS2	20.32	FePt ₃	20:80
KSLSRHDHIIHHH – LS3	20.32	FePt ₃	23:77
KSLSRHD	20.32	FePt ₃	22:78
KSLSRHMHIHHH	20.32	FePt ₃	21:79
KSLSRMDHIIHHH	25.48	FePt ₃	27:73
KSLSMK	5.99	FePt	52:48
KSLSMKH	5.98	FePt	54:46
KSLSMKP	3.64	FePt	52:48
KSLSMKPRP	5.09	FePt	48:52
KSLSMKPSRP	20.29	FePt ₃	22:78
KSLSRHMKPSRP	20.32	FePt ₃	22:78

Finally, room temperature VSM (Figure 8.4.3) was collected for all samples. VSM data shows that FePt synthesised in the presence of peptides exhibit hysteresis and have increased coercivities compared to the control. FePt NPs synthesised in the absence of any peptide have a coercivity of 11 Oe and this is consistent with literature.

The highest coercivities were achieved by using LS1 and KSLSMKPSRP as these gave coercivities of 141 and 140 Oe respectively. Compared to control FePt NPs this is an approximately 15 times increase in coercivity. It was expected that LS1 would produce a high coercivity value as this peptide was originally selected from screening against L1₀ phase FePt. The lowest coercivity observed was from use of LS2 (KTHEIHSPLLHK) which resulted in a value of 36 Oe, which is accounted for by the fact that this peptide was not originally selected for FePt but for CoPt.

LS3 resulted in a coercivity of 114 Oe, this peptide was also originally selected for FePt and so the fact a large increase is observed is understandable. When truncated sequence KSLSRHD was used a coercivity of 125 Oe was obtained. Truncation of LS3 resulted in an increase in coercivity by 11 Oe, suggesting that the full-length peptide is not required to affect the final synthesised NP. Previously, from peptide array screening it was identified that FePt preferred longer peptides however this does not seem to be the case when free peptides are incorporated into synthesis reactions. Two other variations of LS3 were also used, KSLSRHMHIHHH and KSLSRMDHIIHHH, these peptides were selected due to their high affinity for Pt²⁺ and an FePt synthesis reaction. However, when these peptides were used in a synthesis reaction a much lower coercivity was observed compared to LS3. KSLSRHMHIHHH

and KLSRMDHIIHHH had coercivities of 67 Oe and 60 Oe respectively. These coercivities are approximately half that of LS3. This suggests that although these peptides were identified as favourable from peptide array screening, they do not interact in the same way when used as free peptides in a synthesis reaction.

Peptide KLSMKPSRP gave the highest coercivity of 141 Oe, whilst shorter sequences containing a similar region of the sequence resulted in lower coercivities (KLSMK and KLSMKP). Therefore, it is unlikely to be this region of the peptide that gives rise to the increased coercivity observed. Sequence KLSMKPRP also has a low coercivity of ≈ 50 Oe, the only difference between this sequence and KLSMKPSRP is the extra proline and serine residue. It is possible that inclusion of these two residues has an effect on the NPs produced and could result in the increased coercivity.

It would be expected that samples that were identified as A1 FePt would have higher coercivity values than those that were identified as A1 FePt₃. Here samples that were identified (KLSMK, KLSMKH, KLSMKP and KLSMKPRP) as being A1 FePt from XRD and ICP data generally had lower coercivities than expected. This could be accounted for by the fact that although A1 FePt has a closer ratio to what would be desired for L1₀ FePt compared to A1 FePt₃, currently no change in phase has occurred and so lower coercivity values are still observed.

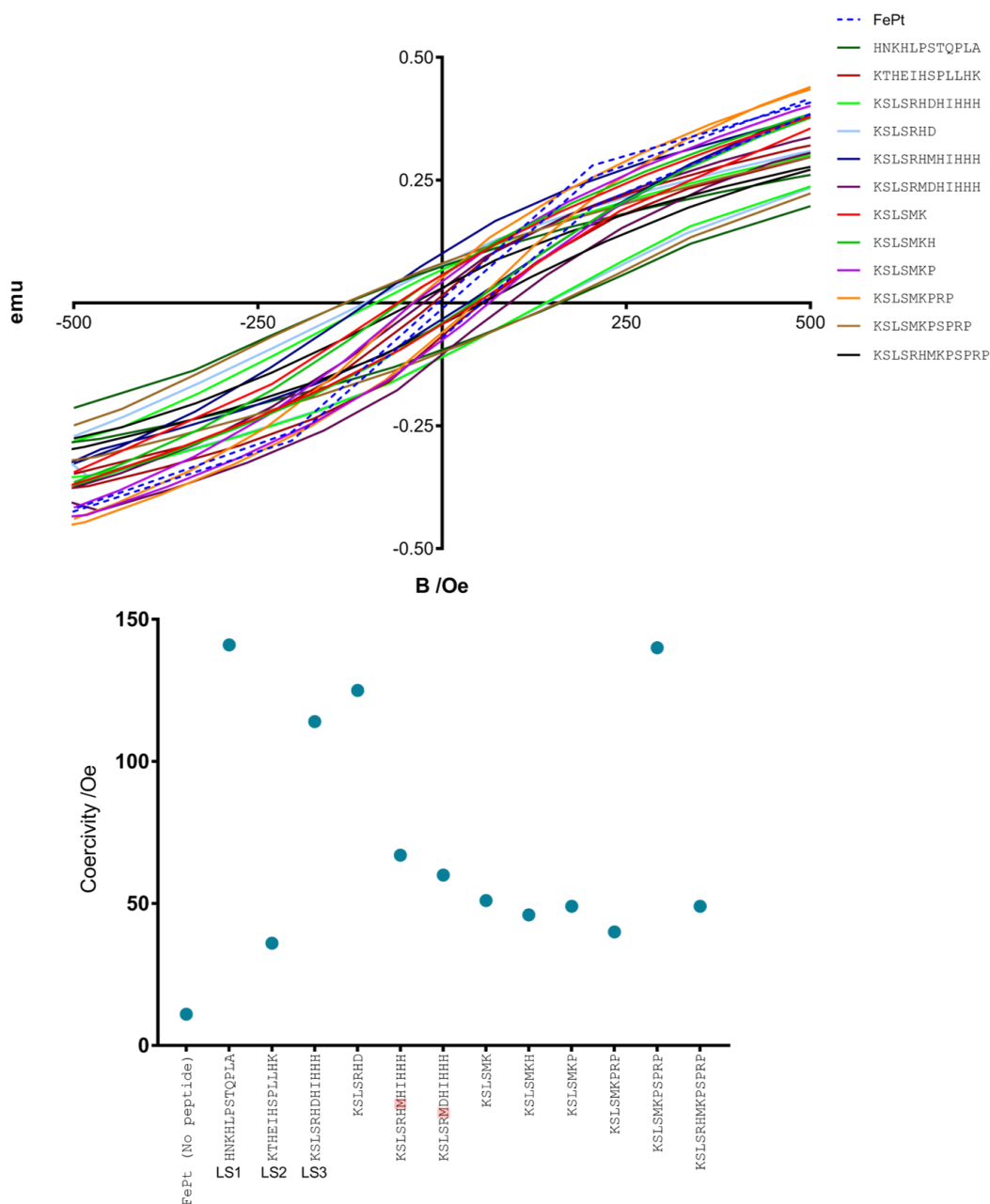


Figure 8.4.3 – **Top:** Room temperature (290 K) VSM data for FePt NPs synthesised in the presence of designed and selected peptides. X axis is magnetic field strength (Oe) and Y-axis is normalised emu. **Bottom:** coercivity values for each sample in oersteds.

8.5 SYNTHESIS OF CoPt WITH PEPTIDES AND BISMUTH DOPING

This section brings together the results obtained from bismuth doping and NPs synthesised in the presence of different peptides. The peptides that resulted in the highest coercivity when used in a CoPt synthesis reaction have now been combined with bismuth doping at 2%. Bismuth doping was chosen as this resulted in the largest increase in coercivity when incorporated into the synthesis of CoPt NPs (chapter 4.3.2), a value of 148 Oe was obtained. Therefore, by combining the use of peptides and bismuth doping it may be possible to increase the coercivity further. Peptides KSLSRHD and KSLSRMDIIHHH were chosen as these

peptides resulted in NPs that had coercivities of 94 and 107 Oe respectively. NPs synthesised in the presence of these two peptides and 2% bismuth were then characterised using ICP-OES, XRD and VSM.

ICP-OES data was collected to investigate the effect that incorporation of bismuth into the synthesis had on the final NP composition (Figure 8.5.1). NPs synthesised in the presence of peptides and 2% bismuth had a higher percentage of cobalt present than those synthesised in the absence of bismuth. Bismuth doping carried out with peptide KLSRHD resulted in 1.97% bismuth present in the NPs and as 2% bismuth (by volume) was added during the synthesis this fits well. Whereas when bismuth doping was carried out with peptide KLSRMDHIHHH this resulted in 5% bismuth present in the sample. Bismuth has a lower solubility than cobalt and platinum and the fact that more bismuth was incorporated is surprising, in all other cases where bismuth doping was carried out a slightly lower than expected amount of bismuth was incorporated.

NPs produced only in the presence of KLSRMDHIHHH had a ratio of 40:60 whereas when the peptide was combined with bismuth doping a ratio of 58:37:5 was obtained. Here the ratio of cobalt to platinum has reversed and there is now more cobalt present than platinum. This suggests that the sample is approaching a composition that is more consistent with a function of Co_3Pt rather than a component of CoPt_3 . This change in ratio could be due to bismuth displacing some of the platinum from the sample.

When peptide KLSRHD was used with bismuth doping a ratio of 55:43:2 was obtained, when this peptide was used in the synthesis alone (no bismuth doping) a ratio of 47:53 was observed. In both cases these ratios suggest that CoPt and not CoPt_3 was synthesised. Therefore, incorporation of bismuth into the synthesis results in a more even ratio of cobalt and platinum being incorporated. This may be due to bismuth displacing some of the platinum and promoting the formation of CoPt (50:50 ratio).

It can also be noted that when a longer peptide was used more bismuth was incorporated into the final NP. As this trend has only been observed for one sample, further testing would be required to investigate this, and this could include carrying out the synthesis in the presence of other longer peptide sequences.

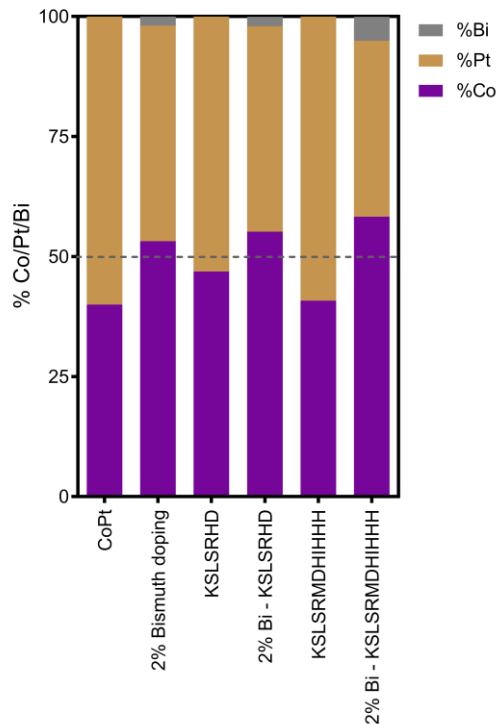


Figure 8.5.1 – ICP-OES data for CoPt NPs synthesised in the presence of peptides and the presence of peptides and 2% bismuth doping. Purple – molar percentage of cobalt, yellow – molar percentage of platinum and grey – molar percentage of bismuth.

To understand what crystal phase is present in the NPs, XRD was carried out. The peaks in the XRD spectrum at $2\theta = 39.9^\circ$, 46.3° , 67.7° and 81.8° correspond to the CoPt planes: (111), (200), (220) and (311). These planes are consistent with A1 phase CoPt and there are no peaks present to indicate any $L1_0$ or $L1_2$ character in the particles. There are no significant peaks present that represent bismuth, this is to be expected as bismuth is added to the synthesis in low amounts. Therefore, this suggests that incorporation of bismuth does not adversely affect the synthesis but has also not resulted in any discernible crystal phase changes (disordered to ordered) of the NPs visible from XRD. Combining the use of peptides and bismuth doping has resulted in the formation of A1 CoPt and A1 Co_3Pt .

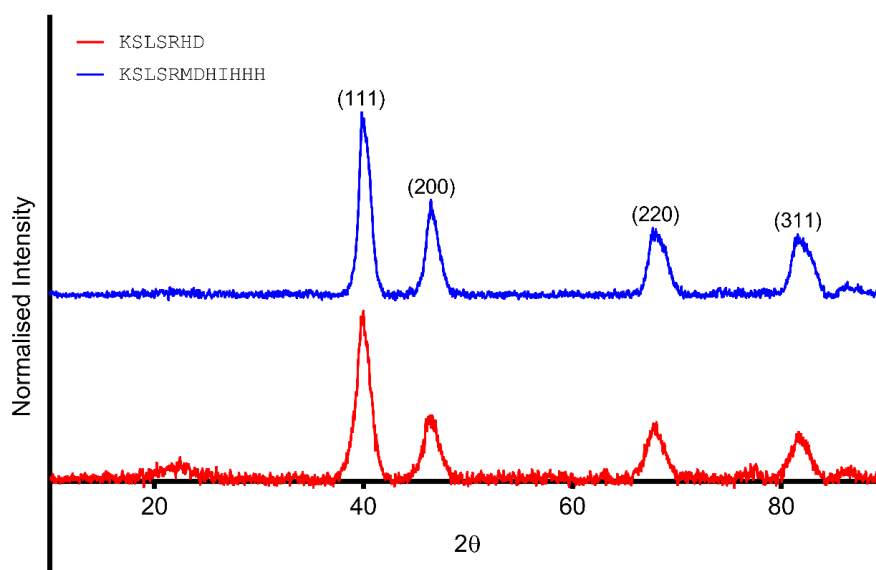


Figure 8.5.2 – XRD data for CoPt NPs synthesised in the presence of peptides KLSLRHD (red) and KLSRMDHIHHH (blue) and 2% bismuth doping. Planes characteristic of CoPt are labelled. Broad peak at $\approx 20^\circ$ is from glass capillary.

Particle size was estimated using the Scherrer equation based on the (111) peak and results can be seen in Table 8.5.1. Sequence KLSLRHD resulted in slightly smaller NPs being formed than sequence KLSRMDHIHHH. However, there is not a significant difference between the two samples and both particle sizes are consistent with literature values. Comparing KLSLRHD to 2% bismuth doped CoPt (11.3 nm) a decrease in particle size is observed suggesting that the presence of the peptide in the synthesis has resulted in the formation of smaller NPs. KLSRMDHIHHH has been compared to 5% Bi CoPt as from ICP-OES it was determined that this sample contained 5% Bi rather than the 2% Bi expected, it can be noted that the two samples have very similar particle sizes (7.80 nm and 7.78 nm).

Table 8.5.1 – Particle sizes calculated using the Scherrer equation for CoPt NPs synthesised in the presence of different peptides and 2% bismuth doping.

Sample	Particle size calculated using the Scherrer equation /nm
CoPt	7.28
2% Bi doped CoPt	11.3
5% Bi doped CoPt	7.80
2% Bi doping and KLSLRHD	6.74
2% Bi doping and KLSRMDHIHHH	7.78

Room temperature VSM (Figure 8.5.3) was performed for NPs synthesised in the presence of both peptides and compared to control CoPt NPs, particles synthesised only in the presence of the peptides (without bismuth doping) and particles synthesised only in the presence of bismuth. Sequence KLSLRHD resulted in a coercivity of 84 Oe being obtained, this is significantly higher than control CoPt NPs (15 Oe) but is lower than NPs synthesised

only in the presence of KLSRHD (94 Oe). NPs synthesised in the presence of 2% bismuth alone (without peptide) resulted in a coercivity of 148 Oe. This suggests that in this case incorporation of bismuth alone, without the use of peptides, may be more beneficial for achieving higher coercivities. It was thought that by combining the effects of bismuth doping and using peptides a larger coercivity would be obtained, this was not observed for peptide KLSRHD. However, this could be explained by bismuth doping only being optimised for CoPt alone and not for synthesis of CoPt in the presence of peptides. Therefore, optimisation of this could result in a different amount of bismuth that is required to increase coercivity.

VSM data for sequence KLSRMDHIHHH and bismuth doping resulted in a coercivity of 125 Oe, this is a significant increase compared to control CoPt NPs (15 Oe) and also an increase on when the peptide is used without bismuth doping (107 Oe). NPs produced in the presence of KLSRMDHIHHH and bismuth doping were identified to be A1 phase Co_3Pt , this composition is known to be more magnetically soft than CoPt_3 (paramagnetic) and so a larger value for coercivity would be expected. From ICP-OES data it was identified that the sample generated from bismuth doping and presence of the peptide resulted in $\approx 5\%$ bismuth being incorporated into the final NP. As a result, VSM data has been compared to 5% bismuth doping (without peptide) instead of the 2% sample. The 5% bismuth doped sample is known to have $\approx 5\%$ bismuth present and so a direct comparison between bismuth doping in the presence and absence of peptide can be made. Bismuth doping alone resulted in a coercivity of 55 Oe whereas bismuth doping and peptide had a coercivity of 125 Oe. Therefore, in this case combination of bismuth and peptides resulted in an ≈ 2.3 times increase in coercivity.

By using KLSRMDHIHHH and bismuth doping coercivity was increased by 41 Oe compared to when KLSRHD was used in combination with bismuth doping. From ICP-OES data it is known that $\approx 5\%$ bismuth was incorporated for KLSRMDHIHHH and only 2% for KLSRHD, this increase in the amount of bismuth incorporated could be why a larger coercivity is observed. This would also support the need for further optimisation of bismuth doping when carried out in the presence of peptides, as it may be that a higher level of doping is required to achieve increases in coercivity.

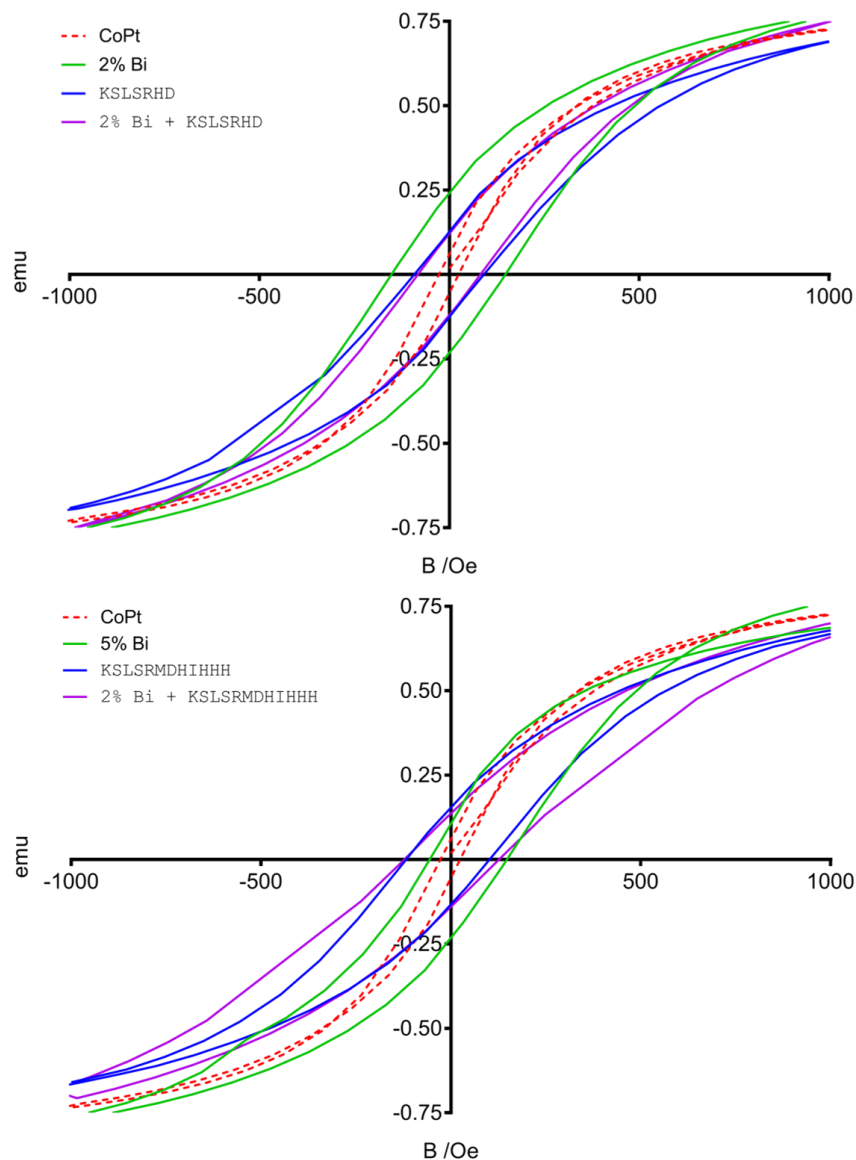


Figure 8.5.3 – Room temperature (290 K) VSM data. CoPt NPs (red), 2% Bi or 5% doped CoPt (green), NPs synthesised in presence of peptide (blue) and NPs synthesised in presence of peptide and 2% bismuth (purple).

8.6 SYNTHESIS OF FePt WITH PEPTIDES AND BISMUTH DOPING

Peptides KLSMKPSRP and KLSLRHD have been combined with bismuth doping in an FePt synthesis reaction. These peptides were chosen as they resulted in the formation of NPs with the highest coercivities of 140 and 125 Oe respectively. Again, bismuth doping was carried out at 2% as this achieved the highest coercivity increase when used in an FePt synthesis reaction, a coercivity of 278 Oe was obtained.

ICP-OES data was collected to investigate the effect that incorporation of bismuth into the synthesis had on the overall NP composition (Figure 8.6.1). NPs that were synthesised in the presence of peptides and bismuth have a much higher overall percentage of iron present than NPs synthesised only in the presence of peptides. Both samples have 1% of bismuth

present, this is lower than expected as 2% bismuth (by volume) was added to the synthesis, suggesting that bismuth is not being incorporated as easily. As bismuth has a lower solubility than both iron and platinum this could help to explain why less bismuth was incorporated.

Incorporation of bismuth appears to be important for controlling the ratio of Fe to Pt, comparing the synthesis with peptide alone to peptide and bismuth doping combined a large change in the composition of the NPs is observed. Previously, using only peptides FePt₃ was synthesised whereas when bismuth was incorporated as well as the peptide this resulted in the formation of FePt. This change in composition could be due to bismuth displacing some of the platinum present in the sample and promoting formation of FePt rather than FePt₃.

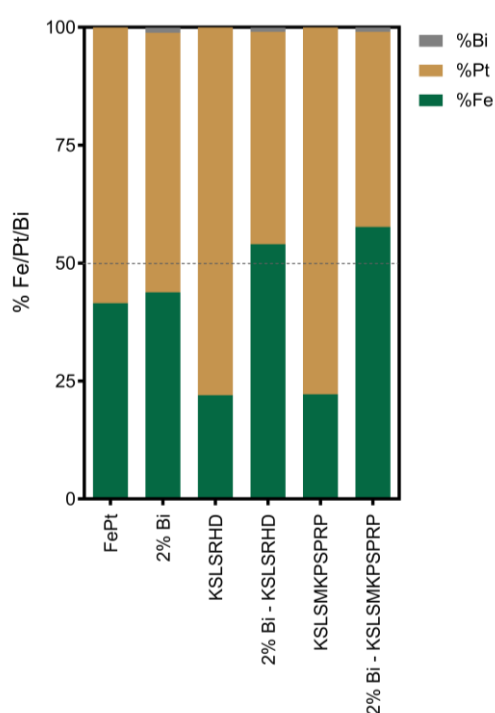


Figure 8.6.1 - ICP-OES data for FePt NPs synthesised in the presence of peptides and the presence of peptides and 2% bismuth doping. Green – molar percentage of iron, yellow – molar percentage of platinum and grey – molar percentage of bismuth.

To identify what phase the NPs were in the NPs were characterised using XRD. Peaks in the spectrum at $2\theta = 39.9^\circ$, 46.2° , 67.8° and 81.6° correspond to the (111), (200), (220) and (311) planes of FePt. These planes are consistent with A1 phase FePt, the characteristic peaks for L1₀ and L1₂ phase FePt are not present. In the spectrum for bismuth doped NPs synthesised in the presence of KLSMKPSRPP there are three extra peaks (marked with *) that are likely to be due to the presence of small amounts of bismuth or BiPt complexes that have formed during synthesis. XRD and ICP-OES data suggest that A1 phase FePt NPs were synthesised in both cases, but synthesis in the presence of KLSMKPSRPP also resulted in the formation of small amounts of BiPt complexes also.

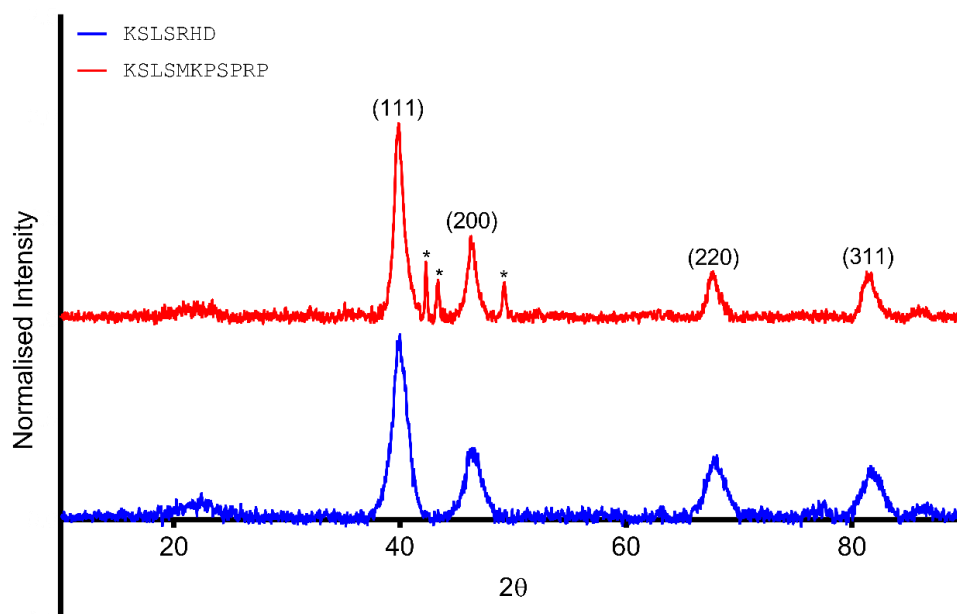


Figure 8.6.2 – XRD data for FePt NPs synthesised in the presence of peptides KLSLRHD (blue) and KLSMKPSRP (red). Characteristic planes of FePt are labelled. * peaks caused by presence of Bi or BiPt in sample.¹⁵⁷ Broad peak at $\approx 20^\circ$ is from glass capillary.

The Scherrer equation was used to calculate particle size (Table 8.6.1). Both particles synthesised in the presence of bismuth and peptides have a larger particle size than control FePt. Although these particle sizes are larger, they are still in the expected range for FePt NPs. Comparing particle size to NPs synthesised in the presence of only the peptides a smaller particle size is observed when bismuth doping is carried out also. This suggests that the presence of bismuth has altered the composition of the NPs (FePt₃ to FePt) and also reduced the size. Smaller NP sizes are typical of FePt and FePt₃ typically have larger particle sizes. This further confirms the change from FePt₃ to FePt.

Table 8.6.1 – Particle sizes calculated using the Scherrer equation for FePt NPs synthesised in the presence of different peptides and 2% bismuth doping.

Sample	Particle size calculated using the Scherrer equation /nm
FePt	5.36
2% Bi doped FePt	6.37
2% Bi doping and KLSLRHD FePt	7.23
2% Bi doping and KLSMKPSRP FePt	10.12
KLSLRHD	20.32
KLSMKPSRP	20.29

Room temperature VSM (Figure 8.6.3) was performed for both peptides and compared to control FePt NPs as well as NPs synthesised in the presence of only the corresponding peptide. KLSLRHD and 2% bismuth doping resulted in a coercivity of 160 Oe and sequence KLSMKPSRP resulted in a coercivity of 167 Oe. Both of these samples show an increase in coercivity compared to when only peptide alone is used and control CoPt NPs, suggesting

that the presence of bismuth has had an effect on the coercivity. However, although an increase in coercivity is observed neither sample has resulted in a coercivity that is higher than 2% bismuth doped particles (278 Oe). Therefore, this suggests that using bismuth doping alone, without the presence of peptides, would be more beneficial to achieve higher coercivity values. It is possible that further optimisation of bismuth doping in the presence of peptides may need to be carried out to ensure that the correct bismuth doping level is used to achieve maximum coercivity. However, as incorporation of bismuth into the synthesis reaction vastly improves the ratios of Fe to Pt in the NP, the level of bismuth doping required is likely to not be too far away from the current level of doping (2%).

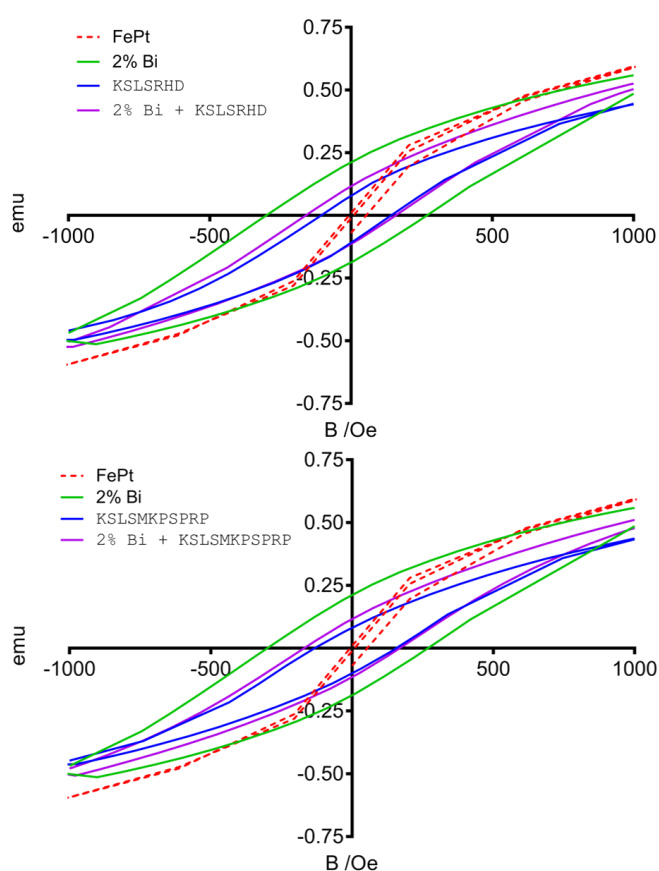


Figure 8.6.3 – Room temperature (290 K) VSM data. FePt NPs (red), 2% Bi doped FePt (green), NPs synthesised in presence of peptide (blue) and NPs synthesised in presence of peptide and 2% bismuth (purple).

8.7 SUMMARY AND DISCUSSION

From all peptide array screening carried out it was possible to identify key trends for both CoPt and FePt, as well as there being similarities and differences between the two materials. The main similarities between the two materials were the importance of basic residues and methionine for binding to NPs, metal precursors and involvement in a synthesis reaction. Another similarity was the adverse effect that glutamic acid has on sequences for both materials. The key difference between the two is that CoPt prefers shorter peptides whilst

FePt prefers longer peptides. One sequence (KLSLRHD) was identified as suitable for both CoPt and FePt from screening against a synthesis reaction, this was the only example of where the same sequence was favourable both materials. These identified trends were then used to select and design peptides that would be suitable for use in CoPt and FePt synthesis reactions. This resulted in three peptides for CoPt and nine peptides for FePt being used in a synthesis reaction. The resulting NPs were then characterised so that the effect of the peptide could be determined.

One trend identified from the inclusion of peptides in CoPt synthesis was that peptides which had a higher affinity for binding to Pt^{2+} resulted in the formation of CoPt NPs with a reduced cobalt content. Whilst those that had a lower affinity for Pt^{2+} resulted in the formation of NPs with a higher cobalt content. This suggests that the peptide is involved in binding to the metal precursors prior to nucleation of the particles and that the peptide plays a direct role in the overall composition of the NPs. A possible mechanism for the synthesis of CoPt NPs could be that precursor metal ions are binding to the peptide creating a nucleation site and on addition of a reducing agent nucleation occurs and NP synthesis and growth occurs. Two peptides, KLSLRHD and KLSLRHMHIHHH, resulted in a composition that was consistent with CoPt rather than $CoPt_3$ which was observed for all other peptides. This suggests that these peptides have influenced the final composition of the NPs.

Shorter peptide KLSLRHD had an increased coercivity compared to its parent sequence, LS3, suggesting that shorter peptide sequences could be favourable for use in CoPt synthesis reactions. Therefore, confirming the trend that shorter peptides were favourable for CoPt identified from peptide array screening. Although the presence of peptides has altered the composition of the NPs formed, a change to the crystal structure was not observed and NPs are still in the A1 phase. However, the quality of the NPs was improved as a seven times increase in coercivity was achieved compared to control NPs (15 Oe), by using peptide KLSLRMDHIHHH (107 Oe). From peptide array screening it was found that methionine was an important residue from all screening carried out. Peptides used in a CoPt synthesis reaction that contained methionine resulted in the highest coercivities, KLSLRMDHIHHH and KLSLRHMHIHHH gave a coercivity of 107 Oe and 104 Oe respectively. Therefore, confirming that methionine is an important residue and plays a role in the synthesis of CoPt NPs.

When the designed and selected peptides were used in an FePt synthesis reaction there were four peptide sequences that resulted in the formation of FePt. These peptides were: KLSLSMK, KLSLSMKH, KLSLSMKP and KLSLSMKPRP. Whereas all other peptides used resulted in the

formation of FePt₃, typically the peptides that resulted in formation of FePt were shorter in length and also consisted of similar amino acids (KSLSMK). This could suggest that these features of the peptide are important during synthesis. Unlike for CoPt NPs it was difficult to draw any conclusions between the peptides ability to bind to Fe²⁺ or Pt²⁺ from peptide array screening and the final composition of the NP. From peptide array screening longer peptides were identified as favourable for FePt and so the fact that shorter peptides may alter the composition of the NPs contradicts this. This could suggest that the same trends may not be observed when peptides are used in a synthesis reaction compared to when anchored on a peptide array. From XRD data all NPs produced were identified as being in the A1 phase. However, it is likely that the presence of the peptide has improved the quality of the NPs produced, as a fifteen times increase in coercivity was observed. The peptide responsible for this increase was KSLSMKPSRP giving a value of 140 Oe. Another trend identified from peptide array screening was the importance of methionine. Although the majority of peptides used in the synthesis of FePt NPs contain methionine it is difficult to conclude whether methionine is important during the synthesis as there is variation in coercivity between all peptides containing methionine.

It is interesting to note that the composition of CoPt NPs does not alter that greatly between all samples with variation being between 39 – 52% cobalt present in the sample. Whereas when the ratios for FePt were investigated a much wider variation was observed from 19 – 54% iron present in the samples. This suggests that there could be more factors involved in the synthesis of FePt compared to CoPt as a wider range of NP compositions have been synthesised. Also, in both cases the control sample (no peptide present) resulted in a composition of 40:60, and this was obtained from an input ratio of 3:1. This suggests that the initial input ratio used is likely close to the ideal as it generates a ratio that is not too far away from the optimum 50:50 composition. However, it is still possible to improve this ratio through the use of peptides.

Peptides were then combined with bismuth doping, this resulted in a change of the overall composition of the NPs and this was true for both CoPt and FePt. Bismuth doping carried out with CoPt resulted in more cobalt being incorporated into the NPs, this could be caused by bismuth displacing platinum and resulting in higher amounts of cobalt present in the NPs. A more noticeable change in composition was observed for FePt, before bismuth doping samples were identified as being FePt₃ and once bismuth doping was carried out the samples now had a composition consistent with FePt. Therefore, in both cases this suggests that incorporation of bismuth into the synthesis is important for altering the ratio of Co/Fe to Pt.

Although the presence of bismuth was able to alter the overall composition of the NPs formed, there were no discernible changes in the crystal phase of the NPs detected using XRD. However, it was possible to detect increases in coercivity. When KSLSRMDHIHHH and bismuth doping were incorporated into a CoPt synthesis reaction this resulted in a coercivity of 125 Oe being obtained, this is larger than synthesis in the presence of only KSLSRMDHIHHH (107 Oe) and control CoPt NPs (15 Oe). This increase in coercivity is also much larger than the coercivity obtained from bismuth doping alone (55 Oe). This suggests that through combination of bismuth doping and synthesis in the presence of peptides it is possible to synthesise NPs with increased coercivities. An increase was observed for FePt but by using a combination of bismuth doping and peptide it was not possible to increase coercivity more than values obtained from bismuth doping alone (167 Oe vs 278 Oe). Further optimisation of bismuth doping levels, when carried out in the presence of peptides, may be required to achieve higher coercivities. The only sample that resulted in higher coercivity values than bismuth doping alone (KSLSRMDHIHHH and 2% Bi), actually had 5% bismuth present when determined using ICP-OES. Whereas all other samples had 2% bismuth present. This suggests that a higher level of doping may be required for synthesis carried out in the presence of peptides and bismuth.

Through the use of SPOT peptide array technology, it was possible to identify trends in the binding of peptides to CoPt and FePt NPs, as well as metal ion binding and screening carried out against a synthesis reaction. These trends were then incorporated into peptides that were used in CoPt and FePt synthesis reactions. By using these peptides, it was possible to influence the overall composition of the NPs and also produce NPs with higher coercivity values compared to the control NPs. However, in some cases peptides that were identified as having high affinities from peptide array screening did not result in improved properties of the NPs synthesised compared to controls. For example, when peptides KSLSRHMHIHHH and KSLSRMDHIHHH were used in an FePt synthesis reaction NPs with low coercivities were synthesised (67 and 60 Oe respectively). Both these peptides were identified as important from screening carried out against an FePt synthesis reaction and Pt^{2+} . Although an increase in coercivity was observed compared to control NPs, other peptides that were identified as important from screening against FePt synthesis reactions (KSLSRHD) had higher coercivities (125 Oe). Therefore, SPOT peptide array technology can only tell us so much about how the peptides interact with the metal precursors and synthesised NPs and may not always be a reliable indicator of how well the peptide would perform in a synthesis reaction.

Although much higher coercivities would be required for the application of BPM, the increases in coercivities achieved here are a step forward to realising this, as previously only very low or no coercivity have been obtained through the use of a room temperature synthesis method.

CHAPTER NINE: CONCLUSIONS AND FUTURE WORK

9 CONCLUSIONS AND FUTURE WORK

Throughout this thesis controlling the formation of L1₀ Pt alloy NPs has been explored through the use of different peptides and the addition of dopants to the synthesis. A focus on the generation of nanoscale patterned surfaces using interferometric lithography was also investigated. Here the main findings of each section of work are discussed as well as ideas for future work. Small incremental pieces of future work have been discussed at the end of each chapter, this will be briefly discussed here as well as the new and future directions that this project could take.

9.1 SYNTHESIS OF MAGNETIC NANOPARTICLES

CoPt and FePt magnetic nanoparticles were successfully synthesised via a room temperature synthesis method. NPs synthesised using this method were identified to be in the disordered A1 phase, due to lack of characteristic peaks for L1₀ phase in XRD. This phase was also confirmed by the presence of a very low coercivity when measured at room temperature, values of 15 and 11 Oe were obtained for CoPt and FePt NPs respectively, this is consistent with literature. Annealing of FePt NPs at 825 °C was carried out to cause the phase transformation from A1 to L1₀ to occur, this was confirmed by the resulting NPs having a very large coercivity value (10.8 kOe) and the expected peaks for L1₀ FePt were present in XRD.

9.1.1 SILVER AND BISMUTH DOPING

Silver and bismuth doping of mineralisation reactions was investigated for both CoPt and FePt. When silver was incorporated into reactions a doping level of 5% resulted in the largest increase in coercivity for CoPt (130 Oe) and a large increase was also observed for FePt (240 Oe). XRD analysis of CoPt indicated that there was some L1₀ character present in the NPs due to the presence of the (001) plane, however presence of the (001) and (110) planes together is required to indicate true L1₀ character. FePt NPs synthesised in the presence of silver were identified as being in the A1 phase. Bismuth doping carried out, at a level of 2%, resulted in an increase in coercivity for both CoPt (150 Oe) and FePt (278 Oe) NPs. As well as an increase in coercivity being observed incorporation of bismuth also resulted in ratios closer to the ideal 50:50 ratio.

9.1.2 SYNTHESIS OF CoPt IN THE PRESENCE OF MJHSP

CoPt NPs were also synthesised in the presence of MJHSP and NPs synthesised using this method had a higher coercivity than control NPs, an increase from 15 Oe to 41 Oe was observed. This coercivity value obtained is lower than that documented in literature for this synthesis method, this was the case even when reaction protocols and conditions were

followed as closely as possible to those given. No $L1_0$ character was identifiable from XRD data for this sample. Only after annealing the sample at 825 °C for 1 hour were the characteristic $L1_0$ peaks observed and a larger coercivity obtained.

Finally, silver and bismuth doping were incorporated into CoPt synthesis reactions that were carried out in the presence of MjHSP. However, no increases in coercivity were observed using this method and ratios of Co:Pt:Bi varied greatly. Suggesting that further optimisation of this synthesis method may be required. The only increase in coercivity observed when combining doping with MjHSP was from silver doping carried out 2%. A coercivity of 61 Oe was obtained, this is an increase by 20 Oe compared to NPs synthesised only in the presence of MjHSP. All other levels of silver doping carried out resulted in much lower coercivities. Therefore, when using doping in combination with MjHSP further optimisation of the synthesis method is required so that ratios are closer to the ideal and higher coercivities can be achieved.

9.1.3 PEPTIDE ARRAY SCREENING

As higher coercivities are required for the application of BPM, SPOT peptide array technology was used to screen peptides identified from literature that had specificity to the $L1_0$ phase of CoPt and FePt. Screening was carried out against CoPt and FePt nanoparticles, precursor metal ions and synthesis reactions. By using SPOT peptide array technology, it was possible to identify amino acids that were favourable and unfavourable for interacting with these materials. It was also possible to identify general trends across all types of screening. By gaining a better understanding of how peptides interact with CoPt and FePt this should allow for improved synthesis and production of higher quality NPs.

As the results from peptide array screening have been discussed in great detail (Chapters 6, 7 and 8) they will only be briefly summarised here. From peptide array screening there were several similarities and differences identified between the two materials. The three key similarities identified were the importance of basic residues, the importance of methionine and the adverse effect of acidic residues. Only one key difference was identified between the two materials and that involved peptide length.

Basic residues were identified as favourable from all types of screening carried out (NP, metal ion and synthesis). This was predominantly identified through truncation of lead sequences and positional scanning. Conversely, acidic residues were identified as being unfavourable for both materials across all types of screening carried out. Positional scanning identified this trend, as incorporation of glutamic acid into the lead sequences resulted in a significant

reduction in intensity. As glutamic acid was the only acidic residue incorporated into sequences future work could involve incorporation of aspartic acid into sequences to identify whether the same trend is observed or if only glutamic acid is unfavourable.

Methionine was identified as important residue from all types of screening carried out. Only LS4 originally had methionine present in the sequence, truncated sequences that no longer contained methionine were significantly reduced compared to those with methionine present. When methionine was incorporated into sequences through positional scanning a significant increase in intensity was observed no matter what the amino acid being replaced was. The largest increase observed was from screening against Pt^{2+} , this is likely due to the strong interaction that is known to occur between platinum and the sulfur group present in methionine.

Peptide length was the only difference identified between the two materials. In general, from all screening carried out it was identified that CoPt prefers shorter peptides whilst FePt prefers longer peptides. Truncation of the lead sequences resulted in this conclusion being drawn as for all other types of screening peptide length was kept constant. The shortest peptide sequences screened were five amino acids in length and the longest consisting of 12. Therefore, future work could investigate what effect shorter and longer peptides, than those previously screened, would have on their ability to interact with CoPt and FePt. Using SPOT peptide array technology, it would be possible to truncate sequences even further, so that sequences as short as three amino acids in length can be generated. This would allow further screening and provide more confirmation of the difference in peptide length observed between the two materials.

9.1.4 SYNTHESIS OF MNPs USING DESIGNED AND SELECTED PEPTIDES

Based on the findings identified from peptide array screening, peptides that would be suitable for use in synthesis reactions were designed and selected. Three peptides were selected for CoPt and nine for FePt. Three control peptides were also incorporated into the synthesis, and these were LS1, LS2 and LS3. These sequences were selected as controls as they are the original lead sequences that new sequences were based on.

When designed and selected peptides were incorporated into the synthesis of CoPt NPs it was possible to alter the ratio of Co to Pt based on the peptides binding ability to Pt^{2+} . Peptides that were identified as having a higher affinity for Pt^{2+} resulted in a lower overall cobalt content, whilst those with a lower affinity for Pt^{2+} had a higher overall cobalt content. This suggests that the peptides are interacting with metal pre-cursors prior to nucleation of

the NPs and that the presence of different peptides had a direct effect on the final composition of the NPs. It was also confirmed that shorter peptide sequences may be possible for use in CoPt synthesis reactions as sequence KLSLRHD had a higher coercivity than its original lead sequence, LS3. Methionine was identified as important from all types of screening carried out and this was also confirmed when sequences containing methionine were used in a synthesis reaction. Sequences KLSRMDHIIHHH and KLSRHMHIIHHH had the highest coercivity values of all peptides screened (107 and 104 Oe respectively). The only difference between these sequences and LS3 is the presence of methionine, therefore it is likely that it is the presence of methionine that accounts for the increase in coercivity. Although an increase in coercivity was observed there was no discernible change in the crystal structure of the NPs from XRD, and so synthesised NPs were in the A1 disordered phase.

Designed and selected peptides were also incorporated into the synthesis of FePt, four peptides resulted in the formation of FePt rather than FePt₃. The peptides responsible for the formation of FePt were: KLSMK, KLSMKH, KLSMKP and KLSMKPRP. Unlike for CoPt there was no correlation between the final amount of iron and platinum in the sample and the peptides ability for binding to Pt²⁺ or Fe²⁺. All samples synthesised were in the A1 phase, but all had increased coercivity values compared to control FePt NPs (11 Oe). The highest coercivity (140 Oe) was achieved by using peptide KLSMKPSRP.

Finally, synthesis in the presence of peptides was carried out in combination with bismuth doping. For CoPt peptides KLSLRHD and KLSRMDHIIHHH were used alongside 2% bismuth. Incorporation of bismuth into the synthesis increased the amount of cobalt present in the NPs. No distinct changes of crystal structure were detected by XRD and so synthesised NPs were in the A1 phase. Combining bismuth doping and KLSRMDHIIHHH resulted in an increase in coercivity (125 Oe), using only peptide had a value of 107 Oe and bismuth doping alone had a value of 55 Oe. Therefore, through combination of bismuth doping and use of peptides it has been possible to achieve an approximately eight times increase in coercivity compared to control CoPt NPs (15 Oe).

When bismuth was incorporated into the synthesis of FePt NPs, the ratio of Fe to Pt was changed, and the NPs formed were consistent with FePt rather than FePt₃. Although a change in the composition of the NPs was observed there was no detectable change in the crystal phase of the NPs. A slight increase in coercivity was observed compared to when only peptide was present in the synthesis, for KLSMKPSRP coercivity was increased from 140 to

167 Oe and for KSLSRHD from 125 to 160 Oe. However, bismuth doping alone (without the presence of peptides) resulted in the highest coercivity of all (278 Oe).

Future work involved with the synthesis of NPs in presence of peptides could involve further optimisation of the bismuth doping levels. It may be that a different level of doping is required when carried out in the presence of peptides, finding this optimised level could then result in further increases in coercivity being observed.

All of the methods investigated for the synthesis of CoPt and FePt NPs have resulted in synthesised NPs being in the A1 disordered phase. Although increases in coercivity were observed much larger coercivities than those generated here would be required for the application of BPM. Therefore, carrying out further refinement and optimisation of every stage in the synthesis process could result in the production of higher quality NPs that could possess some L1₀ character. Another area that could be investigated is annealing of NPs synthesised in the presence of peptides and bismuth. By using bismuth and peptides it has been possible to alter the composition of the final NP and also increase coercivity. NPs are now much closer in composition to what is required for the L1₀ phase. Therefore, much lower annealing temperatures may be required to cause the phase transformation from the A1 to L1₀ phase. Finally, through genetic modifications to MjHSP it would be possible to replace the peptide that is currently present on the interior of the cage with one of the peptides identified from peptide array screening. The newly designed peptides resulted in a higher coercivity than LS2, when used in the synthesis of CoPt and FePt NPs. Therefore, by incorporating one of these sequences into MjHSP it could be possible to generate NPs with higher coercivities whilst also controlling the morphology of the NPs produced.

Through the use of SPOT peptide array technology, it has been possible to identify key trends for the binding of CoPt and FePt NPs, metal precursor ions and synthesis reactions to a range of different peptides. Incorporation of these designed and selected peptides into synthesis reactions has made it possible to control the overall composition of the NPs and increase coercivity. Although much higher coercivities than those obtained here would be required for the application of BPM, this is still a step forward to achieving this as previously only very low or no coercivity has been obtained through the use of a room temperature synthesis method.

9.2 NANOSCALE PATTERNING

Attachment of peptides/proteins to an amine terminated SAM was investigated in this chapter through the use of different crosslinkers. Crosslinking was carried out using an APTES

SAM on titania and both glutaraldehyde and GMBS crosslinkers were assessed. A basic assessment using SEM was carried out to identify the optimum conditions for crosslinking. From the SEM images obtained it was difficult to identify whether one method over the other would be more suitable for use. However, it was possible to optimise the conditions for both reactions. The optimised conditions identified for GA crosslinking were that the reaction should be carried out in 1 step, a 3-hour incubation and a peptide concentration of 0.1 mg/ml would be used. For GMBS crosslinking, following the protocol set out by ThermoFisher produced good results when a peptide concentration of 0.25 mg/ml was used. As only a basic assessment using SEM was carried out, a more detailed assessment of crosslinking and peptide/protein attachment would be required before attachment to patterned surfaces is achieved. It would be possible to monitor peptide/protein attachment through the use of quartz crystal microbalance with dissipation (QCM-D) to ensure that the peptide is successfully attached to the surface before being placed into a NP mineralisation reaction. Obtaining higher resolution SEM images would also be beneficial so that surface coverage can be assessed more accurately, as well as the possibility of obtaining energy dispersive x-ray analysis (EDX) from SEM. This would provide elemental identification of material on the surface to ensure that material observed is consistent with CoPt or FePt NPs. Currently, optimisation of crosslinking was only carried out on titania surfaces with an APTES SAM and as nanoscale patterns were generated on gold surfaces with an amine terminated SAM further optimisation of crosslinking with this SAM may be required.

Nanoscale patterning was successfully achieved, on gold surfaces, through the use of interferometric lithography. Using this method, it was possible to produce periodic line and dot patterned arrays. An amine terminated thiol was first formed on a gold surface, followed by exposure to a laser beam set up in a Lloyds mirror arrangement. An exposure angle of 20° and a dose of 48 Jcm⁻² was used to generate a line pattern array with a period of 158 nm. Rotation of this sample through 90° followed by a second exposure resulted in a dot pattern array being formed with a period of 204 nm. Previous work in the Staniland group has only focused on the production of line arrays and so the generation of dot arrays is one step closer to achieving BPM. However, for BPM to become a reality much smaller features (≈ 20 nm) would be required than those generated here. Using interferometric lithography, it would be possible to achieve these sizes by increasing the angle of exposure. Using a larger angle of exposure is experimentally more difficult so the process may require optimisation. It is possible that the exposure dose may also require further optimisation when a different angle of exposure is used.

9.3 OUTLOOK AND FUTURE DIRECTIONS

In this thesis it has been shown that it is possible to generate periodic line and dot pattern arrays using the technique of interferometric lithography and through further optimisation of the fabrication process it would be possible to achieve the much smaller nanoscale features that are required for BPM. As previous work within the group has focused on the generation of nanoscale patterns but encountered problems with the magnetic properties of Pt alloy NPs a great deal of time was spent investigating and improving the synthesis of these NPs. Through the use of SPOT peptide array technology, it was possible to identify peptides that would be suitable for use in NP mineralisation reactions. Synthesis of NPs in the presence of these peptides resulted in coercivity values that were much higher than control NPs suggesting that the presence of peptides can improve NP quality. Doping the synthesis with both silver and bismuth was also shown to have a positive effect on the final composition of the NPs and their coercivity. Therefore, in this study through the use of peptides and doping increased coercivity values were obtained from room temperature synthesis reactions. Although work in this study is a great step forwards in identifying a material suitable for BPM, the next step would be to combine the nanoscale patterned surfaces with attachment of the designed peptide sequences so that biotemplated arrays of magnetic nanoparticles can be achieved (Figure 9.3.1).

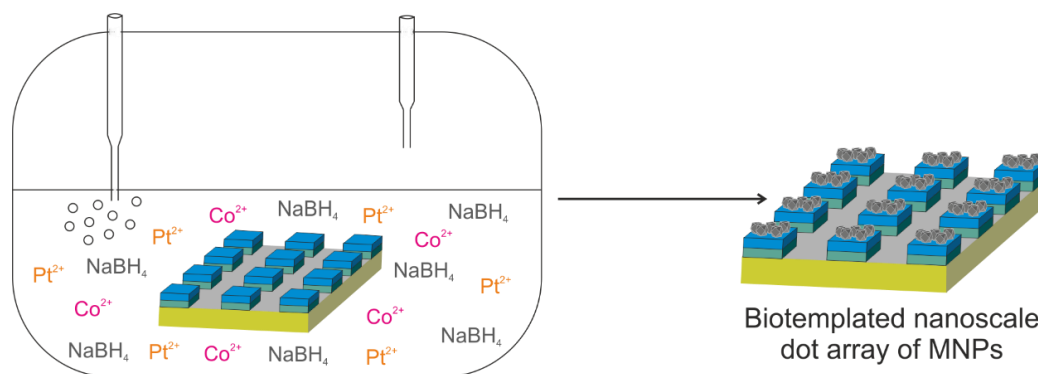


Figure 9.3.1 – Schematic showing the process of incorporating dot arrays into a nanoparticle mineralisation reaction for the production of biotemplated nanoscale dot arrays of MNPs.

It could also be possible to take this one step further and achieve a truly biotemplated nanoscale patterned surface through the use of surface layer proteins (S-layers). S-layer proteins are capable of forming a porous mesh with repeatable units in the range of 3 – 30 nm and have pore sizes between 2 – 8 nm.¹⁷³ These proteins are known to self-assemble onto solid substrates (Figure 9.3.2) and it is possible that they could form a template for mineralisation of nanoparticles.¹⁷³ This would be possible through the adaptation of this layer to display either a CoPt or FePt binding peptide. Therefore, this approach could result

in the formation of a truly biotemplated array of magnetic nanoparticles that would be suitable to use for BPM.

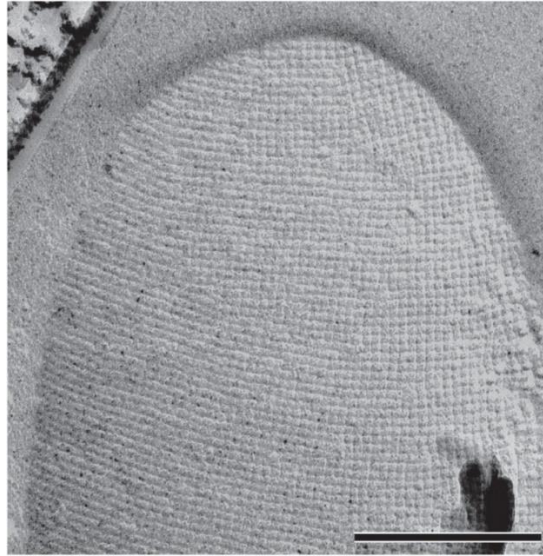


Figure 9.3.2 – TEM of a freeze etched and metal shadowed bacterial cell (*Desulfotomaculum nigrificans* strain NCIB 8706) revealing an s-layer with square lattice symmetry. Scale bar represents 200 nm. Reprinted from Figure 1 in Pum, D. and U.B Sleytr, Reassembly of s-layer proteins. Nanotechnology, 2014 with permission from Nanotechnology, Institute of Physics.

10 REFERENCES

- 1 N. Spaldin, *Magnetic Materials: Fundamentals and Applications*, Cambridge University Press, Second., 2010.
- 2 S. Blundell, *Magnetism in Condensed Matter*, Oxford University Press, 2001.
- 3 J. L. Beeby, *Phys. Rev.*, 1966, **141**, 781–788.
- 4 P. Weiss and P. W. L., *J. Phys. Theor. Appl.*, 1907, **6**, 661–690.
- 5 F. Bitter, *Phys. Rev. Lett.*, 1931, **38**, 1903.
- 6 B. D. Cullity and C. . Graham, *Introduction to magnetic materials*, John Wiley & Sons Limited, Second., 2009, vol. 47.
- 7 R. Kelsall, I. Hamley and M. Geoghegan, *Nanoscale Science and Technology*, John Wiley & Sons Limited, First., 2005, vol. 34.
- 8 R. Kelsall, I. W. Hamley and M. Geoghegan, *Nanoscale Science and Techonology*, John Wiley & Sons Limited, 2005.
- 9 H. J. Richter, A. Y. Dobin, O. Heinonen, K. Z. Gao, R. J. M. Veerdonk, R. T. Lynch, J. Xue, D. Weller and S. Technology, *IEEE Trans. Magn.*, 2006, **42**, 2255–2260.
- 10 E. F. Kneller and F. E. Luborsky, *J. Appl. Phys.*, 2003, **656**, 13–16.
- 11 F. Jorgensen, *J. Magn. Magn. Mater.*, 1999, **193**, 1–7.
- 12 S. . Piramanayagam, *Developments in Data Storage: Materials Perspective*, Wiley-IEEE Press, 2011.
- 13 S. Chikazumi, *Physics of Ferromagnetism*, Oxford University Press, Second., 2009.
- 14 S. . Piramanayagam and T. C. Chong, *Developments in Data Storage: Materials Perspective*, Wiley-IEEE Press, 2011.
- 15 A. S. Hoagland, *IEEE Trans. Magn.*, 2003, **39**, 1871–1875.
- 16 IBM, IBM 350 Disk Storage Unit, https://www-03.ibm.com/ibm/history/exhibits/storage/storage_350.html, (accessed 20 September 2016).
- 17 B. D. Terris and T. Thomson, *J. Phys. D. Appl. Phys.*, 2005, **38**, 199–222.
- 18 H. J. Richter, *J. Phys. D. Appl. Phys.*, 2007, **40**, 149–177.
- 19 Seagate, Seagate reaches One Terabit per Square Inch Milestone in Hard Drive Storage with New Technology Demonstration | News Archive | Seagate UK, <https://www.seagate.com/gb/en/news/news-archive/terabit-milestone-storage-seagate-master-pr/>, (accessed 30 May 2019).
- 20 Scan.co.uk, <https://www.scan.co.uk/products/14tb-seagate-st14000dm001-barracuda-pro-35-hdd-sata-30-6gb-s-7200rpm-256mb-cache-512e-ncq-oem>, (accessed 25 April 2019).
- 21 D. Weller and A. Moser, *IEEE Trans. Magn.*, 1999, **35**, 4423–4439.

- 22 C. A. Ross, *Annu. Rev. Mater. Res.*, 2001, **31**, 203–235.
- 23 Z. Hedayatnasab, F. Abnisa and W. M. A. W. Daud, *Mater. Des.*, 2017, **123**, 174–196.
- 24 J. Kudr, Y. Haddad, L. Richtera, Z. Heger, M. Cernak, V. Adam, O. Zitka, J. Kudr, Y. Haddad, L. Richtera, Z. Heger, M. Cernak, V. Adam and O. Zitka, *Nanomaterials*, 2017, **7**, 243.
- 25 D. Guo, G. Xie and J. Luo, *J. Phys. D. Appl. Phys.*, 2014, **47**, 1–25.
- 26 X. Li, J. Wei, K. E. Aifantis, Y. Fan, Q. Feng, F.-Z. Cui and F. Watari, *J. Biomed. Mater. Res. Part A*, 2016, **104**, 1285–1296.
- 27 V. F. Cardoso, A. Francesko, C. Ribeiro, M. Bañobre-López, P. Martins and S. Lanceros-Mendez, *Adv. Healthc. Mater.*, 2018, **7**, 1700845.
- 28 K. Chokprasombat, *Walailaki J. Sci. Technol.*, 2011, **8**, 87–96.
- 29 L. Mohammed, H. G. Gomaa, D. Ragab and J. Zhu, *Particuology*, 2017, **30**, 1–14.
- 30 S. Sun, C. B. Murray, D. Weller, L. Folks and A. Moser, *Science*, 2000, **287**, 1989–92.
- 31 Z. Meng, G. Li, H.-F. Wong, S.-M. Ng, S.-C. Yiu, C.-L. Ho, C.-W. Leung, I. Manners and W.-Y. Wong, *Nanoscale*, 2017, **9**, 731–738.
- 32 J. M. Silveyra, E. Ferrara, D. L. Huber and T. C. Monson, *Science (80-.)*, 2018, **362**, 1–9.
- 33 C. Desvaux, C. Amiens, P. Fejes, P. Renaud, M. Respaud, P. Lecante, E. Snoeck and B. Chaudret, *Nat. Mater.*, 2005, **4**, 750–753.
- 34 M. Muthana, A. J. Kennerley, R. Hughes, E. Fagnano, J. Richardson, M. Paul, C. Murdoch, F. Wright, C. Payne, M. F. Lythgoe, N. Farrow, J. Dobson, J. Conner, J. M. Wild and C. Lewis, *Nat. Commun.*, 2015, **6**, 1–11.
- 35 Z. R. Stephen, F. M. Kievit and M. Zhang, *Mater Today (Kidlington)*, 2011, **14**, 330–338.
- 36 Y. Liu, Y. Jiang, X. Zhang, Y. Wang, Y. Zhang, H. Liu, H. Zhai, Y. Liu, J. Yang and Y. Yan, *J. Solid State Chem.*, 2014, **209**, 69–73.
- 37 D. Weller, A. Moser, L. Folks, M. E. Best, W. Lee, M. F. Toney, M. Schwickert, J. U. Thiele and M. F. Doerner, *IEEE Trans. Magn.*, 2000, **36**, 10–15.
- 38 D. E. Laughlin, K. Srinivasan, M. Tanase and L. Wang, *Scr. Mater.*, 2005, **53**, 383–388.
- 39 J. Aboaf, S. Herd and E. Klokhholm, *IEEE Trans. Magn.*, 1983, **19**, 1514–1519.
- 40 L. Ford, *Platin. Met. Rev*, 1957, **1**, 84–86.
- 41 Y. Wang, X. Zhang, Y. Liu, Y. Jiang, Y. Zhang and J. Yang, *J. Sol-Gel Sci. Technol.*, 2014, **70**, 528–533.
- 42 X. Sun, Z. Y. Jia, Y. H. Huang, J. W. Harrell and D. E. Nikles, *J. Appl. Phys.*, 2004, **95**, 6747–6749.
- 43 S. Cheng-Min, H. Chao, Y. Tian-Zhong, X. Cong-Wen, E. Shu-Tang, D. Hao and G. Hong-Jun, *Chinese Phys. Lett.*, 2008, **25**, 1479–1481.
- 44 S. Sun, S. Anders, T. Thomson, J. E. E. Baglin, M. F. Toney, H. F. Hamann, C. B. Murray

- and B. D. Terris, *J. Phys. Chem. B*, 2003, **107**, 5419–5425.
- 45 V. Tzitzios, D. Niarchos, G. Margariti, J. Fidler and D. Petridis, *Inst. Phys. Publ. Nanotechnol. Nanotechnol.*, 2005, **16**, 287–291.
- 46 Y. K. Takahashi, M. Ohnuma and K. Hono, *Jpn. J. Appl. Phys.*, 2003, **42**, 350–352.
- 47 C. Liu, X. Wu, T. Klemmer, N. Shukla, X. Yang, D. Weller, A. G. Roy, M. Tanase and D. Laughlin, *J. Phys. Chem. B*, 2004, **108**, 6121–6123.
- 48 M. P. Pileni, *Langmuir*, 1997, **13**, 3266–3276.
- 49 J. P. Chen, K. M. Lee, C. M. Sorensen, K. J. Klabunde and G. C. Hadjipanayis, *J. Appl. Phys.*, 1994, **75**, 5876–5878.
- 50 C. Petit, A. Taleb and M.-P. Pileni, *Adv. Mater.*, 1998, **10**, 259–261.
- 51 K. Kiraga, A. C. C. Yu, M. Mizuno, Y. Sasaki, H. Kondo and K. Hiraga, *Appl. Phys. Lett.*, 2002, **81**, 3768.
- 52 Y. J. Zhang, Y. T. Yang, Y. Liu, Y. X. Wang, L. L. Yang, M. B. Wei, H. G. Fan, H. J. Zhai, X. Y. Liu, Y. Q. Liu, N. N. Yang, Y. H. Wu and J. H. Yang, *J. Phys. D. Appl. Phys.*, 2011, **44**, 295003.
- 53 Y. Liu, Y. Yang, Y. Zhang, Y. Wang, X. Zhang, Y. Jiang, M. Wei, Y. Liu, X. Liu and J. Yang, *Mater. Res. Bull.*, 2013, **48**, 721–724.
- 54 X. Du, M. Inokuchi and N. Toshima, *J. Magn. Magn. Mater.*, 2006, **299**, 21–28.
- 55 Q. Dong, W. Qu, W. Liang, K. Guo, H. Xue, Y. Guo, Z. Meng, C.-L. Ho, C.-W. Leung and W.-Y. Wong, *Nanoscale*, 2016, **8**, 7068–7074.
- 56 S.-C. Yiu, A. Nunns, C.-L. Ho, J. H.-L. Ngai, Z. Meng, G. Li, J. Gwyther, G. R. Whittell, I. Manners and W.-Y. Wong, *Macromolecules*, 2019, **52**, 3176–3186.
- 57 A. E. Rawlings, J. P. Bramble, A. A. S. Tang, L. A. Somner, A. E. Monnington, D. J. Cooke, M. J. McPherson, D. C. Tomlinson and S. S. Staniland, *Chem. Sci.*, 2015, **6**, 5586–5594.
- 58 U. Seker and H. V. Demir, *Molecules*, 2011, **16**, 1426–1451.
- 59 A. Artzy-Schnirman, E. Abu-Shah, M. Dishon, H. Soifer, Y. Sivan, Y. Reiter, I. Benhar and U. Sivan, *J. Pept. Sci.*, 2014, **20**, 446–450.
- 60 C. Tiede, A. A. S. Tang, S. E. Deacon, U. Mandal, J. E. Nettleship, R. L. Owen, S. E. George, D. J. Harrison, R. J. Owens, D. C. Tomlinson and M. J. McPherson, *Protein Eng. Des. Sel.*, 2014, **27**, 145–155.
- 61 B. D. Reiss, C. Mao, D. J. Solis, K. S. Ryan, T. Thomson and A. M. Belcher, *Nano Lett.*, 2004, **4**, 1127–1132.
- 62 K. K. Kim, R. Kim and S. H. Kim, *Nature*, 1998, **394**, 595–9.
- 63 M. T. Klem, D. Willits, D. J. Solis, A. M. Belcher, M. Young and T. Douglas, *Adv. Funct. Mater.*, 2005, **15**, 1489–1494.
- 64 J. M. Galloway, J. E. Talbot, K. Critchley, J. J. Miles and J. P. Bramble, *Adv. Funct. Mater.*, 2015, **25**, 4590–4600.
- 65 E. Eteshola, L. J. Brillson and S. C. Lee, *Biomol. Eng.*, 2005, **22**, 201–204.

- 66 A. J. Love, V. Makarov, I. Yaminsky, N. O. Kalinina and M. E. Taliany, *Virology*, 2014, **449**, 133–139.
- 67 A. A. A. Aljabali, J. E. Barclay, O. Cespedes, A. Rashid, S. S. Staniland, G. P. Lomonosoff and D. J. Evans, *Adv. Funct. Mater.*, 2011, **21**, 4137–4142.
- 68 A. A. A. Aljabali, S. N. Shah, R. Evans-Gowing, G. P. Lomonosoff and D. J. Evans, *Integr. Biol.*, 2011, **3**, 119–125.
- 69 B. H. San, S. Lee, S. H. Moh, J.-G. Park, J. H. Lee, H.-Y. Hwang and K. K. Kim, *J. Mater. Chem. B*, 2013, **1**, 1453.
- 70 T. Douglas, E. Strable, D. Willits, A. Aitouchen, M. Libera and M. Young, *Adv. Mater.*, 2002, **14**, 415–418.
- 71 E. Mayes, A. Bewick, D. Gleeson, J. Hoinville, R. Jones, O. Kasyutich, A. Nartowski, B. Warne, J. Wiggins and K. K. W. Wong, *IEEE Trans. Magn.*, 2003, **39**, 624–627.
- 72 N. D. Chasteen and P. M. Harrison, *J. Struct. Biol.*, 1999, **126**, 182–184.
- 73 B. Warne, O. I. Kasyutich, E. L. Mayes, J. A. L. Wiggins and K. K. W. Wong, *IEEE Trans. Magn.*, 2000, **36**, 3009–3011.
- 74 C. N. Chinnasamy, B. Jeyadevan, K. Shinoda and K. Tohji, *J. Appl. Phys.*, 2003, **93**, 7583–7585.
- 75 J.-I. Park and J. Cheon, *J. Am. Chem. Soc.*, 2001, **123**, 5743–5746.
- 76 M. Chen and D. E. Nikles, *J. Appl. Phys.*, 2002, **91**, 8477.
- 77 E. V. Shevchenko, D. V. Talapin, A. L. Rogach, A. Kornowski, M. Haase and H. Weller, *J. Am. Chem. Soc.*, 2002, **124**, 11480–11485.
- 78 Q. Dong, W. Qu, W. Liang, K. Guo, H. Xue, Y. Guo, Z. Meng, C.-L. Ho, C.-W. Leung and W.-Y. Wong, *Nanoscale*, 2016, **8**, 7068–7074.
- 79 M. S. Wellons, Z. Gai, J. Shen, J. Bentley, J. E. Wittig and C. M. Lukehart, *J. Mater. Chem. C*, 2013, **1**, 5976–5980.
- 80 K. E. Elkins, T. S. Vedantam, J. P. Liu, H. Zeng, S. Sun, Y. Ding and Z. L. Wang, *N*, 2003, **3**, 1647–1649.
- 81 S. Sun, C. B. Murray, D. Weller, L. Folks and A. Moser, *Science (80-.)*, 2000, **287**, 1989–1992.
- 82 Shouheng Sun, E. E. Fullerton, D. Weller and C. B. Murray, *IEEE Trans. Magn.*, 2001, **37**, 1239–1243.
- 83 R. Frank, *Tetrahedron*, 1992, **48**, 9217–9232.
- 84 K. Hilpert, D. F. Winkler and R. E. Hancock, *Biotechnol. Genet. Eng. Rev.*, 2007, **24**, 31–106.
- 85 Y.-J. Wei, K.-A. Li and S.-Y. Tong, *Talanta*, 1996, **43**, 1–10.
- 86 H. Gausepohl and C. Behn, in *Peptide Arrays on Membrane Supports*, Springer, Berlin, Heidelberg, 2002, pp. 55–68.
- 87 K. Hilpert, D. F. H. Winkler and R. E. W. Hancock, *Nat. Protoc.*, 2007, **2**, 1333–1349.

- 88 F. Toepert, T. Knaute, S. Guffler, J. R. Pirés, T. Matzdorf, H. Oschkinat and J. Schneider-Mergener, *Angew. Chemie Int. Ed.*, 2003, **42**, 1136–1140.
- 89 H. Wenschuh, R. Volkmer-Engert, M. Schmidt, M. Schulz, J. Schneider-Mergener and U. Reineke, *Biopolymers*, 2000, **55**, 188–206.
- 90 F. Molina, D. Laune, C. Gougat, B. Pau and C. Granier, *Pept Res*, 1996, **9**, 151–155.
- 91 A. Kramer, T. Keitel, K. Winkler, W. Stö, W. Hö and J. Schneider-Mergener, *Cell*, 1997, **91**, 799–809.
- 92 A. A. Weiser, M. Or-Guil, V. Tapia, A. Leichsenring, J. Schuchhardt, C. Frö and R. Volkmer-Engert, *Anal. Biochem.*, 2005, **342**, 300–311.
- 93 G. B. Bolger, G. S. Baillie, X. Li, M. J. Lynch, P. Herzyk, A. Mohamed, L. H. Mitchell, A. McCahill, C. Hundsrucker, E. Klussmann, D. R. Adams and M. D. Houslay, *Biochem. J.*, 2006, **398**, 23–36.
- 94 M. Liang, M. Mahler, J. Koch, Y. Ji, D. Li, C. Schmaljohn and E. K. F. Bautz, *J. Med. Virol.*, 2003, **69**, 99–107.
- 95 U. Reineke, C. Ivascu, M. Schlieff, C. Landgraf, S. Gericke, G. Zahn, H. Herzel, R. Volkmer-Engert and J. Schneider-Mergener, *J. Immunol. Methods*, 2002, **267**, 37–51.
- 96 D. Lenze, E. Berg, R. Volkmer-Engert, A. A. Weiser, A. Greiner, C. Knö Rr-Wittmann, I. Anagnostopoulos, H. Stein and M. Hummel, *Blood*, 2006, **107**, 1141–1148.
- 97 L. K. Weber, A. Isse, S. Rentschler, R. E. Kneusel, A. Palermo, J. Hubbuch, A. Nesterov-Mueller, F. Breitling and F. F. Loeffler, *Eng. Life Sci.*, 2017, **17**, 1078–1087.
- 98 A. M. Müller, M. Bockstahler, G. Hristov, C. Weiß, A. Fischer, S. Korkmaz-Icöz, E. Giannitsis, W. Poller, H. P. Schultheiss, H. A. Katus and Z. Kaya, *Clin. Immunol.*, 2016, **173**, 64–75.
- 99 A. Kume, S. Kawai, R. Kato, S. Iwata, K. Shimizu and H. Honda, *J. Biosci. Bioeng.*, 2017, **123**, 230–238.
- 100 E. Shishkova, H. Zeng, F. Liu, N. W. Kwiecien, A. S. Hebert, J. J. Coon and W. Xu, *Nat. Commun.*, 2017, **8**, 1–13.
- 101 M. Okochi, T. Sugita, Y. Asai, M. Tanaka and H. Honda, *Biochem. Eng. J.*, 2017, **128**, 178–185.
- 102 E. Lin, A. Sikand, J. Wickware, Y. Hao and R. Derda, *Acta Biomater.*, 2016, **34**, 53–59.
- 103 K. Kanie, Y. Kondo, J. Owaki, Y. Ikeda, Y. Narita, R. Kato, H. Honda, K. Kanie, Y. Kondo, J. Owaki, Y. Ikeda, Y. Narita, R. Kato and H. Honda, *Bioengineering*, 2016, **3**, 31.
- 104 M. Tanaka, I. H. Harlisa, Y. Takahashi, N. A. Ikhsan and M. Okochi, *RSC Adv.*, 2018, **8**, 8795–8799.
- 105 M. Tanaka, A. W. L. Alvin and M. Okochi, *RSC Adv.*, 2018, **8**, 5953–5959.
- 106 A. W. Liang Alvin, M. Tanaka and M. Okochi, *J. Biosci. Bioeng.*, 2017, **123**, 621–624.
- 107 M. Tanaka, S. Hikiba, K. Yamashita, M. Muto and M. Okochi, *Acta Biomater.*, 2017, **49**, 495–506.
- 108 J. C. Love, L. A. Estroff, J. K. Kriebel, R. G. Nuzzo and G. M. Whitesides, *Chem. Rev.*,

- 2005, **105**, 1103–1169.
- 109 F. Schreiber, *Prog. Surf. Sci.*, 2000, **65**, 151–256.
- 110 C. Vericat, M. E. Vela, G. Benitez, P. Carro and R. C. Salvarezza, *Chem. Soc. Rev.*, 2010, **39**, 1805–1834.
- 111 L. H. Dubois and R. G. Nuzzo, *Annu. Rev. Phys. Chem.*, 1992, **43**, 437–440.
- 112 N. C. Iii, *Langmuir*, 2004, **20**, 1199–1206.
- 113 A. Ulman, *Chem. Rev.*, 1996, **96**, 1533–1554.
- 114 T. W. Odom, J. C. Love, D. B. Wolfe, K. E. Paul and G. M. Whitesides, *Langmuir*, 2002, **18**, 5314–5320.
- 115 J. M. Galloway, J. P. Bramble, A. E. Rawlings, G. Burnell, S. D. Evans and S. S. Staniland, *J. Nano Res.*, 2012, **17**, 187–146.
- 116 A. Bernard, A. Bietsch, J. Renault and H. Wolf, *IBM J. Res. Dev.*, 2001, **45**, 697–719.
- 117 J. M. Behm, K. R. Lykke, M. J. Pellin and J. C. Hemminger, *Langmuir*, 1996, **12**, 2121–2124.
- 118 B. Liedberg, M. Wirde, Y.-T. Tao, P. Tengvall and U. Gelius, *Langmuir*, 1997, **13**, 5329–5334.
- 119 M. Zharnikov and M. Grunze, *J. Vac. Sci. Technol. B*, 2002, **20**, 1793.
- 120 S. Friebel, J. Aizenberg, S. Abad and P. Wiltzius, *Appl. Phys. Lett.*, 2000, **77**, 2406–2408.
- 121 G. Tizazu, O. El-Zubir, S. R. J. Brueck, D. G. Lidzey, G. J. Leggett and G. P. Lopez, *Nanoscale*, 2011, **3**, 2511–2516.
- 122 N. Diep, W. Ping, J. Hung, C. Chen and C. Hsiung, 2005, **13**, 187–191.
- 123 J. M. Galloway, S. M. Bird, J. E. Talbot, P. M. Shepley, R. C. Bradley, O. El-Zubir, D. A. Allwood, G. J. Leggett, J. J. Miles, S. S. Staniland and K. Critchley, *Nanoscale*, 2016, **8**, 11738–11747.
- 124 S. M. Bird, O. El-Zubir, A. E. Rawlings, G. J. Leggett and S. S. Staniland, *J. Mater. Chem. C*, 2016, **4**, 3948–3955.
- 125 R. Reed, D. Holmes, J. Weyers and A. Jones, *Practical Skills in Biomolecular Sciences*, Pearson, Third., 2007.
- 126 R. Frank, *J. Immunol. Methods*, 2002, **267**, 13–26.
- 127 J. F. Watts and J. Wolstenholme, *An Introduction to Surface Analysis by XPS and AES*, John Wiley & Sons Limited, First., 2003.
- 128 S. Patole, C. Vasilev, O. E.-Z. L. Wang, M. P. Johnson, A. J. Cadby, G. J. Leggett and C. N. Hunter, *Interface Focus*, 2015, **5**, 1–9.
- 129 G. Cao and Y. Wang, *Nanostructures and Nanomaterials: synthesis, properties and applications*, World Scientific Publishing, Second., 2011.
- 130 C. A. Schneider, W. S. Rasband and K. W. Eliceiri, *Nat. Methods*, 2012, **9**, 671–675.
- 131 W. L. Bragg, *Scientia*, 1929, **23**, 153.

- 132 A. L. Patterson, *Phys. Rev.*, 1939, **56**, 978–982.
- 133 S. Foner, *Rev. Sci. Instrum.*, 1959, **30**, 548–557.
- 134 Perkin Elmer, *Tech. Note ICP-Mass Spectrom.*, 2001, 1–8.
- 135 P. Eaton and P. West, *Atomic Force Microscopy*, Oxford University Press, First., 2010.
- 136 J. M. Galloway, J. P. Bramble, A. E. Rawlings, G. Burnell, S. D. Evans and S. S. Staniland, *Small*, 2012, **8**, 204–208.
- 137 S. M. Bird, J. M. Galloway, A. E. Rawlings, J. P. Bramble and S. S. Staniland, *Nanoscale*, 2015, **7**, 7340–7351.
- 138 D. Janssen, R. De Palma, S. Verlaak, P. Heremans and W. Dehaen, *Thin Solid Films*, 2006, **515**, 1433–1438.
- 139 A. Krishnan, Y.-H. Liu, P. Cha, R. Woodward, D. Allara and E. A. Vogler, *Colloids Surfaces B Biointerfaces*, 2005, **43**, 95–98.
- 140 B. Bhushan, K. J. Kwak, S. Gupta and S. C. Lee, *J. R. Soc. Interface*, 2009, **6**, 719–733.
- 141 M. Ciaccia and S. Di Stefano, *Org. Biomol. Chem.*, 2014, **13**, 646.
- 142 ThermoFisher, *GMBS and Sulfo-GMBS Protocol*, 2010.
- 143 A. Tsargorodska, O. El Zubir, B. Darroch, M. L. Cartron, T. Basova, C. Neil Hunter, A. V Nabok and G. J. Leggett, *ACS Nano*, 2014, **8**, 7858–7869.
- 144 M. Moxey, A. Johnson, O. El-Zubir, M. Cartron, S. S. Dinachali, C. N. Hunter, M. S. M. Saifullah, K. S. L. Chong and G. J. Leggett, *ACS Nano*, 2015, **9**, 6262–6270.
- 145 H. Notsu, W. Kubo, I. Shitanda and T. Tatsuma, *J. Mater. Chem.*, 2005, **15**, 1523–1527.
- 146 O. Polat and E. Seker, *J. Phys. Chem. C*, 2016, **120**, 19189–19194.
- 147 T. Nagata, Y. Tokuoka, T. Kato, D. Oshima and S. Iwata, *Journals Magn. Soc. Japan*, 2016, **40**, 13–17.
- 148 O. Kitakami, Y. Shimada, K. Oikawa, H. Daimon and K. Fukamichi, *Appl. Phys. Lett.*, 2001, **78**, 1104–1106.
- 149 V. Karanasos, I. Panagiotopoulos, D. Niarchos, H. Okumura and G. C. Hadjipanayis, *Appl. Phys. Lett.*, 2001, **79**, 1255–1257.
- 150 Y. Khemjeen, S. Pinitsoontorn, A. Chompoosor and S. Maensiri, *J. Appl. Phys.*, 2014, **116**, 53910–53915.
- 151 T. Maeda, T. Kai, A. Kikitsu, T. Nagase, J. Akiyama, T. Maeda, T. Kai, A. Kikitsu, T. Nagase and J. Akiyama, *Appl. Phys. Lett.*, 2002, **80**, 2147–2149.
- 152 C. L. Platt, K. W. Wierman, E. B. Svedberg, R. Van De Veerdonk and J. K. Howard, *J. Appl. Phys.*, 2002, **92**, 6104–6109.
- 153 S. R. Lee, S. Yang, Y. K. Kim and J. G. Na, *Appl. Phys. Lett.*, 2001, **78**, 4001–4003.
- 154 Y. Wang, X. Zhang, Y. Liu, Y. Jiang, Y. Zhang, J. Wang, Y. Liu, H. Liu, Y. Sun, G. Beach and J. Yang, *J. Appl. Phys. D*, 2012, **45**, 485001.
- 155 H. L. Wang, Y. Zhang, Y. Huang, Q. Zeng and G. C. Hadjipanayis, *J. Magn. Magn.*

- Mater.*, 2004, **272–276**, 1279–1280.
- 156 F. M. Abel, V. Tzitzios, D. J. Sellmyer and G. C. Hadjipanayis, *AIP Adv.*, 2016, **6**, 0–5.
- 157 M. V. Maphoru, S. K. Pillai and J. Heveling, *J. Catal.*, 2017, **348**, 47–58.
- 158 M. L. Flenniken, D. A. Willits, S. Brumfield, M. J. Young and T. Douglas, *Nano Lett.*, 2003, **3**, 1573–1576.
- 159 L. Melnick and K. Smith, *Virology*, 1962, **17**, 480–490.
- 160 J. Bass, D. Wilkinson, D. Rankin, B. Phillips, N. Szewczyk, K. Smith and P. Atherton, *Scand J Med Sci Sport.*, 2017, **27**, 4–25.
- 161 T. Topală, A. Bodoki, L. Oprean and R. Oprean, *Clujul Med.*, 2014, **87**, 215–219.
- 162 X.-F. Liu, Y.-M. Xia and Y. Fang, *J. Inorg. Biochem.*, 2005, **99**, 1449–1457.
- 163 S. A. Blank-Shim, S. P. Schwaminger, M. Borkowska-Panek, P. Anand, P. Yamin, P. Fraga-García, K. Fink, W. Wenzel and S. Berensmeier, *Sci. Rep.*, 2017, **7**, 1–11.
- 164 Y. Mikata, Q. He and S. J. Lippard, *Biochemistry*, 2001, 7533–7541.
- 165 O. Pinato, C. Musetti, N. P. Farrell and C. Sissi, *J. Inorg. Biochem.*, 2013, **122**, 27–37.
- 166 L. Messori and A. Merlino, *Inorg. Chem*, 2014, **53**, 3929–3931.
- 167 J. A. Bornhorst and J. J. Falke, *Methods Enzymol.*, 2000, **326**, 245–254.
- 168 S. Mukherjee, I. Mitra, V. P. Reddy B, S. Mahata, J. C. Bose K, S. Dasgupta, W. Linert and S. Ch Moi, *Polyhedron*, 2016, **119**, 84–97.
- 169 J. T. Miller and D. C. Koningsberger, *J. Catal.*, 1996, **162**, 209–219.
- 170 X. Ji, K. T. Lee, R. Holden, L. Zhang, J. Zhang, G. A. Botton, M. Couillard and L. F. Nazar, *Nat. Chem.*, 2010, **2**, 286–293.
- 171 S. Li, N. K. Goto, K. A. Williams and C. M. Deber, *Proc. Natl. Acad. Sci.*, 1996, **93**, 6676–6681.
- 172 J. S. Olson, A. J. Mathews, R. J. Rohlf, B. A. Springer, K. D. Egeberg, S. G. Sligar, J. Tame, J.-P. Renaud and K. Nagai, *Nature*, 1988, **336**, 265–266.
- 173 D. Pum and U. B. Sleytr, *Nanotechnology*, 2014, **25**, 312001.

11 APPENDIX

11.1 SPOT PEPTIDE ARRAY DATA

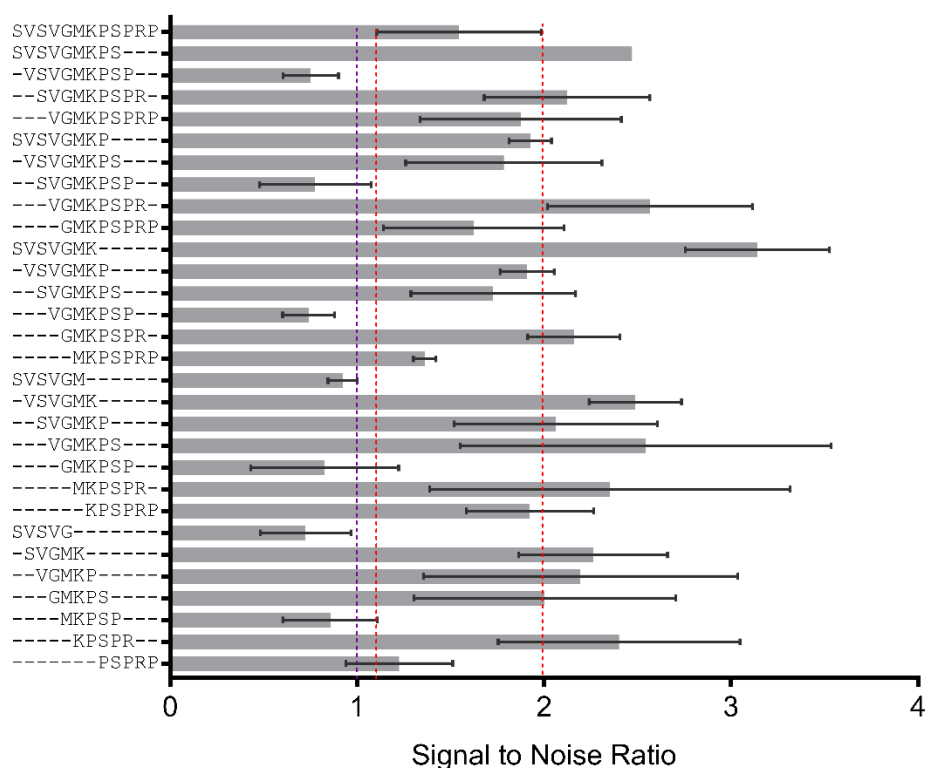


Figure 11.1.1 – Truncation data for LS4 from screening against CoPt NPs. White – reduced SNR, grey – similar SNR and teal – increased SNR.

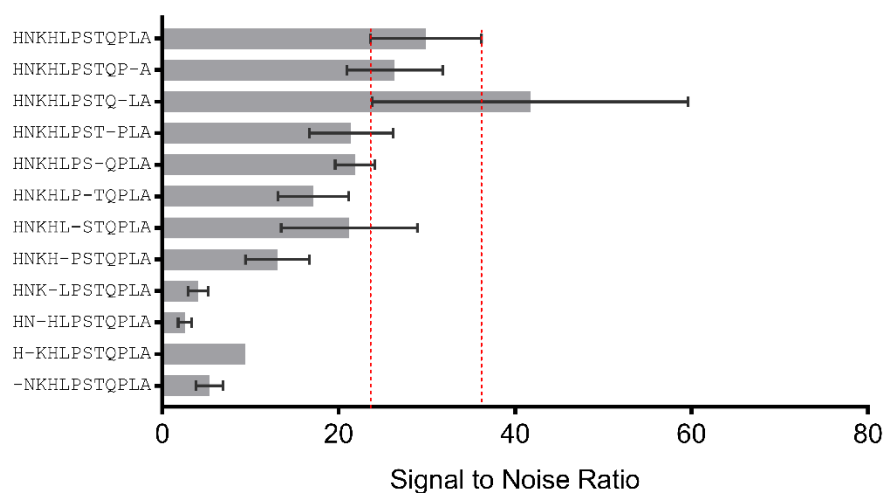


Figure 11.1.2 – Alanine scanning data for LS1 from screening against Pt²⁺.

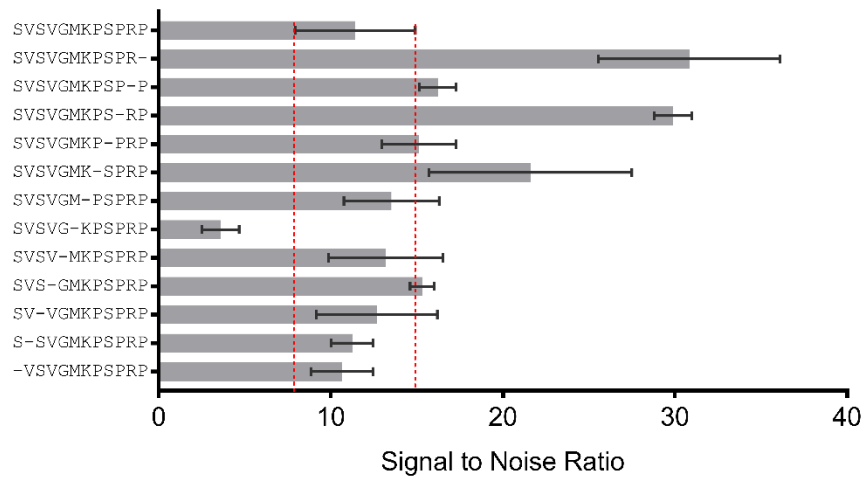


Figure 11.1.3 – Alanine scanning data for LS4 from screening against Pt²⁺.

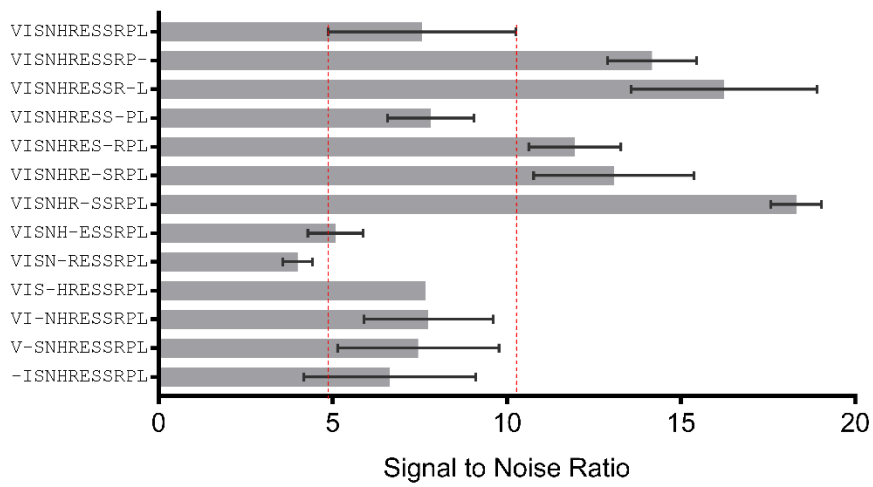


Figure 11.1.4 – Alanine scanning data for LS5 from screening against Pt²⁺.

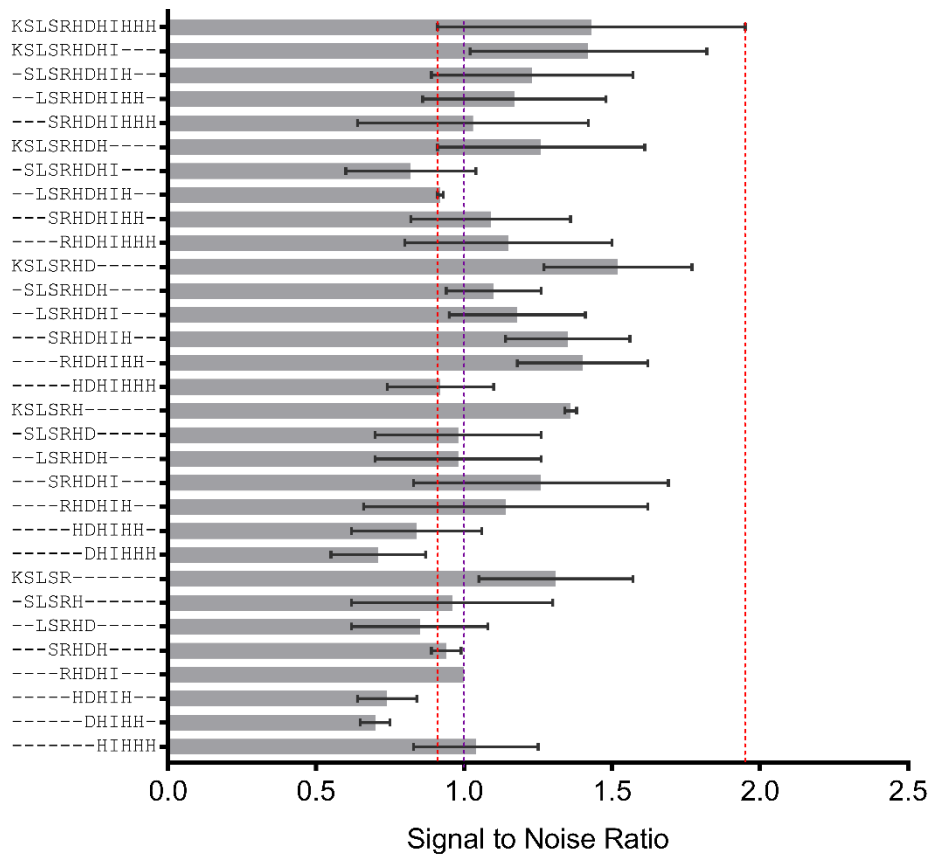


Figure 11.1.5 – Truncation data for LS3 from screening against a CoPt synthesis reaction.

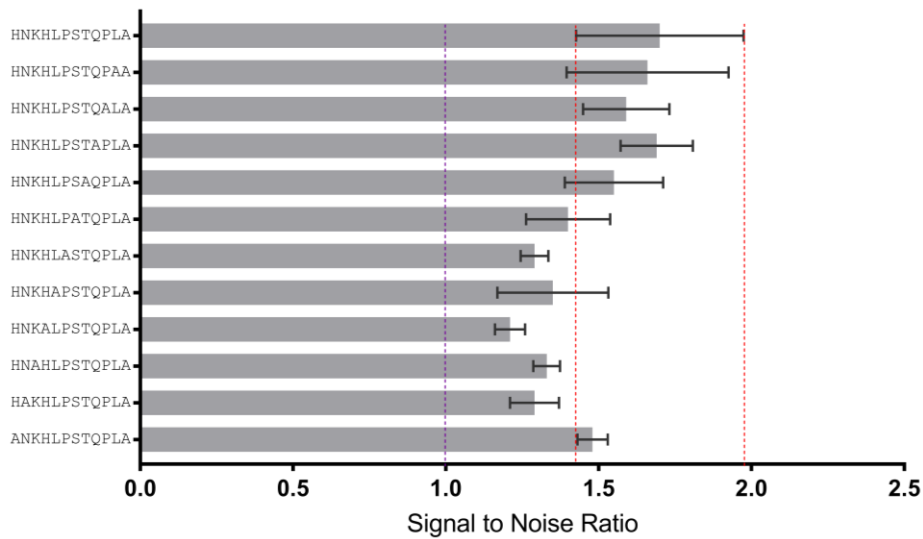


Figure 11.1.6 – Alanine scanning data for LS1 screened against FePt NPs.

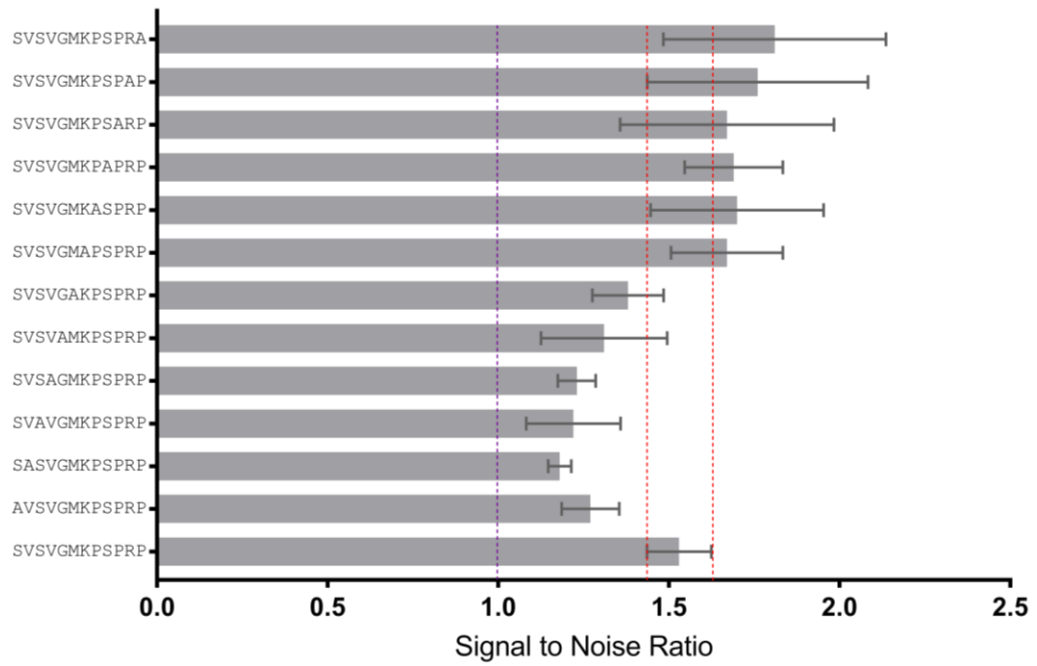


Figure 11.1.7 – Alanine scanning data for LS4 from screening against FePt NPs.

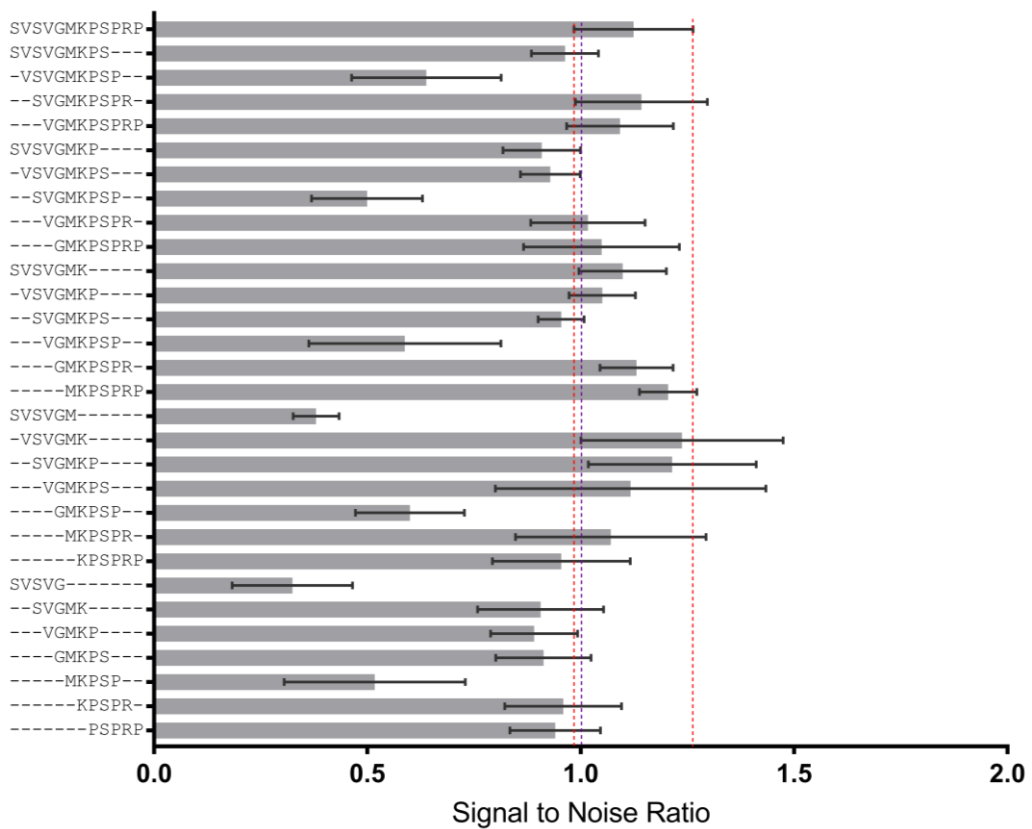


Figure 11.1.8 – Truncation data for LS4 from screening against FePt NPs.

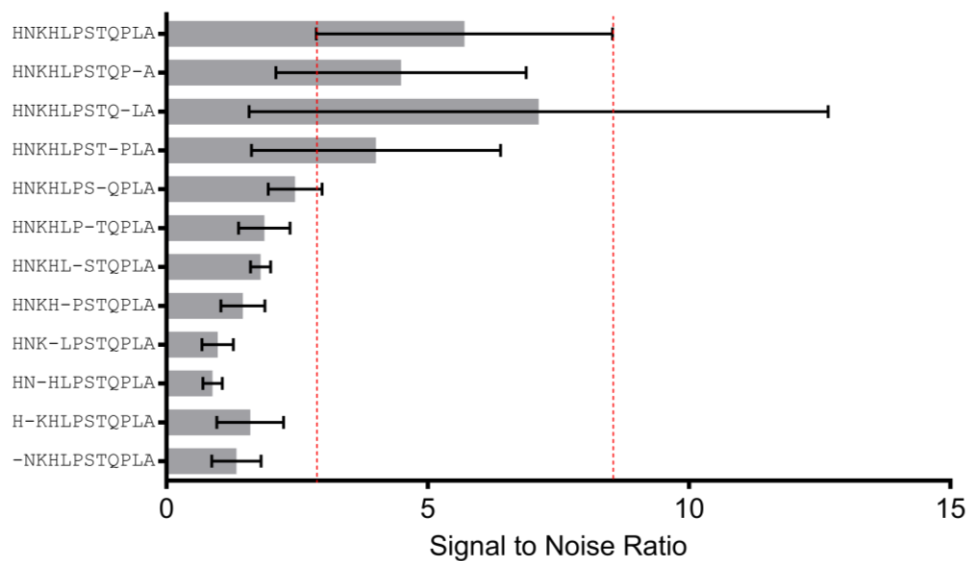


Figure 11.1.9 – Alanine scanning data for LS1 screened against Fe²⁺.

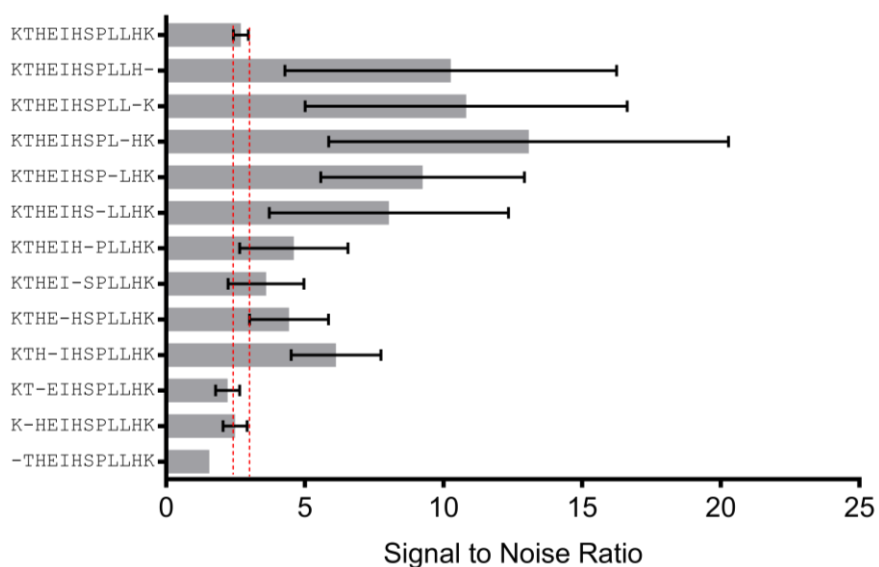


Figure 11.1.10 – Alanine scanning data for LS2 screened against Fe²⁺.

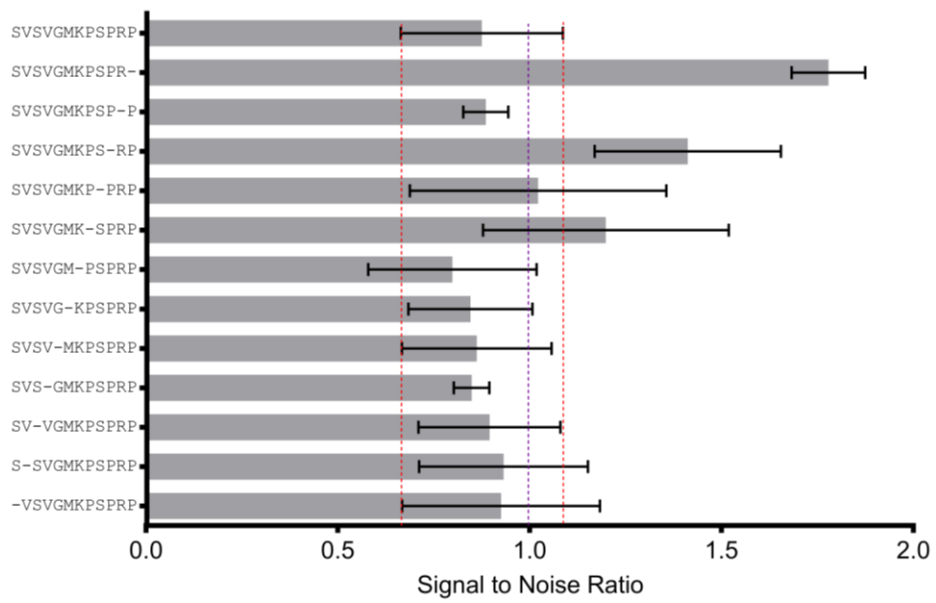


Figure 11.1.11 – Alanine scanning data for LS4 screened against Fe²⁺.

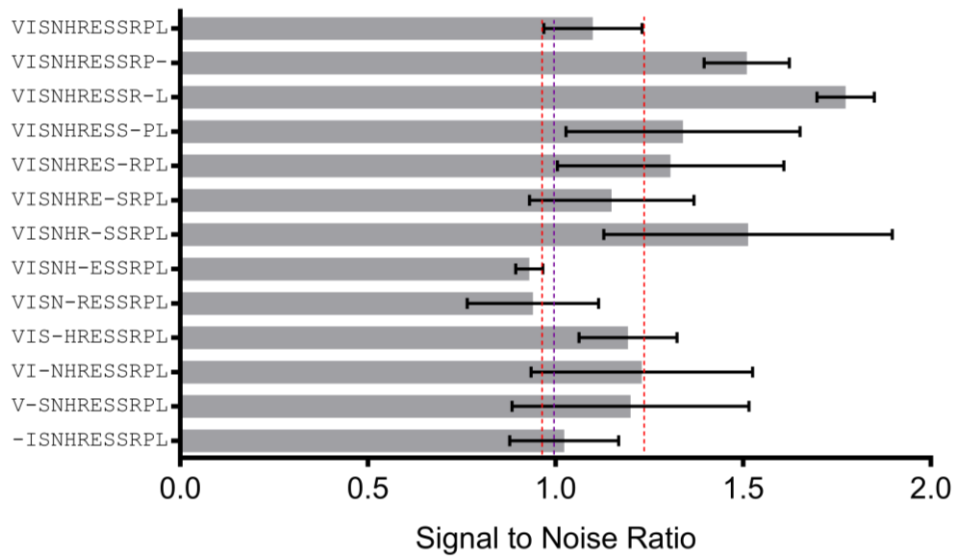


Figure 11.1.12 – Alanine scanning data for LS5 screened against Fe²⁺.

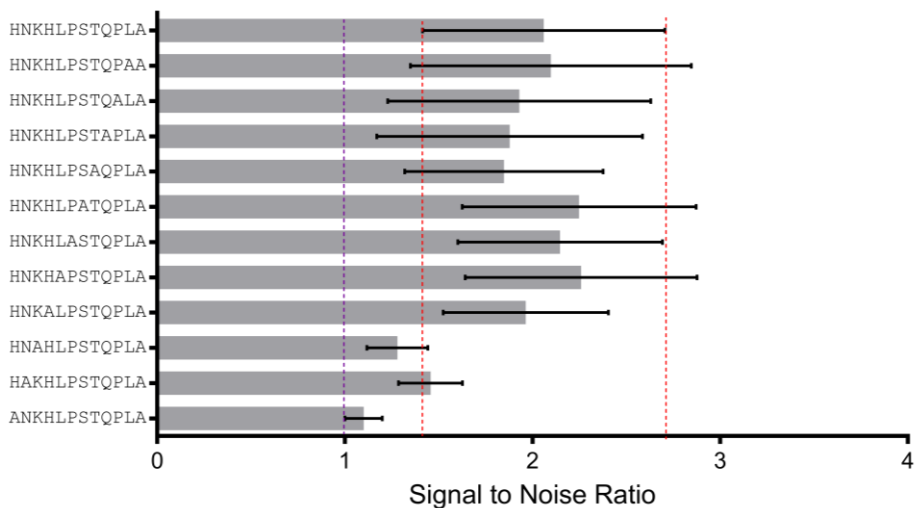


Figure 11.1.13 – Alanine scanning for LS1 screened against an Fe²⁺.

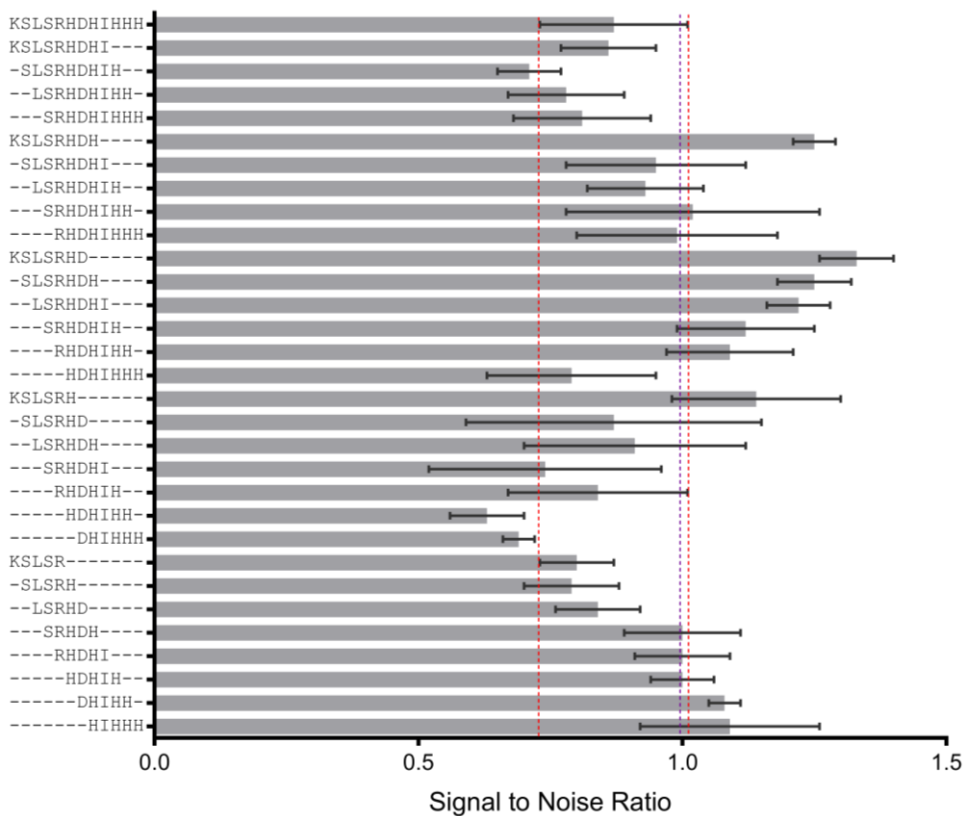


Figure 11.1.14 – Truncation data for LS3 from screening against an FePt synthesis reaction.

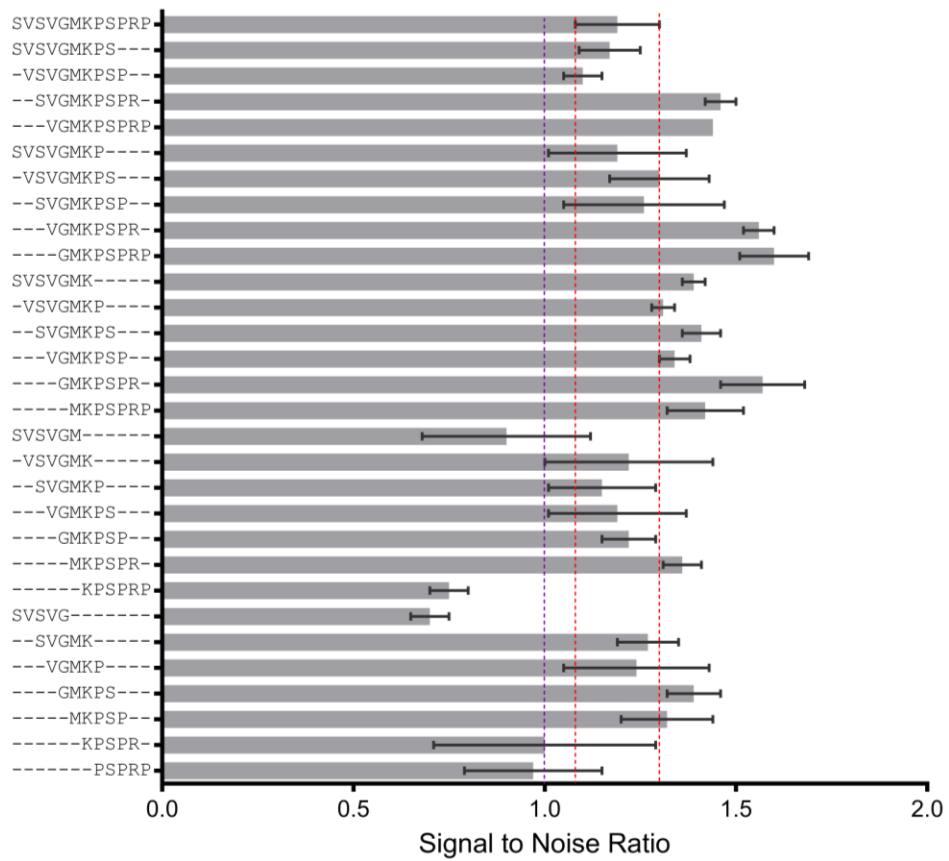


Figure 11.1.15 – Truncation data for LS4 from screening against an FePt synthesis reaction.

11.2 XPS DATA

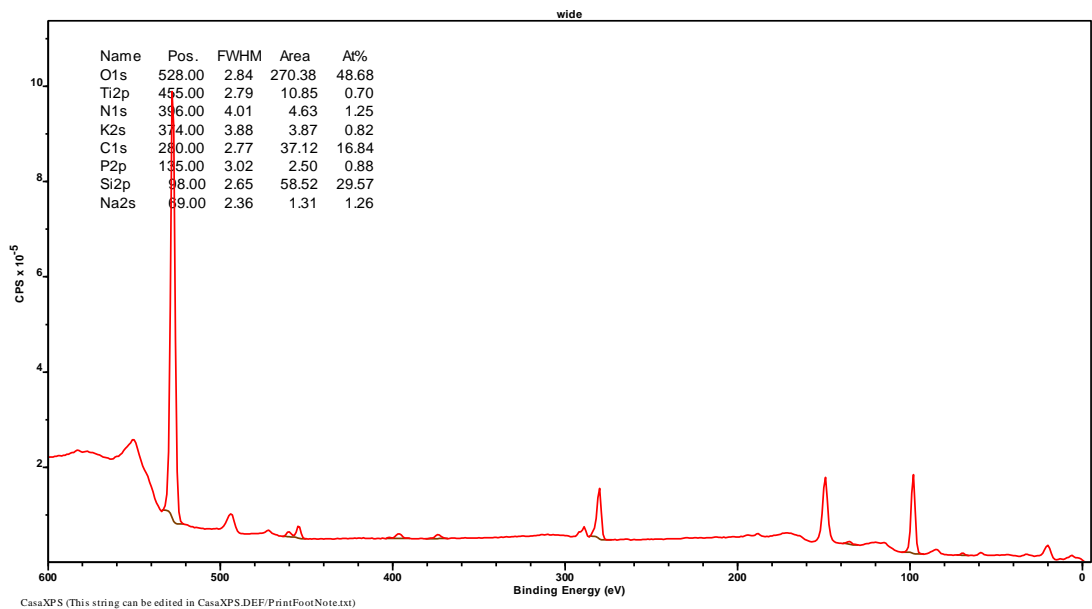


Figure 11.2.1 – Survey scan for APTES on Ti at 0 degrees.

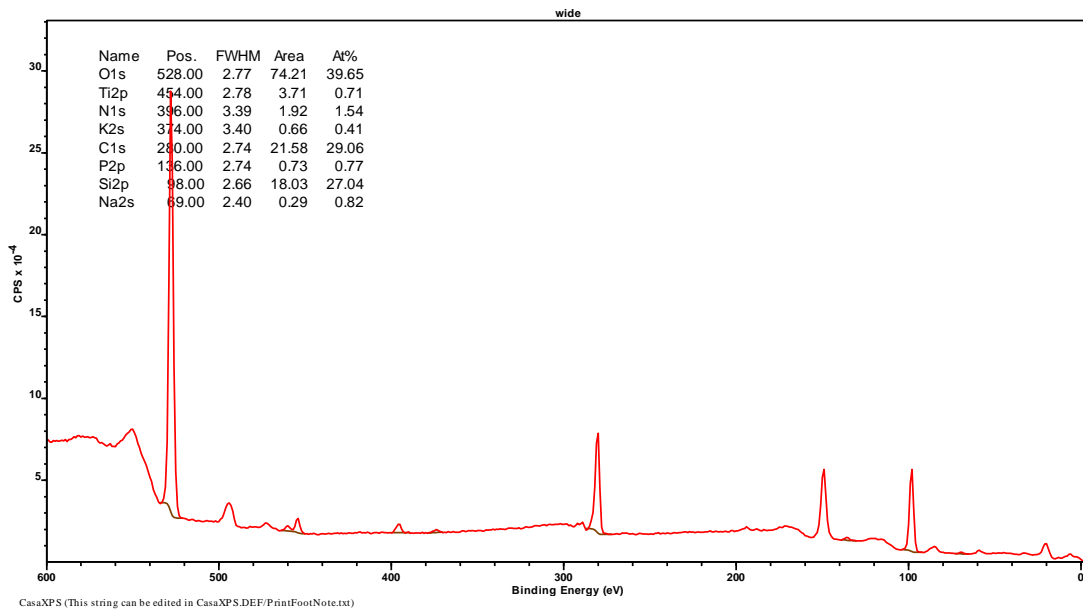


Figure 11.2.2 – Survey Scan for APTES on titania at 53 degrees.

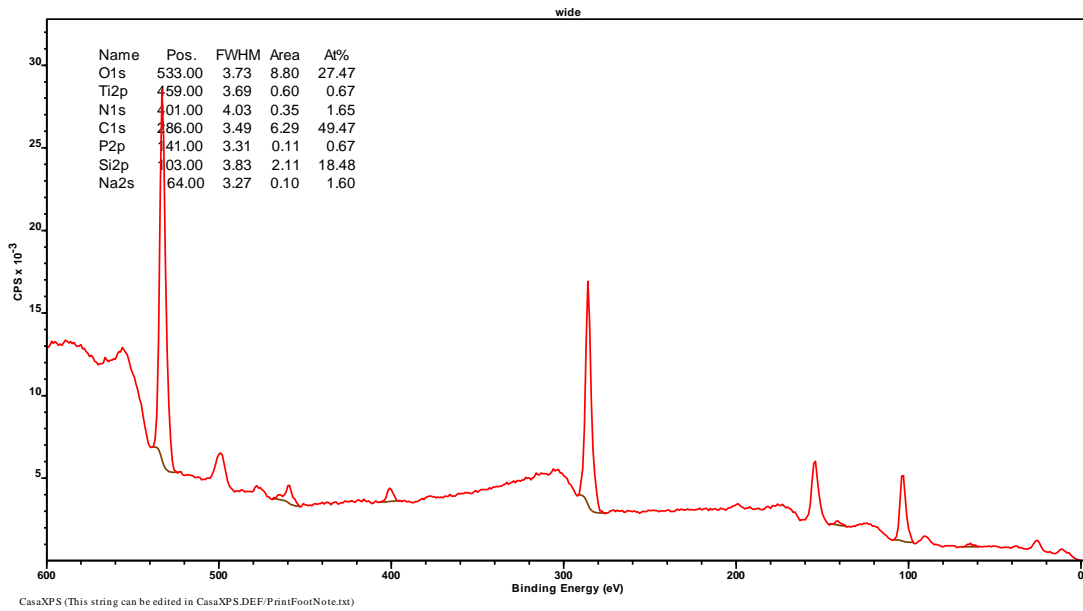


Figure 11.2.3 – Survey scan for APTES on titania at 78 degrees.

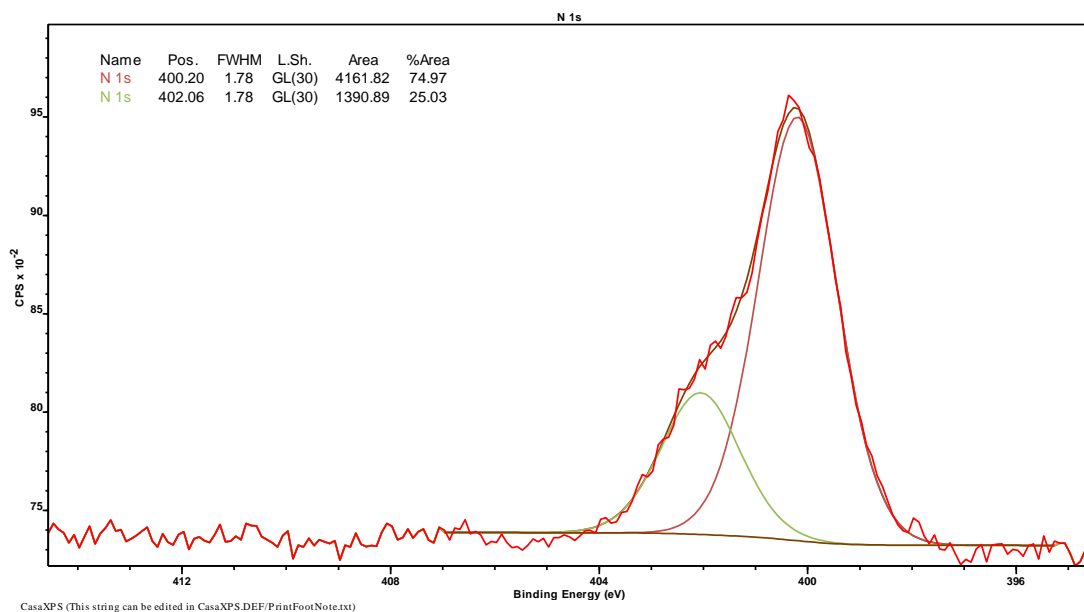


Figure 11.2.4 – Nitrogen 1s scan for APTES on titania at 0 degrees.

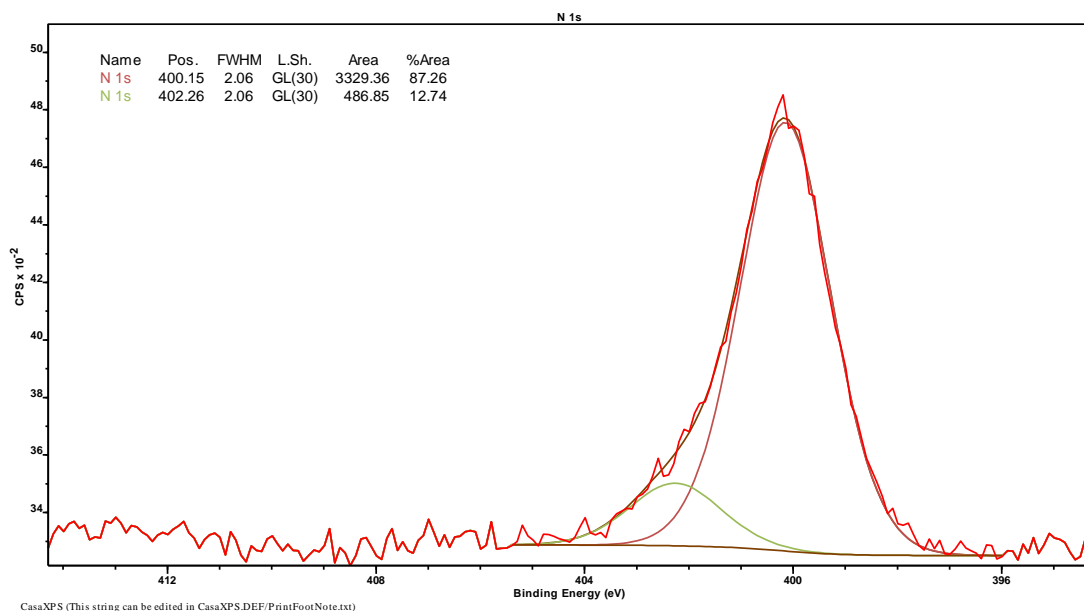


Figure 11.2.5 – Nitrogen 1s scan for APTES on titania at 53 degrees.